Energy- and Time-Resolved Liquid-Microjet Photoelectron Spectroscopy of Paradigmatic Aqueous-Phase Polyatomic Molecules

Dissertation

zur Erlangung des Grades eines

Doktors der Naturwissenschaften

(Dr. rer. nat.)

am Fachbereich Physik

der Freien Universität Berlin

vorgelegt von

Md Sabbir Ahsan

Berlin, 2023

Erstgutachter/in: Dr. Iain Wilkinson
Zweitgutachter/in: Prof. Dr. Karsten Heyne

Tag der Disputation: 07.02.2024

The work presented here has been carried out at the Helmholtz Zentrum Berlin (HZB). The financial support provided by HZB to carry out this doctoral research is acknowledged.

Declaration of Authorship

Last Name: Ahsan

First name: Md Sabbir

I declare to the Freie Universität Berlin that I have completed the submitted dissertation independently and without the use of sources and aids other than those indicated. The presented thesis is free of plagiarism. I have marked as such all statements that are taken literally or in content from other writings. This dissertation has not been submitted in the same or similar form in any previous doctoral procedure.

I agree to have my thesis examined by a plagiarism examination software.

Date:13.02.2024 Signature:

"In the name of Allah, the Most Gracious, and the Most Merciful"

Acknowledgements

I would like to give thanks to Dr. Iain Wilkinson for giving me the opportunity to perform my doctoral research in Photon Science division at HZB and supervising my doctoral research work. Iain has guided me in all aspects of my doctoral thesis work, from teaching the basics of spectroscopy to my laboratory work. I benefited a lot from our weekly scientific discussion on my projects, and his feedbacks were very important in improving my critical thinking about my scientific work. Without his kind supervision and detailed review of my thesis, I would not be able to finish my doctoral thesis successfully. He is not only a good supervisor to me but also a great mentor and motivator to continue my scientific work.

I would also like to thank to Prof. Karsten Hayne for showing interest in my research and acting as a second supervisor for my research activities. I also thank him for his kind review on my doctoral thesis. His feedback on my scientific presentation and thesis writings were very beneficial to me.

I would also like to thank Dr. Robert Seidel for introducing me to the liquid-jet XPS experimental setups at the BESSY II synchrotron radiation facility. I acknowledge his kind support and fruitful discussions during the synchrotron beamtime at BESSY II. I thank and acknowledge Dr. Igor Kiyan for his kind support and supervision in the ULLAS lab facility at HZB. Moreover, his kind support and suggestions after reviewing my doctoral thesis helped me to improve the scientific communication of my results. I also thank Dr. Sergey Bokarev and Vladislav Kochetov for fruitful discussions and performing excellent calculations and spectral simulations that greatly helped in the interpretation of some of my experimental results. I acknowledge their kind support in my research work.

I am also grateful to Florian Gores for designing the hollow core fiber setup and associated vacuum chamber that allowed me to study ultrashort pulse generation. I also acknowledge his kind support in designing the biasable liquid microjet system for my experiments in the laser lab. I thank Dr. Christoph Merschjann for sharing his valuable experience in preparing the data analysis program in Python.

It was a pleasure for me to work and sharing beamtimes with Dr. Nataliia Kuzkova, Dr. Karen Mudryk, and Dr. Hajialamadari Mojtaba, Dr. Dennis Hein, and Dr. Garlef Wartner. I learned a lot by working with all of them. Igor, Daniel, Siqi, Azhar, Karen, and Natalia supported me a lot during the beamtime in the laser lab. I acknowledge the support of my co-workers in my synchrotron and laser laboratory experimental work. Without their kind support, I could not finish all of my measurements. I am really grateful to all of you.

I thank Freie Universität Berlin and HZB workshop members. I acknowledge their kind support in preparing my experimental setups during my doctoral research.

I would like to thank and express my gratitude to Dr. Daniel Walke, Dr. Sreeju Sreekantan, Dr. Abdullah Saif Mondol for spending their valuable time proof reading my doctoral thesis.

Finally, I want to thank my family members- my wife, Mehnaj Tabaksum, my son, Taif Ahsan my parents, Md Ahsanul Islam and Mst Sajeda Khatun and my relatives. All of them inspire me to carry on my doctoral research in abroad. Without their kind support, I could not have finished my thesis.

List of Publications

Included in this Thesis

1. **Ahsan, Md Sabbir**, Vladislav Kochetov, Dennis Hein, Sergey I. Bokarev, and Iain Wilkinson, *"Probing the molecular structure of aqueous triiodide via X-ray photoelectron spectroscopy and correlated electron phenomena."*, Phys. Chem. Chem. Phys. 24 (2022), 15540-15555. **Details will be provided in Chapter 4.**

Author's Contributions: The author performed the UV-Vis measurements to characterize the triiodide aqueous solutions and performed the X-ray photoelectron spectroscopy experiments at BESSY II. The XPS spectra recorded at the PETRA III facility were measured by Iain Wilkinson. The author performed the analysis of the experimental data. The experimental data were interpreted with the help of theoretical calculations and spectral simulations, which were performed by Vladislav Kochetov and Sergey I. Bokarev. Dennis Hein provided support in operating the experimental facilities at BESSY II. The author has prepared and actively reviewed the manuscript.

2. Vladislav Kochetov, **Ahsan, Md Sabbir**, Dennis Hein, Sergey I. Bokarev, and Iain Wilkinson, *"Valence and core photoelectron spectra of aqueous I_3^- from multi-reference quantum chemistry"*, MDPI Molecules 2023, 28(14), 5319. **Minor Details will be provided in Chapter 4.**

Author's Contributions: The author performed the XPS experiments at BESSY II. The XPS spectra recorded at PETRA III were measured by Iain Wilkinson. The author performed the analysis of the experimental data. Dennis Hein provided support in operating the experimental facilities at BESSY II. The author participated in the preparation and reviewing of the manuscript.

3. **Md Sabbir Ahsan**, Shivalee Dey, Igor Yu. Kiyan, Stephen E. Bradforth, Iain Wilkinson, *"Electronically excited state and associated non-adiabatic dynamics in aqueous pyrazine"*, Article is in preparation. **Details will be provided in Chapter 6.**

Author's Contributions: The author planned and performed the steady-state and femtosecond-time-resolved photoemission experiments at the ULLAS facility at HZB. The author performed the photoemission data analysis and participated in the preparation and reviewing of the manuscript.

Partially Included in this Thesis

4. Igor Kiyan, Nataliia Kuzkova, **Md Sabbir Ahsan**, Alexander Firsov, and Iain Wilkinson, *"Monochromatization of ultrashort light pulses from high harmonic generation in the 10 - 100 eV photon energy range with the use of reflective zone plates"*, in preparation. **25^{th} harmonic results are included in Chapter 3.**

Author's Contributions: The author participated in the commissioning of the monochromator, including alignment and measurement of the output spectral and temporal profiles of the beamline. The author participated in the review of the manuscript.

Abstract

Energy and charge transfer processes in aqueous solution play important roles in biochemical processes, where the mechanisms of such phenomena are affected, and even driven, by aqueous-phase reactant-water interactions. Such processes and interactions have been probed using the Liquid-Jet (LJ)-based Photoelectron Spectroscopy (PES) technique. Energy-tunable, ionizing-radiation sources and the non-resonant, resonant, steady-state, and ultrafast-time-resolved PES techniques have been applied to probe the surface or bulk and valence or core-level electronic, and by extension molecular, structure of several archetypal, highly-soluble, aqueous-phase molecular systems: triiodide, pyrimidine, pyridazine, and pyrazine. The chemically-important, lowest vertical ionization energies and characteristic, atom- and isomer-specific core-level (I 3d/ 4d, C and N 1s) spectra of the four studied systems are presented here. Ultrafast time-resolution studies of the excited-state dynamics of aqueous pyrazine solutions are also presented.

With the help of electronic structure theory and spectral simulations, the experimental triiodide X-ray PES results suggest a near-linear geometric structure and increased asymmetry of the anion in aqueous solution, compared to in ethanol and methanol. This asymmetry was found to be greater at the surface-vacuum interface than in the aqueous solution bulk. Additionally, non-resonant and C and N pre-K-edge resonant X-ray PES experiments were performed on the aqueous diazine molecules, revealing the vertical ionization potentials, bonding character and atomic parentage, intra- and intermolecular charge re-arrangement, and degree of localization of the valence band Molecular Orbitals (MOs).

Having measured the ground-state ionization energetics, UV-pump (267 nm), EUV-probe (32.1 nm) femtosecond time-resolved LJ-PES measurements were performed on aqueous pyrazine solutions under Pump-Induced-Space-Charge (PISC) minimized conditions. Global fit analyses of the LJ-PES data revealed an initial 40 ± 20 fs internal conversion (IC) timescale, with subsequent population transfer to lower-lying states occurring in 35 ± 10 ps and 120 ± 30 ps. Slower relaxation behaviors were found in aqueous pyrazine solution in comparison to previously reported gas-phase studies. Associated solvent-induced relaxation mechanisms have been proposed. Furthermore, it is suggested that the relaxation dynamics of aqueous pyrazine are altered when similar experiments are performed under PISC conditions.

In general, this thesis highlights the sensitivity of LJ-PES to solution-phase electronic structure, molecular geometries, and dynamic photophysicochemical processes. The experimental results provide the necessary information to enhance the implemented experimental techniques, model general polyatomic molecular behaviors in aqueous solutions, and better understand the photochemical processes that underly numerous real-world applications.

x

Kurzfassung

Energie- und Ladungsübertragungsprozesse in Lösungen in Wasser spielen eine wichtige Rolle in biochemischen Prozessen, bei denen die Mechanismen solcher Phänomene durch Wechselwirkungen zwischen Reaktanten und Wasser in der wässrigen Phase beeinflusst und sogar angetrieben werden. Solche Prozesse und Wechselwirkungen wurden mit der auf Flüssigkeitsstrahlen (LJ) basierenden Photoelektronenspektroskopie (PES)-Technik untersucht. Energieabstimmbare, ionisierende Strahlungsquellen und die nichtresonanten, resonanten, stationären und ultraschnellen zeitaufgelösten PES-Techniken wurden angewendet, um die Oberfläche oder Masse und die Valenz- oder Kernebene elektronischer und im weiteren Sinne molekularer, Struktur mehrerer archetypischer, hochlöslicher molekularer Systeme in wässriger Phase: Triiodid, Pyrimidin, Pyridazin und Pyrazin. Hier werden die chemisch wichtigen, niedrigsten vertikalen Ionisierungsenergien und charakteristischen, atom- und isomerspezifischen Kernebenenspektren (I 3d/ 4d, C und N 1s) der vier untersuchten Systeme vorgestellt. Außerdem werden ultraschnelle zeitaufgelöste Studien der Dynamiken angeregter Zustände wässriger Pyrazinlösungen vorgestellt.

Mit Hilfe der Theorie der elektronischen Struktur und Simulationen von Spektren deuten die experimentellen Triiodid-Röntgen-PES-Ergebnisse auf eine nahezu lineare geometrische Struktur und eine erhöhte Asymmetrie des Anions in wässriger Lösung im Vergleich zu Ethanol und Methanol hin. Diese Asymmetrie wurde an der Oberfläche-Vakuum-Grenzfläche stärker als in der wässrigen Lösungsmasse gefunden. Zusätzlich wurden an den wässrigen Diazinmolekülen nichtresonante und C- und N-K-Pre-Edge resonante XPS Experimente durchgeführt, welche die vertikalen Ionisierungspotentiale, den Bindungscharakter und dessen atomare Abstammung, die intra- und intermolekulare Ladungsumordnung, und den Grad der Lokalisierung der Valenzband-Molekülorbitale (MOs) aufdeckten.

Nach der Messung der Grundzustandionisationsenergetik wurden zeitaufgelöste Femtosekunden-LJ-PES-Messungen mit UV-Pump- (267 nm) und EUV-Probepulsen (32,1 nm) an wässrigen Pyrazinlösungen unter minimierter pumpen-induzierter Raumladung (PISC) durchgeführt. Globale Anpassungsanalysen an den LJ-PES-Daten ergaben eine anfängliche Zeitskala für die interne Konvertierung (IC) von 40 ± 20 fs, wobei der anschließende Besetzungstransfer in tiefer gelegene Zustände in 35 ± 10 ps und 120 ± 30 ps erfolgte. Im Vergleich zu vorherigen Gasphasenstudien wurde in wässriger Pyrazinlösung ein langsameres Relaxationsverhalten festgestellt. Es wurden damit verbundene lösungsmittelinduzierte Relaxationsmechanismen vorgeschlagen. Darüber hinaus wird vermutet, dass sich die Relaxationsdynamik von wässrigem Pyrazin verändert, wenn ähnliche Experimente unter PISC-Bedingungen durchgeführt werden.

Im Allgemeinen unterstreicht diese Arbeit die Empfindlichkeit von LJ-PES gegenüber der elektronischen Struktur der Lösungsphase, Molekülgeometrien und dynamischen photophysikochemischen Prozessen. Die experimentellen Ergebnisse liefern die notwendigen Informationen, um die implementierten experimentellen Techniken zu verbessern, allgemeine polyatomare molekulare Verhaltensweisen in wässrigen Lösungen zu modellieren und die photochemischen Prozesse, die zahlreichen Anwendungen in der Praxis zugrunde liegen, besser zu verstehen.

List of Abbreviations

APPLE-2 Advanced Planar Polarized Light Emitter-2

BE Binding Energy

BOA Born-Oppenheimer Approximation

CC Cross-Correlation

CTTS Charge-Transfer-to-Solvent

DFT Density Functional Theory

DLD Delayline Detector

EAL Effective Attenuation Length

ETMD Electron Transfer Mediated Decay

EUV Extreme UltraViolet

FWHM Full Width Half Maxima

HHG High Harmonic Generation

HOMO Highest Occupied Molecular Orbital

HPLC High-Pressure Liquid Chromatography

IC Internal Conversion

ICD Intermolecular Coulombic Decay

IET Intra- and Intermolecular Energy Transfer

ISC Intersystem Crossing

IVR Intramolecular Vibrational Energy Redistributions

KE Kinetic Energy

LADM Low-Angular Dispersion Mode

LJ Liquid-Microjet

LJ-TRPES Liquid-Microjet-Based Time-Resolved Photoelectron Spectroscopy

LJ-XPS Liquid-Microjet-Based X-ray Photoelectron Spectroscopy

LMCT Ligand-to-Metal Charge Transfer

LUMO Lowest Unoccupied Molecular Orbital

MADM Medium-Angular Dispersion Mode

MO Molecular Orbital

PAD Photoelectron Angular Distribution

PADs Photoelectron Angular Distributions

PCET Proton-Coupled-Electron Transfer

PCM Polarized Continuum Model

PE Photoelectron

PES Photoelectron Spectroscopy

PEY Partial-Electron-Yield

PISC Pump-Induced-Space-Charge

RIXS Resonant-Inelastic X-ray Scattering

RPES Resonant Photoelectron Spectroscopy

SFG Sum-Frequency Generation

SHG Second Harmonic Generation

SU Shake-Up

TAS Transient Absorption Spectroscopy

Ti:Sa Titanium:Sapphire

TOF Time-of-Flight

TRPES Time-Resolved Photoelectron Spectroscopy

TRXAS Time-Resolved X-ray Absorption Spectroscopy

UV Ultraviolet

VIE Vertical Ionization Energy

VIEs Vertical Ionization Energies

WAM Wide-Angle Mode

XA X-ray Absorption

XAS X-ray Absorption Spectroscopy

XPS X-ray Photoelectron Spectroscopy

Contents

List of Figures

List of Tables

Chapter 1

Introduction

Chemical equilibrium is reached at the equilibrium geometry associated with the ground states of stable molecular and material systems. However, if sufficient energy is provided to excite such systems, they will absorb energy and be driven away from such an equilibrium. According to the Bohr model, electrons will be promoted to produce an excited state, changing the electronic configuration when it is irradiated at resonant frequencies. The excited electron will relax through lower-lying states and eventually return to the ground state. The electronic configuration of the perturbed molecular or material structure will evolve in time as it progresses to reestablish an equilibrium. The associated electronic rearrangements and nuclei readjustments are the basis of chemical transformations. Electronic rearrangement refers to the change of the dominant electronic configurations *i.e.* a change in the electronic state, and nuclei readjustment refers to the change of the bond lengths and angles.

The electronic states of molecules are coupled to each other, crossing each other in multi-dimensional co-ordinate space, and any upper electronic state can efficiently transform into a lower electronic state in the vicinity of the state intersection point(s). In this picture, electronic potential energy surfaces define the reaction pathways, while the electronic state gradients and gaps between the electronic states largely define the rates of state-to-state population transfers. The intrinsic properties of a molecule are dependent on the underlying electronic structure. These include the absorption and emission properties, place of the connection points where electronic states cross each other, dipole moments, photophysical and photochemical properties and dynamics, stability, etc[1]. Such intrinsic properties of an isolated molecule may change, depending on its environment. The environment generally perturbs the molecular electronic structure and can change the intrinsic properties of the molecular system, influencing chemical reaction mechanisms, pathways and or reaction rates.

The research carried out in this thesis work aims to understand the changes of intrinsic electronic structure and associated relaxations and reaction pathways of polyatomic molecules in an aqueous environment. The water solvent in aqueous solutions plays important roles in all aspects of our life. More than 50% of the human body is comprised of water[2]. Water defines many materials around us[3], plays important roles in defining protein and nucleic acid structure, and their activities, and/ or even cell communication systems[4]. Aqueous solutions are key in driving energy and charge transfer processes in bio-chemical environments[4]. Water is also broadly applied across chemical, material, and environmental sciences etc[2].

The Hydrogen (H) atoms in the water molecules in aqueous solutions interact with the neighboring oxygen (O) atoms through H-bonds. During the solvation process of a solute molecule, some of the hydrogen-bonds are broken and new hydrogen-bonds are created with the solute[2,5]. Moreover, a fluxional and time-dependent

electronic interaction arises between the solute and solvent molecules[6,7]. The degree of this interaction depends on the intrinsic properties of the solutes and solvents[8,9]. Due to these electronic interactions, the solvent molecular H-bond structure adjusts to accommodate the solute molecules (to lower the energy of the system) and the solute and solvent molecules are polarized. Such changes of the electronic and nuclear distributions result in changes to the associated molecular symmetry and in turn cause changes in the electronic state energetics of the solute and solvent molecules. This can result in changes to reaction rates and pathways in strongly interacting solvents like water.

A liquid/solution medium may be divided into two different regions according to the depth within that medium: a liquid-vacuum-interface (also refered to as a surface) and the liquid bulk. The surface region starts from the transition region of the gas to the liquid phase and extends below the air-water interface by about 1-2 nm inside the solution (depending on the concentration and type of solutes)[10–12]. A solute molecule in the bulk of a solution experiences a similar environment, on average throughout the liquid bulk. In the liquid-vacuum-interface or liquid-gas interface region, there is an asymmetry in the environment experienced by the interfacial solute and solvent molecules. Thus, solute molecules generally experience different molecular environments and intermolecular potentials and forces in the surface region compared to in the bulk of the solution[13]. A difference in the molecular environment can lead to a solute molecule to having a potential orientation and exhibiting a different potential energy surface compared to in the bulk region of a solution. A modification in the potential energy surface in the surface region can lead to a change of reaction rate[13–19] and potentially reaction mechanism[15].

In order to shed light on aqueous-phase molecular behavior and associated photochemical processes, it is important to understand how the solute molecules respond when they are embedded in their applied environment, where the focus in this thesis is on solvation in an aqueous solution. Such environmental responses are imprinted on the molecular bond-length distributions and associated symmetry of the molecule and effect the electron energetics of the system and, hence, the system reactivity. Any change of molecular bond-length or symmetry is reflected in the electronic structure of the solute molecule. Thus, understanding the electronic structure of a molecule in its applied environment is a prerequisite to understanding it's chemical reactivity. Experiments are required that allow access to the electronic structure of the molecule with respect to some well-defined energy reference. Thus, the Photoelectron Spectroscopy (PES) technique has been used to characterize the electronic structure of selected hydrated molecules with respect to the vacuum level[20,21]. In order to study high-vapor-pressure aqueous solutions, the microjet technique has been combined with PES. This approach will be referred to as Liquid-Microjet (LJ)-based PES[22] in the following. This is a powerful technique that can probe either the surface or bulk region of liquids by varying the excitation photon energy[10,11,23].

The research reported here has been conducted to answer a number of scientific questions by characterizing ground and excited state electronic structure using the LJ-based PES technique. These questions include: is the molecular symmetry or geometric structure of archetypal polyatomic molecules altered in an aqueous environment? How can the electronic structure be characterized in an aqueous environment? Is the molecular symmetry or the geometric structure different at the liquid-vacuum-interface (surface) compared to in the bulk region of the solution? How are photophysical or photochemical pathways and relaxation time-scales affected in an aqueous solution?

Considering the scientific questions introduced above, the research reported here was carried out on four different hydrated molecular systems. These are triiodide, pyridazine, pyrimidine and pyrazine, as shown in Figure 1.1. The first, the triiodide molecule exhibits Ultraviolet (UV) photodissociation behavior in that gas-phase, ethanol and methanol solution, and coherent photoproduct vibrational wavepacket motion[24–36].

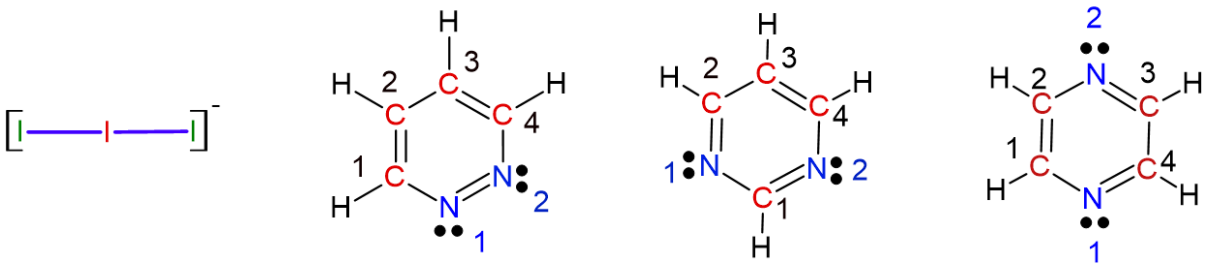

(a) Triiodide ($D_{\infty h}$) (b) Pyridazine (C_{2v}) (c) Pyrimidine (C_{2v}) (d) Pyrazine (D_{2h})

Figure 1.1: Gas-phase molecular structure and symmetry of the triiodide, pyridazine, pyrimidine, and pyrazine molecules.

Such processes have also been studied in the aqueous phase[31–33]. The last three molecules consist of a benzene ring where two C-H bonds have been replaced with two N atoms. The three isomers are called diazine molecules and are known as proton acceptors[37]. Collectively, following photoexcitation, the polyatomic molecules exhibit almost all of the general properties of photoinduced excited state processes. For example, the gas-phase diazine molecules highlight Internal Conversion (IC), Intersystem Crossing (ISC), and Intramolecular Vibrational Energy Redistributions (IVR) after UV excitation and are also expected to undergo such processes in the aqueous phase[38]. Moreover, all of the molecules considered here have high UV photoabsorption cross-sections, making them particularly suitable for time-resolved studies of their photoexcited state dynamics.

This thesis work is divided into two parts. The first part is associated with the characterization of the ground- and ionized-state electronic structure of the aqueous solutions. The second part describes investigations of the excited-state electronic structure and associated relaxation dynamics in aqueous solution. The X-ray Photoelectron Spectroscopy (XPS) technique was used to characterize the ground state of the aqueous molecules. Modern beamlines at synchrotron facilities, *e.g.* U49-2 PGM-1, BESSY II, Berlin and P04, PETRA III, Hamburg provide a wide range of tunable photon energies spanning upto 3000 eV that allow valence and core electronic structure of hydrated molecule to be studied and characterized. Such tunable photon energies also enable solution depth-dependent Photoelectron (PE) spectroscopy experiments to be performed to obtain information about aqueous solutes. Moreover, the solute molecules can be resonantly excited using XPS, in so called Resonant Photoelectron Spectroscopy (RPES) experiments, to provide additional electronic structure information about the studied systems. XPS and RPES provide electron binding energies (BE). Such ground state information is required to design, perform and interpret Time-Resolved Photoelectron Spectroscopy (TRPES) experiments, including UV pumped and Extreme UltraViolet (EUV) probed experiments, which are used to explore excited state dynamics, electronic structure and associated electronic relaxation dynamics in aqueous solutions.

Following this introduction to the presented thesis work, **Chapter 2** describes the sceintific background and available information that provides the basis of the scientific work reported in this thesis. **Chapter 3** highlights the methods, instrumentation and related experimental setups used in the research work presented here.

Chapter 4 describes XPS studies on the aqueous triiodide molecule. Aqueous triiodide solutions were prepared by mixing iodine and sodium iodide in aqueous solutions and the $I_{2(aq.)}$-to-$I_{3(aq.)}$ conversion efficiencies of the different mixtures were characterized using UV-Visible (Vis) absorption spectroscopy. Liquid-microjet based, non-resonant XPS studies were performed on the triiodide aqueous solutions to investigate the valence and core, ground-state electronic structure and molecular bond-length asymmetry of the anion, in both liquid-surface- and more bulk-sensitive experiments. The experimental results were combined with the

computational chemistry results and spectral simulations (performed by Vladislav Kochetov and Sergey I. Bokarev) to identify the molecular structure and symmetries of the involved electronic states, which were related to the experimentally observed photoelectron peaks. The experimental results suggest that the molecule remains near-linear, on average, in the aqueous solution and that the molecular asymmetry is higher in the surface region of the solution compared to the bulk region.

Non-resonant and resonant XPS studies on the diazine molecules are presented in **Chapter 5** . Similar to the triiodide studies, surface-and bulk-sensitive non-resonant XPS studies were undertaken, which investigated the valence and core level electronic structure of the molecules. Since the ionizing transition energies of the aqueous diazines overlap with many of the water solvent transition energies, limited information can be obtained about the solute electronic structure in the non-resonant ionization experiments. Such limitations were partially overcome by using resonant excitation and ionization approaches, which allowed additional solute valence band features to be identified and the associated orbital characters to be analyzed. The aqueous diazine results have also been compared to previously reported gas-phase results to identify solvent-induced changes in the solute ground state electronic structure. The experimental results and associated comparisons suggest intra- and intermolecular charge re-arrangements, Molecular Orbital (MO) localization/ delocalization, and changes in molecular bonding character and bond-lengths in the aqueous solutions.

Chapter 6 presents a UV-pumped-EUV-probed TRPES study on aqueous pyrazine solutions. Performing condensed-phase UV/ EUV TRPES experiments using a low-repetition-rate laser system is challenging due to the Pump-Induced-Space-Charge (PISC) effect. PISC causes the measured photoelectron Kinetic Energies (KEs) to be shifted from their native values, potentially obscuring the photorelaxation processes under investigation. Such shifts are dependent on the intensity and time-delay of the laser pulses. They are particularly apparent on longer pump-probe time-delays (above $\sim$100 ps) and are less obvious for shorter time-delays (below $\sim$1 ps). Seemingly uniquely for liquid-phase experiments using high-harmonic-based EUV sourced, a pump-pulse intensity that minimized the PISC effect below detectable levels was implemented in these experiments, which still allowed TRPES studies to be performed. The excited state energetics and the relaxation time-scale have been identified and characterized under these conditions by modeling the experimental spectra. The results are compared to those of previously reported gas-phase studies. It was found that the photoemission peaks are broadened and shifted in the aqueous-phase in comparison to in similar gas-phase experiments. The relaxation processes are relatively slower in the aqueous phase compared to the previously gas-phase studies[39,40]. The overall aqueous-phase excited state populations are also longer-lived and a number of different relaxation pathways seem to be involved in returning to the ground state.

Performing a UV/ EUV TRPES studies using relatively high pump-intensity reduces the acquisition time and allows TRPES datasets to be recorded with a better signal-to-noise ratio. Lower pump-pulse intensities increase the required integration time to achieve reasonably good signal-to-noise ratios. Almost all of the previously reported UV/EUV time-resolved studies have been performed using relatively high pump-pulse intensities that created a PISC effect[41–43]. It has generally been assumed that the PISC effect induces negligible effects at shorter pump-probe delays and therefore had no impact on the probed relaxation dynamics. To test this assumption, an experimental study was performed with aqueous pyrazine to determine the impact of the PISC effects on the shorter time relaxation processes, specifically comparing the relaxation time-constants measured with PISC effects and where they were minimized. The result highlights the importance of implementing appropriately low pump pulse intensities when studying liquids, otherwise the PISC effect can modify the solution electronic structure and solute relaxation time-scales.

Finally, **Chapter 7** describes the main conclusions, limitations, and possible extensions of the research work presented in this thesis.

Chapter 2

Scientific Background

The constituent atoms, bonding environment, and electronic configuration of a molecule determines its structural and functional properties. In order to understand and drive energy, charge, and mass transfer processes in numerous applications, it is crucial to characterize the electronic structure of a molecule (and material systems) on an absolute energy scale. Several spectroscopic methods are available to understand electronic structure, such as photon absorption spectroscopy, photon emission spectroscopy, and photoelectron spectroscopy. This chapter presents the scientific background of the experimental techniques used in this thesis work. Since this research focuses on studying molecules in aqueous solutions, the previously reported scientific background on the solvent and studied solute molecules that are relevant to this research work are also presented.

2.1 Molecular Orbitals and Electronic Structure

A simple system like a hydrogen atom, has only one electron. Solutions of the Time-Independent Schrödinger Equation (TISE) of the one-electron system provide the wavefunctions and atomic orbitals. In a one-electron molecule such as H_2^+, the molecular orbitals can be formed by taking linear combinations of the atomic orbitals of the participating atoms[44]. The valence molecular orbitals are delocalized over the atomic centers, lowering the system energy, and allowing atoms to be coupled to each other through chemical bonding[45]. Orbitals of one-electron wavefunctions can be connected to experimental observables. The square of the wavefunctions gives the electron probability distributions in space, which can be probed experimentally[45]. Different electronic structures can be modeled by different MO populations, which can be related to different observables. Dyson orbitals are usually used to describe the experimental observations related to PES, which are the overlaps between the N-electron wavefunctions of the neutral orbitals and the N-1 electron wavefunctions of the ionized orbitals. In contrast, natural transition orbitals can be related to experimental observables in other linear spectroscopies such as UV-Vis or x-ray absorption[45].

The orbital concept is not so readily applied to molecules with multiple electrons. Their wavefunctions depend on the coordinates of all of the electrons, which are nonseparable and correlated. Therefore, an appropriate model requires some approximation to describe the electron configuration and electronic correlation of an N-electron system. According to the Hartree-Fock model with N electrons, the correlated electron orbital is given by the antisymmetrized product of N orbitals, called Slater determinants[45]. The fundamental properties, such as the electronic energy of a correlated electron system, do not depend on the specific choice of orbitals. Any linear combination of the occupied Hartree-Fock orbitals can describe a multi-electron system's electronic configuration. The minimum energy configuration of the linear combination of the occupied Hartree-Fock

orbitals is used to define the ground electronic state of the system. Via light-matter interactions, electrons can be promoted to form an excited electronic state when a ground-state molecule absorbs a photon of sufficiently high energy. Generally, a MO electronic structure framework can often be usefully applied to describe the electronic structure of stable electronic ground states and the low-lying photooxidised states that are produced in single-photon ionizing transitions. Correspondingly, simple MO formalisms are used to describe the ground electronic and initially produced photooxidised state electronic structures of the triiodide and diazine systems that are discussed in detail in Chapters 4 and 5.

The simple molecular orbital descriptions of an electronic state generally fails to describe excited electronic configurations of polyatomic molecules. This case is illustrated in panel A in Figure 2.1, which shows the electronic configuration of the pyrazine molecule, which is considered in detail in Chapter 6. S_0 denotes the ground-state, and S_1 and S_2 label the excited-state electronic structures. The Koopmans correlated cationic electronic configurations (D_0, D_1, and D_3) are shown in Panel (A) in Figure 2.1 and will be discussed in Sections 2.4.1, 2.4.5, 2.5.4. When an electron is excited from the $1b_{1g}$ to $2b_{3u}$ molecular orbitals, the resulting configuration of the molecule becomes $(1b_{1g})^{-1}(2b_{3u})^{1}$ and the molecule has $^1B_{2u}$ symmetry. Similarly, an electron can be excited from the $1b_{2g}$ to $1a_u$ molecular orbitals, to also result in a $^1B_{2u}$ molecular symmetry. Both transitions have $\pi\pi^*$ characters and yield similar energetics. In this case, the electronic character of the $^1B_{2u}$ (S_2) excited electronic state is better described by the weighted superposition of two dominant MO configurations rather than a single set of molecular orbital populations. The inability of a single MO diagram to characterize the electronic structure is due to significant electron configuration interaction, which commonly has to be considered when describing excited-state electronic structure. The linear combination of single electron MO combinations can more generally be used to characterize electronically excited states and the resultant electronic configurations.

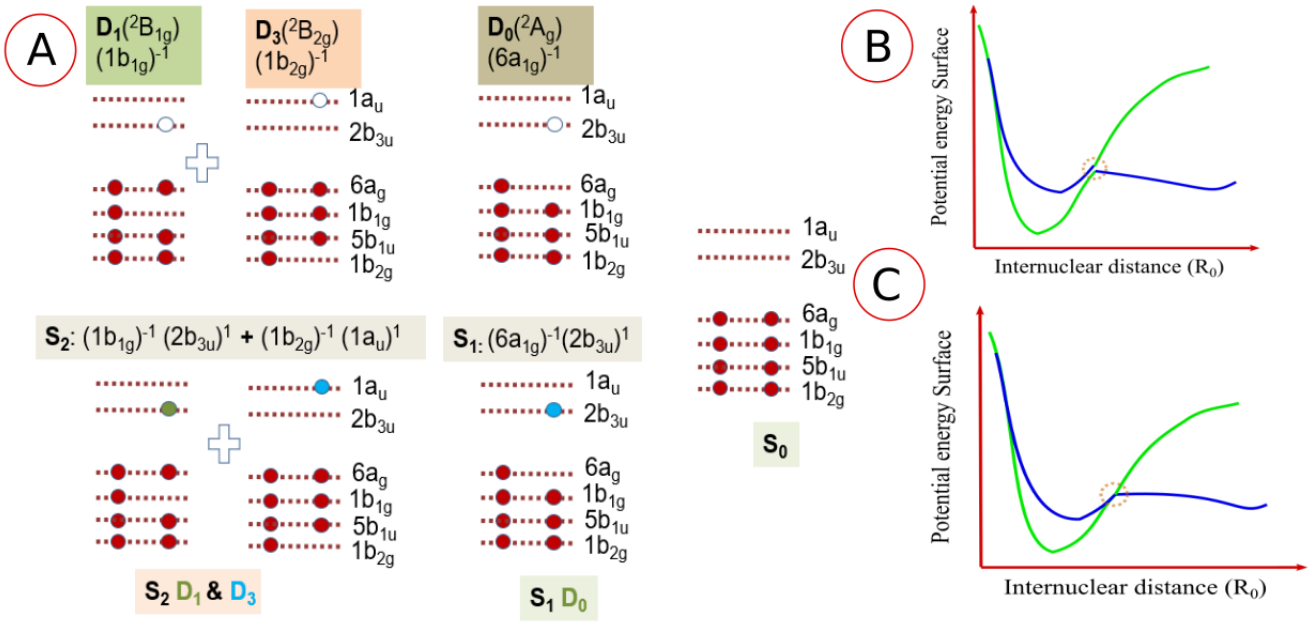

Figure 2.1: Panel (A) shows molecular orbital diagrams and determined electronic configuration of some excited, neutral, singlet, and ionized, doublet states of pyrazine molecule along with their (Koopman's) correlations. The S_0, S_1 and S_2 neutral electronic configurations are specifically shown where the S_2 configuration is represented by a weighted superposition of molecular orbital diagram. These correlated cationic electronic configurations (D_0, D_1, and D_3) are shown above each neutral molecular orbital diagram. The illustration based on the concept from reference 39. Panel (B) and (C) show a schematic representation of adiabatic and diabatic potential energy surfaces, respectively.

The S_2 $^1B_{2u}$ electronic state described above is predominantly described by the following electronic configu-

ration at the Frank-Condon point between the S_0 electronic ground state and S_2 excited state. The '0.70' and '0.50' pre-factor are the so-called the configuration interaction coefficients, the squares of which describes the total contribution of the two considered electron configurations to the excited state.

$$\Psi_{S_2} = 0.70\ \Phi\Big[(1b_{1g})^{-1}(2b_{3u})^{+1}\Big] + 0.5\ \Phi\Big[(1b_{2g})^{-1}(1a_u)^{+1}\Big] \tag{2.1}$$

Where Φ denotes the wavefunction of each of the electronic configuration that can form the S_2 state. In the cases where configuration interaction must be considered, simple MO theory and Koopmans' theorem fails[46,47]. In this situation, an electronic state picture is more intuitive than the orbital picture[48] in describing the electronic structure and potential relaxation processes, particularly from electronically excited states. This is particularly true when electronic-state couplings and non-adiabatic dynamics[47,49] are considered, such as those occurring between the S_1 and S_2 $^1B_{2u}$ ($(6a_g)^{-1}$ $(2b_{3u})^1$) states of pyrazine via a ν_{6a} vibronic coupling mode[39,50].

2.2 Electronic State Representation

The electronic states of a molecule are represented by a potential energy surfaces, which will be discussed below. These surfaces are obtained by solving TISE of the molecule in the full electronic and nuclear coordinates

$$\mathrm{H(r,R)}\Psi\mathrm{(r,R)} = \mathrm{E}\Psi\mathrm{(r,R)} \tag{2.2}$$

The Hamiltonian of the molecular system, H, combines the electron kinetic and potential energy, nuclear kinetic and potential energy, and electron-nuclear potential energy. The wavefunction is the energy eigenfunction in the entire coordinate space. The nuclear mass is large enough compared to the electron mass that a seperation of electronic and nuclear variables becomes possible. Thus, in order to simplify equation 2.2, the Born-Oppenheimer Approximation (BOA) is formulated to separates electronic motion from the nuclear motion[51]. Within the BOA, the adiabatic potential energy surface can be defined for electronic state potential energies as a function of internuclear separations and angles. These adiabatic state surfaces preserve state ordering in energies, as shown in panel (B) in Figure 2.1. However, at some internuclear separations, the electronic and nuclear degrees of freedom are coupled and not separable. These points are called an avoided crossing, where electronic and nuclear degrees of freedom evolve on the same timescale and the BOA is not valid anymore. Therefore, another class of potential energy surfaces can be defined, called "diabatic potential energy curves," as shown in panel (C) in Figure 2.1. In the adiabatic case, the electronic character changes dramatically, whereas, in the diabatic representation, the dominant electronic character remains the same as a function of the nuclear coordinates[51]. The adiabatic states are more readily calculated and are appropriate when the nuclear motion is slow compared to the electronic motion. On the other hand, in the limit of fast nuclear motion, the diabatic states are more appropriate but more difficult to calculate[51].

2.3 Photophysiochemical Processes and Timescales

Following electronic photoexcitation of a molecule, the electronic structure of a molecule is no longer in equilibrium. The molecular system has gained potential energy that can be redistributed in several ways via radiative and non-radiative processes[1]. Upon exictation, the nuclear coordinate dependence of the potential energy provides a driving force for an evolution of the nuclear structure and potentially towards regions of

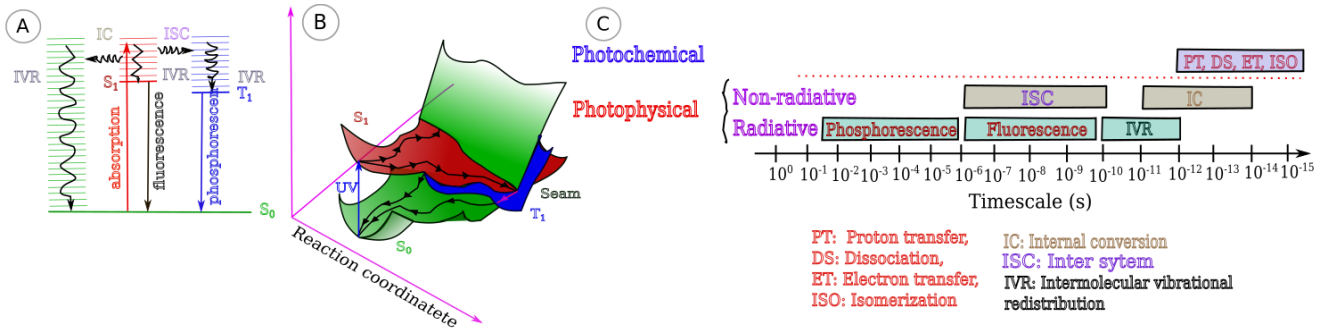

Figure 2.2: Panel (A) shows non-radiative and radiative relaxation processes of a molecule in Jablonski diagram[52]. Panel (B) shows, potential energy surfaces of a polyatomic molecule and possible nuclear coordinate trajectories upon UV excitation. Panel (C) shows associated timescales of different photophysical and photochemical processes. The figures are presented based on the concepts presented in Reference 1.

coordinate space that efficiently lead to electronic conifguration chnages, e.g., at avoided crossings or points in coordinate space that exhibit high degrees of spin-orbit coupling. The usefulness of electronic potential energy surfaces lies in their ability to describe the driving forces and behaviors of molecular systems away from equilibrium. Panel (A) in Figure 2.2 shows different processes following photoexcitation of a molecule via a Jablonski diagram[52]. The molecule can relax radiatively by emitting a photon via fluorescence or phosphorescence. Fluorescence occurs to generally enable electronic relaxation on ns timescales. In contrast, phosphorescence results in electronic relaxation to produce a lower-lying state with different multiplicity via spin-changing transition on μs timescales. Depending on the strength of the coupling between the electronic states, the molecule can also relax via non-radiative processes, such as IC and ISC, resulting in the production of a different electronic configuration with similar or different multiplicity, respectively. The former process is governed by the non-adiabatic coupling between vibrational and electronic degress of freedom[53], whereas the latter is due to relativistic spin-orbit coupling effects[54]. Non-adiabatic dynamics, i.e., IC, play an important role in determining the photochemistry of almost all polyatomic molecules[53,55,56] and are the heart of many core concepts in molecular electronics[57]. Important examples are the photobiological processes such as vision and photosynthesis[58,59]. ISC also plays an important role in the photophysics and photochemistry underlying numerous applications, such as molecular photonics, biological photosensors, photodynamic therapies, and material science[54]

IC generally occurs on a fs timescale, whereas ISC generally happens ps timescale (at least for molecules containing light elements). The non-radiative and radiative relaxation channels compete, but the non-radiative processes generally dominate due to their faster rates. The overall excited-state relaxation timescale can be described by $1/\tau = 1/\tau_{\mathrm{r}} + 1/\tau_{\mathrm{nr}}$[1], where τ_{r} and τ_{nr} defines the radiative and non-radiative relaxation time constants, respectively. The radiative processes must often occur at the minimum energy configuration of the excited state potential energy surface, which is normally reached via IVR, with such vibrational relaxation generally occurring on a faster (ps) timescale than radiative decay. On the other hand, the non-radiative processes most efficiently occur at the molecular configuration where the electronic states are degenerate, known as conical intersection points or seams[1], in the case of IC and states of the same multiplicity. Following UV excitation, possible excited state molecular trajectories that pass via conical intersection points in exemplary potential energy surfaces are shown in panel (B) of Figure 2.2. The different colors denote different diabatic electronic states. Moreover, following excitation in the UV spectral range or via thermal – i.e., via vibrational excitation of the electronic ground state – the excited molecules will often undergo unimolecular chemical transformations by crossing activation barriers and undergoing electronic state switches. Examples of such processes include excited-state proton-transfer, electron-transfer, dissociation, or isomer-

ization reactions that occur before relaxation to the initial or a new vibronic ground state on a ps-fs timescale[1]. Panel (C) shows the typical associated timescales for different photophysical and photochemical processes, which generally occur following photoexcitation.

The outcome of a chemical reaction depends on the shape of the potential energy surface and the associated molecular configuration, where the excited state relaxation often occurs in the vicinity of the atomic nuclear configuration associated with accessible conical intersections[1]. Therefore, it is necessary to understand the molecule's geometric and electronic structure and associated potential energy surfaces. This generally requires appropriate experimental methods that probe the ground and excited state features and dynamics. Such experimental observations need to be interpreted with state-of-the-art dynamic calculations and spectral simulations to identify the electronic energetics and nuclear geometries of the key features associated with these potential energy surfaces[1]. These include the conical intersections and avoided crossing points, which are often described as transition states in excited state manifolds[1].

2.4 Review of Experimental Techniques

2.4.1 Photoelectron Spectroscopy

PES is a technique that gives access to the electronic structure of matter by irradiating a sample, measuring the electron KEs and extracting the BEs of photoelectrons[60–63]. The principle of the PES technique is based on the photoelectric effect, which was observed by Heinrich Hertz[64] in 1887 and later explained by Albert Einstein using the quantization of light[65] in 1905. In the PES technique, ionizing radiation, *e.g.* soft x-ray, EUV, or UV photons, produce photoelectrons from a solid, liquid, or gaseous sample. Figure 2.3a shows a PE spectrum from a liquid (water) sample. The Kinetic Energy (KE) distributions of the PEs are recorded to obtain BEs, and potentially angular and spin-state information about the oxidized, final states. The signature of the different final states appear as a PE band in the recorded spectrum. These are generally denoted as D_0, D_1, D_2,...etc. In addition, Photoelectron Angular Distributions (PADs) can also be recorded to discern symmetry information about initial, and photoexcited intermediate, and final states, which will be discussed below in Section 2.4.4. PE spectra and PADs reveal important information about the electronic structure of the investigated sample[60]. In the limit of negligible inelastic electron scattering and neglecting secondary photoemission (i.e., Auger) effects, the electron Binding Energy (BE) information is encoded into the measured PE KE distributions and is given by the following equation:

$$KE = \hbar\omega - BE_{\mathrm{F}} - \phi_s \tag{2.3}$$

In Equation 2.3, $\phi_{\mathrm{s}} = \mathrm{E}_0^{\mathrm{vac}} - \mathrm{E}_{\mathrm{F}}$ is the work function of the sample, an important quantity in both the solid and liquid phases. In liquid samples, the work function measurement is the subject of ongoing research[66]. In the condensed phase, BEs are generally measured with respect to the Fermi level (E_{F}) of the sample. In aqueous solution study, the system Fermi levels lies within the band gap of the solutions, and liquids more generally, where there is no electron density. Therefore, the measured BEs are more conveniently referenced with respect to the local vacuum level ($\mathrm{E}_0^{\mathrm{vac}}$)[66], although recent studies have developed approaches to reference liquid-phase photoemission spectra to the Fermi level[66–69]. During photoionization, the sample absorbs energy from the light field, initiating a transition from the initial state to a photooxidized and free electron state. Thus, in the limit of negligible electron scattering, the measured BE is the difference in total energy between the molecule's N and N-1 electron system. Like in the solid phase, the liquid phase PES technique can be described using the three-step model[70]. The model was developed by spicer[71] and applied to liquids by

Delahey[72,73]. In the first step, an electron is promoted from the valence (or core) band to the conduction band. Then the electron propagates in the conduction band before traversing the liquid-gas interface, surmounting any interfacial potential before being detected.

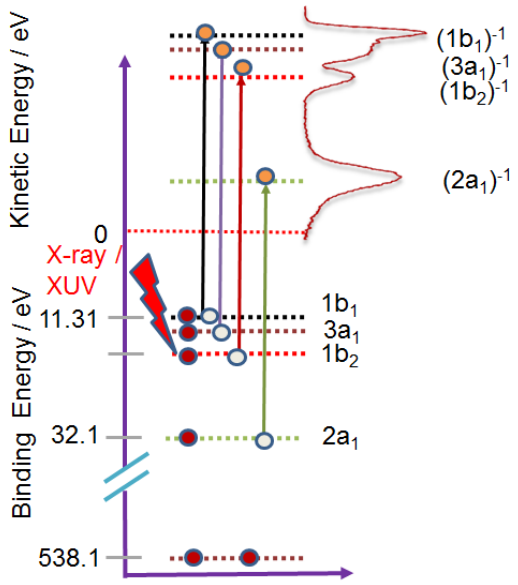

(a) MO diagram and valence band PE spectrum of liquid water

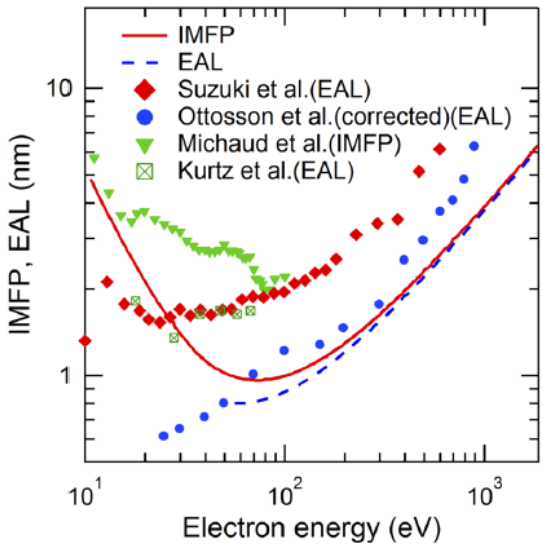

(b) EAL and IMFP curve of liquid water

Figure 2.3: Panel (a) shows MO diagram and valence band photoelectron spectrum of liquid water. Upon photoexcitation, electrons are ionized from the ground state, producing a range of photoionized states. The signature of these different final states appear as bands in the photoelectron spectra. More details are provided in section 2.5.1. Panel (b) shows the effecttive attenuation length (EAL) and inelastic mean free path (IMFP) curve of liquid water. The minimum EALs occur around $\sim$ 50-150 eV in KE. This indicates that 50-150 eV photoelectrons are detected with maximum surface sensitivity, corresponding to a 1-2 nm probing depth. On the other hand, at higher electron KEs, the photoemitted electrons are more bulk sensitive, with 600 eV electrons being detected with 3-5 nm 1/e probing depths. The figure in panel (b) is reprinted from Reference 70, with the permission of AIP Publishing.

The relative angle-resolved photoionization probabilites are often described by Dyson orbitals, which are the overlaps between the N-electron wavefunction of the initial state and the N-1 electron wavefunction of the ionized state.

$$\Phi^{\mathrm{d}}(1) = \sqrt{\mathrm{N}} \int \Psi_{\mathrm{I}}^{\mathrm{N}}(1,2,.....,\mathrm{n}) \Psi_{\mathrm{F}}^{\mathrm{N-1}}(2,....,\mathrm{n})\ \mathrm{d}2...\mathrm{dn} \tag{2.4}$$

$\Phi^{\mathrm{d}}(1)$ is called the Dyson orbital[45], N is the number of electrons, 1,2,....,n are the indexes of the electron, and $\Psi_{\mathrm{I}}^{\mathrm{N}}$ and $\Psi_{\mathrm{I}}^{\mathrm{N-1}}$ denote the initial and final states, respectively. The introduction of the Dyson orbital allows different ionization probabilities to be calculated and for an extension of the MO formalism and Koopmans' correlation to describe multi-electronic effects during photoionization[45,74]. According to the Koopmans' correlation[75], each of the ionization channels in a multi-electronic system is connected to a specific MO. Figure 2.3a shows such an example of the PE spectrum of a liquid water, where the PE bands/final states, D_0, D_1, D_2, and D_3, are assigned to the $(1b_1)^{-1}$, $(3a_1)^{-1}$, $(1b_2)^{-1}$, and $(2a_1)^{-1}$ electronic configurations, respectively. As the simple orbital picture is not valid in describing multielectronic states, neither is it valid in describing the PE spectra that involve multiple electronic contributions. In this case, as introduced above, the electronic structure is described using configuration interaction coefficients and ionisation processes can

be described using Dyson orbital approaches and the MO fractional parentages of the involved electronic states. This is particularly important when dynamic electronic structure is considered in electronically excited states[45].

PES in Liquid Samples Water is a ubiquitous solvent and the basis of aqueous solutions. The pioneering PES work that investigated the electronic structure of liquid samples was performed by Lugor[72], Delahay[73], and Siegbahn[76] between the nineteen sixties and nineteen eighties. Delahay sampled the thin layer of volatile liquid samples on a rotating disk to determine the photoionization threshold energies using VUV photoexcitation[73,77,77]. Siegbahn and co-workers used a rotating wetted wire method to introduce the liquid in vacuum for XPS measurements[76]. They also reported XPS measurements of a non-volatile liquid beam of 0.2 mm diameter, where the technique could be implemented with non-volatile solvents at a vacuum pressure less than 1 Torr[78]. In the late 1980s, Faubel and co-workers pioneered the liquid microjet technique, producing free jets of about 10 μm diameter to introduce continuously-replenished, volatile liquid samples into vacuum for PES measurements[79]. The highly pressurized liquid was injected into the vacuum system through a pinhole. Later, fused silica capillaries were used as discharging media[80]. The associated liquid beams have small surface areas and travel at speeds higher than 10 m/s, minimizing sample evaporation and suppressing spontaneous freezing by evaporative cooling. Using the LJ, Faubel performed PES measurements of liquids using HeI photon sources[22]. Kohno and co-workers[81] also reported photoionization mass spectroscopy experiments. Subsequent progress with the LJ technique was made when Winter and Faubel implemented the LJ-based PES technique with intense and continuously tunable soft X-ray sources at the BESSY II[82,83].

Surface-to- Bulk Sensitivity and Electron Scattering The KE of the photoelectrons can be varied by changing the excitation photon energy of the experiment. One of the strengths of condensed-phase PES techniques is that depending on the KE of the measured PEs, the material (in this case a solution) can be predominantly probed either at the sample-vacuum interface region or in the bulk of the material. In this case, during electron transport following photoionization, some of the conduction band electrons travel towards the liquid-vacuum interface, and the electrons generally undergo elastic, vibrational-inelastic, and electronic inelastic scattering with the solvent molecules[84]. If the elastic scattering is improbable, the inelastic mean free path can be represented by an Effective Attenuation Length (EAL), that defines the scattering efficiency, the distance over which the electron KE and angular-dependent electron flux reduces by 1/e. Figure 2.3b highlights the electron scattering length in terms of the EAL following a photoemission event, as a function of electron KE. This characteristic energy dependence displays an inverse-bell-shaped curve and is referred to as the "universal curve" of electron scattering; it is commonly encountered in the condensed phase, *i.e.* in solid and liquid, PES. The minima of the curve lies between $\sim$50-150 eV. The electronic inelastic scattering dominates at high electron KE (>150 eV)[10,11]. The EAL length increases with electron KE, making the liquid-phase PES technique increasingly bulk-sensitive as ionizing photon energies are increased[10,11]. On the other hand, at low KE, elastic scattering dominates[84], which causes zig-zag electron motion and increases electron scattering events[11]. In the low KE range (< 50 eV) in liquids, the magnitude of the electron scattering cross-sections is still not precisely known and ongoing studies aim to quantify the associated differential cross-sections[10,84]. It particular, at low BEs (< 8 eV in water) vibrational scattering processes dominate[84]. At such low electron KEs, liquid-phase photoelectron spectra have been found to be significantly distorted. Consequently, nascant PE spectra of liquid samples should be recorded with photon energies that are high enough to generate PEs with KEs $\geq$ 25 eV, to mitigate vibrational scattering effects and allow electron BEs to be precisely measured.

2.4.2 Non-resonant Photoelectron Spectroscopy

In the case of non-resonant excitation, the x-ray photon energy is generally chosen to be tens to hundreds of eV above the ionization threshold of interest and to avoid any resonant absorption effects. Non-resonant excitation leads to direct ionization from the investigated sample solutions and leaves an electron hole inside the sample. Figure 2.4 shows the initial, intermediate, and final states of such a non-resonant photoionization process for the specific case of diazine molecules in aqueous solution and where a core-level electron is initially ejected following photoabsorption. X-ray irradiation photoionizes the solute and solvent molecule species in the aqueous solutions. Panel (A) shows a primary, direct photoionization processes associated with non-resonant x-ray excitation. For illustrative purposes, only the ionization from the solute molecule is shown. Panel (B) shows that ionization of one core electron from the solute by an x-ray beam creates an electron hole in the molecule, called a one-hole (1h) state. The 1h state is the unstable intermediate state of solute ionization. The core hole can be refilled either by a valence electron or a higher-lying core electron. In the former case, a single electron from the valence level of the ionized solute molecule refills the core-hole and another valence electron is near simultaneously be ejected (as shown in panel (B)), leading to a 2h final state (as shown in panel (C)). The process that leads two-hole (2h) final state formed by non-resonant x-ray excitation and the process depicted in panel (B), is referred to as "non-resonant" Auger decay.

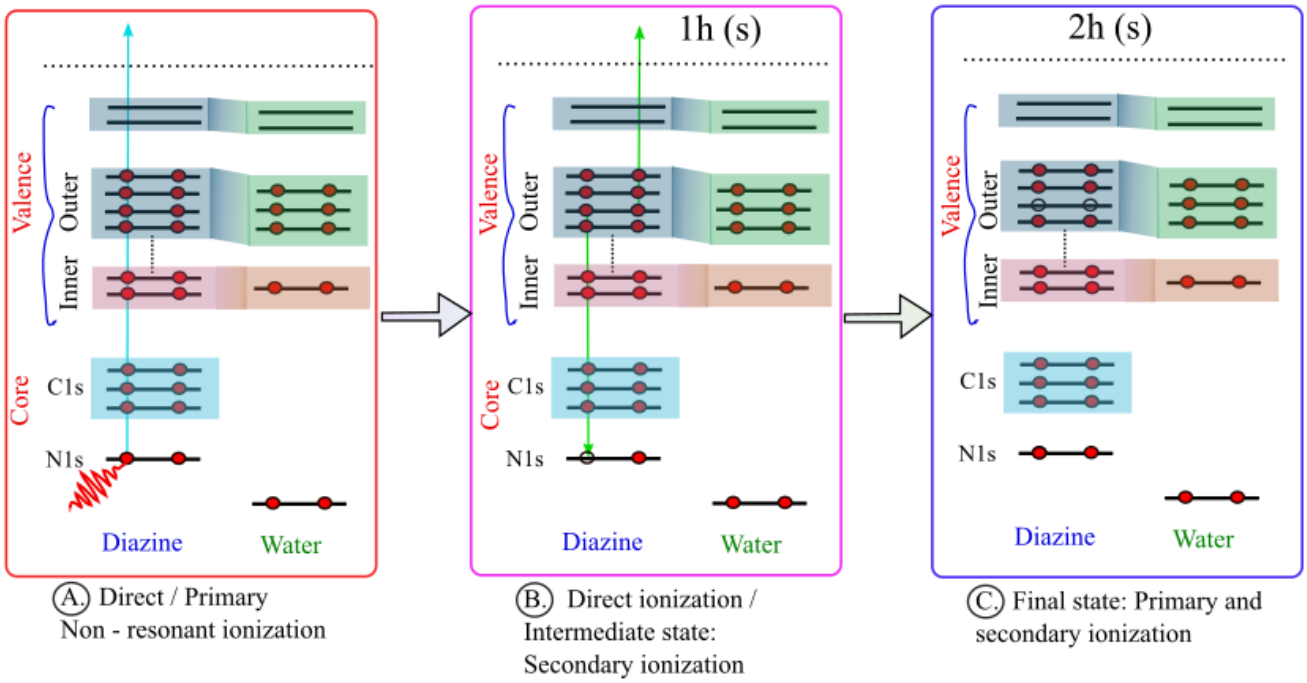

Figure 2.4: The primary and secondary photoemission channels associated with non-resonant, core-level photoelectron spectroscopy. The panel (A) shows the initial step of non-resonant photoionization of a N 1s core electron. The panel (B) shows the intermediate step of refilling the core hole, either with C 1s electrons or valence electrons, leading to Auger electron emission. The panel (C) shows the final state that is produced following emission of an Auger electron, denoted as a non-resonant Auger photoelectron. More details are in the main body of the text.

2.4.3 Resonant Photoelectron Spectroscopy

In the case of resonant x-ray excitation, the photon energy is tuned to resonantly excite a core electron to an unoccupied (generally virtual valence) molecular orbital, creating a core hole. Figure 2.5 shows a schematic of the resonant x-ray excitation PES process, with a focus on subsequent local Auger decay processes.

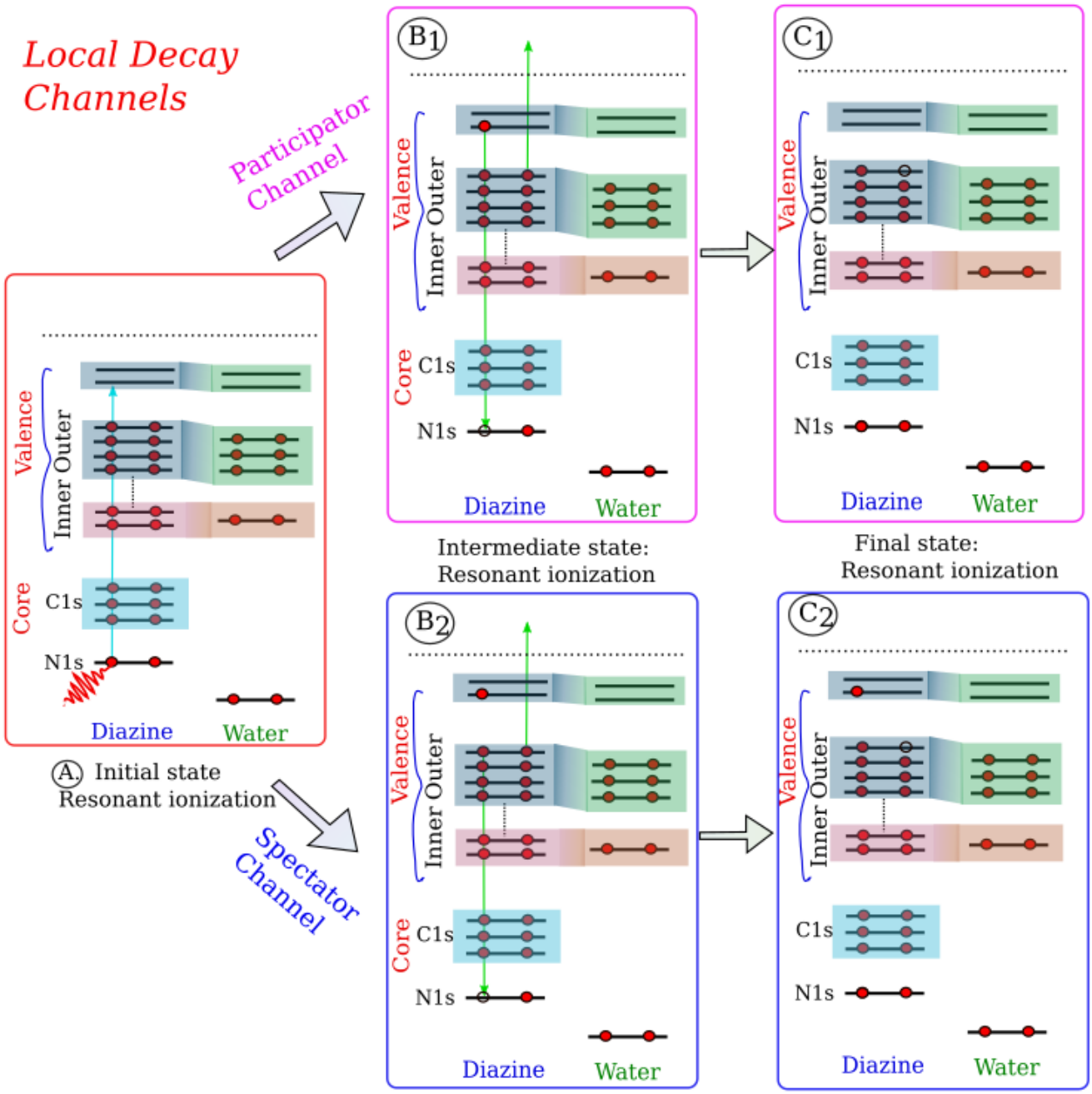

Figure 2.5: Local electron decay channels in resonant photoelectron spectroscopy. Panel (A) shows the initial step where the molecule is resonantly excited, leading to local decay channels. Panel (B_1) and (C_1) show the participator channels, where the excited core electron refill the core hole and another electron is ejected. Panel (B_2) and (C_2) represent the spectator channels, where the excited core electron stays in the excited state and another electron refills the core hole. More details are provided in the main body of the text.

Local Auger Decay Channels: X-ray photoexcited core-to-virtual-valence excited states generally have very short lifetime (hundred of as to tens of fs)[85,86] Two different intramolecular predominantly occur within such a core-hole lifetime[20,87] following resonant excitation: participator and spectator Auger decay[20,87]. The initially excited state can relax by refilling the core hole with the initially excited electron, with the recovered energy resulting in valence (or higher-lying core level) ionization of the initially excited state. This is called a participator Auger process, leading to the indirect ionization of a valence electron, as shown in panels (A), (B_1), and (C_1) in Figure 2.5. The participator process has the same final state as produced in non-resonant (direct) photoionization processes, where an x-ray is used to directly ionize valence electron. Due to energy conservation, when resonantly exciting, the valence electron can alternatively be photoionize directly, as the

system absorbs sufficient energy to liberate a valence electron and produce an electron with the same kinetic energy and final state as in the participator process. The quantum interference between the direct and indirect (resonant Auger) ionization channels leads to an enhancement and potential reduction of the solute signals, depending on the emission phase of the two ionization channels[20]. The underlying participator intramolecular (or local) resonant photoemission process is illustrated in panels (B_1), and (C_1), Figure 2.5. Alternatively, following core-to-virtual-valence resonant excitation, the excited electron can stay in the formerly unoccupied molecular orbital, the valence electron can refill the core hole, and hence, an alternative electron can be ionized. This process is called a spectator Auger process and is illustrated in panels (B_2) and (C_2) in Figure 2.5. Such autoionizing, indirect ionization channels, *i.e.*, participator and spectator-Auger channels, are activated following resonant excitation and differ from non-resonant Auger decay in that they lead to formation of 1h and 2h1e final states, respectively. Resonant photoemission processes are also generally more efficient than otherwise equivalent non-resonant ones, specifically because the absorption cross-section for the relevant partial ionization channel is usually much higher at the absorption edge than tens to hundreds of electron volts above it. Here, local refers to the intramolecular processes occurring in the solute or solvent molecules that absorbed x-ray radiation.

Comparing the Auger processes, non-resonant Auger decay produces a 2h process final states, whereas resonant spectator Auger processes have 2h1e final states. During non-resonant processes, the initially excited electron is directly promoted to the ionization continuum, increasing the charge of the absorbing solute or solvent molecules. In spectator Auger processes, the initially excited electron remains bound and stays in the formerly unoccupied molecular orbital, while higher-binding-energy electrons refill the core hole and are ejected. As a result, the Auger electron associated with the non-resonant excitation process generally appear at lower KE than the spectator Auger photoelectrons[88]. In the absence of electron-electron correlations, the subsequent electronic rearrangement process will be the same, whether the excitation is non-resonant or resonant[89]. Thus, with negligible electron correlation effects, both processes reveal similar spectral information, but the spectral intensity profiles and the photoelectron KE energy spectra are different between the two processes[89]. These spectral intensity variations between the two processes are due to the photon energy-dependent cross-section and the realities of electron correlation effects.

High energy x-ray ionization of molecules leads to the formation of electronically excited states, which relax either via radiative (fluorescence emission) or non-radiative (Auger-electron emission) channels[90]. Auger processes are most probable following the core-ionization of lighter elements in the periodic table[91], intramolecular Auger decay effectively competes with intermolecular Auger processes and X-ray fluorescence and is the dominant relaxation process. Following selective ionization, a number of factors are involved in determining the spectral intensity of the different open Auger processes. Firstly, the photoabsorption cross-section needs to be high enough to drive the resonant Auger process. In a randomly oriented sample this predominantly depends on the magnitude of the electronic transition dipole matrix element and potentially the Frank-Condon overlap integral of the core-to-unoccupied-valence transitions. If the valence orbital is localized, the valence orbital overlap with the core orbital will be generally be significant[92]. During a participator process, an electron makes a transition from the initial state to a super-excited state[86], which decays to form a more positively charged state. This transition also depends on the electronic wavefunction and potentially Frank-Condon overlap between the final and intermediate states, where the latter decays to produce the former via the Auger transition. Similarly, during a spectator process, a valence electron is promoted to a superexcited state which decays to produce a doubly-excited, singly-ionized state through photoionization[86]. Thus, in light-atom systems, the resonant Auger process can be dominantly described as a convolution between the photoabsorption and Auger events occurring in the molecule.

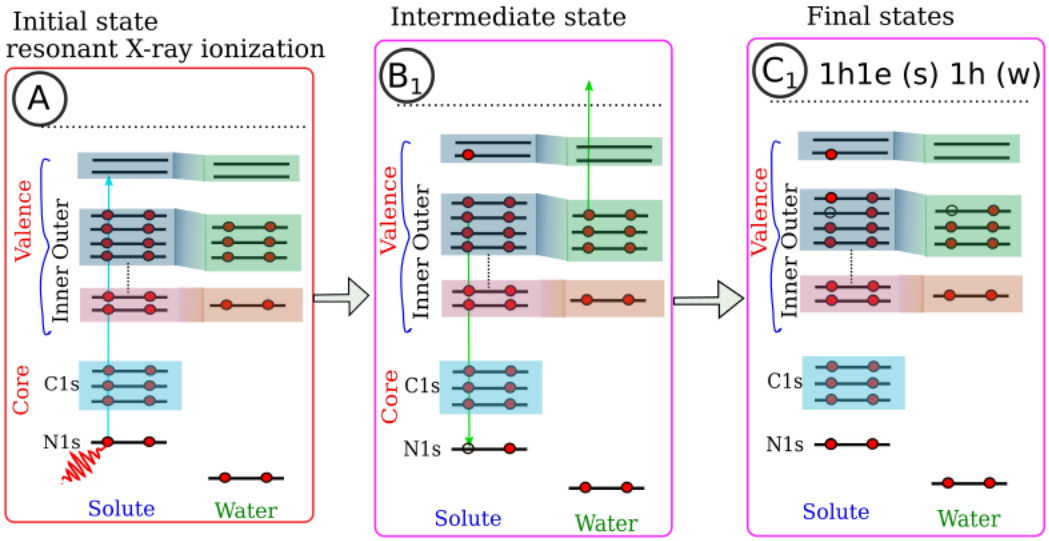

Figure 2.6: Schematic of a non-local Auger decay process that can occur in the dense matter following resonant excitation and be observed using photoelectron spectroscopy. Panel (A) shows the initial step where the molecule is resonantly excited. This can lead to non-local decay channel, Intermolecular Coulombic Decay (ICD). A resonant ICD process is illustrated in panel (B_1) and (C_1). The (s) and (w) labels in panel (C_1) denote solute and water electronic structure changes, respectively. More details are provided in the main body of the text.

The participator Auger electron process are the result of different ionization channels that lead to the same final state with a +1 charge-state as is produced in direct, non-resonant photoemission[20]. The participator features can be considered to imprint information about the initial and ionized molecular orbitals, as well as the molecular bonding character of the probed system. In contrast, a spectator process is driven by electron configuration interaction and subsequent ionization. These processes can reveal information about ultrafast decay channels (during the core-hole lifetime) as well as electronic hybridization[93] within a molecule. By identifying the spectator or participator features in resonantly enhanced photoemission spectra, it is possible to extract additional and meaningful information about the electronic structure of molecules in an aqueous solutions.

Non-Local Auger Decay Channels: The resonant ionization channels mentioned above are promoted by selectively exciting the solute molecules, with little dependence on the solvent. Additional intermolecular photoionization channels may also be present, such as Intermolecular Coulombic Decay (ICD), Electron Transfer Mediated Decay (ETMD) in dense matter[90,94,95], however. Such processes are illustrated in Figures 2.6 and 2.7, considering a solute molecule and a solvent (water) molecule. Two types of resonant ICD processes can be considered. The first is participator-initiated ICD[94], and the second is spectator-initiated ICD[93]. Initially, the N1s core electron of the exemplary solute is excited to an unoccupied valence orbital, and any electron, either from the valence or C 1s core levels, can refill the N 1s core hole. Here, the illustration is made in panels (B_1) and (C_1) in Figure 2.6 for a spectator-like resonant ICD process with a valence electron refilling the core hole. The resulting internal energy in the solute molecule can then be considered to liberate a valence electron of a solvent molecule in the first solvation shell of the solute.

ETMD can be initiated by non-resonant ionization using high energy x-ray radiation[95]. In the ETMD process, the core hole of the solute molecule is refilled by an electron of the solvent, with another low BE electron of the solvent being ionized[86]. That leads to a two hole (2h) final state, where two holes are created in the solvent water, as illustrated in panel (B_2) and (C_2) in bottom panel of Figure 2.7. In this case, different types

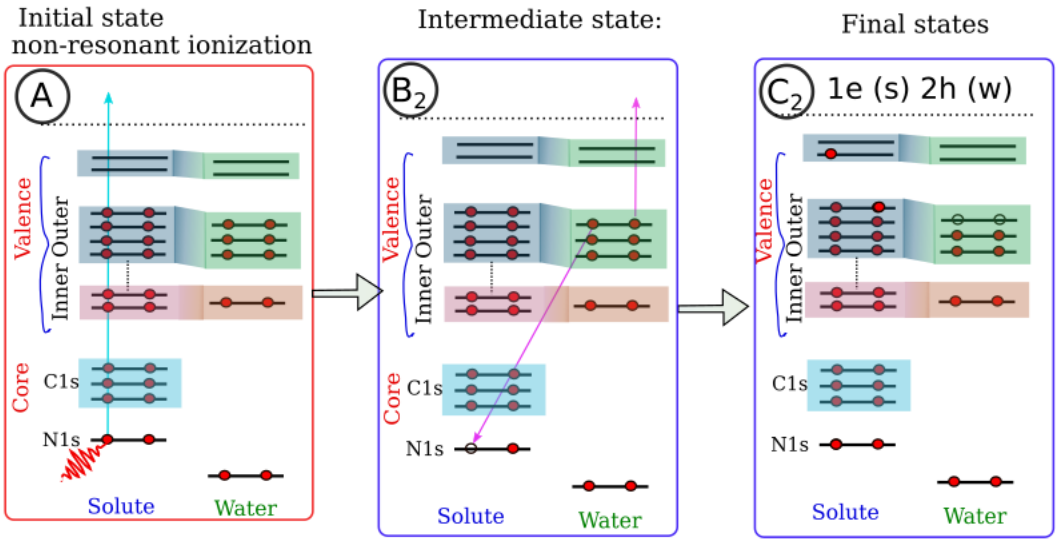

Figure 2.7: Schematic of a non-local Auger decay process that can occur in the dense matter following non-resonant excitation and be observed using photoelectron spectroscopy. Panel (A) shows the initial step where the molecule is non-resonantly excited. This can lead to non-local decay channel, Electron Transfer Mediated Decay (ETMD). A non-resonant ETMD process is illustrated in panel (B_2) and (C_2). The (s) and (w) labels in panel (C_2) denote solute and water electronic structure changes, respectively. More details are provided in the main body of the text.

of ETMD processes may occur. One with 2h on a single-solvent molecule, one with holes in two different solvent molecules and one with holes on a solvent and a different solute. The difference between the local and non-local decay process is the final state.

2.4.4 Photoelectron Angular Distributions

The single-photon Photoelectron Angular Distribution (PAD) of a non-aligned or oriented sample, ionized by linearly polarized light, can be described by the following equation[96]:

$$\frac{d\sigma}{d\Omega} = \frac{\sigma_0}{4\pi}[1 + \beta_2 P_2(\cos\Theta)] \tag{2.5}$$

Where, σ and σ_0 are the total and absolute photoionization cross-section, respectively, Ω is the solid angle, Θ is the polar emission angle with respect to the polarization of the incoming light. β_2 is the asymmetry or anisotropy parameter defined by the total angular momentum of the ionized state and state of the continuum populated through the ionization process. P_2 is the second-order Legendre polynomial. For the static experiments, σ, β_2 and σ_0 have only energy-dependence. Equation 2.5 can be written as:

$$\begin{aligned}\frac{d\sigma}{d\Omega} &= \frac{\sigma_0}{4\pi}[1 + \frac{\beta_2}{2}(3\cos^2\Theta - 1)] \\ &= \frac{\sigma_0}{4\pi}[1 + \frac{\beta_2}{4}(3\cos(2\Theta) + 1)]\end{aligned} \tag{2.6}$$

The right panel of Figure 2.8 highlights an arbitrary experimental geometry where the detector is placed at an arbitrary angle Θ with respect to light polarization. A few critical points regarding PADs are introduced below[96,97].

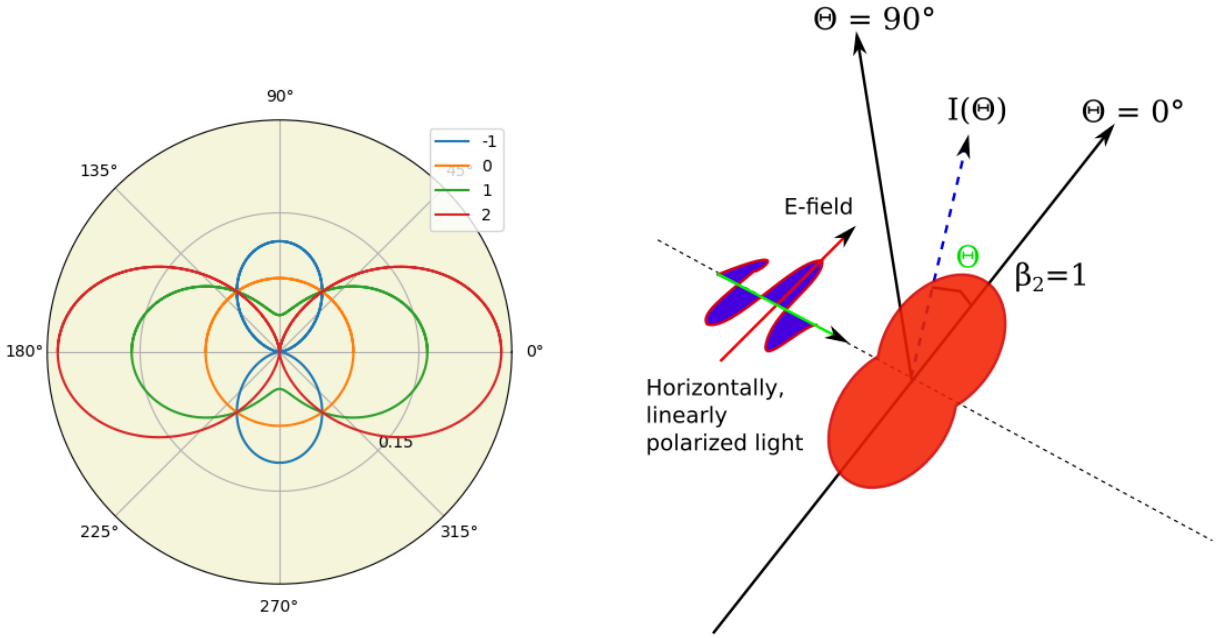

(a) Angular distribution

(b) Experimental geometry

Figure 2.8: Exemplary photoelectron angular distributions associated with single-photon ionization with linearly polarized light. The left panel shows exemplary photoelectron angular distributions in the polar plane upon ionizing with a horizontally polarized light pulse. The right panel illustrates the experimental geometry, and θ is the angle between the light polarization and detector position. The photoelectron intensity distributions vary due to the angular distribution pattern. For β_2=2, the detector collects maximum signal at θ=0, while at θ=90°, the intensity is minimized.

The outgoing electron wavefunctions are usually described in terms of different spherical harmonics with different amplitudes and phases, allowing for interference between them[96,215]. The PADs can correspondingly be thought of as having two components: a radial and an angular part. The radial part defines the amplitude, that is, the initial and final wavefunction overlap. The relative phases can vary significantly as excitation energy into the photoionization continuum is changed[96]. The anisotropy parameter β_2, depends on the relative phase of the photoionization channels as a function of the electron kinetic energy and it can vary between -1 to 2[96]. Figure 2.8 shows the PADs for different exemplary β_2 values. The photoelectrons are preferentially emitted perpendicular to the light-field polarization for negative β_2 values. For positive values of β_2, the photoelectrons are emitted along the polarization of the light field. β_2 =0 corresponds to a purely isotropic distribution of the photoelectrons, which means electrons are generated with no angular preference. Finally, when β_2 =2 or -1, the photoelectrons have purely $\cos^2\Theta$ or $\sin^2\Theta$, behaviors. For single-photon ionization processes and linearly polarized light, the angular distribution term is independent of the anisotropy parameter for Θ =54.7°, as shown in Equation 2.6. This angle is the so-called magic angle. At this collection angle, the PE detection is insensitive to the PADs.

When multiple photons are absorbed in the course of an ionization process, for example in a pump-probe experiment, the PAD can take on a more complicated form[96,98,99], as characterized by equation 2.5:

$$\frac{d\sigma(E,\theta,t)}{d\Omega} = \frac{\sigma_0(E,t)}{4\pi}[1+\beta_2(E,t)P_2(\cos\theta)+\beta_4(E,t)P_4(\cos\Theta)] \tag{2.7}$$

where E, Θ, t, and P_4 are the photoelectron KE, ejection angle with respect to the laser polarization direction, the pump-probe time-delay, and 4$^{\text{th}}$-order Legendre polynomials, respectively. In the pump-probe experi-

ments, The three quantities, σ_0, β_2, and β_4, have both energy and time-dependence, and provide dynamical information of the system under investigation. In the (1+1') pump-probe experiments, two linearly-polarised photons (a pump and a probe) are absorbed, leading to higher-order angular momenta components in the PADs, i.e. β_2 and β_4 components[96,98,99]. For the more complex pump-probe case, the magic angle for the β_4 term is also close to 55°.

In this research work, the experimental setup for performing X-ray PES was oriented in a perpendicular or magic angle geometry with respect to the polarization of the incoming light source. Alternatively, in the TR-PES experiments, the spectrometer was oriented parallel to the light polarization vector. According to the discussion above, with a spectrometer oriented either perpendicular or parallel to the light, the collected photoelectron intensity distribution may be influenced by both the anisotropy parameter, β_2, and or the photoelectron cross-section, σ, any scattering events that occur to prior to electron detection. However, when a spectrometer is oriented at the magic angle, it is only influenced by the photon energy-dependent cross-section σ, the ionization dynamics of the system, and any scattering events. Photoionization from the condensed phase samples, *i.e.*, aqueous solution, results in secondary electron background[84]. The associated elastic and inelastic scattering events in condensed phase decreases the anisotropy[100].

2.4.5 Time-Resolved Studies Using Ultrashort Pulses

The coupled electron and nuclear motions in a molecular or material system drive chemical transformations and associated reaction dynamics, *i.e.*, bond-breaking and bond-making processes. A deeper understanding of the time-dependent coupled electronic and nuclear motion is the foundation for extracting the underlying reaction mechanisms. Static PES measurements provide us with electronic and potentially geometric structural information about the sample. Furthermore, time-resolved measurements provide us with not only the signature of the electronic states but also the time-dependent population of the transient chemical species[70,101], albeit often with lower energy resolution. Incorporating time-resolved experimental measurements[70,101,102] with state-of-the-art theoretical calculations and spectral simulations[103,104], a more complete picture of the coupled electronic and nuclear motion can be obtained. Such experimental and computational method development allows us to investigate a molecule in an applied and complex environment, such as in the aqueous phase. Although several time-resolved experimental techniques exist, only the TRPES technique is discussed in detail here.

The core elements of the TRPES method are illustrated in Figure 2.9. In this technique, two laser pulses are used: pump and probe laser pulses. In this illustration, GS denotes the ground-state, S_1 and S_2 denote the excited states, D_0 and D_1 are the cationic states which are correlated to the S_1 and S_2 states, respectively via their Koopmans' correlations. A pump pulse is used to excite an electron to an excited state, S_2, and a probe pulse can photoionize the photoexcited electron distribution to produce a cationic state, D_1, and an electron KE, KE_1, is measured. An introduction of a time-delay (Δt) between the pump and probe pulses allows the initially excited electron population to be transferred to another excited state, S_1. A time-delayed probe pulse photoionizes the produced electron distribution to form a different cationic state, D_0 and an electron KE, KE_2, is measured. Therefore, varying the time-delay between the pump and probe pulses allows us to record the time-dependent KE, and by extension BE, distribution of the photoexcited electronic distribution and, with a sufficiently high probe photon energies, monitor the electron dynamics over the entire reaction coordinate with fs time-resolution[53,105–107]. Such measurements become possible in the aqueous phase by combining the liquid-microjet-based PES technique with ultrashort laser pulses. Details of the mathematical description of TRPES experiments can be found in References 53,105,107. Briefly, in this technique, a pump pulse is

used to create a wavepacket in the electronically excited neutral state, $\Psi(\mathrm{t})$[107]

$$|\Psi(\mathrm{t})\rangle = \sum_{\mathrm{n}} \mathrm{A_n} \mathrm{e}^{-\mathrm{i}[\mathrm{E_n t}/\hbar + \phi_\mathrm{n}]} |\Psi_\mathrm{n}\rangle \tag{2.8}$$

Where, $\mathrm{E_n}$ is the eigenstate and ϕ_n is the phase, and $\mathrm{e}^{-\mathrm{i}[\mathrm{E_n t}/\hbar + \phi_\mathrm{n}]}$ defines the time-dependent phase. In PES measurements, the initially prepared wavepacket at the electronically excited state, Ψ_i, is ionized to the continuum and creates a specific final ionic state, Ψ_f, via a probe laser pulse. Within the dipole approximation and for perturbative light-matter interactions, the photoionization matrix element can be written as:[108]

$$\begin{aligned} \mathrm{d_{i \rightarrow f}}(\mathrm{t}) &= \langle \Psi_\mathrm{f}; \Psi_\mathrm{e} | \hat{\mu} \cdot \mathrm{E_{probe}} | \Psi_\mathrm{i}(\mathrm{t}) \rangle \\ &= \sum_{\mathrm{n}} \mathrm{A_n}(\mathrm{t}) \mathrm{e}^{-\mathrm{i}[\mathrm{E_n t}/\hbar + \phi_\mathrm{n}]} \mathrm{d_{n \rightarrow f}} \end{aligned} \tag{2.9}$$

Here the subscripts i, f, and e refers to the initial, final, and photoelectron wavefunctions. $\hat{\mu}$ is the dipole operator, and $\mathrm{E_{probe}}$ is the incident ionizing radiation field. The above photoionization matrix element is usually described as the mapping of the N-electron wavefunction, Ψ_i, onto the ionization continuum that is comprised of one or more N-1 electron final state wavefunctions, Ψ_f, and outgoing photoelectron wavefunctions, $\Psi_\mathrm{e}(\mathrm{k})$, with wavevector k[107]. $\mathrm{d_{n \rightarrow f}}$ is the time-independent basis state ionization matrix element, which has both a co-ordinate and energy dependence. Therefore, the measured photoionization dipole matrix element $\mathrm{d_{i \rightarrow f}}(\mathrm{t})$ can be a complicated function that has dependence on co-ordinate, energy, and time[107].

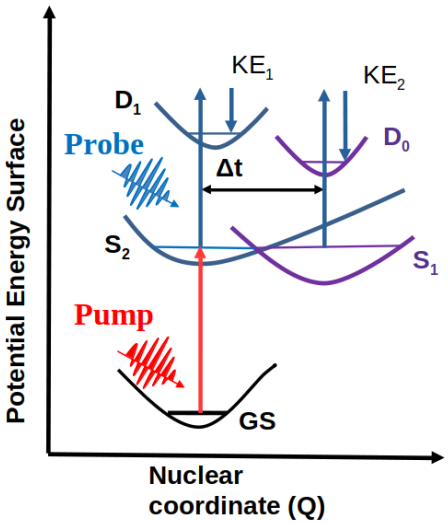

Figure 2.9: Schematic of the pump-probe method in TRPES. A short pump pulse initiates reaction and a probe pulse monitors the excited-state or reaction dynamics by photoionizing the molecule at different pump-probe delay times. The time-dependence of the studied process is recorded by recording the data with pulse durations that are equal to or shorter than the dynamics of interest and by recording data at specifically chosen and well-defined pump-probe delays. The figure is based on the concepts presented in Reference 105.

TRPES of Liquid Systems The first liquid-phase, ultrafast PES measurements were performed to investigate hydrated electrons ($\mathrm{e^-_{aq.}}$) in 2010[109–111]. Solvated electrons are the transient species that are generated within the band gap of liquid water. They are highly reactive[112] and have short lifetimes[109,113]. They are cor-

respondingly investigated using time-resolved experiments, which often adopt pump-probe methodologies. Optical lasers can be used ot excite Charge-Transfer-to-Solvent (CTTS) bands and Liquid-Microjet-Based Time-Resolved Photoelectron Spectroscopy (LJ-TRPES) allows the energetics and relaxation dynamics of the solvated electrons to be measured[110,113–121]. Moreover, LJ-TRPES has also been applied to study excited electronic state relaxation processes such as Ligand-to-Metal Charge Transfer (LMCT), IC, ISC, and solvation dynamics of aqueous solutions[41–43,122–127] and to study proton transfer processes[119,128]. In the following brief literature review, UV-pumped LJ-TRPES experiments are categorized as either UV-probed or EUV-probed measurements. These classes of experiments are discussed below.

UV probed TRPES: The UV-pump-UV-probe experiments have spanned measurements of hydrated electron BEs[111], the wavelength dependence of solvated electron generation in different solvents[117], and measurements of the lifetime and relaxation mechanism of hydrated electrons via IC in a non-equilibrium solvent environment[118]. Buchner *et al.*[114] studied the solvated electron by exciting CTTS bands of different aqueous solutions with different cations. TRPES allowed them to extract the transient hydrated cation complex at the liquid vacuum interface[114]. Kumar *et al.*[120] investigated the electronic structure and non-adiabatic dynamics of indole. The relaxation dynamics of thymine and its derivatives, thymidine and thymidine monophosphate, were studied by the Neumark group using LJ-TRPES and it was found that the relaxation differs compared to the gas phase[124]. LJ-TRPES studies also have been extended to record the angular distributions of aqueous 1,4-Diazabicyclo [2,2,2] Octane (DABCO) solutions to monitor the charge transfer from DABCO to bulk water[129] and the non-adiabatic dynamics of hydrated electrons in liquid water, which occur in 60 fs[122].

UV-pump-UV-probe LJ-TRPES techniques offer a good signal-to-noise ratio for the photoemission signals from the transient species. The UV probe photon energies are not usually high enough to ionize the solvent water molecule; consequently under single-photon absorption conditions, all of the electron signals arrise from the solute molecules. However, to monitor the complete electronic relaxation dynamics, such low UV photon energies are insufficient to ionize the involved singlet and triplet states, as well as the recovery of the ground states, of the studied molecules[124], especially following relaxation processes in solution. Notably, the UV probing method suffers a significant problem, the measured KEs (or extracted BEs) are particularly distorted due to the inelastic vibrational scattering processes that dominate at low electron kinetic energies in aqueous solutions. Consequently, retrieval algorithms are required to correct the measured data and to try to cover the true BEs[115,116,123]. Such retrieval methods have been exemplified in studying the internal conversion of the solvated electron in water, methanol, and ethanol, where a spectral retrieval method was applied to correct inelastic scattering contributions and to isolate ground state and excited state energetics[115]. Further applications include the study of hydrated electron formation, solvation, and recombination dynamics, as well as scavenging processes[113].

EUV-probed TRPES: Alternatively, liquid-phase transient species can be monitored using higher photon energies (>30 eV), in the EUV region or above[116]. Applying sufficiently high EUV photon energies in studying the aqueous solutions allows the photoionization of almost all occupied valence electronic states and enables measurement of electron BEs with suppression of vibrational inelastic scattering effects[66]. Note that inelastic scattering effects are not really suppressed in the EUV, rather they are predominantly electronic, with $>$4 eV energy losses, which can be recognized in the EUV PES results. EUV-probed LJ-TRPES has been successfully applied to investigate the electronic structure and relaxation dynamics of a dilute aqueous solution of quinoline yellow water-soluble compound[128]. Following optical excitation, the solvent rearrangement and excited state intramolecular proton transfer happened in 250 $\pm$ 70 fs[128]. Ojeda *et al.* studied photoinduced

LMCT reactions in the aqueous $Fe^{2+/3+}$ redox-pair solution[43]. Titov *et al.* studied the electronic relaxation of aqueous aminoazobenzenes using LJ-TRPES and interpreted the spectra using surface hopping TDDFT dynamics calculations[125]. Moguilevski *et al.* applied EUV LJ-TRPES to track the relaxation mechanism as well as the branching ratio from low-to-high spin state population transfer in the aqueous iron tris-bipyridine complex, $[Fe(bpy)_3]^{2+}$[41]. Engel *et al.* used optical excitation to initiate ligand-to-metal charge transfer in ferricyanide transition-metal-complex aqueous solution and studied the spin cross-over dynamics with 100 fs time resolution[42]. Raheem *et al.* studied aqueous sodium nitroprusside ($Na_2[Fe(CN)_6NO]$) solution and reported ultrafast isomerization dynamics occurring in 240 fs[130]. West *et. al.* investigated the excited-state dynamics of aniline aqueous solutions using EUV LJ-TRPES[126]. The study identified a change in electronic relaxation pathways in the aqueous phase compared to in gas-phase aniline. With the advancement of ultrafast laser technology, EUV-probed LJ-TRPES experimental setups have been further developed[131] to monitor the ultrafast processes that occur in a liquid environment with attosecond time resolution. This allowed the effect of the solvent on the photoemission time delay between liquid and gas phase water to be inferred[132].

Sill, challenges remain for performing UV pump and EUV probe TRPES experiments with condensed phase sample using relatively low repetition rate laser systems. Achieveable Near Infrared (NIR)-to-EUV conversion efficiencies with common 800 nm, $\sim$50 fs pulse duration kHz repetition rate lasers amount to 10^{-5} to 10^{-7} per harmonic between 20-50 eV[133]. With common, mJ-pulse-energy, kHz repetition rate Titanium:Sapphire (Ti:Sa) laser drivers, this leads to EUV photon numbers of 10^{10}-10^{9} photon/pulse per harmonic at the generating cell, which is generally reduced an order of magnitude or two by ultrashort-pulse-maintaining monochromatization[134]. This results in a EUV probe photon numbers of 10^{8}-10^{7} photon/pulse on target[134]. In contrast, nJ to μJ UV probe pulse energies are generally applied. This corresponds to probe photon number of 10^{9}-10^{12} photon/pulse. Moreover, up to μJ UV pump pulse energies and intensities pump exceed 10^{12} W/cm^2 can be readily applied. Applying such pump intensity levels in a liquid-solution, UV-pumped-EUV-probed TRPES experiment will lead to a PISC effect. This effect generally results in modification of the system dynamics and the electron energetics extracted on longer timescales[126,135]. More details are in the Section 3.4, Chapter 3. Therefore, liquid-phase TRPES studies should use lower pump pulse intensities in order to avoid PISC effects, as reported here, in Section 6.3, Chapter 6. Lowering the pump-pulse intensity reduces the excited state populations, and, therefore, results in relatively long time integration being required, in comparison to UV-pump and UV-probe experiments to achieve good S/N TRPES data with kHz lasers.

2.5 The Electronic Structure of the Studied Molecules and Existing Literature

2.5.1 Water

The symmetry of the gas-phase water molecule is C_{2v} and its ground state electronic structure is described within a molecular orbital framework as $(1a_1)^2(2a_1)^2(1b_2)^2(3a_1)^2(1b_1)^2$. $(1a_1)^2$ is the core MO associated with the O 1s electrons. The remaining electron pairs correspond to the valence MOs. Among them, the $2a_1$ MO is the inner valence orbital with O 2s character. The $(1b_2)^2(3a_1)^2(1b_1)^2$ electron pairs are the outer valence orbitals that have substantial combined H 1s and O 2p characters.

The liquid-phase water molecules are connected through hydrogen bonding[137]. Several differences are observed between the gas-phase and liquid-phase water PES spectra. The water molecule is polar, with the oxygen atom slightly negatively charged and the hydrogen atom slightly positively charged. In a liquid environment, the molecule is electrostatically stabilized through H-bonding by coordinating the H-site (O-site)

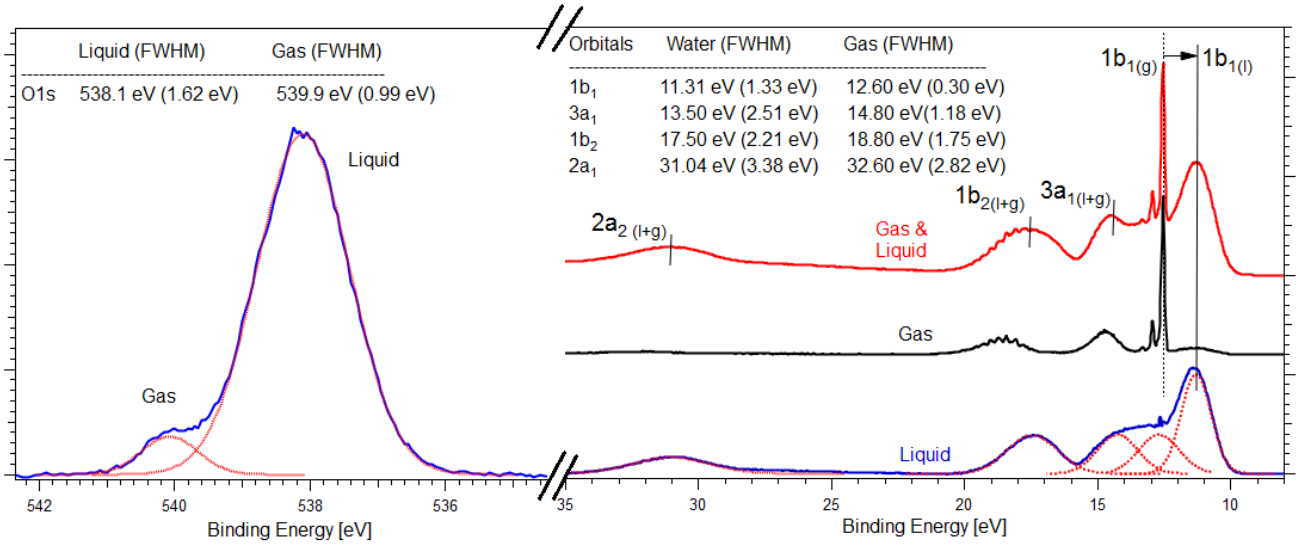

Figure 2.10: Valence (right) and core-level (left) PE spectra of liquid water. Linearly polarized soft x-rays were used to record the valence band specta with a photon energy of 150 eV. The core level PE spectrum were recorded using a 1070 eV photon energy. The liquid water valence PE spectrum (bottom, right) was obtained by subtracting the gas phase (middle, right) water spectrum from the as measured PE spectrum of liquid water which has both gas and liquid phase contributions (top, right). The table highlights the BEs extracted from Gaussian fitting of the liquid phase contributions. The numbers in the parentheses indicate the Full Width Half Maxima (FWHM)s of the PE bands. The valence band and core level PE BEs are energy referenced using the water $1b_1$ and O 1s VIEs of 11.33 ± 0.04 eV[66] and 538.1 ± 0.1 eV[136], respectively.

to the nearest neighboring O-sites (H-site). The H-sites are called H-bond donators, and O-sites are called H-bond acceptors. Winter *et al.*[136] studied hydrogen bonds in the liquid water using O 1s core-level PE spectroscopy. The study concluded that four water molecules surround each water molecule in a tetrahedral configuration; two are donors, and two are acceptors. The bulk of an aqueous solution has a different local hydrogen bonding environment to the aqueous surface regions, which have broken hydrogen bonds in the transition region from the liquid surface to the bulk *i.e.*, one or two dangling OH bonds is directed towards the vacuum or gas-phase side[136,138]. Later Niskane *et al.*[139] reported that each water molecule donates and accepts 1.7 hydrogen bonds, i.e. there are 3.4 hydrogen bonds per water molecule, which is essentially consistent with Bernd Winter's findings.

The significant differences between liquid and gas-phase water are summarized below[82,140,141].

I Valence electron delocalization occurs between the water monomers in liquid water. The interaction between the valence electrons of the nearest neighbour water molecules results in a local orbital mixing[82,142]. Such orbital mixing has been observed in liquid water's $3a_1$ orbital ionization signatures, where the nearest neighbour water molecules are thought to experience intermolecular bonding and nonbonding interactions[82,142]. Thus, the monomeric $3a_1$ orbital is split in the liquid environment to form a broad structure with in-phase and out-of-phase orbital bonding components. The stronger the bonding, the more significant the splitting, as is the case in solid-water (ice)[82,140]. Notably, these intermolecular bonding interactions can be disrupted by adding solute to the water solvent[142].

II The valence and core level MO BE's of the water molecules are red-shifted in the liquid phase compared to in the gas phase. Associated spectra are shown in Figure 2.10. The three potential contributions to these shifts are electric polarization, surface dipoles, and changes to the electronic structure due to H-bonding[82]. Such gas-to-liquid-phase peak shifting is due to the difference in electrostatic energy gain between the initial and final states upon formation of H-bonds, which is often associated with the

liquid polarization screening[82]. A simple dielectric model reveals a ∼1.4 eV shift[82] in going from the gas to the liquid phase. However, the energy shift due to H-bonding is found to be orbital-specific[142]. The existence of a net surface dipole at the water-air/vacuum interface results in an electric potential related to the orientation of the water molecule at the interfaces. The surface potential of liquid water is known to be very small, <50 meV[66]. In addition, the shift also arises due to the differences in internal molecular relaxation contributions of the final states between the gas and liquid phase. Furthermore, intermolecular charge screening, polarization effects induced by the surrounding water molecules, and the long-range interactions among the water molecules in the liquid environment may also contribute gas-to-liquid-phase shift[140].

III There is a variation of the gas-to-liquid-phase red-shift among the valence and core MOs of the water molecule. Such variations reflect the change in orbital character due to charge redistribution upon H-bonding in the liquid environment[82,140,142]. The core MOs experience a more significant shift compared to the valence MOs. This indicates a lower electrostatic stabilization of the delocalized valence orbitals compared to the highly localized core O 1s orbital[140].

IV The photoelectron peak widths are also different in the liquid phase, with significant broadening observed in the liquid compared to the gas phase. The broadening of the peak widths reflects the distributions of local H-bond coordination structures, leading to different BE energies. The broadening of the $3a_1$ peak is usually more significant due to orbital mixing effects. A pair of two Gaussian profiles are correspondingly used to fit this bandlike feature[82,140], with single peaks generally being implemented to fit the other photoelectron peaks.

V Angle-resolved PES measurements measured the anisotropy parameters, β, of the liquid water photoelectron peaks[10,100,143]. The study highlights that the valence states of bulk liquid water molecules have similar localized electronic characters to the gas-phase water molecules, only energetically shifted. However, due to scattering, there is a 20% decrease in the anisotropy parameter, β, in the bulk liquid water compared to from the gas phase molecules[45,100].

2.5.2 Triiodide Anions: I_3^-

The presented content in this subsection has been adapted or directly taken from the publication: MS Ahsan, V Kochetov, D Hein, SI Bokarev, and I Wilkinson. *"Probing the molecular structure of aqueous triiodide via x-ray photoelectron spectroscopy and correlated electron phenomena",* Physical Chemistry Chemical Physics, 24(25):15540–15555, 2022. DOI: https://doi.org/10.1039/D1CP05840A. Published by the PCCP Owner Societies. This work is licensed under the Creative Commons Attribution 3.0 Unported License.

Triiodide is a well-studied polyatomic molecular system that highlights solvent-induced electronic and geometric structural changes[25,28,144] in the solution phase. The redox properties of I_3^- allow it to be combined with the I^- anion as an electrolytic component in dye-sensitized solar cells[145–150]. Its photofragmention dynamics have also been studied in the gas[36,151–154] and liquid phase[24,34,155]. Numerous experimental[25,31,32,144,156,157] and theoretical[26–28,144,158–161] studies have been performed to investigate the electronic and geometrical properties of the I_3^- anion. In the gas-phase, this anion is known to be a linear and centrosymmetric molecule[36,151–154,162]. However, the molecular bond lengths become asymmetric in going from the gas to the liquid phase. Depending on the type of solvent used to produced the triiodide solution, the bond

length asymmetry increases[28,158]. The asymmetry increases in a stronger hydrogen bonding environment, from methanol to ethanol and then to an aqueous protic solvent, where it is maximized[28,158]. In aqueous solution, the fluxional hydrogen bond environment significantly modifies the geometric structure of the triiodide anion[28,144]. Therefore, the I_3^- anion behaves like a weakly bound (I_2—I^-) adduct in aqueous solution, where one part of the molecule acts like an ionic (i) atom and another as a neutral but perturbed I_2 molecule. On average, the ionic part accepts more hydrogen bonds than the neutral part of the I_3^- anion[144]. Koslowski *et al.*[27] reported bent equilibrium geometric structure of the I_3^- anion, and a bond angle, $\angle(III)$ of 153° has been extracted in aqueous solution using X-ray scattering experiments following photoexcitation[31,33]. Theoretical studies highlight a loose angular potential in the aqueous phase electronic ground state[28] and a $\sim$170° average bond angle[31]. Therefore, the strong interaction of the solute and solvent in the aqueous solution influences the anion's electronic and geometric structure. Such interactions affects the solution's photophysics and photochemistry. Thus, this relatively simple polyatomic I_3^- anion offers the opportunity to study solute-solvent interactions, associated changes in the overall electronic structure, and electronic-excitation-induced molecular symmetry changes in the liquid phase[24–35].

Valence band PES spectra of $I^-_{3(\mathrm{aq.})}$ with a low signal-to-noise ratio, have already been reported[163]. Associated spectral analysis and PE band assignments have yet to be published. I $4d^{-1}$ core-level XPS studies highlighted the solvent effect on the anion electronic structure[157] and an increased averaged bond length asymmetry[144]. Later, Norell *et al.* performed theoretical XPS studies to quantify the degree of molecular asymmetry by comparing the Shake-Up (SU) (2h1e) and main (1h) peak intensities[160]. However, the theoretical calculations and spectral simulations in that study did not consider the multi-electron ionization dynamics of an *asymmetric and bent* $I^-_{3(\mathrm{aq.})}$ anion nor the polarization and screening effects of an aqueous environment. Additionally, the XPS spectral changes due to increasing bond length asymmetry could not be fully resolved in the previously reported valence and I $4d^{-1}$ core-level XPS studies. Firstly, this was due to a lack of a good signal-to-noise ratio in the recorded spectra[163]. Secondly, this was due to a the choice of the counter ion. The Li^+ in the studied $LiI_{3(\mathrm{aq.})}$ solutions. Li 1s ionization features from the studied $LiI_{3(aq.)}$ solutions energetically overlapped with the I 4d SU ionization features,[144,160] preventing a complete analysis of the latter. Moreover, the inhomogeneous peak broadening in the aqueous solution and high density of I $4d^{-1}$ final states resulted in significant spectral congestion and feature overlap in the relevant 50-65 eV BE region. Hence, an experimental approach with a high S/N ratio is desirable, as is the use of a suitable counter ion that will show spectrally separated ionization features from the $I^-_{3(\mathrm{aq.})}$ signals. The spectral congestion of the photoemission features may be overcome by probing the deeper core levels, *e.g.*, I 3d; the energetic separation between the I 3d photoionization features is expected to be greater and yield further information about the anion electronic and nuclear structure.

In this thesis work, three different $I^-_{3(\mathrm{aq.})}$ solutions (500 mM NaI / 250 mM I_2, 350 mM NaI / 250 mM I_2, and 420 mM NaI / 210 mM I_2) have been investigated using XPS experiments. The first two solutions were studied in experiments at BESSY II[168], whereas the latter mixture was studied at PETRA III[169]. As proposed in Reference 157, the aqueous triiodide solutions were prepared by mixing NaI and I_2 in water. The solubility of iodine in an aqueous solvent is very low, just 1.3 mM at 25°C[170]. When I_2 is dissolved in water alone, I_2–H_2O charge-transfer complexes are known to be predominantly formed, with only a small fraction of the coordinated I_2 species oxidizing the water molecule and forming $I^-_{3(\mathrm{aq.})}$[171]. The situation changes when iodide salt is added to the solutions. All the aqueous solutions studied by XPS in this thesis work were prepared by adding an excess amount of NaI and mixing with I_2. Therefore, the triiodide aqueous solutions in the XPS studies contain residual iodide ions that are expected to contribute to the recorded spectra. An example of such iodide spectral contributions are highlighted in a UV-VIS measurement shown in Figure 2.11, which

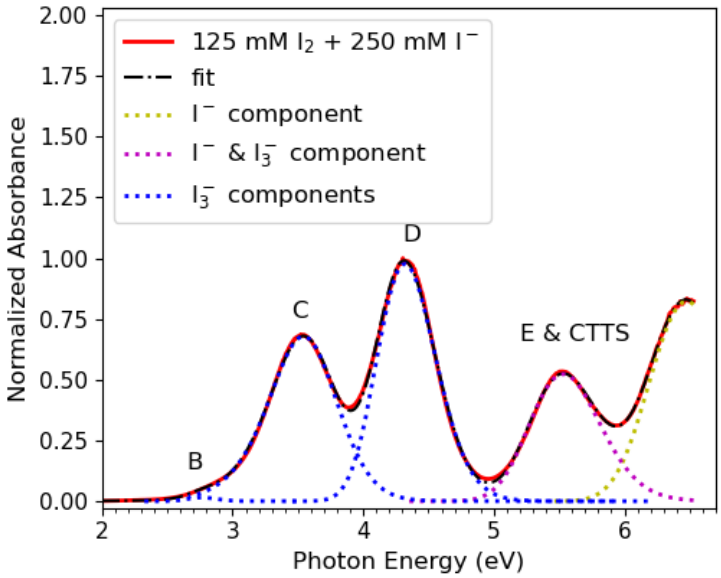

Figure 2.11: UV-Vis absorption spectrum of a 250 mM NaI and 125 mM I_2 mixture in aqueous solution (red curve) and their associated fits (dashed-dotted black curve). The electronically excited state contributions of the $I^-_{3(aq.)}$ anion[162,164] are highlighted as B, C, D, and E. The charge-transfer-to-solvent (CTTS) states of the first $^2P_{\frac{3}{2}}$ and second $^2P_{\frac{1}{2}}$ configuration of the $I^-_{(aq.)}$ anion[165,166] are labeled CTTS 1 and CTTS 2 (colored, dotted curves). The figure is reproduced with permission from Reference 167, licensed under the Creative Commons Attribution 3.0 Unported License.

was recorded with a 10 µm-thickness absorption cell. A commercial UV-Vis spectrometer system (Shimadzu UV 2700i, 1.4- 6.5 eV operating range) was used to perform the abosorption measurements using 10 μm to 10 mm path length absorption cells. Four different peaks are modeled in the spectrum shown in Figure 2.11 using Gaussian peak fits, with the peaks labeled as C, D, E & CTTS 1, and CTTS 2. The peaks are assigned based on the previously reported theoretical calculations in the References 162,164–166. The dominant C (∼3.53 eV, ∼351 nm) and D (∼4.30 eV, ∼288 nm) bands are spin-orbit coupled[164] and originate from the lowest excitation-energy mixed singlet-singlet and singlet-triplet n/$\pi \rightarrow \sigma^*$ valence electronic transitions of $I^-_{3(aq.)}$; further details are provided in Reference 162. An additional weaker peak is denoted as B (∼2.75 eV, 451 nm) and is due to the low-energy singlet-to-triplet transition in $I^-_{3(aq.)}$[164]. The lowest-energy $I^-_{(aq.)}$ $^2P_{\frac{3}{2}}$ and $I^-_{(aq.)}$ $^2P_{\frac{1}{2}}$ charge-transfer-to-solvent (CTTS) states are observed around 5.49 eV (226 nm, CTTS 1) and 6.44 eV (193 nm, CTTS 2)[165,166]. Weaker contributions associated with the $I^-_{3(aq.)}$ anion also contribute around 5.5 eV, witch are labeled as E. This feature is attributed to a higher-energy triiodide excited state. Such $I^-_{3(aq.)}$ and $I^-_{(aq.)}$ spectral overlap prevents the direct estimation of the residual $I^-_{(aq.)}$ content in the mixed solutions.

Although triiodide in aqueous solutions was studied previously by Erikson *et al.*[157] using the XPS technique, the amount of residual iodine, iodide, and triiodide conversions was not characterized. This is essential to characterize the prepared solution's components before performing XPS studies, as further discussed in Section 4.1.2, Chapter 4. More details about the sample preparation and characterization of the aqueous triiodide solution using UV-VIS absorption spectroscopy will be discussed in Section 4.1, Chapter 4, where the surface- and bulk-sensitive valence and core-level electronic energetics of the aqueous triiodide solutions are reported. The role of solute molecular symmetry, solute-solvent interactions, and the effects of electronic correlation on its ionization behaviors are also further explored. Notably, in this work, $I^-_{3(aq.)}$ XPS measurements were recorded with $Na^+_{(aq.)}$ counter ions, allowing the isolation and interpretation of the full I

$4d^{-1}$ spectrum. Complementary I $3d^{-1}$ measurements that allow a complete separation of the single- and multi-active-electron (SU) photoionization features are also reported.

2.5.3 Diazine Molecules

Pyridazine, pyrimidine, and pyrazine are isomers of each other and are collectively called diazines. Gas-phase pyrimidine and pyridazine have C_{2v} symmetry, whereas pyrazine has D_{2h} symmetry. Each molecule contains two non-bonding orbitals originating from the nitrogen lone pair electrons. These heterocyclic nitrogen-containing aromatic molecules can act as proton acceptors and form extensive hydrogen (H) bonding networks[37]. The isolated (gas) phase diazine molecular species exhibit rich excited state dynamics, and photochemical properties[172]. Due to their high solubilities and absolute absorption cross sections, these species are also ideal candidates to study ultrafast excited state behaviors such as IC, ISC, and Intra- and Intermolecular Energy Transfer (IET)[38] of polyatomic solutes in aqueous solution. The electronic structure of these molecules has been studied extensively in the gas phase using UV-Vis spectroscopy[173,174], X-ray absorption spectroscopy[175], and EUV photoelectron spectroscopy[172,176–181]. Previous studies of the isolated molecule allow the intrinsic properties of the molecules to be understood in the absence of environmental effects. RPES studies have been reported on pyrazine on top of a Cu substrate[182]. The inherent, intrinsic properties will be altered if we study them in a strongly-interaction environment, such as on a copper (Cu) substrate[182] or in aqueous solutions. As we put these molecules into aqueous solutions, electrostatic interactions and the dynamic, fluxional reorganization of the solvent molecules around the solute molecules may impact the solute molecular symmetry, electronic structure, and associated intra- and intermolecular charge re-arrangement dynamics. These effects are explored in Chapter 5.

UV-Vis Absorption Studies: Solvent effects have already been studied via UV-Vis absorption spectroscopy on diazines[37,184–188]. Here, 500 mM aqueous diazine solutions have been studied using the XPS technique to characterize the ground state electronic structure. A TRPES study was also performed on 500 mM aqueous pyrazine solutions to provide a basis for the study of the excited state electronic structure and associated relaxation dynamics. The goal of such measurements on aqueous molecules is to study the monomer in the aqueous phase, *i.e.* a single diazine molecule surrounded by and interacting with water molecules, without interaction with other solute species. Therefore, concentration-dependent UV-Vis and XPS studies have been performed to identify any spectral change due to dimer or higher-order complex formation. A previous study showed the effects of dimerization in pyrimidine and pyrazine at 500 mM concentration[189]. However, the measurements reported here suggest no dimer or higher-order complex formation of the diazine molecules at the implemented concentrations. Associated details are given in Appendix B.

Figure 2.12 shows the S_1 and S_2 state UV-Vis absorption spectra of all three diazines in previos gas and aqueous phases. Two dominant absorption bands are observed and assigned based on the gas-phase studies[174,177]. The first absorption bands are $n\pi^*$ type in all of the aqueous diazines and are found to be vibrationally structureless. The second absorption bands are $\pi\pi^*$ type and display vibrational structure. These excited states are noted to have more complex, multi-reference electronic characters[174,177]. The first aqueous-phase absorption band of pyrimidine is assigned to the $n\pi^*$ transition and $^1B_1$ state formation, populated via a $7b_2 \rightarrow 2a_2$ transition and with a peak absorption cross-section at $\sim$ 4.6 eV. Around $\sim$ 5.15 eV the second $^1B_2$ absorption band is observed and ascribed a $\pi\pi^*$ character. This state is populated via two different electronic transitions, $2b_1 \rightarrow 2a_2$ and $1a_2 \rightarrow 3b_1$[174,177]. The first absorption band of aqueous pyrazine is associated with the $^1B_{3u}$ state, accessed around $\sim$ 4.2 eV and assigned to a $6a_g \rightarrow 2b_{3u}$ transition. The second band peaks at 4.8 eV and is associated with the $^1B_{2u}$ state, which is populated via two electronic

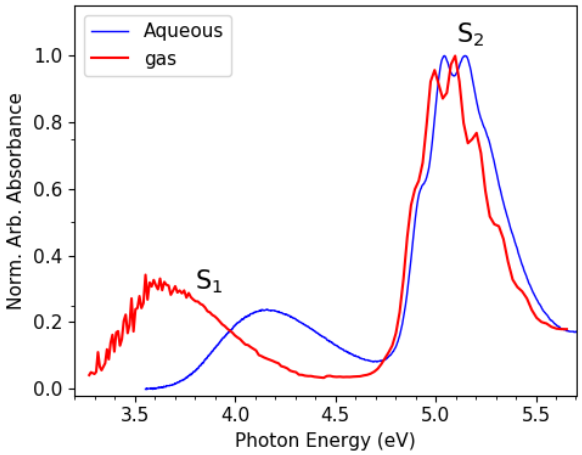

(a) Pyridazine gas-phase (red) and aqueous solution (blue) spectra

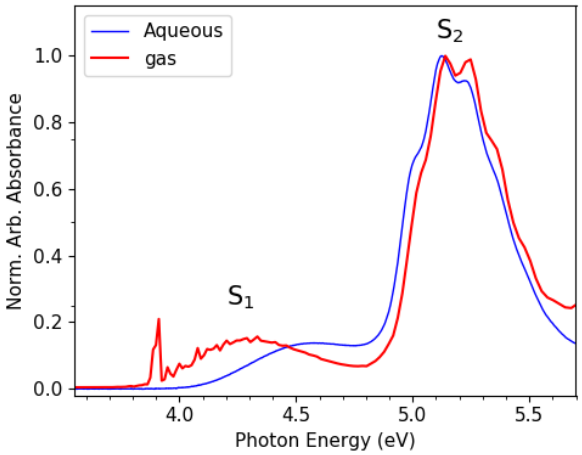

(b) Pyrimidine gas-phase (red) and aqueous solution (blue) spectra

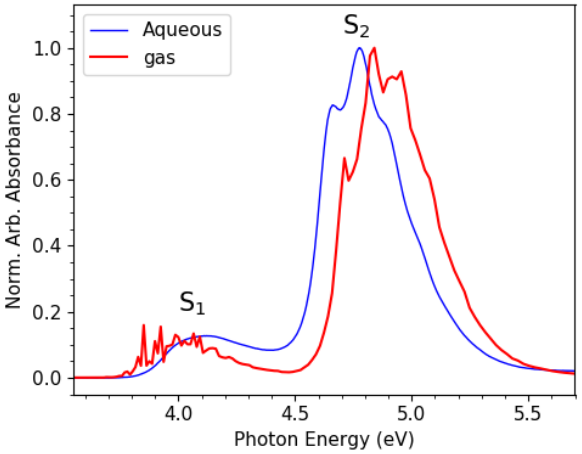

(c) Pyrazine gas-phase (red) and aqueous solution (blue) spectra

Figure 2.12: UV-Vis absorption measurements of the diazine gas-phase molecules and 500 mM aqueous solutions. The intensities of all the spectra are normalized to 1.0. The gas-phase measurements are reprinted from Reference 183, Copyright (2020), with permission from Elsevier.

transitions, $1b_{1g} \rightarrow 2b_{3u}$ and $1b_{2g} \rightarrow 2b_{3u}$. For aqueous pyridazine, the first absorption band is associated with the $^1B_1$ state and peaks at around $\sim$ 4.1 eV. It is assigned to a $8b_2 \rightarrow 2a_2$ transition. The second transition to a state $^1A_1$ peaks at $\sim$5.15 eV and is assigned to $1a_2 \rightarrow 2a_2$ and $2b_1 \rightarrow 3b_1$ transitions[174,177].

Comparing the gas-and aqueous-phase UV-Vis measurements, changes are observed in the spectral profiles for the S_1 and S_2 states for all three diazines. Specifically, the S_1 state transitions are all $n\pi^*$-like, where two heteroatoms of all of the diazines are involved. These transitions offer a possibility to study either localization or delocalization effects[185]. The Highest Occupied Molecular Orbital (HOMO) and Lowest Unoccupied Molecular Orbital (LUMO) are involved in this transition, where the HOMO is associated with the nitrogen lone-pair MO. The nitrogen lone-pair MO's are stabilized in the aqueous phase due to hydrogen bonding with the water solvent molecules. The aqueous solvent surrounding the diazine molecules affects both the spectral band positions and the band shapes. For the pyridazine system, shown in Figure 2.12a, the S_1 and S_2 state bands are blue-shifted in going from the gas to the aqueous phase. The S_1 state in the pyrimidine system is blue-shifted, while the S_2 state does not significantly shift, see Figure 2.12b. Finally, the S_1 state of the pyrazine system is also blue-shifted in the aqueous solution. However, in contrast to other diazines, the pyrazine S_2 state is red-shifted in the aqueous pyrazine system and the S_1 and S_2 states of all of the diazines

are differently shifted in going from the gas- to the aqueous-phase, and the amount of spectral shift varies among the diazine solutes. The former observation indicates a difference between the electronic structure of the diazine solutes, i.e. that the S_1 and S_2 state polarizabilities are different. This highlights that the solvent effect is electronic state and molecule specific[190]. Due to spectral inhomogeneous (and potentially lifetime) broadening, the S_1 state signals do not show the signature of vibrational features, as are present in the gas-phase spectra. For the S_2 states, all molecules and solutes show signatures of vibrational features, at least close to their electronic state origins. However, these features are not as sharp in the aqueous-phase as in the gas-phase. Several studies have been performed on the diazine molecules in the aqueous-phase to understand the effect of hydrogen bonding with water in the S_1 electronically excited states[37,185–188].

The origin of the S_1 state blue shifts in going from the gas-phase to an aqueous solution, which is attributed to a multiple of processes. Traditionally, n $\rightarrow \pi^*$ excitation leads to breaking of H-bonds in the delocalized excitation picture, where both N atoms are equally affected[37,190]. Additional effects *i.e.*, bond rearrangements, photohydrolysis and excited state Proton-Coupled-Electron Transfer (PCET) reactions are theoretically predicted in the localized excitation picture[185]. In that case the excitation affects only one symmetry pair and spontaneous symmetry breaking occurs. The excited state is stabilized with a π-like bonding structure, where the hydrogen atoms of the water molecules stay closer to a diazine ring nitrogen atom and hydrogen bonding appears to occur to the nitrogen π orbital.

Raman Spectroscopy Studies on Aqueous Diazine Solutions: Solvent effects on the pyrimidine molecule were also studied using Raman spectroscopy and Density Functional Theory (DFT) calculations[191–193]. The former study highlighted blue-shifting of the vibrational frequencies (ν_1, ν_{8a},ν_{8b}), where such blue-shifting was correlated with the charge transfer from the solute molecule to the solvent water molecule[191]. Two water molecules are connected with the diazine molecules, making four H-bonds. Among them, two strong N$\cdots$H-O and two weak C-H$\cdots$O bonds are formed with the pyrimidine molecule[193]. The solute-to-solvent charge transfer process has been reported to substantially decreases the nitrogen lone pair electronic density. Associated charge rearrangement also occurs between the CCC and NCN region of the molecule, and such rearrangements are likely linked to the polarization of the π electron cloud in the aqueous environment[191]. In addition to shifting the cationic or neutral state energetics, such changes may also be linked to the changes of the gas-to-aqueous BE energies, as will be discussed in Chapter 5. Some of the σ and π bonds are notably weakened, whereas some of them become stronger in the aqueous phase due to the intramolecular charge rearrangement effects in the aqueous diazine[191].

X-ray Spectroscopy Studies on Aqueous Diazine Solutions: Recently, an X-ray Absorption Spectroscopy (XAS) study highlighted the solvent's role in determining the electronic structure of aqueous pyridazine solutions. The solute electronic structure is perturbed and the MOs orbital are delocalized in the aqueous phase[92]. Pyrimidine aqueous solutions have been investigated using the Resonant-Inelastic X-ray Scattering (RIXS) technique[194], where these studies revealed solvent-induced Jahn-Teller effects in the aqueous solution that lift the degeneracy of the N 1s core orbitals and break the molecular symmetry. The dominant effect of the solvent is to elongate the C-N bond lengths of the molecule in the aqueous solution. The study further predicted that the other isomers, aqueous pyridazine and pyrazine might behave similarly[194]. Although the decension of molecular symmetry happens in aqueous pyrimidine, the MOs belonging to the C_{2v} symmetry group were used to interpret the valence electronic structure in the RIXS emission spectrum.

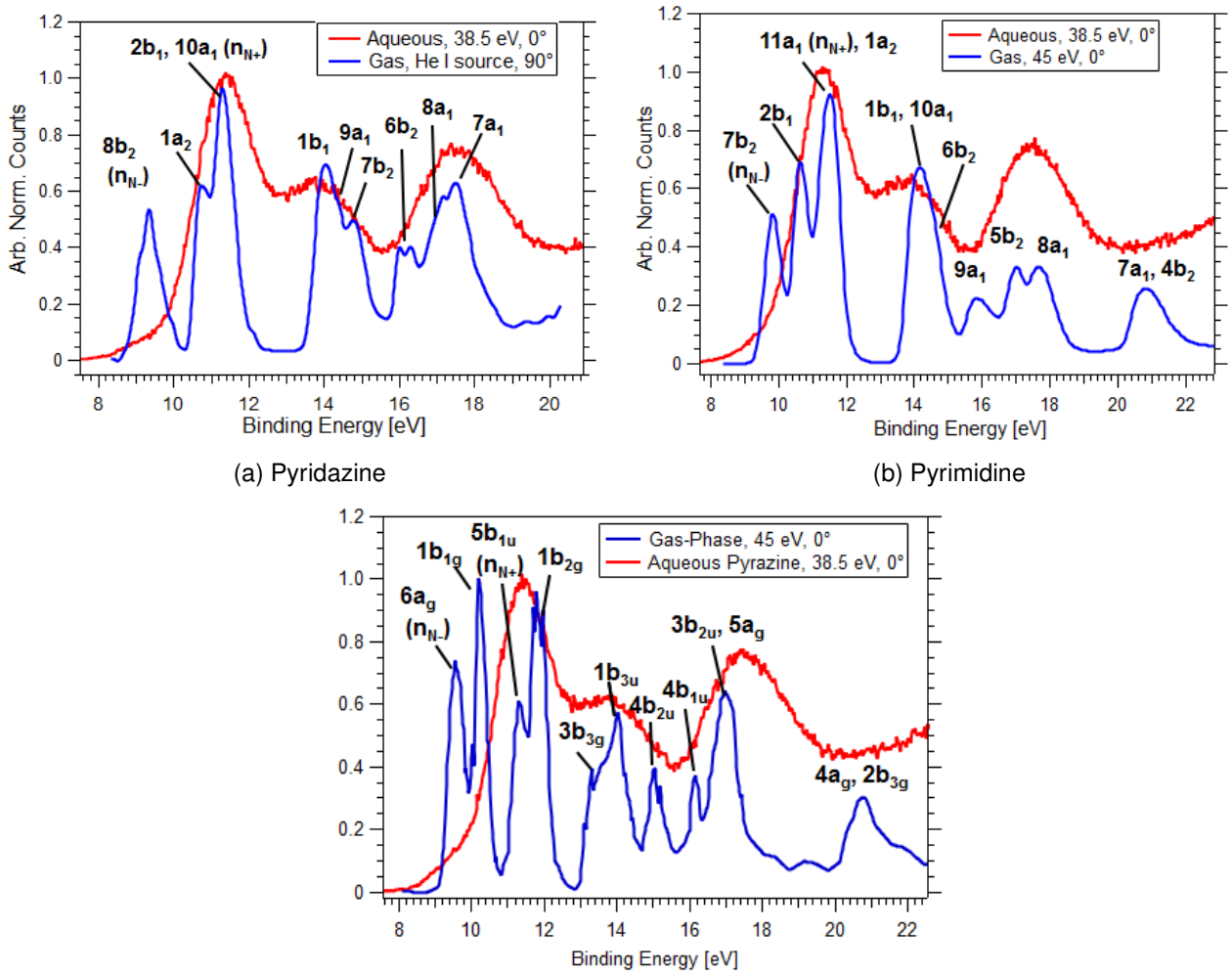

(a) Pyridazine

(b) Pyrimidine

(c) Pyrazine

Figure 2.13: Valence photoelectron spectra of gas- and aqueous phase diazine molecules. Pyridazine, pyrimidine, and pyrazine spectra are shown in panels (a), (b), and (c), respectively. The gas-phase valence PE spectra were reproduced from References 176,195 using the webplot digitizer[196]. The gas-phase pyridazine PE spectra was recorded using a He I source using 42.5 eV excitation energy, and the spectrometer was oriented at 90°. Gas-phase pyrimidine and pyrazine spectra were recorded at 0° using 45 eV excitation energies. The 500 mM aqueous-phase PE spectra were recorded using a bised (V=-40 V) liquid jet[66,197], and a 38.5 eV photon energy. The Time-of-Flight (TOF) spectrometer was oriented at 0° to the incoming light polarization vector and the data acquired using the spectrometer in drift mode. The bias-induced liquid phase spectral energy calibration was done using the water $1b_1$ position of 11.33 $\pm$ 0.04 eV[66]. The gas-phase PE spectra have been normalized to the maximum signal position, whereas the aqueous phase PE spectra were normalized by the solvent water $1b_1$ ionization peak position. The panel (a) is reprinted from Reference 195, with permission from copyright @2000, American Chemical Society. The panel (b) and (c) are reprinted from Reference 176, with permission from Elsevier.

PES Studies on the Gas and Aqueous Phase Diazines: The complete overviews of the gas-phase valence electronic structure has been reported for pyrimidine and pyrazine[176]. The ionization processes of the outer valence orbitals were interpreted using a single-hole model, where multi-electronic effects were deemed to influence the inner valence orbitals (BEs >15 eV). In addition, the same study highlighted the orbital characters, photoelectron angular distributions, and the shape resonances of the gas-phase species. Pyridazine PES studies have also been reported up to an ionization energy of 18 eV[195]. The HOMO of the diazine molecules are non-bonding orbitals, where the other non-bonding orbitals are HOMO-2, HOMO-3 and HOMO-1 for the pyrimidine, pyridazine and pyrazine molecules, respectively. Associated C and N K-edge

RPES studies have been performed on the isolated (gas-phase) pyrimidine molecule[88]. RPES studies have also been reported on pyrazine on top of a Cu substrate[182]

In this research work, liquid-microjet-based non-resonant and resonant PES techniques have been applied to study the aqueous diazine molecules and investigate the electronic structure and associated molecular bondings. The spectral shifts, peak widths, and relative intensities of the recorded PE spectra are compared to the previously reported isolated molecule literature to highlight the environmental (solvent) effects. Figure 2.13 shows a preliminary comparison between the gas- and aqueous-phase valence PE spectra. More details are provided in Chapter 5. The gas-phase PE spectra (blue) are reproduced from References 176,195, the PE spectra have been digitized using the webplot digitizer[196]. A biased liquid-microjet setup and pulsed 38.5 eV EUV photoexcitation source was used to record aqueous-phase valence PE spectra (red). A Time-of-Flight (TOF) PE spectrometer was oriented at 0° with respect to the incoming light polarization vector, to record the 0.5 M diazine aqueous-solution PE signals. PE signal from the diazine molecules in the aqueous-phase are expected to overlap with the dominant water PE signal, as shown in Figure 2.13. Furthermore, due to the solute-solvent electrostatic interactions and reorganization of the solvent molecules, the solute binding energies also expected to be shifted and inhomogeneously broadened. In addition, as shown in the gas-phase spectra, the molecules have high densities of states in the BE region of 9.5-12 eV, resulting in spectral congestion. The solvent electronic structure may also be perturbed by the presence of solute molecules[66], which is an ongoing research field, which is beyond the scope of this research work.

2.5.4 Time-Resolved Studies of Gas-Phase Pyrazine

Pyrazine is one of the diazine molecules that allows excited-state chemistry and hydrogen-bonding dynamics to be studied in aqueous solution[185]. Here, the solvent changes the ground and excited state potential energy surface topologies and the relaxation dynamics compared to in the gas phase. This has been exemplified in several experimental studies[119,120,124,126,132]. The molecule shows a broadband UV-Vis absorption around 240-270 nm[38], as shown in Figure 2.12c. UV-Vis absorption studies highlight several singlet and triplet excited states in this system[174] . As shown in Figure 2.14, some are optically bright, and some are optically dark. Here, a concerted effort was made to observe the relaxation dynamics following photoexcitation from the ground S_0 state to the S_2 excited state in the aqueous phase. Similar studies have already been carried out in the gas phase[39,40,50,198]. A comparison of the experimental results with previous gas-phase measurements has also correspondingly been made, allowing the role of the aqueous solvent in modifying the excited-state electronic structure and relaxation dynamics of the pyrazine molecule to be probed. As a basis to describe the aqueous-phase work, a short review of gas-phase literature is presented below.

The ultrafast $S_2 \rightarrow S_1$ IC process in pyrazine has been extensively studied[200]. The S_2 to S_0 photorelaxation processes have been investigated using the TRPES[39] and Time-Resolved X-ray Absorption Spectroscopy (TRXAS)[40] methods. Several theoretical studies have been performed to study vibrionic coupling and the conical intersections between the S_2/S_1 potential energy surface[199,201–205]. In the isolated (gas) phase, the Frank-Condon region of the S_2 state is very close to the S_2/S_1 conical intersection, resulting in IC within one excited-electronic-state vibrational period (<30 fs)[39]. High-time resolution TRPES experiments using sub-20 fs laser pulses were used to monitor the relaxation dynamics from the S_2 state following photoexcitation using broadband UV pulses cantered at 263 nm[50,198], reporting a S_2 to S_1 population transfer that occurs in 22 fs via IC[50]. The gas-phase TRPES experiments identified the signature of the neutral S_2 excited state via ionization to a number of cationic states, D_0-D_3[39]. Among them, D_3 gives a clear signature of the S_2 excited state, while the others overlap with other ionization channels. A global fitting analysis of the gas-

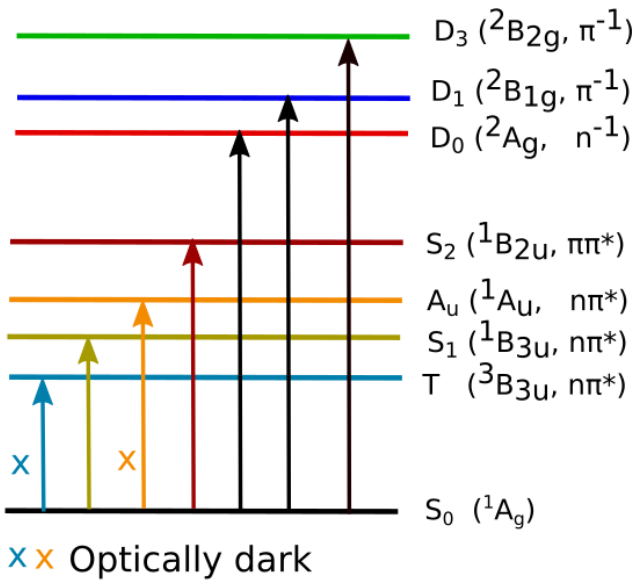

Figure 2.14: Optically allowed and optically forbidden bands of pyrazine in the UV range. The diagram is based on the concept presented in Reference 199.

phase TRPES data retrieves two spectral components of the S_2 electronic state, one is broad (BEs of 6.0-7.8 eV), and another is relatively narrow (BEs of 4.5-5.5 eV). The S_1 and optically-dark A_u neutral states are both expected to most favorably ionize to the D_0 cationic state[39,40]. The gas-phase theoretical calculation indicates that the equilibrium geometry of the Au state lies above the S_1 state, suggesting that it may not be populated following the S_2 excitation or $S_2 \rightarrow S_1$ IC[206].

Several theoretical studies have been performed to analyze the involvement of the singlet, neutral A_u state during transfer of population from the S_2 state to S_1 state through IC[206–208]. Werner *et al.*[205] theoretically predicted that the S_2 decays to the ^1A_u state and that the associated population is subsequently transferred to the S_1 state. Although the role of the ^1A_u state in the relaxation dynamics was theoretically proposed, its involvement is highly dependent on the level of theoretical calculations used to calculate the excited electronic state features[199,205–208]. The ^1A_u state was not experimentally identified in VUV-probed TRPES experiments and a number of reasons for this have been proposed[39]. Since TRPES[39,98] did not extract the signature of ^1A_u state, it was suggested that some part of the population from the S_1 state internally converted back to the ground state, and the rest of the excited state population transferred to the tripet state. The triplet state is long-lived, and an associated lifetime following S_2-state photoexcitaiton was not reported. Dietz *et al.*[209] reported that the triplet state decays on μs timescale following S_1-state photoexcitation.

The first row of Table 2.1 summarizes the TRPES kinetic models applied to describe the S_2 and subsequently-populated-state dynamics excited state. In contrast to the TRPES data and analysis, the gas-phase TRXAS data and analysis suggested that the population from the ^1A_u state is transferred to the ground state as summarized in the second row in Table 2.1. The alternative method of transient optical absorption spectroscopy was suggested to probe the molecule and identify any role of ^1A_u state[210,211]. Following theoretical prediction by Tsuru *et al.*[211], the x-ray transient absorption technique at the C K-edge was shown to reveal the involvement of the ^1A_u state in the relaxation dynamics[40]. Later, Kaczun *et al.*[212] calculated the UV-pumped soft-x-ray probe transient absorption spectra at the N pre-K-edge and identified the involvement of the dark ^1A_u state, which is populated from S_1 at a delay of 65 fs.

Table 2.1: Summary of the gas-phase experimental results and associated UV-excited-state population lifetimes of the pyrazine molecule. In all cases, UV pulses of 263-267 nm promotes the molecule from the ground to the excited state via a $\mathrm{S}_0 \longrightarrow \mathrm{S}_2$ transition.

Experiment	Model	Time-constants
Gas-phase TRPES[39,50,198] Broadband UV centered at 263 nm	$\mathrm{S}_2 \xrightarrow{\tau_1} \mathrm{S}_1 \begin{array}{l} \xrightarrow{\tau_3} \mathrm{S}_0 \\ \xrightarrow{\tau_2} \mathrm{T} \end{array}$	$\tau_1 = 22$ fs $\tau_2 = 112$ ps $\tau_3 = 14$ ps
Gas-phase TRXAS[40] 267 nm excitation	$\mathrm{S}_2 \xrightarrow{\tau_1} \mathrm{S}_1 \xrightarrow{\tau_2} \mathrm{A_u} \xrightarrow{\tau_3} \mathrm{S}_0$	$\tau_1 = 22 \pm 3$ fs $\tau_2 = 200 \pm 50$ fs $\tau_3 = 15$ ps

Chapter 3

Experimental Techniques: Methods and Instrumentation

This research focuses on the study of the photophysical, photochemical and functional properties of aqueous solutions. In this thesis work, such properties were investigated by studying the electronic structure and excited-state relaxation dynamics using PES techniques (see Sections 2.4.1 and 2.4.5, Chapter 2). Aqueous solutions studies were performed using steady state and time-resolved experimental techniques. The steady state XPS experiments described in this thesis work were performed using synchroton-based x-ray sources, whereas the time-resolved TRPES experiments were performed using laser-based EUV sources. The light sources and principles of their operation are described in Section 3.1.

3.1 Light Sources and Facilities

Modern soft x-ray synchrotron facilities, such as BESSY II[168] and PETRA III[169], provide widely tunable, bright, high-energy-resolution soft x-ray that enable the energy-domain study of aqueous solutions. On the other hand, laboratory- or accelerator-based ultrashort-pulse EUV sources allow experiments to be performed with a femtosecond time resolution. In the case of PES experiments, studies of the electronic structure and excited-state relaxation process on an absolute BE scale in aqueous solutions requires a proper choice of the ionizing photon energy, as discussed in the following sub-section.

3.1.1 Choice of Photon Energies for PES in the Liquid Phase

Following the photoionization process, the produced electrons can lose KE energy due to the inelastic scattering processes that generally occur in the condensed-phase. Such inelastic scattering creates a secondary electron background signal and can affect the primary PE spectrum, which is generally of primary interest. Such inelastic scattering processes can cause a BE shift of the PE peaks, particularly in cases where relatively small amounts of energy are transferred from primary photoelectrons to the surrounding medium via vibrationally-inelastic scattering events. Such effects have been investigated in Reference 66, which showed the extracted Vertical Ionization Energy (VIE) of the water $1b_1$ peak at different photon energies, see Figure 3.1. It was found that when an aqueous solution is probed with a photon energy below $\sim$30 eV, the measured BE of the water $1b_1$ peak is altered due to the inelastic scattering of the photoelectrons, leading to the extraction of an erroneously high BE energy. On the other hand, when the probe photon energy is above $\sim$30 eV then the BE of the primary water $1b_1$ PE peak does not change within the error limit. Rather, the inelastic scattering processes are predominantly electronic in nature, leading to readily discernible, additional

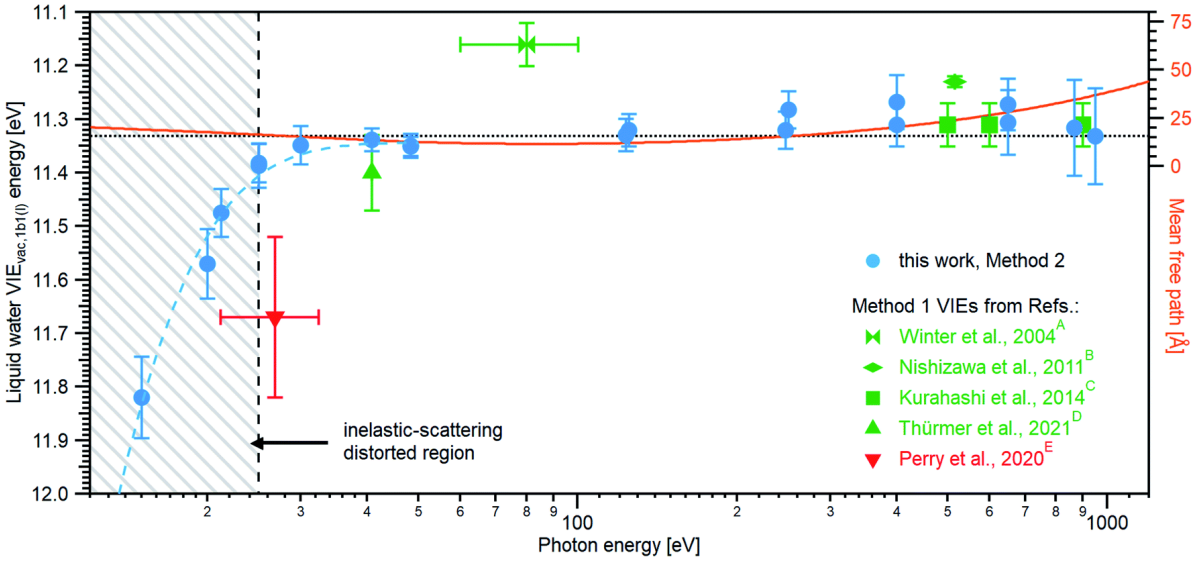

Figure 3.1: Photon-energy-dependent Vertical Ionization Energy (VIE) and mean free path of the PEs generated from the $1b_1$, normally non-binding electrons liquid water as a function of photon energy. At lower photon energies, vibrational inelastic scattering dominates in the condense-phase photoemission process and causes the measured BEs to be erroneously modified. The figure is reprinted with permission from Reference 66, published by the PCCP Owner Societies. This work is licensed under the Creative Commons Attribution 3.0 Unported License.

inelastic scattering features in the photoelectron spectra. For this reason, in order to reduce the secondary electron background underneath the primary photoelectron peaks, which can influence the recovered KE/ BE energies of the generated PEs of the studied aqueous solutions, EUV and X-ray ionizing-radiation sources were used in this thesis work. Specifically, the photon energies used in the x-ray experiments were 150 eV or above, whereas the EUV based experiments were performed using a ∼38.5 eV photon energy.

3.1.2 Synchrotron Sources

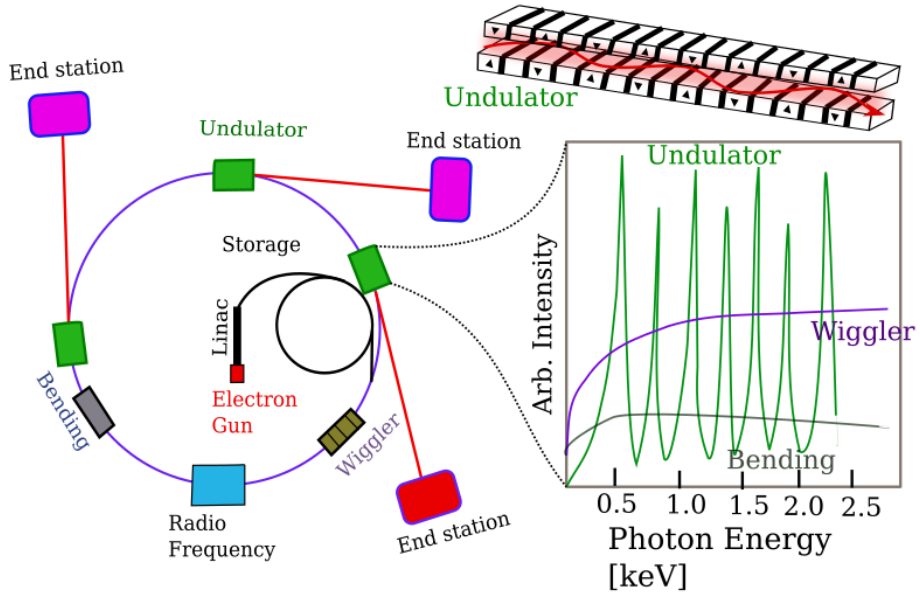

Figure 3.2: Generation of synchrotron radiation. A schematic view of storage ring is shown on the left side. The top-right shows a schematic of an undulator and the bottom-right image shows the emitted radiation pattern of synchrotron radiation.

In generating synchrotron radiation, charged particles (electrons) are accelerated and travel at a relativistic velocity in a circular orbit and through magnetic structures, which force the electrons to oscillate and emit radiation. This results in a narrow-cone light emission pattern in the laboratory frame[213,214]. Figure 3.2 shows a schematic diagram of a synchrotron radiation facility. The electrons are generated using an electron gun, then subsequently pre-accelerated in a linear accelerator and a booster synchrotron[215]. This pre-acceleration section is called the injection chain. A high voltage power supply ($\sim$100-120 kV) is applied at the electron gun to create a pulse of accelerated electrons, and after the linear accelerator, the electron beam is accelerated to an energy of $\sim$50-60 MeV and is injected into the booster synchrotron. The electrons are accelerated to their final energy in about half a second in the booster synchrotron, before being injected into the storage ring, where the electrons travel at 99.99 $\%$ of the speed of light[215].

Third-generation synchrotron facilities are optimized for producing high-intensity radiation with the use of insertion devices. These devices are the magnetic structures that have an alternating polarity and a transversal or helical configuration, which are placed into the straight sections of the electron storage ring[215]. The relativistic electrons injected into the storage ring are guided by the insertion devices, see Figure 3.2. However, the electrons are mutually repulsive to each other. Thus, the tightly focussing beam trajectory can only be maintained in a storage ring by using additional quadrupole-, sextu- or octupole turning and focusing magnets. Insertion devices cause the electron to be centripetally accelerated by the Lorentz force, toward the center of the circular path. As a result, synchrotron radiation is produced when the electron passes through the insertion devices and the electron beam losses energy, which must be recovered elsewhere in the storage ring to maintain the electron beam orbit[215]. There are three different kinds of magnetic structures that are used to produce synchrotron radiation: bending magnets, wigglers, and undulators. Bending magnets force the electrons to follow a single curved trajectory and emit a fan of radiation around the bend structure. Undulators and wigglers consist of an array of dipole magnets, which increase the photon beam intensity compared to bending magnets, as shown in Figure 3.2. The undulator and wiggler can be distinguished by the dimensionless parameter K[213,214]. For K $>>$ 1, the insertion device behaves like a wiggler. The radiation is similar to bending magnets, but due to a higher magnetic field, the emitted radiation is shifted to higher photon energy. The photon flux is also increased by the number of magnets. Alternatively, for K $<<$ 1, the insertion device is an undulator. The emitted radiation cones from each associated wiggler overlap coherently, and for an undulator periods of N, the associated interference results in an N^2 increase in the photon flux[215]. The period of the dipole magnets determines the wavelength of the emitted radiation. In the relativistic limit, the emitted wavelength is given by[216,217]:

$$\lambda = \frac{\lambda_{\mathrm{u}}}{2\gamma^2} \tag{3.1}$$

Where λ_{u} is the magnet structural period and γ is the Lorentz factor. For λ_{u}= 5 cm and γ= 9$\times 10^6$, the radiation wavelength in the laboratory frame of reference is 2.8 nm corresponding to photons with an energy of 442.8 eV. The electron beam loses energy in emitting synchrotron radiation and is accelerated by a radio frequency accelerator cavity placed into the storage ring. Moreover, the circulating electrons collide with the residual gas in the ultrahigh vacuum environment of the synchrotron ring, and the beam current decreases slowly at an exponential rate. Thus, a new beam injection is commonly performed every 10-12 hours[215].

Synchrotron beamlines: Both beamlines used in this thesis work implemented undulators and delivered high-flux tunable X-ray light for experiments. The tunability of the undulator-based x-ray sources is obtained by changing the gap of the dipolar magnetic structure. Details of the beamlines can be found in the refer-

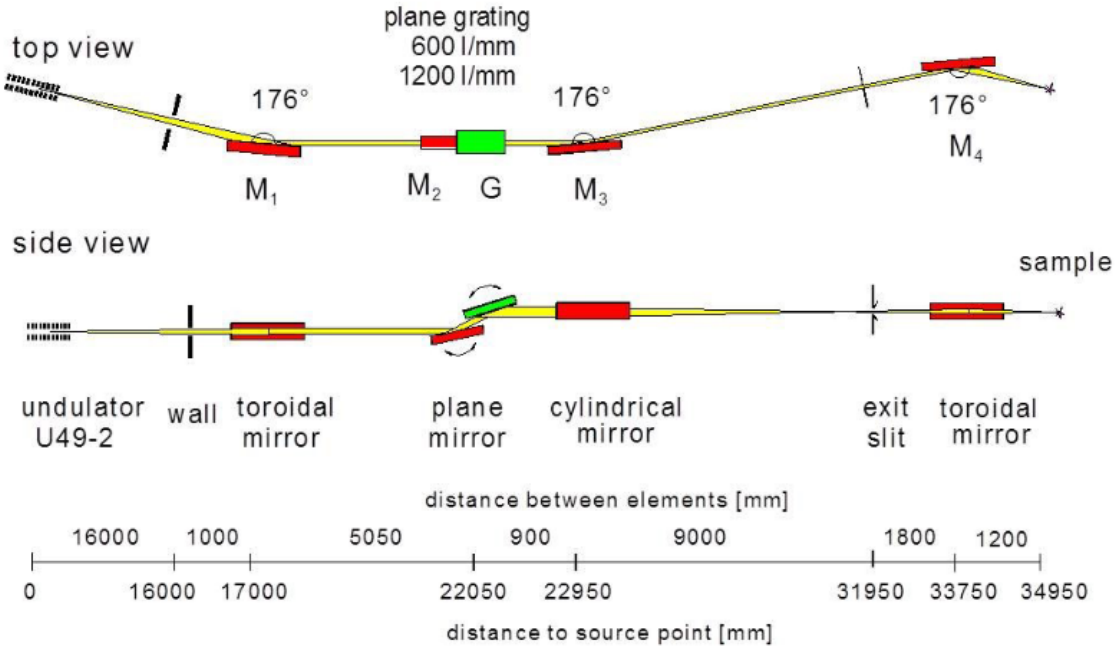

Figure 3.3: Optical layout of the U49-2 PGM-1 beamline at BESSY II. M_1, and M_4 are the toroidal mirrors, M_2 is a plane mirror, M_3 is a cylindrical mirror, and G is the plane grating. The figure has been reproduced with permission from Reference 168, licensed under a Creative Commons Attribution 4.0 International License.

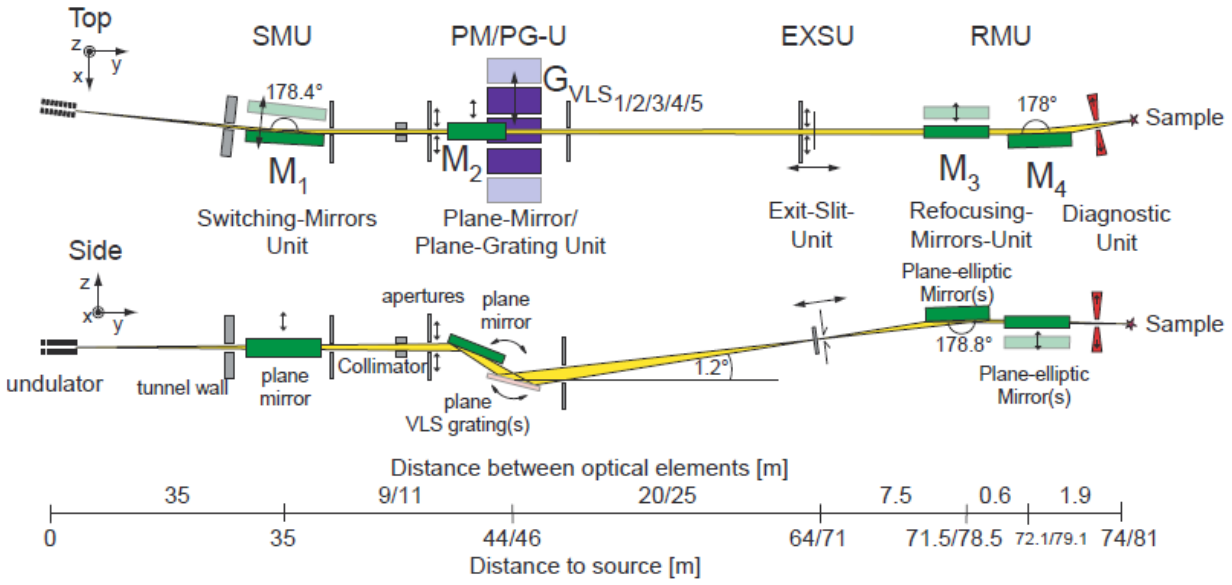

Figure 3.4: Optical layout of the P04 beamline at PETRA III. SMU denotes switching-mirrors unit, PM/PG-U denotes plane-mirror/plane-grating unit, EXSU denotes exit-slit unit, RMU is the refocusing mirror unit. M_1 and M_2 are plane mirrors, M_3 and M_4 are plane-elliptic mirrors. The figure has been reproduced from Reference 169, Copyright 2013, with permission from Elsevier.

ences[168,169]. The U49/2 PGM-1 beamline at BESSY II has a planar hybrid undulator and the P04 beamline at PETRA III has an Advanced Planar Polarized Light Emitter-2 (APPLE-2) undulator. In both setups, undulator radiation is subsequently monochromatized using a combination of mirrors and a grating before refocusing and delivering synchrotron light to the experimental end station. The U49/2 PGM-1 beamline has a 600 line/mm grating and offers relatively low resolving power, whereas P04 beamline at PETRA III offers a significantly energy resolution due to its longer length and implementation of up to 1200 l/mm gratings. The important parameters of U49/2 PGM-1 and P04 beamlines are summarized in Table 3.1

Table 3.1: Important paramters of U49/2 PGM-1, BESSY II and P04, PETRA III synchrotron beamlines. Beamline parameters are taken from the References 168,169

Parameters	**U49/2 PGM-1, BESSY II**	**P04, PETRA III**
Undulator	Planer hybrid period: 84 mm, gap: 16 mm	APPLE-2 period: 72 mm, gap: 11 mm
Photon energy	85-1600 eV	250-3000 eV
Resolving power	6000 (@150 eV with a 50 μm) exit slit	10000 (up to > 3 $\times$ 10^4 @1 keV)
Photon flux	10^{13} photons/s (85 - 500 eV) 10^{12} photons/s (500 - 1500 eV)	1– 5 $\times$ 10^{12} photons/s
Spot size	$\sim$100 $\times$ 80 μm^2	10 $\times$ 10 μm^2, 50 $\times$ 50 μm^2
Polarization	Linear, horizontal	Circular (<0.1 Hz switching rate)

3.1.3 Femtosecond Laser System and Generation of Ultrashort Pulses

A Ti:Sa femtosecond laser system is the main driving source used to generate short pulses in the UV or in the EUV spectral range in the ULLAS laboratory at the Helmholtz-Zentrum Berlin. The commercial laser system delivers ultrashort pulses initially from a seed oscillator using the Kerr-lens mode-locking technique and then uses an amplification scheme to produce ultrashort pulses of 25 fs Full Width Half Maxima (FWHM) pulse duration, 2.5 mJ pulse energy, and 800 nm central wavelength at a 5 kHz repetition rate. Figure 3.5 shows a schematic diagram of the laser system. The oscillator (Ti:Sa COHERENT Vitara, Coherent Inc.) is pumped by a continuous wave laser (Coherent-Verdi-G5, Coherent Inc.) at 532 nm with 5 W average power and operates at a repetition rate of 80 MHz.

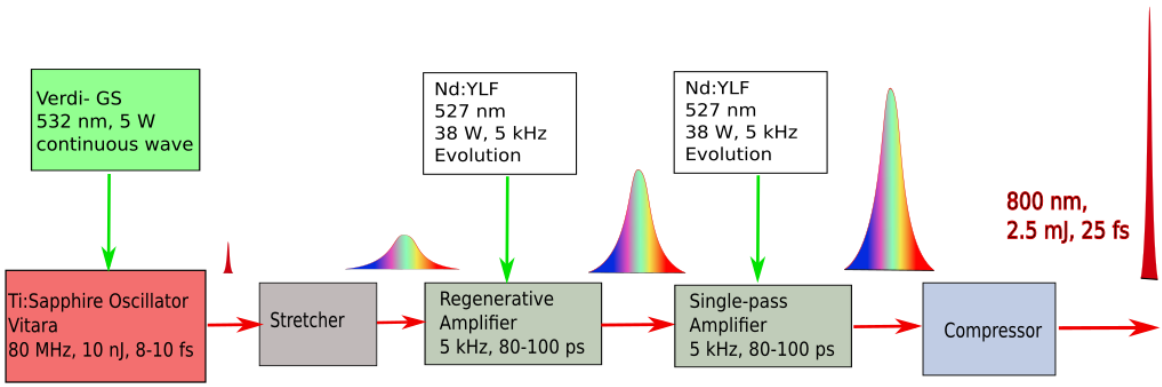

Figure 3.5: Schematic diagram of the femtosecond Ti:Sa laser system that delivers 25 fs laser pulses at a center wavelength of 800 nm at a 5 kHz repetition rate.

Initially, the Kerr-lens mode-locking technique is implemented to generate a train of pulses at 800 nm central wavelength and a 80 MHz repetition rate. The oscillator output at 5 nJ pulse energy is rather small, and it requires further amplification to drive high-order non-linear optical processes. The amplification scheme includes three stages: stretcher, regenerative amplifier, single-pass amplifier, and compressor. The stretcher is used to elongate the pulses to a 80-100 ps time duration in order to avoid damage of the optical components due to high peak intensity. The Ti:Sa regenerative amplifier is used for the amplification of the pulses to mJ-level. These pulses are subsequently amplified in second single-pass-amplifier Ti:Sa crystal. Finally, the compressor grating and mirror set compresses the pulse to a 25 fs temporal duration. Such an amplification process is known as chirped-pulse amplification (CPA)[218]. During the amplification process, the stretched ps laser pulses are amplified in the regenerative amplifier. The amplifier consists of a resonator cavity, a Ti:Sa crystal, and two pockels cells with polarizers. The crystal is pumped by half of the output of an Nd:YLF pulsed

laser (COHERENT Evolution, Coherent Inc.) at 527 nm, with an average power of 38 W. The repetition rate of the laser pulse initially decreases by selectively injecting oscillator pulses through pockels cells operating at 5 kHz. Then the incident oscillator pulses make several round trips through the pumped Ti:Sa crystal, and during each round trip, the pulse gains energy. After the amplification is saturated, a second Pockels cell operating at 5 kHz re-directs the amplified pulse out of the cavity. The amplified pulses are then further amplified in a single-pass amplifier, in a second Ti:Sa crystal, pumped by the second half of the Nd:YLF laser output. Finally, the amplified pulses are compressed by a dual grating compressor that introduces a chirp of the opposite sign with respect to the stretcher and the dispersion introduced by the amplifier components.

Generation of UV Laser Pulses

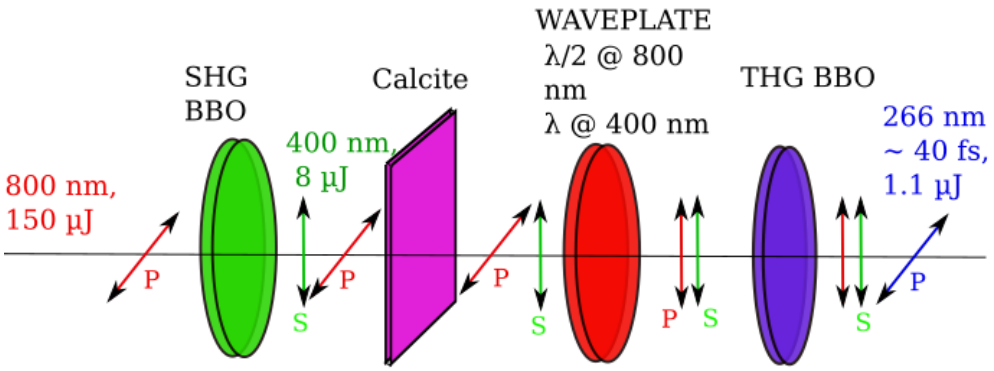

Figure 3.6: Generation of 267 nm pulses by mixing 800 nm and 400 nm beams using a Sum-Frequency Generation (SFG) scheme in a collinear geometry. The setup consists of Second Harmonic Generation (SHG) and SFG non-linear crystals, a dual waveplate and a calcite plate delay compensator. S and P refers to the horizontal and vertical polarization of the beams, respectively.

267 nm laser pulses were produced via Sum-Frequency Generation (SFG) of the 800 nm beam and its second harmonics. The SFG setup is schematically shown in Figure 3.6. The p-polarized fundamental beam of 150 μJ pulse energy was passed through a 100 μm thick Beta Barium Borate (BBO) crystal cut at a θ=29.2° phase matching angle to generate 400 nm laser pulses. Due to the type I phase matching scheme of the Second Harmonic Generation (SHG) stage, the generated second harmonic is s-polarized. The generated 400 nm pulses travel slower through the subsequent optics and in air in comparison to the 800 nm pulses, due to the normal, negative refractive index dependence with increasing wavelength. Therefore, the two collinear but orthogonally polarised beams were passed through the delay compensator calcite plate that changes the propagation ordering of the beams and delays the 800 nm pulse compared to the 400 nm. In order to generate 266 nm pulses using efficient, type I phase matching using a SFG process, both the 800 nm and 400 nm beam polarizations need to be the same. A dual waveplate is used to rotate the polarizations of the 800 nm and 400 nm beams by 90° and 180°, respectively. Finally, both beams propagate collinearly, are overlapped spatially and temporally in the SFG BBO, cut at a phase matching angle of θ=44.3°, and a p-polarized 267 nm beam is generated.

Ultrashort EUV Pulses Generation

EUV pulses were produced via gas-phase High Harmonic Generation (HHG), a strong-laser-field, non-perturbative process. In this process, the laser wavelength is converted into shorter wavelengths through high-order non-linear light-matter interactions in a gas medium. The HHG process was first described semi-

classically by Paul Corkum[219] and later it was also decribed quantum mechanically[220]. In both theoretical descriptions, it is assumed that only a single outer electron of an atom and molecule participates in the HHG process (single active electron approximation), whereas other electrons are essentially frozen. The HHG process is represented by a three-step model that includes tunnel ionization, propagation, and recombination. These three steps are described in more detail below

Step 1, Ionization: Ionization in the laser field can be classified into two different processes, multiphoton ionization and tunnel ionization[221]. The transition between these two phases is expressed using the Keldyish parameter (where atomic units are used in the following):

$$\gamma = \sqrt{\frac{\mathrm{I_p}}{2\mathrm{U_p}}} \tag{3.2}$$

$$\mathrm{U_p} = \frac{\mathrm{E}^2}{4\omega^2} \tag{3.3}$$

Where $\mathrm{I_P}$ is the ionization potential of the ionized medium, and U_p is the electron ponderomotive energy in a laser field with an electric strength amplitude, E, and angular frequency, ω. For $\gamma >$1, ionization has a multiphoton character. This happens at lower intensities and higher frequencies of the laser field. On the other hand, for $\gamma <$1, ionization acquires a tunneling character. At even higher intensity conditions, for $\gamma \ll$1, the system enters the above barrier ionization limit[222]. Electron rescattering takes place and HHG spectra can be seen in the multiphoton[223] and tunneling regime. Under the typical conditions of the HHG process, where a strong laser field of infrared wavelength is applied, the initial ionization step is of tunneling character. In this case, the laser electric field is strong enough so that it distorts the atomic Coulomb potential experienced by the electrons and enables an electron to escape the potential through tunneling, see step 1 in Figure 3.7a for an illustration. Under low-frequency, high-intensity conditions, the electric field varies so slowly during the ionization process that it can be approximated by a static electric field (quasi-static approximation), and time is simply entered as a parameter[221]. This tunnel ionization frees the active electron resulting in it appearing in the combined laser and Coulomb filed with near zero kinetic energy and momentum.

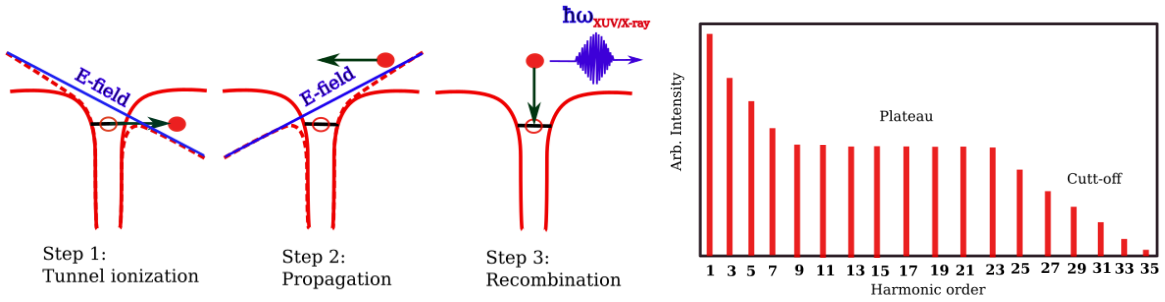

(a) Semiclassical three-step model.

(b) Schematic of HHG emission spectra

Figure 3.7: Panel (a), HHG process represented by the semiclassical three-step model[219], which includes tunnel ionization (left panel), propagation of the free electron (middle panel) and recombination of the electron to the parent ion (right panel). Panel (b), schematic representation of the HHG emission spectrum produced by a many-cycle driving laser and from an isotropic medium.

Step 2, Propagation: After tunnel ionization, the electron propagates in the laser field. Since the laser electric field dominates, the Coulomb potential of the residual core can often be neglected. This is known as Strong-Field Approximation (SFA)[221]. Step 2, shown in Figure 3.7a, illustrates the ionized-electron propagation. Newtons equations can describe the motion of the electron. The free electron is accelerated in the

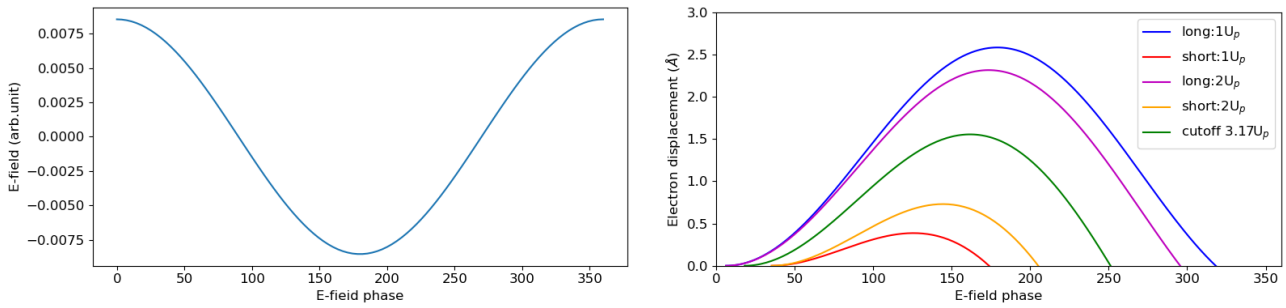

(a) Laser electric field

(b) Electron trajectories

Figure 3.8: Electron trajectories within the driving laser electric field. The panel (a) shows a fraction of the laser electric field oscillation cycle, without an intensity envelope. The considered laser field has central wavelength of 800 nm and an intensity of about 10^{14} W/cm^2. The panel (b) shows the electron displacements of the short and long trajectories. The above figures are plotted based on the concepts presented in Reference 221.

presence of the laser field and gains KE, with the E-field eventually changing direction and potentially driving the free electron back towards the ion-core. The KE gain and probability to return to the ion core strongly depends on the phase of the laser field at the time of tunnel ionization. For a linearly polarized laser field, E=E$_0$ cos(ωt), the position and velocity of the electron as a function of time described as follows:[221]

$$\mathrm{x(t)} = \frac{\mathrm{E}}{\omega^2}[\cos(\omega \mathrm{t_0}) - \cos(\omega \mathrm{t}) + \omega(\mathrm{t_0} - \mathrm{t})\sin(\omega \mathrm{t_0})] + \mathrm{x(t_0)} \tag{3.4}$$

$$\mathrm{v(t)} = \frac{\mathrm{E}}{\omega}[\sin(\omega \mathrm{t}) - \sin(\omega \mathrm{t_0})] \tag{3.5}$$

Where, t$_0$ is the time of ionization. This description assumes that the initial electron position and velocity is zero.

Step 3, Recombination: The recombination time is obtained by solving equation 3.4 for x(t$_r$)=0. The electron recombines with the parent atom and emits a high energy photon. The total KE can be obtained from the final velocity of the electron and is given by:

$$\begin{aligned} \mathrm{E_{kin}} &= \frac{1}{2}\mathrm{v}^2 \\ &= 2(\sin(\omega \mathrm{t_r}) - \sin(\omega \mathrm{t_0}))^2 \mathrm{U_p} \end{aligned} \tag{3.6}$$

Figure 3.8 illustartes the electron trajectories in the linearly polarized laser field. When the electron is ionized, within $\pi/2 < \omega \mathrm{t_0} < \pi$ (modulo 2π), it does not return back to the parent ion. On the other hand, if tunnel ionization takes place within the interval $0 < \omega \mathrm{t_0} < \pi/2$ (modulo 2π), the electron comes back to the parent ion[221]. The maximum KE gain by the electron in the laser field is 3.17U$_p$. For a particular KE gain, there are two possible trajectories. One trajectory, called the long trajectory, initiates within 0$< \omega t < 17°$ and returns to the core at $\omega t_r > 250°$. Another trajectory called the short trajectory starts within 17$< \omega t < 90°$ and returns to the core at $\omega t < 250°$. Figure 3.8b highlights different trajectories at KE positions of 1U$_p$, 2U$_p$ and 3.17U$_p$. At the maximum cutoff energy position, long and short trajectories are merged with each other. The cut-off photon energy is defined by the sum of the KE gain due to the laser field and the ionization potential (IP)[221] of the atom using Equation 3.7[219]. Due to the combined symmetry of the laser field as well as the isotropic non-linear medium, only odd-harmonics are generated[224,225], see Figure 3.7b.

$$\mathrm{E_{cut-off}} = 3.17\mathrm{U_p} + \mathrm{IP} \tag{3.7}$$

Phase Matching in the HHG Process: The phase matching condition is achieved by engineering the constructive interfence of the harmonic waves generated at different positions in the generating non-linear medium. The harmonic yield of the $\mathrm{q^{th}}$ harmonic depends on the wavevector mismatch, $\Delta\mathrm{k}$, between the laser-induced polarization at the harmonic frequency, $\mathrm{q}\omega$, and the fundamental driving frequency, ω. The phase matching condition is:

$$\Delta\mathrm{k} = \mathrm{k}(\mathrm{q}\omega) - \mathrm{k}(\omega) = 0 \tag{3.8}$$

The phase mismatch defines the coherence length:

$$\mathrm{L_c} = \frac{\pi}{\Delta k} \tag{3.9}$$

Macroscopic phase matching of the high order harmonics can be described by the following four terms[222,226]:

$$\Delta\mathrm{k} = \underbrace{\Delta\mathrm{k_N}}_{\substack{\text{Neutral gas}\\ >0}} + \underbrace{\Delta\mathrm{k_P}}_{\substack{\text{Plasma}\\ <0}} + \underbrace{\Delta\mathrm{k_G}}_{\substack{\text{Geometric}\\ <0}} + \underbrace{\Delta\mathrm{k_A}}_{\substack{\text{dipole phase}\\ >0\ (<0)\ \text{for z}>0\ (\text{z}<0)}} \tag{3.10}$$

Where $\Delta\mathrm{k_N}$ is the dispersion in the neutral gas, $\Delta\mathrm{k_P}$ is the dispersion in the plasma created by strong-field ionization, $\Delta\mathrm{k}_G$ is the laser geometrical phase mismatch, and $\Delta\mathrm{k_A}$ is associated with the dipole phase contributions. For the complete phase matching of the harmonics, the four contributions need to be compensated by each other within the non-linear medium over the longitudinal and radial coordinates. The neutral and plasma dispersion terms are coupled. In the case of a strong enough laser field, one can fully ionise the medium. The associated neutral concentration and gas dispersion will correspondingly change every half laser cycle. The neutral gas dispersion, plasma dispersion, and dipole phase match terms depend on the spatial and temporal coordinates. In contrast, the geometric phase term depend on the spatial coordinates only[226]. Neutral gas dispersion mismatch depends on the frequency of the laser light and results in positive dispersion. The plasma and the geometrical phase dispersion contributions are of negative sign[222]. The phase mismatch of the atomic dipole depends on the laser trajectory in the three-step model, as shown in Figure 3.7a, and it varies linearly with intensity. A spatial variation of the laser intensity also leads to a variation of the dipole phase, which in turn causes a reduction of the harmonic yield. The dipole term can be well approximated as $\Delta\mathrm{k_A} = -\alpha_\mathrm{q}\partial\mathrm{I(t)}/\partial\mathrm{z}$[222]. The proportionality constant, α_q, is relatively small for short trajectories and large for long trajectories[227]. During phase matching of the HHG process, the dipole phase can be balanced with the geometric phase, $\Delta\mathrm{k_G} = \frac{\mathrm{q}\lambda}{\pi\mathrm{w_0^2}}$. This can be achieved by focusing the laser before the gas cell. This also ensures the rejection of the long trajectories, selectively only the short trajectories for high harmonic generation. The negative dispersion profile of the generated free-electron plasma usually balances the positive dispersion due to neutral gas pressure. However, such a balance can only be maintained for a low level of ionization yield. The critical ionization level is the maximum ionization limit that allows phase matching in HHG. For an Ar generating gas and an 800 nm driving laser field, it is $\sim 4\%$[222].

Moreover, the generated harmonics can be easily reabsorbed by the interaction medium. Therefore, reabsorption plays an essential role in the phase-matching process and the generation of EUV or soft x-ray beams with maximum flux. Generally the absorption length sets a lower limit of the medium interaction length for

efficient high harmonic generation. In order to balance the reabsorption of the harmonic beam with the generation efficiency, the criteria is $L_{int} > 3L_{abs}$ [228], where the absorption length is defined as $L_{abs} = \frac{1}{\sigma\rho}$. σ and ρ are the absorption cross-section and density of the gas media for generating high harmonic generation, respectively. The lower the gas pressure in the interaction medium, the longer the absorption length, and larger the limit for the interaction length. For example, 50 mbar and 10 mbar Ar gas pressures correspond to 0.26 mm and 1.29 mm absorption lengths, respectively. The Ar gas-pressure of 50 mbar reported here is notably not the local pressure at the light-matter interaction region, it is rather the pressure within the gas-supply line and the generating gas pressure can be much lower than at the light-matter interaction region. The effective gas-pressure can be well below the optimum phase matching pressure for efficient high-harmonic generation, increasing the lower limit of absorption limited interaction length. Therefore, due to low effective phase-matching gas-pressure and higher absorption length, the $L_{int} > 3L_{abs}$ condition may not be fulfilled and it is difficult to maintain the local pressure of 50 mbar. More details on phase matching for efficient generation of high order harmonics are given in the References 222,226,228–231.

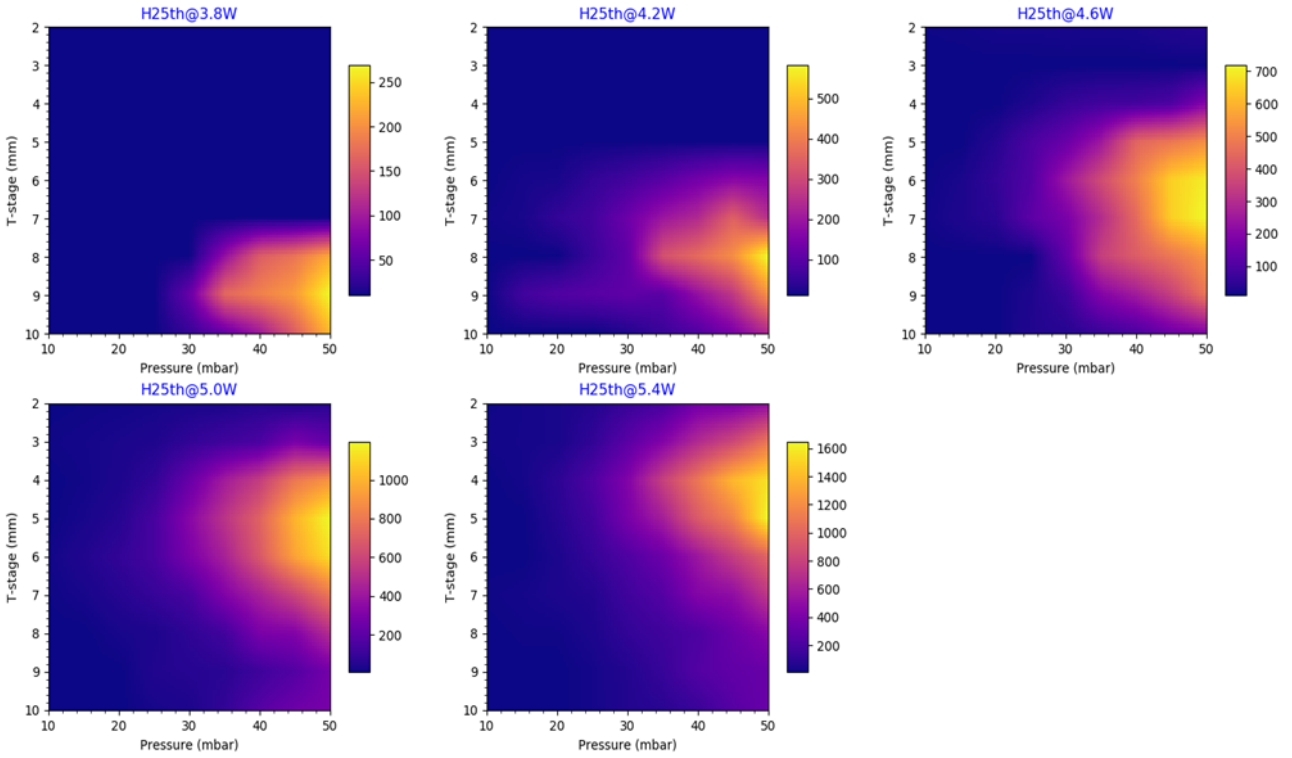

Figure 3.9: HHG phase-matching optimization, specifically focusing on the generation of the 25th harmonic of Ti:Sa in an Ar generating gas. This optimization was performed by monitoring the PE count rate from Ar gas with the use of a TOF electron spectromter while tuning the Ar gas-pressure, the driving laser pulse intensity, and adjusting the laser focus position in the nonlinear medium.

HHG, Monochromatization, and Optimization of the 25$^{\text{th}}$ Harmonic: Considering the four terms in Equation 3.10, the control parameters for phase matching in HHG are the laser intensity, the gas pressure and the focus position in the interaction medium. An earlier-version of HHG setup used in the present work is described in References 134,232. The setup has undergone numerous upgrades over the last few years, some of which are described below. For the experiments reported here, the HHG-driving laser beam was focused into a 4 mm cell filled with Ar gas, and precisely positioned inside a vacuum chamber. The diameter of the 800 nm harmonic generating beam at the focus was $\sim$90 μm ($1/e^2$). The periodic, multi-cycle driving laser field generated a frequency comb of different harmonics via HHG, as shown schematically in Figure

3.7b. For the TRPES experiment, a single harmonic needed to be selected and isolated. In this work, the 25^{th} harmonic was chosen and isolated using a monochromator setup, partially described in the References 134,232. Here, an off-axis reflection zone plate was used to disperse the harmonics in space and focus the 25^{th} harmonic to a slit plane to select only the 25^{th} harmonic light. The zone-plate has a about 50.8 mm in diameter and has seven gold-coated zone structures fabricated on a single silicon substrate. The zone-plate is designed to spatially separate and isolate the 7^{th}, 9^{th}, 17^{th}, 21^{st}, 25^{th}, 51^{st} or 65^{th} harmonics. The slit width can be adjusted, and its typical width setting is tens of mirometers. An Aluminium filter of 200 nm thickness is used after the zone-plate to block the residual, scattered 800 nm laser beam and pass only the diffracted and focused 25^{th} harmonics. The HHG flux is monitored by a removable photodiode just after the Aluminium filter with appropriate slit-width settings, the intensity of the 23^{rd} and 27^{th} harmonics are diminished by the zone-plate and slit assembly to between 1/2000 to 1/5000 times the intensity of the transmitted 25^{th} harmonic.

The generated and selected harmonic is used to ionize an Ar gas sample, introduced just in front of a TOF spectrometer input aperture, which is used to monitor the PE count rate. For a fixed, at a HHG-cell focus laser intensity of 1.4×10^{14} W/cm^2, a three-dimensional (focus position, gas-pressure, and harmonic flux) optimization was performed to maximize the photon flux of the 25^{th} harmonic, see Figure 3.9. The variation of the intensities within the interaction medium is around $1\times10^{14}\ \mathrm{W/cm^2}$. Considering the implemented focal spot diameter of 90 μm (1/e^2), the calculated Ar gas phase-matching pressure in the interaction region for generating the 25^{th} harmonic is around $\sim$90 mbar[231]. This calculation (see, Equation 3.11) considers only the short electron trajectories and a 50$\%$ fraction of the critical ionization of the Ar medium; associated results are shown in Figure 3.10.

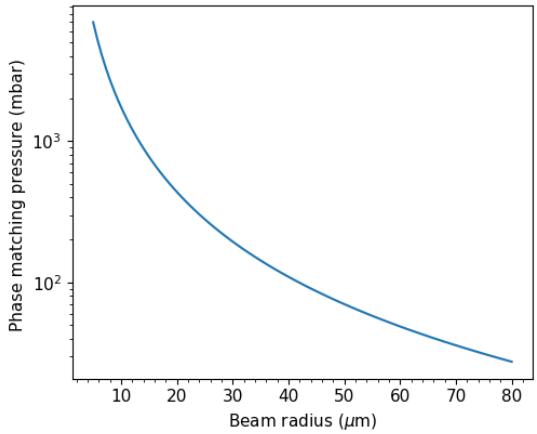

Figure 3.10: Focal spot dependent calculated phase matching pressure[231] for the generation of the 25^{th} harmonic with an 800 nm driving laser.

The HHG phase matching pressure at the laser focus can be calculated using the following equation:[231]

$$\mathrm{P} = \mathrm{P}_0 \frac{\lambda^2}{2\pi^2 \mathrm{w}_0^2 \Delta\delta (1 - \frac{\eta}{\eta_\mathrm{c}})} \tag{3.11}$$

Where, P_0 is the standard pressure (1013 mbar), λ is the driver wavelength, 800 nm, w_0 is the beam waist, $\Delta\delta$ is the refractive index difference between 800 nm and 32.1 nm (the 25th harmonic of 800 nm), η is the ionization fraction, η_c is the critical ionization fraction, η/η_c is the fraction of critical ionization. The laser beam is focused just before the interaction medium to minimize the geometric phase and long trajectory contributions in HHG spectra[229]. Figure 3.9 highlights that the highest harmonic yield was found for a 50 mbar

chamber pressure at a in-gas-cell intensity of $\sim 3 \times 10^{14}$ W/cm^2 and at the 4 mm relative position of the lens with respect to the gas cell. A chamber pressure above 50 mbar could not be applied over TRPES measurement timescales due to the limitation of the HHG-chamber differential pumping scheme implemented at that time. Otherwise, a differential pumping scheme around the gas-cell was required to maintain efficient pumping conditions at the HHG chamber. When the pressure of the Ar gas was increased to around $\sim$80 mbar or more (not shown) for a short period of time, the harmonic intensity was significantly increased. However, the resulting pressures in the HHG chamber could not be safely sustained on the timescale of the time-resolved experiments, mentioned in Chapter 6. This indicates that the phase matching for getting the optimum harmonic yield is still not maximized in the situation implemented to produce Figure 3.9.

It is noted that at the high, at-focus laser intensities implemented in the HHG setup, the plasma dispersion HHG phase-matching term can readily exceed the neutral dispersion term, $\Delta k_P \gg \Delta k_N$. However, it is possible to mitigate the possibility and further increase the 25th harmonic flux by increasing the at-focus spot size of the laser beam and introducing an additional differentially pumped section around the HHG gas cell, as was implemented at the end of this thesis work.

3.2 Liquid Microjet Technique

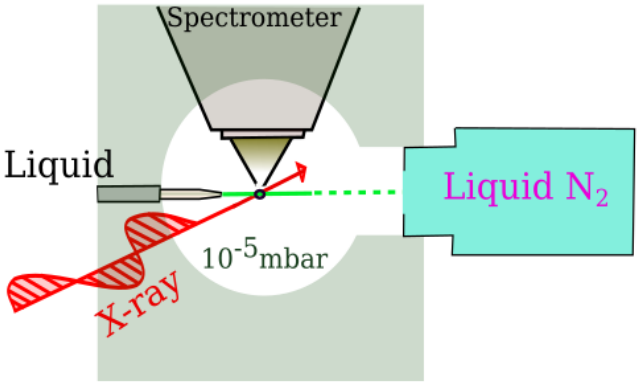

Figure 3.11: Schemetic representation of the PE experiments using an X-ray beam and liquid microjet. The figure is drawn based on the concept presented in Reference 233.

By combining a LJ sample environment with the PES technique, it is possible to investigate the molecular structure of liquid samples. For such experiments, it is essential to maintain the high vacuum conditions required for photoelectron spectroscopy. With the LJ technique, a laminar flow of a liquid jet is created inside a vacuum chamber by forcing the liquid through a nozzle at a high backing pressure. Different liquid microjet setups were used in this work. In the XPS experiments performed at BESSY II and PETRA III, the liquid backing pressure was around 1-2 bar using liquid jet capillary diameters of $\sim 25 \pm 5$ μm and setting liquid flow rates of 0.6-0.8 mL/min. The experiments used High-Pressure Liquid Chromatography (HPLC) pumps to set a well-defined liquid flow rate and create a laminar liquid flow inside the vacuum chamber. The PEs generated in a liquid suffer elastic and inelastic collisions both within the liquid and in the surrounding evaporated gas, which can alter their KEs[84]. The liquid microjet evaporates in vacuum and creates a vapor layer surrounding the liquid jet. The vapor layer has a cylindrical symmetry around the liquid jet, and the gas density (n_v) at a particular point depends on the jet radius (r_0) and distance (r) from the jet. The relationship can be coarsely defined as follows: $n_v = n_0 \frac{r_0}{r}$ [79], where n_0 is the equilibrium vapor pressure at the jet surface. The distance over which the PEs travel without collisions with gas molecules is called the mean free path, λ, which is defined by the following equation 3.12[79]. The mean free path increases by decreasing the gas density, n_v, and the gas density falls off by lowering the jet radius, r_0, and the distance from the jet, d.

$$\lambda = \frac{\mathrm{kT}}{\mathrm{n_v}\sqrt{2}\rho_\mathrm{v}} \tag{3.12}$$

Where k is the Boltzmann constant, T is the temperature, n_e is the equilibrium vapor pressure, and ρ_v is the molecular collision cross-section. Under typical experimental conditions, the electron mean free path becomes $\sim$ 1 mm at the entrance of the electron spectrometer[233]. The LJ flow remains laminar over a few mm distance from the tip of the injection nozzle, and the length of the laminar flow depends on the nozzle's inner diameter and the flow rate inside the nozzle. After the laminar region, the liquid breaks into droplets and is collected and frozen by the liquid N_2 cold trap, which also significantly reduces the average pressure in the sample chamber.

3.2.1 Electrokinetic Charging

Electrokinetic charging can cause problems for LJ-PES. This effect arises when the liquid flow disrupts the electric double layer at the liquid contact surface with the inner capillary walls of the injection walls. In the case of pure water flowing through the nozzle, this situation is particularly problematic due to the autoprotolysis of water[234]. More details about the interaction of the liquid sample with the inner nozzle surface and the resulting streaming potential can be found in References 22,234.

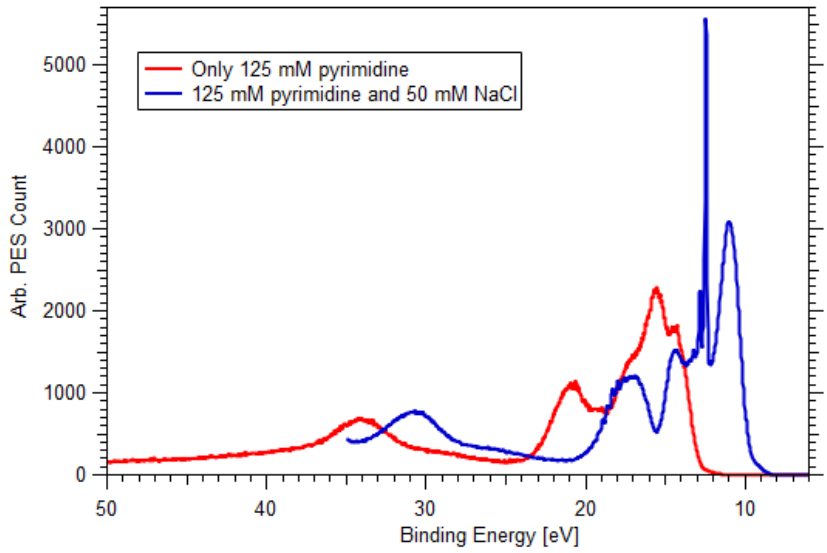

Figure 3.12: Electrokinetic charging effect is illustrated by recording the PE spectra from 125 mM aqueous pyrimidine without (red) and with (blue) 50 mM NaCl added to the solution.

The surface potential due to electrokinetic charging can be relatively high in LJ experiments with non-conducting samples. Therefore, salts (*e.g.* 50 mM NaCl) are admixed into aqueous solutions to make them electrically conductive, and, thus, minimize electrokinetic charging effects. Figure 3.12 illustrates such a situation in a XPS study on 125 mM aqueous pyrimidine. Aqueous pyrimidine is a non-conducting solution. The red colored spectrum represents the XPS spectrum of pure aqueous pyrimidine that suffers from electrokinetic charging. The blue-colored spectrum is obtained after adding 50 mM NaCl to the solution. Due to the electrokinetic charging effect, the sample Fermi and local vacuum levels have an offset. Therefore, Figure 3.12 shows a KE energy shift between the red- and blue-colored spectra. As will be discussed in Section 3.3.3, any potential gradient between the LJ and the spectrometer makes the PE spectra from the gas phase strongly dependent on the light focus position with respect to the LJ and electron analyzer.

3.3 Experimental End Stations Used for PES Measurements

In the present work, three different photoelectron spectrometers were applied. Two different hemispherical electron analyzers were used to perform the XPS experiments and and a TOF electron analyzer was used to perform the TRPES experiments.

3.3.1 LJ-XPS End Stations

SOL^3 Facilities at U49-2 PGM-1 Beamline BESSY II

A detailed description of the SOL^{3}PES end station can be found in Reference 235 . Briefly, it consists of three main components- a beamline differential pumping section, interaction chamber and the analyzer. The experimental geometry of the SOL^{3}PES end station is shown in Figure 3.13a.

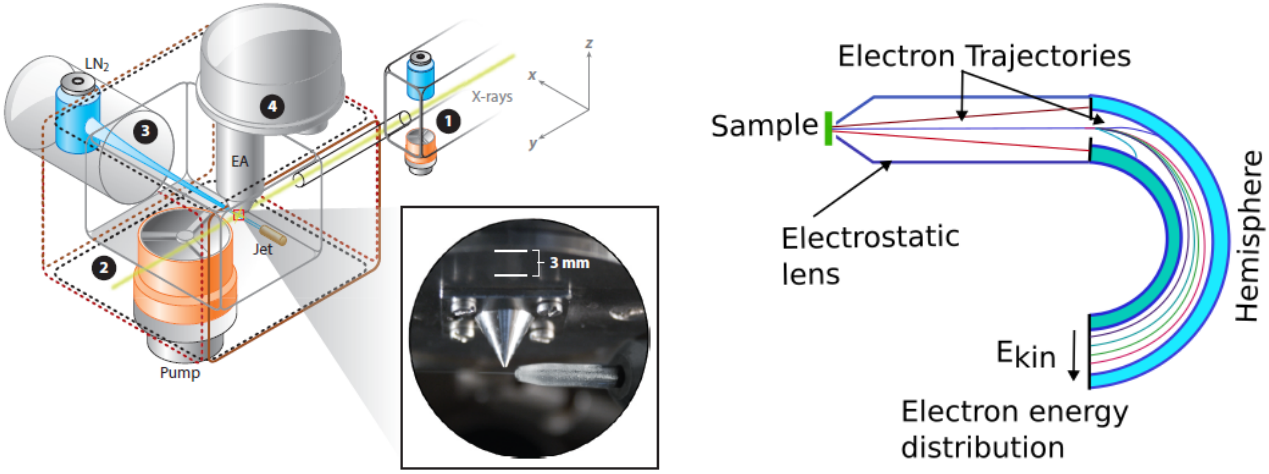

(a) Experimental geometry of SOL^3 end station

(b) Electron trajectories

Figure 3.13: The panel (a) illustrates the experimental setup at BESSY II. The panel (b) highlights the electron trajectories inside the hemispherical electron analyszer. The image in panel (a) is reproduced from References 21, with permission of Annual Reviews, Inc., permission conveyed through Copyright Clearance Center, Inc. The panel (b) is plotted based on the concept presented in Reference 236.

The purpose of the differential pumping stage is to keep the beamline refocusing mirror section at a residual gas pressure below $< 10^{-8}$ mbar while operating the interaction chamber at any pressure up to 1 bar. A small aperture with a variable pinhole size (1-3 mm) is implemented in the differential pumping section when connecting the interaction chamber to the beamline. The non-magnetic stainless steel interaction chamber (27$\times$27 $\times$42 cm^3) facilitates the delivery of liquid sample solutions using a LJ setup, holds the electron analyzer, provides a port for the incoming soft X-ray beam for PES experiments, and provides a mounting base for the associated vacuum pumps. A turbomolecular pump with a N_2-gas operating pumping speed of 1600 l/s is used to evacuate the chamber. While running the LJ inside the chamber, the chamber pressure is maintained at a $\sim 10^{-4}$ mbar level using two liquid-nitrogen-filled cold traps (total surface area $\sim$1000 cm^2, corresponding to a water-vapor-pumping speed of up to 30 000 l s^{-1}). The earth's magnetic field is compensated in 3D coordinates (x, y, and z) using Helmholtz coils installed around the interaction chamber.

A Scienta Omicron R4000 HiPP-2 high-resolution hemispherical electron energy analyzer is used to collect the PEs in the SOL^{3}PES setup. It consists of a skimmer, a linear electrostatic lens system, a pair of half-

spheres, and a detector. Figure 3.13b shows the electron trajectories inside the hemispherical electron analyzer. Photoelectrons are collected within an up to 0.07 sr solid angle, as defined by the spectrometer entrance aperture and applied electrostatic lens conditions, and guided between the half-spheres. At the right spherical electrode potentials, the photoelectrons follow a circular path, where the radius of curvature depends on the electron KE, applied voltage (V) and the diameter of the central, arced trajectory between the spherical electrodes (d). At the end of the hemisphere, a detector is placed to record a fraction of the PE energy distributions. The electrons are given a preset pass energy by the electrostatic pre-lens systems before traversing the region between the hemispherical electrodes. The energy-dispersed electrons are projected onto a two dimensional detector that simultaneously records the spectrum over a KE range defined as the analyzer pass energy $\pm$ 8$\%$. The detector consists of a pair of micro-channel plates, a phosphor screen, an optical lens system, and a CCD camera.

This analyzer can be operated at pressure conditions in the interaction chamber of up to tens of mbar. More details can be found in Reference 237 and on the Scienta Omicron website*. The electron analyzer is connected to the interaction chamber and can be rotated together with the chamber in such a way that the PEs can be collected at any angle between 0° and 90° with respect to the polarization axis of the x-ray beam, including at the magic angle of 54.7°. The experimental energy resolution depends on a number of parameters, such as the beamline and spectrometer slit setting and the bandwidth of the x-ray pulses.

EASI Spectrometer at the P04 Beamline, PETRA III

The presented content in this paragraph has been adapted or directly taken from the publication: MS Ahsan, V Kochetov, D Hein, SI Bokarev, and I Wilkinson. *"Probing the molecular structure of aqueous triiodide via x-ray photoelectron spectroscopy and correlated electron phenomena",* Physical Chemistry Chemical Physics, 24(25):15540–15555, 2022. DOI: https://doi.org/10.1039/D1CP05840A. Published by the PCCP Owner Societies. This work is licensed under the Creative Commons Attribution 3.0 Unported License.

In experiments with the EASI spectrometer, the liquid-jet sample chamber can be maintained at a residual gas pressure of 2–3$\times 10^{-5}$ mbar during the LJ operation. Such vacuum condition were achieved using a combination of turbo molecular pumping ($\sim$2700 l s^{-1} pumping speed for water vapour) and three liquid nitrogen-filled cold traps (3000 cm^2 total surface area, up to a $\sim$45000 l s^{-1} pumping speed for water vapour). The circularly polarized soft X-ray beam from the P04 beamline was delivered to the interaction region via a windowless, two-stage differential pumping assembly and orthogonally intersected the laminar region of the liquid microjet. The PEs were collected by a differentially pumped hemispherical analyser system (Scienta Omicron HiPP-3). The pre-lens axis of the spectrometer was aligned at a 50° angle relative to the light propagation axis, close to the Magic Angle of 54.7°. This experimental configuration will be denoted as the Magic angle measurement geometry, which suppresses angular distribution effects in the recorded PE spectra[238]. More details of the spectrometer configuration and experimental geometry can be found in Reference 238.

3.3.2 LJ-TRPES End Station at the ULLAS Laser Laboratory:

Two different sample delivery systems have been used with the LJ-TRPES setup, which allows switching between the sample and reference solutions without breaking the vacuum conditions. A syringe pump (

*http://www.scientaomicron.com/en/products/354/1179 (date:June 2017)

TELEDYNE ISCO model 500 D syringe pump, which generally operated with a backing pressure of ∼5-6 bar) delivered the pyrazine aqueous solutions, and the reference water solvent sample was delivered using a regular HPLC pump (Techlab Economy 2ED, Techlab GmbH). Two liquid N_2 cold traps were used in the PES interaction chamber to collect the frozen liquid samples. A liquid N_2 trap was placed under the LJ position to collect the frozen droplets. Another liquid N_2 cold trap was placed inside the vacuum chamber to collect the evaporated liquid samples and serves as an additional vacuum pump for our setup. This liquid N_2 cold trap, along with a turbomolecular pump (pumping speed for N_2 gas 1500 l/s), helps to pump the experimental chamber more efficiently to maintain a sample-chamber base pressure of 10^{-4}-10^{-5} mbar in the LJ-TRPES experiments. In the pyrazine LJ-TRPES experiments, a THEMIS 600 EP TOF electron analyzer was operated with a 5 kHz repetition rate laser system. A liquid flow velocity of ∼0.65 ml/min was set with the syringe pump to create sample velocity of ∼ 22 m/s (or $22\times10^3\mu$m/ms)†. When performing the LJ experiments with the use of a 5 kHz laser system, such a flow velocity ensures a complete refreshing of the sample between light pulses and thereby excludes any cumulative sample damage effects[239].

The TOF electron spectrometer measures the flight time, t, of the photoelectrons from the interaction region to the detector, relative to the EUV laser pulse arrival time at the liquid jet, as shown in Figure 3.14a. In the spectrometer drift mode, The KE of PEs is determined according to the following relation:

$$E_k = \frac{m_e}{2}\frac{L^2}{(t-t_0)^2} \tag{3.13}$$

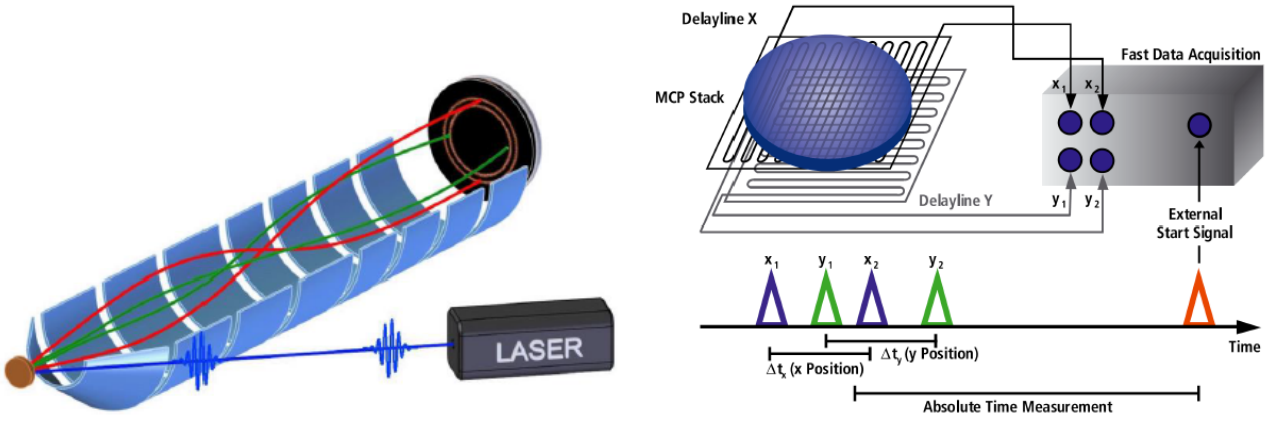

(a) Electron trajectories TOF spectrometer

(b) Schematic of the Delayline Detector (DLD)

Figure 3.14: Panel (a), schematic of the electron trajectories inside TOF electron analyszer, specifically in the wide angle mode of the analyzer. Panel (b), schematic of the DLD that allows to record the position as well as the arrival times of the PEs. The triangles underneath the device schematic represent electron pulses hitting the timing electronic inputs of the delayline detector. The figures are reprinted with permission from References 240 and 241, respectively.

Where t_0 is called the time zero†, and represents the time when the light pulse hits the sample. m_e is the electron mass, and L is the spectrometer length. This applies to the spectrometer drift mode. However, in the Low-Angular Dispersion Mode (LADM) and Wide-Angle Mode (WAM), the relation is more complex and the energy calibration is correspondingly achieved using a defined time-of-flight distance and electron trajectory simulations, and based on the applied electrostatic lens voltages. More generally, for example, in the LADM and WAM of the spectrometer, the spectrometer is operated with a two-stage electrostatic lenses to collect and guide the photoelectrons to the detector. The spectrometer can only accurately produce photoelectron

†considering a 12.5 μm radius of the liquid-jet nozzle

†This is not necessarily the pump-probe time-zero but is the time when the EUV probe light hits the sample.

spectra and angular distributions when the electron flight distance is well-defined and stray magnetic fields in the interaction region are mitigated (in this case using sets of Helmholtz-like coils). By implementing the electrostatic lenses in the spectrometer, the electron collection efficiency can be optimized to a 0.2 sr level using the so called wide-angle mode of the spectrometer. For amplification and detection of the photoelectron signal, a pair of MCPS and a 2D-Delayline Detector (DLD) is used. The detector consists of a chevron multi-channel plate pair, the delay line and a vacuum-compatible readout unit. The readout unit is sensitive to the electron arrival positions at the detector. Figure 3.14b highlights the 2D DLD detector. The detector includes a grid-like structure of two crossed wires to record two-dimensional information of the arrival x, and y position coordinates. The DLD detector can extract both the arrival times and positions of the photoelectrons at the detector, which can be converted to the KEs as well as to the angular distributions using electron trajectory simulations, the electrostatic lens voltages, and the spectrometer software conversion algorithm. The readout unit is connected to the fast electronics for fast data acquisition and triggered by the 5 kHz laser system. Thus, the TRPES experiments can be reliably performed at a count rate of up to 5 kHz, limited by the repetition rate of the laser, under the proviso two electrons do not hit the detector within its 10 ns dead time. At higher count rates, when more than one electron is detected per laser shot, the readout unit can become overloaded, depending on where a second event occurs at the detector surface. In order to keep the count rate below the 5 kHz safe limit, one can close the front aperture of the spectrometer or apply a retardation voltage to a grid mounted in front of MCPs. Closing the front aperture improves the energy resolution but hides the photoelectron angular information (which was not the objective of the present work). However, it also decreases the lifetime of the detector due to selective irradiation of a central detector section.

Selection of the Spectrometer Mode: Depending on the electrostatic lens setting, the TOF spectrometer can operate in a number of modes, such as drift mode, LADM, Medium-Angular Dispersion Mode (MADM), and WAM. The drift mode provides the highest energy resolution but has a small collection angle of $\pm 1^{\circ}$, corresponding to a poor electron collection efficiency. This mode allows spectra to be recorded over essentially the entire KE range that covers the valence band contributions of both the solute and solvent. Thus, it is chosen for steady-state measurements. For TRPES measurement, the stability of experimental conditions is very important, and the measurement needs to be done for a relatively short time interval at each time-delay point (further details are provided in section 3.4) that requiring a higher collection efficiency. This can be achieved by applying the LADM, MADM, or WAM modes of the spectrometer, which have planer collection angles of $\pm 7^{\circ}$, $\pm 10^{\circ}$ and $\pm 15^{\circ}$, respectively, and smaller converted KE region widths in going from the LADM to MADM to WAM modes. Considering our probed energy window, excitation energy, energy resolution, and signal statistics for a relatively good signal-to-noise ratio, the LADM mode was chosen for then time-resolved measurements.

3.3.3 Energy Calibation:

Once the LJ is introduced into the interaction region, the electric potential between the sample solution and the electron analyzer must be considered in order to calibrate the BE scale properly.

Figure 3.15, panel (a) shows a schematic of misaligned vacuum levels in a LJ-PES setup. The Fermi levels of the solutions, and analyzer are aligned in equilibrium, but the local vacuum levels are not aligned due to the differences in the work functions, determined by the electronic structure of the material and the sample and analyzer surface conditions[242]. Generally with a volatile liquid sample, the photoelectrons emitted by the gas-phase molecules will experience a different potential due to the potential gradient between the liquid and entrance skimmer of the spectrometer. Although the water $1b_1$ gas-phase BE is known, the steep potential

gradient experienced by the gas molecules and the spatial range over which the gas-phase molecule are ionized around the LJ prevents this reference BE value from being used for a reliable energy calibration.

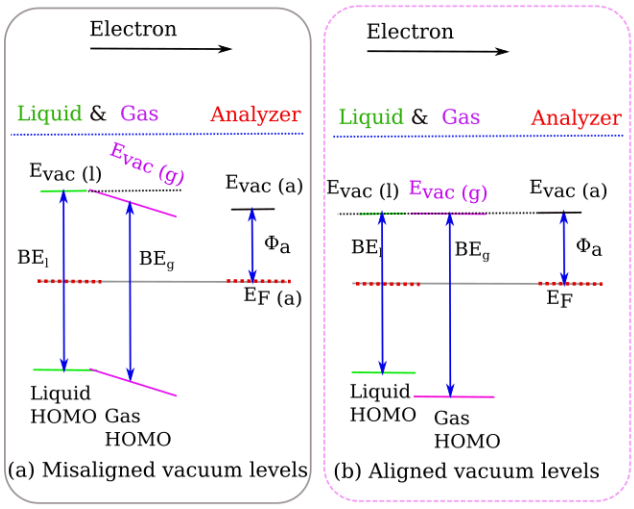

Figure 3.15: Potential situation in LJ-based PES measurements, panel (a) shows a misalignment of the vacuum levels of the sample and electron analyzer, panel (b) shows a the situation where the liquid and gas-phase vacuum levels are aligned. l, g, and a denotes liquid samples, gas samples, and analyzer, respectively. The figures are plotted based on the concepts presented in Reference 242.

Panel B in Figure 3.15 shows more favorable conditions for energy referencing. In this case, the gas- and liquid-phase vacuum levels are aligned to each other, and the PE KE from the gas-phase molecules are independent of the position of the LJ. This situation occurs particular experimental conditions and at a specific concentrations of the considered sample. In a specific instrument in Japan, it was found for aqueous NaCl and NaI samples, that the concentrations of 50 mM and 30 mM delivered from a fused silica capillary with 25 μm diameter at a flow rate of 0.5 mL/min minimized the vacuum level offset between the sample and electron detector, *i.e.* that these solute concentrations resulted in a balance of the streaming potential, the work function difference between sample and analyzer, and any ionizing-light-induced sample charging effects[243]. In the results reported here, is it is assumed that similar aqueous alkali halide solution concentrations will result in vacuum level alignment between the samples and analyzers and that the liquid water $1b_1$ BE in the studied sample solutions is equivalent to that in nearly-neat liquid water *i.e.* 11.33 ± 0.04 eV[66]. The spectra reported here were correspondingly recorded with 30 mM or 50 mM of NaI or NaCl added to the solution and the sectra are BE-shifted to set the center of the $1b_1(l)$ peak to the nearly neat-water reference value. Although the liquid and gas vacuum levels can be aligned when sample charging effects are mitigated, the sample and analyzer local vacuum level (those just outside of the sample and detector) will generally still be different. In the schematic representation shown in panel b, it is assumed that the analyzer's work function is higher than that of the skimmer, which raises the vacuum level of the analyzer and thereby decelerates the PEs from the sample. As described in Reference 243, the total potential difference between the vacuum level of the sample and analyzer can be zeroed by minimizing the width of the gas-phase spectral peak. While this can, in principle, enable LJ-PES energy referencing with respect to the vacuum level at infinity, it is inappropriate for a more general energy referencing of liquid samples to the local vacuum and system Fermi levels. The implementation of these more general LJ-PES referencing schemes was the subject of ongoing research throughout this thesis work[66,197] and these more involved referencing schemes are not implemented here.

3.4 TRPES Experiment and Associated Procedures

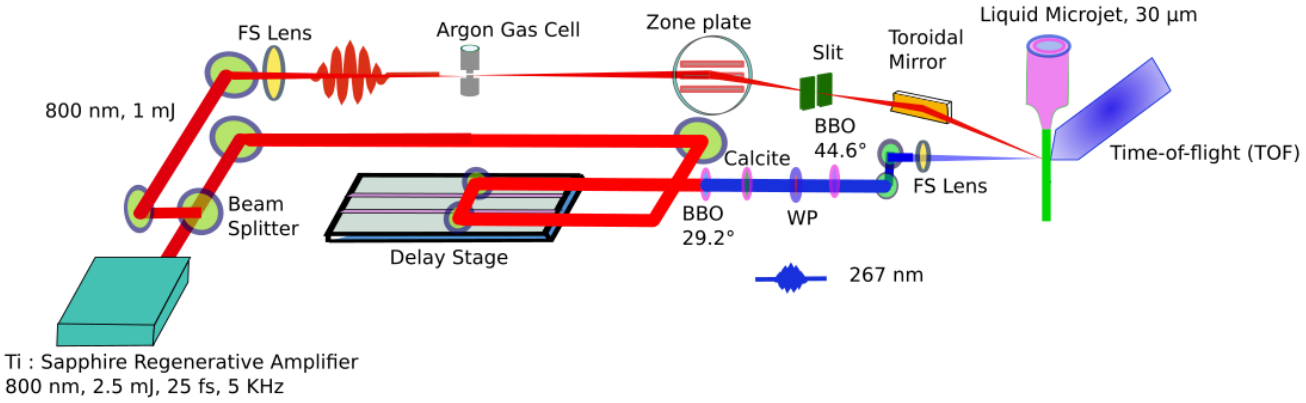

Figure 3.16: Schematic presentation of the experimental setup for TRPES experiments.

The experimental setup, implemented to produce the results presented in chapter 6 for TRPES, is illustrated in Figure 3.16. The 800 nm beam output of the laser system described in Section 3.5 is divided into two arms using a beamsplitter, one 800 nm arm with a 250 μJ pulse energy is used to generate a 267 nm laser beam by sum-frequency generation (SFG), specifically by mixing 800 nm and 400 nm beams in a collinear geometry, see Section 4.1. The 267 nm laser beam is focused using an uncoated CaF_2 lens (f= 260 mm) onto the LJ inside the sample vacuum chamber. The focusing lens is situated on a translational stage that can move in three dimensions, x, y, and z. The output pulse energy of the 267 nm laser beam before the FS lens setup is up to 2-3 μJ but can be continuously attenuated by rotating the half-waveplate in the in-line SFG setup. Another fundamental laser arm delivers $\sim$1 mJ, 800 nm pulses to a 675 mm or 750 mm focal length lens, which focuses the laser into an Ar gas cell to generate higher order harmonics through a strong field light-matter interaction (more details are provided in section 3.1.3). The pulse energy of the 800 nm laser beam for HHG was adjusted by a waveplate and a reflective polarizer combination. The implemented HHG gas cell had a cylindrical tube shape, laser input and output holes that were covered by aluminum tape, and has an output diameter of 4 mm. The Ar gas was supplied to the gas cell within the HHG vacuum chamber through a gas feed-through. A dosing valve was used to control the gas pressure inside the vacuum chamber. The entrance and exit aperture of the aluminum foil was created by focusing the fundamental 800 nm pump laser beam inside the cell, burning holes of the necessary size to allow the high harmonic radiation to pass down the beamline. Harmonics were generally and specifically generated using 28 fs (FWHM), 4.85 W (0.97 mJ), 800 nm laser pulses with an Ar gas pressure of 50 mbar. The generated harmonics were subsequently monochromatized for PES experiments. The TRPES experiments reported here were performed using the 25^{th} harmonic of the input laser, corresponding to a 38.5 eV photon energy. The HHG optimization and monochromatization processes are described in section 3.1.3.

Following harmonic monochromatization, a gold-coated toroidal mirror was used to refocus the 25^{th} harmonic beam into the LJ interaction chamber and onto the LJ. This mirror is mounted in a motorized stage system that has three translational and three rotational degrees of freedom. This allows the focus position of the EUV beam to be precisely positioned in front of the skimmer of the electron analyzer. The mutual angle between the pump and probe beam was $\sim$1-2°. A delay stage in the UV pump laser arm controlled the pump-probe delay with a smallest step size of 1.6 fs and covered a delay range up to 2 ns. Both the pump and probe beam spot size were characterized by scanning a razor blade across the beam and measuring the photon flux behind the blade with the use of a photodiode and picoammeteram *i.e.* the Keithley current amplifier. The FWHM spot size of the pump and probe beams were 90 $\pm$ 8 μm and 60 $\pm$ 6 μm, respectively. Under the

conditions implemented in the aqueous pyrazine TRPES experiments, a pump pulse energy of 36 nJ of the beam was measured using a power meter in air in the spectrometer vacuum chamber, corresponding to a pump photon flux of 4.8 $\times$ 10^{10} ph/pulse at 5 kHz. In contrast, a photon flux of 10^6 photon/pulse of the probe beam was measured using a calibrated photodiode and picoammeter, which corresponds to a probe pulse energy of 15 pJ.

Photon Energy Calibration: There are three unknowns when energy-calibrating TOF-based photoelectron spectra: the spectrometer time-zero (determined via photon TOF), the kinetic energy offset of the analyser (for example due to undesirable fields between the sample and spectrometer or the position of the light source with respect to the detector), and the photon energy (which depends on the laser and HHG conditions). Initially the time zero offset, t_0, needs to be determined by monitoring the photon peak in the spectrometer, which can be detected using the EUV-beam reflection from the sample to the MCP and DLD detector. In order to calibrate the photon energy of the EUV beam, photoelectron spectra of Ar gas were recorded on a daily basis. A typical average pressure of Ar was applied in the interaction chamber was 7-8 $\times$ 10^{-4} mbar. The calibration spectra were recorded using the drift mode of the spectrometer. Figure 3.17a highlights the PE spectra of Ar gas obtained using the 25$^{\text{th}}$ harmonic of the laser system, where two distinct PE peaks are visible due to the 3s and 3p (spin-orbit split but unresolved) ionization channels. The corresponding PE peaks were subsequently fits using Gaussian profiles to determine the KE positions. A single Gaussian profile was used to fit the 3s photoelectron peak, whereas two Gaussian profiles were used to fit the spin-orbit split $3p_{3/2}$ and $3p_{1/2}$ ionization peaks. Taking into account the obtained KE positions and the reported BEs in the literature (3s: 29.24 eV[244,245] and $3p_{3/2}$: 15.76[245] and spin-orbit splitting 0.18 eV[60]), the photon energy at the 25$^{\text{th}}$ harmonic was determined. This procedure resulted in a photon energy of 38.50 +/- 0.05 eV being determined, which varied within the error range on a day-to-day basis. In this procedure, the sample density was sufficiently low to avoid inducing any undesireable fields between the sample and spectrometer. However, this may not be true while performing experiments in the condensed phase. Therefore, the liquid-phase photoelectron spectra energy calibrations were performed using the neat liquid water, $1b_1$, photoemission peak, as mentioned in Section 3.3.3.

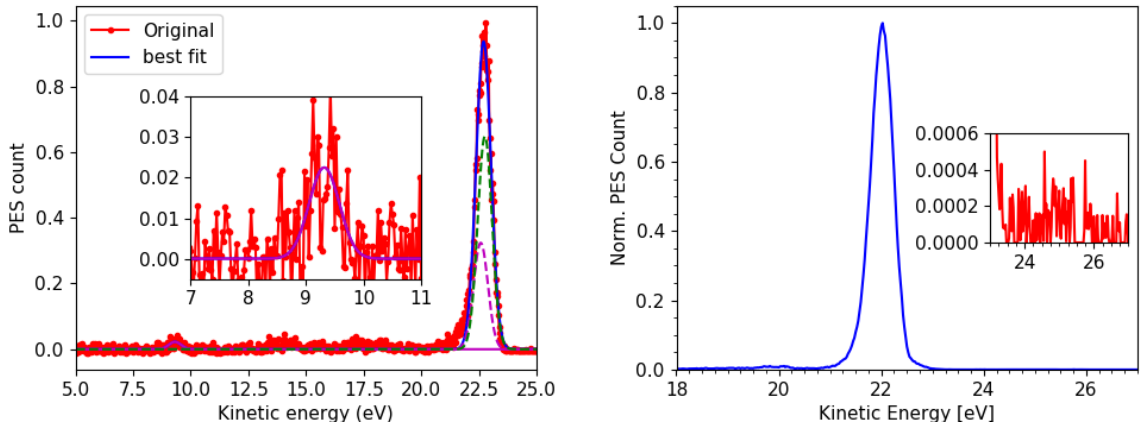

(a) Calibration in DM (b) Contrast in WAM

Figure 3.17: Harmonic contrast and photon energy calibration determined by recording PE spectra of Ar gas in the sample chamber. The left panel shows the spectral contrast of 25$^{\text{th}}$ to 27$^{\text{th}}$ harmonics, which is >4000:1, when recorded in WAM. The right panel shows the photon energy calibration of 25th harmonic recorded using the spectromter drift mode.

Figure 3.17b shows an exemplary PE spectra recorded from Ar gas using the 25$^{\text{th}}$ laser harmonic and the

spectrometer WAM. To record this data, the interaction chamber was filled with Ar gas to a residual Ar gas pressure of $\sim$7-8$\times10^{-4}$ mbar, as measured using the sample chamber pressure gauge. The dominant PE contribution is due to the 25^{th} harmonic at KEs of $\sim$22 eV, and with PE peaks also being produced by the neighbouring 23^{rd} and 27^{th} harmonics at around $\sim$19.5 eV and $\sim$25.3 eV, respectively. The intensity ratio between the 25^{th}-to-23^{rd} harmonics is around $\sim$100:1 and the 25^{th}-to-27^{th} harmonic is around 4000:1 in the recorded PE spectra. It is important to minimize the higher-order harmonic contributions, which would produce ground-state ionization signals in the spectral range of the low-BE pump-probe signals. The KE range where the 27^{th} harmonic produces photoelectrons is crucial in the TRPES experiments, so a high 25^{th}-to-27^{th} harmonic signal ratio was favored when setting up the monochromator. In the pump-probe experiments, significant ground state signal contributions from the 27^{th} harmonic will overlap with the excited state signals produced with the 3^{rd} harmonic pump and 25^{th} harmonic probe. Therefore, the monochromator settings were adjusted to achieve high contrast between 25^{th}-to-27^{th} harmonic. The PE spectrum recorded in the WAM highlights a better than 3500:1 contrast between the 25th and 27th harmonics. The photon energy and harmonic contrast were determined before each TRPES measurement set experiments. The same procedure was implemented on a daily basis to confirm that the experimental conditions remained stable throughout the experimental beam times.

Spatial and Temporal Overlap of the Pump and Probe Beam on a Conductive Solid: Finding a spatial and temporal overlap of the pump and probe laser beams is time-consuming. Using a liquid microjet for this purpose is not ideal for a number of reasons, such as sample consumption, instability of the liquid microjet etc. Thus, an alternative solid target, a 100 μm thin Au wire, was used to preliminarily find the spatial and temporal overlap of the pump and probe beams. The pump and probe beams can be spatially overlapped by monitoring the space-charge effect on the wire using a charged-particle spectrometer. The space-charge effect arises when an intense (2×10^{11}W/cm^2, 267 nm) pump laser pulse efficiently ionizes the sample via the process of multi-photon ionization[246]. When the beams are spatially overlapped and at a 10-100 ps pump-probe delay[246], the KE of the PE produced by an EUV probe pulse will increase in the presence of the pump laser pulse and a higher PE count rate will be observed within a selected energy window at higher KEs. The fine spatial overlap is obtained by adjusting the pump beam focus position on the Au wire to increase the PE count rate. Once the spatial overlap is maximized, the Cross-Correlation (CC) signal can be recorded to find the temporal overlap of the pump and probe pulse that defines the time zero in the TRPES study. The CC signal also provides information of the time resolution about the pump-probe experiment. This CC temporal width depends on the pump and probe temporal widths, and this quantity again depends on the wavelengths of the pump and probe beams, the associated dispersion due to propagation through the transparent media, and diffraction from any grating optics. Since the NIR laser fundamental compressor was set so that HHG process is optimized for efficient harmonic generation, the dispersion in the pump beam arm was fine-tuned either by adding or removing some glass plates in the pump beam propagation path. The thickness of the glass plates was adjusted by measuring the CC signal and minimizing the CC width.

Space-Charge Effects in Liquids: Although, a photon energy above 30 eV is desireable to investigate the electronic structure of an aqueous solution and minimize the inelastic scattering effcts, performance of such TRPES studies using such photon energies has some disadvantages, as mentioned in Section 2.4.5, Chapter 2. As mentioned above, the available EUV pulse energy is around$\sim$15 pJ for performing the TRPES experiment. On the other hand, the available pulse energy of the UV laser pulse can be very high, on the order of μJ or more, that can easily implemented to ionize a solid, liquid, or gas. Therefore, the avalable photon flux for performing PES is very low in comparison to the UV pulse (10^6 photon/pulse versus 10^{13}

photon/ pulse)

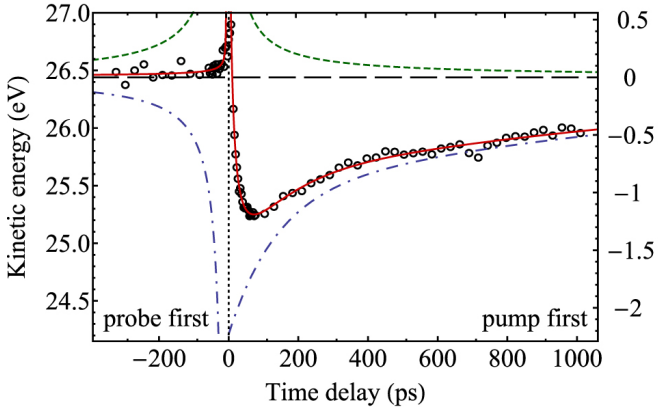

(a) PISC effects on $Fe(CN)_6{}^{4-}$ aqueous solutions.

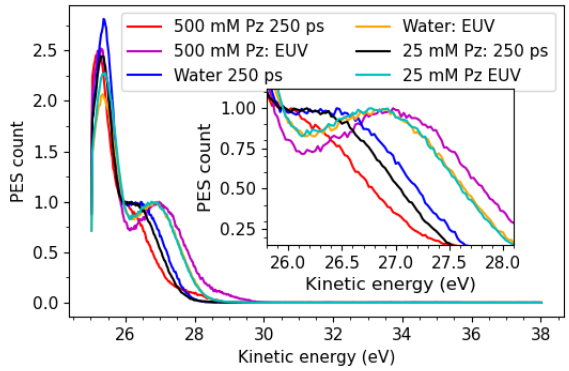

(b) Concentration-dependent PISC effects in water and aquoeus pyrazine solutions

Figure 3.18: (Panel a) Measured PE KE of Fe 3d(t_{2g}) band photoelectron KE as a function of pump-probe time-delay, illustrates space-charge effects in aqueous $Fe(CN)_6{}^{4-}$ solution following photoexcitaiton at 4.7 eV and probing at 32.6 eV. The effect has been modelled using a mean-field approach. (Panel b) Concentration-dependent PISC effects in water and aqueous pyrazine solutions. Pz denotes aqueous pyrazine. Ground state (EUV only) and excited state spectra (at a pump-probe delay of 250 ps) of 500 mM and 25 mM aqueous pyrazine, and neat water (50 mM NaCl in water) spectra are compared. The spectrum in panel (a) has been reproduced with permission from Reference 135, licensed under the Creative Commons Attribution 3.0 Unported License.

Figure 3.18a illustrates an example of the space-charge effects studied using a liquid microjet and ultrafast photoelectron spectroscopy in the aqueous phase[135]. The KE of the photoelectron peak of the $Fe(CN)_6{}^{4-}$ HOMO feature is plotted as a function of pump-probe delay. We see two different behaviors in Figure 3.18a. At negative time delays, the PE KE shifts to higher values; in the positive time delay range, the KE shifts to lower values. Negative time delay means when the probe pulse (EUV) comes first, and the pump pulse (UV) comes later. The situation is the opposite in the positive time delay range, where the pump pulse comes first. Obaidi *et al.*[135] described the underlying space charge effects in aqueous solutions using a mean-field model. This model assumes that the EUV-induced charging is negligible within the energy resolution of a given experimental setup. The space-charge effects that lead to spectral shifts of the generated PEs in aqueous solutions depends on the wavelength and intensity of the pump pulse and it has a non-linear dependence on the pump pulse intensity[135]. It also depends on the type of molecule under investigation, sample interaction volume, sample concentration, and the polarizability of the studied electronic states. Figure 3.18b highlights space-charge effects where the KE shift depends on the sample concentration and absorption profile. The red, brown, and orange color curves denote the PE spectra recorded using the EUV pulses for a 50 mM aqueous NaCl, 25 mM pyrazine and 50 mM NaCl, and 500 mM pyrazine and 50 mM NaCl aqueous solutions, respectively. These EUV-only PE spectra are compared to the PE spectra recorded at a 250 ps pump-probe time-delay, where an intense pump pulse (267 nm, 2.13 mW, $\sim$40 fs duration) is used to initiate the dynamics, and a weak XUV pulse is used to probe. The green, violet, and blue colored spectra denote the PE spectra of 50 mM NaCl, 25 mM pyrazine and 50 mM NaCl, and 500 mM pyrazine and 50 mM NaCl aqueous solutions, respectively. Aqueous NaCl does not absorb 267 nm, while aqueous pyrazine absorbs 267 nm. The resulting pump-induced KE shift for 50 mM NaCl aqueous solutions is 0.35 eV, whereas for the UV-absorbative 25 mM and 500 mM aqueous pyrazine solutions it is 0.45 eV and 1 eV, respectively. It is also noted that, a larger diameter of the liquid microjet nozzle leads to a larger surface area in the interaction regions and allows more hole density to be generated by the intense pump-pulses. As the XUV flux is low, lower concentrations only results in lower photoelectron count rates. For a given concentration of the sample solutions, the controlled

parameters for minimizing the space-charge effects are correspondingly the nozzle diameter and liquid flow rate, pump-pulse energy, laser beam spot sizes, and laser pulse durations.

Spatial and Temporal Overlap of the Pump and Probe Beams on a Liquid Sample: The TRPES measurements have been performed using the LADM mode. Initially, the 50 mM NaCl aqueous solution ran through the liquid microjet nozzle, and the liquid water valence band spectra was optimized in the spectrometer drift mode. The photoemission signal was maximized by overlapping the liquid microjet with the EUV beam and positioning the jet in front of the aperture to center the signal on the detector face. Then the spectrometer was switched to the WAM to find the spatial and temporal overlap of the pump and probe laser beams. The spatial overlap was achieved by maximizing the space-charge effects.

After the liquid microjet was aligned onto the EUV beam, then a positive time delay of around 100 ps or above was set to obtain the charging effect. Due to the space-charge effect in the aqueous solution, the electron KEs are decreased at hundreds-of-ps to ns delays[135]. This causes the PE distribution to partially move out of the spectrometer detection window and decrease the overall count rates, specifically when a low-KE-electron filter is applied to the spectrometer (achieved by negatively biasing a grid before the front face of the detector). As long as the pump pulse energy is not too high, in this situation, the integrated PE signal will be reduced compared to the probe only signal due to the space charge effects, see Figure 3.18a. The PE signal is then minimized at the maximum pump-probe spatial overlap at a given (approximately few-hundred-ps) pump-probe delay position. Determining the spatial overlap is easier using a sample that absorbs the pump wavelength. As a result, an aqueous pyrazine solution that absorbs at 267 nm was usually used to find the spatial overlap. Usually, the relatively high pump power of $\sim$5 mW was applied when finding the spatial overlap. The most important readings to note down at the pump-probe overlap position are the count rate ratio between the pump-probe and probe-only signal, the applied pump pulse energy, the pump beam size before the lens, the focal length of the lens, and the distance from the lens to the sample jet. These reference readings are used to periodically recheck the spatial overlap during the TRPES measurements and between different experimental campaigns.

Once the pump-probe overlap was maximized, the 50 mM aqueous NaCl solutions were used to measure the CC signal. The reason to use the 50 mM aqueous NaCl solutions is that it does not absorb resonantly 267 nm photons, at least at the single-photon level; aqueous pyrazine solutions absorb 267 nm and result in asymmetric time decays on top of the CC signal. More details about the CC measurements are presented in Section 6.2, Chapter 6. After measuring the CC signal in water, the sample solution (aqueous pyrazine) is switched in to the LJ chamber to find the experimental conditions that minimize the space-charge effects. The associated procedure is described in Section 6.3 Chapter 6. The pump pulse energy, pump beam spot size, and associated readings are recorded for the rest of the TRPES study. The pump-pulse intensity is one of the most important parameters for performing the TRPES experiments in the aqueous phase. Space-charge effects change the energetics of the electronic states and the associated dynamics, as discussed in Sections 6.3 and 6.7, Chapter 6.

Finally, the TRPES studies were performed on aqueous pyrazine solutions using variable pump-probe delay steps to record the time-resolved signal using the spectrometer LADM. Unfortunately, the liquid microjet measurement conditions are generally unstable. Each set of measurements was correspondingly performed for 20 minutes or less, where data was recorded at each delay point for 20-30 s. After 40 minutes of total measurements, the spatial overlap was checked again by changing the spectrometer mode to WAM, and the maximum available pump pulse energy was used to check the spatial overlap by monitoring the charging effect. Similarly, the temporal overlap was checked by switching to water and by measuring the CC before

doing any further TRPES measurements with aqueous pyrazine. Usually, recording a TRPES spectra with a good signal-to-noise ratio under space-charged minimized conditions takes a few days at a 5 kHz laser repetition rate. As a result, neighboring harmonic contrast, photon energy calibration using Ar gas, and spatial and temporal overlap characterization measurements were carried out on a routine basis every morning before the TRPES measurements were started. More details on the associated data processing and further analyses are described in Section 6.4, Chapter 6.

Chapter 4

Electronic Structure and Molecular Bonding Asymmetry in Aqueous Triiodide Solutions

Chapter Objectives and Scientific Contributions:

1. Characterization of aqueous triiodide solution concentrations containing a mixture of $I_{3\ (aq.)}^-$ and $I^-{}_{(aq.)}$ using UV-Vis absorption spectroscopy (See Section 4.1).
2. Investigation of surface- and bulk-sensitive valence and core-level (I 4d and I 3d) electronic structure of $I_{3\ (aq.)}^-$ solutions using Liquid-Microjet-Based X-ray Photoelectron Spectroscopy (LJ-XPS) (See Section 4.4).
3. Based on the theoretical predictions by Norell *et al.*[160], determination of molecular bond-length asymmetry in triiodide aqueous solutions, and investigation of surface versus bulk environmental effects on the anion structure (See Section 4.6).
4. Comparison of the aqueous-phase molecular bond length asymmetry with those in other solvents, *e.g.*, ethanol (Section 4.7).
5. Based on comparisons of the experimental results and theoretical calculations and spectral simulations, investigation of the predominant molecular structure of I_3^- in aqueous solution (See Section 4.8).

The presented content in this chapter has been adapted or directly taken from the publication: MS Ahsan, V Kochetov, D Hein, SI Bokarev, and I Wilkinson. *"Probing the molecular structure of aqueous triiodide via x-ray photoelectron spectroscopy and correlated electron phenomena",* Physical Chemistry Chemical Physics, 24(25):15540–15555, 2022. DOI: https://doi.org/10.1039/D1CP05840A. Published by the PCCP Owner Societies.

Following the sample characterization work performed using UV-Vis absorption spectroscopy, aqueous triiodide solutions have been investigated using the LJ-XPS technique. The solute molecular symmetry, solute-solvent interactions, and the effects of electronic-correlation are all imprinted on the single- (1h) and multi-electron (2h1e) ionization processes in the I 3d and I 4d core-level XPS experiments. The spectral assignment of the 1h and 2h1e processes are made based on the experimentally determined PE BEs of the collected PEs and associated theoretical calculations. Chemical shifts, changes in intensity distributions, and comparisons between single-and multi-electron ionization features allow the extraction of the valuable information about the $I_{3(aq.)}^-$ anionic molecular structure. The experimental work presented in this chapter highlights the sensi-

tivity of the LJ-XPS technique to absolute electron energetics, correlated-electron phenomena, and nuclear geometric structure in the aqueous-phase.

4.1 Sample Preparation and Characterization

UV-Vis absorption spectroscopy was used to characterized the aqueous solutions implemented in the XPS measurements and characterized the underlying equilibrium shown in Equation 4.1. Three different $I^-_{3(aq.)}$ solutions were investigated in the XPS experiments: 500 mM NaI / 250 mM I_2, 350 mM NaI / 250 mM I_2, and 420 mM NaI / 210 mM I_2. The latter mixture was studied at PETRA III, while the other two were implemented in BESSY II experiments.

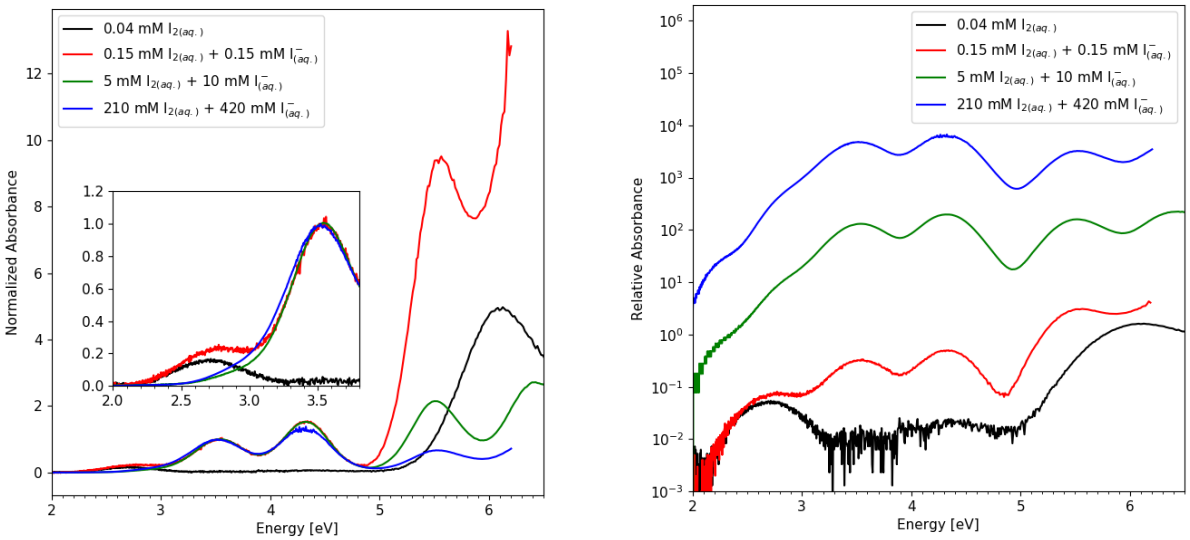

(a) Normalised UV-Vis absorption spectra of $I^-_{2(aq.)}$, $NaI_{(aq.)}$ mixtures

(b) Path-length-scaled UV-Vis absorption spectra of $I^-_{2(aq.)}$, $NaI_{(aq.)}$ mixtures

Figure 4.1: UV-Vis absorption spectra of the $I_{2(aq.)}$–water complex (black) and $I_{2(aq.)}$ + $NaI_{(aq.)}$ mixed solutions at different concentrations (red, green, blue). Panel (a) highlights reactant-concentration-dependent $I^-_{3(aq.)}$ spectra, which are normalized to the peak height of the C absorption bands (∼3.5 eV). Panel (b) highlights similar spectra without normalization but with signal intensity-scaling according to the implemented absorption cell length. More details are provided in the main body of the text. Figures are reproduced with permission from Reference 167, licensed under the Creative Commons Attribution 3.0 Unported License.

The triiodide solutions were prepared by mixing NaI and I_2 in an aqueous solvent. The solubility of iodine in an aqueous solvent is particularly low, just 1.3 mM at 25°C[170]. When I_2 is dissolved in water alone, I_2–H_2O charge-transfer complexes are known to be predominantly formed, with only a small fraction of the coordinated I_2 species oxidizing the water molecule and forming $I^-_{3(aq.)}$[171]. This situation is changed by adding salts to the solution. This results in the water-coordinated I_2 molecules being consumed by the $I^-_{(aq.)}$ anions to form $I^-_{3(aq.)}$[171], see Figure 4.1. Here it has been found, through UV-Vis spectroscopy, that the degree of formation of $I^-_{3(aq.)}$ anions in aqueous solution depends on the mixing concentration ratio between iodine and iodide. All of the solutions studied in this thesis work were prepared by adding excess amounts of NaI to I_2 in water. The solutions were stirred for some time and degassed in a supersonic bath. Applying this approach, triiodide anions are formed in the aqueous phase. By mixing iodide in the solutions at excessive concentrations, the $I_{3(aq.)}$ is pushed towards the desired product, in accord with the following chemical equation:

$$I_{2(\mathrm{aq.})} + I^-_{(\mathrm{aq.})} \rightleftharpoons I^-_{3(\mathrm{aq.})} \tag{4.1}$$

The prepared $I^-_{3(\mathrm{aq.})}$ sample solutions correspondingly contain residual $I_{2(\mathrm{aq.})}$ and $I^-_{(\mathrm{aq.})}$ components. Thus, it is important to quantify the residual $I_{2(\mathrm{aq.})}$ and $I^-_{(\mathrm{aq.})}$ species that are present in the $I^-_{3(\mathrm{aq.})}$ sample solutions. UV-Vis absorption spectroscopy measurements have been applied to characterize the sample solutions, and the residual components. A commercial UV-Vis spectrometer system (Shimadzu UV 2700i, 1.4-6.5 eV operating range) was used to perform the absorption measurements using 10 μm to 10 mm path length cells. These UV-Vis absorption measurements were, on average pimarily sensitive to the bulk region of the prepared mixed solutions.

4.1.1 Residual $I_{2(\mathrm{aq.})}$ and Iodine-Water Complexes

UV-Vis absorption spectra of $I_{2(\mathrm{aq.})}$ (black curves) and $I_{2(\mathrm{aq.})}$ + $NaI_{(\mathrm{aq.})}$ mixed (red, green, and blue curves) solutions are presented in Figure 4.1. 0.04 mM (black) and 0.15 mM $I_{2(\mathrm{aq.})}$ / 0.15 mM $NaI_{(\mathrm{aq.})}$ mixed (red) solution data were recorded using a 10 mm cell length. A 0.1 mm cell length was used to record 5 mM $I_{2(\mathrm{aq.})}$ / 10 mM $NaI_{(\mathrm{aq.})}$ (green) and a 10 μm path length cell was used to record 210 mM $I_{2(\mathrm{aq.})}$ / 420 mM $NaI_{(\mathrm{aq.})}$ (blue) mixed solution data. The data in Panel (a) are normalized to the C absorption band peak heights centered at ~3.5 eV[162,164], where the black $I_{2(\mathrm{aq.})}$ curve is scaled with a similar scaling factor as used in normalizing the red 0.15 mM $I_{2(\mathrm{aq.})}$ / 0.15 mM $NaI_{(\mathrm{aq.})}$ curve. The black color curve in panel (a) shows an absorption band centered at ~2.7 eV, a signature of the I_2–H_2O charge-transfer complex[171]. When NaI is added to the solution to 0.15 mM concentration and the nominal $I_{2(\mathrm{aq.})}$ concentration is increased from 0.04 mM (black) to 0.15 mM (red), the triiodide absorption signal, shown in a red color at 3.5 eV, vastly increases. The ~2.7 eV absorption band is further diminished with respect to the $I^-_{3(\mathrm{aq.})}$ ~3.5 eV C-band signal when the solute concentrations are increased beyond the $I_{2(\mathrm{aq.})}$-only solubility limit. This signal increase has been achieved using a 2:1 excess of NaI to I_2, as shown by the green and blue curves in Figure 4.1a. Increasingly intense $I^-_{3(\mathrm{aq.})}$ absorption bands at ~2.8 eV, ~3.5 eV, and ~4.4 eV[162,164], as well as $I^-_{(\mathrm{aq.})}$ absorption bands at ~5.5 eV and ~6.5 eV[165,166], are found with increasing reagent concentrations, as shown by the green and blue curves in Figure 4.1a.

The data presented in Figure 4.1a are shown with an alternative logarithmic intensity scale in Figure 4.1b. The as-recorded black and red curve absorption data are presented, while the green and blue curves, representing the mixed solution data, are intensity-scaled by a factor of 100 and 1000, respectively. The high concentration data, green and blue curves, and scaling factors were respectively set based on the Beer-Lambert law and the cell path lengths used to record the different data sets (10 mm/0.1 mm=100 and 10 mm/0.01 mm=1000). This allows a relative comparison of the relative absorbance of the four different solutions recorded with different path-length cells. A close inspection at the $I^-_{3(\mathrm{aq.})}$ C-band signals shown in Figure 4.1b indicates that the $I^-_{3(\mathrm{aq.})}$ concentration increases by more than four orders of magnitude in going from a 0.15 mM/0.15 mM to a 210 mM/420 mM mixed $I_{2(\mathrm{aq.})}$/$NaI_{(\mathrm{aq.})}$ solution. A consumption of $I_{2(\mathrm{aq.})}$ is highlighted in the overlapping ~2.8 eV $I^-_{3(\mathrm{aq.})}$ and ~2.7 eV $I_{2(\mathrm{aq.})}$ absorbance signals. When $NaI_{(\mathrm{aq.})}$ is added in excess amounts and solute concentrations are increased to 210 mM $I_{2(\mathrm{aq.})}$ and 210 mM $NaI_{(\mathrm{aq.})}$, the absorption signal at ~2.7 eV increases by around three orders of magnitude. This again demonstrates the consumption of $I_{2(\mathrm{aq.})}$ and the formation of $I^-_{3(\mathrm{aq.})}$ species in the solution. However, the spectral overlap of the $I_{2(\mathrm{aq.})}$ and $I^-_{3(\mathrm{aq.})}$ visible absorption features, and the high-solute-concentration absorption features, prevented the $I^-_{3(\mathrm{aq.})}$-to-$I_{2(\mathrm{aq.})}$ concentration ratio from being directly extracted from the solutions used in the XPS studies. Therefore, previously-reported thermodynamic data has been used to extract the $I^-_{3(\mathrm{aq.})}$-to-$I_{2(\mathrm{aq.})}$

concentration ratio and interpret the high-concentration UV-Vis spectra.

Equation 4.1 and its associated equilibrium constant (K=698$\pm$10)[247] are considered to determine the relative equilibrium concentrations of $I^-_{3(aq.)}$ with respect to $I_{2(aq.)}$ for known $NaI_{(aq.)}$ concentrations. For excess NaI concentrations of 170–285 mM, implemented in the XPS study, a large 1.2-1.8$\times10^5$ $I^-_{3(aq.)}$ concentration-excess is expected. The black curve in Figure 4.1a was cumulatively fit with a set of Gaussian peaks to determine an area ratio of about $\sim$31.5 between the visible $\sim$2.7 eV and ultraviolet $\sim$6.1 eV $I_{2(aq.)}$ bands. Taking into account the relative peak molar extinction coefficients for the $\sim$3.5 eV $I^-_{3(aq.)}$ C band ($\sim$16770 M^{-1} cm^{-1}) and $\sim$6.1 eV $I_{2(aq.)}$ ultraviolet charge-transfer band ($\sim$9100 M^{-1} cm^{-1}), which are reported in Reference 171, a visible, 2.7-eV-band $I_{2(aq.)}$ peak extinction coefficient of $\sim$290 M^{-1} cm^{-1} can be determined. This allows the estimation of the relative $I^-_{3(aq.)}$ contribution to the $\sim$2.8 eV absorption feature in the blue mixed-solution spectra shown in Figure 4.1. The $I^-_{3(aq.)}$ contribution should be $\sim$290 M^{-1} cm^{-1} / $\sim$16770 M^{-1} cm^{-1} * $\sim1.5\times10^5 \approx$ 2590 times higher than that of $I_{2(aq.)}$. This indicates that the $I_{2(aq.)}$ visible absorbance contributions are negligible, $\sim$0.2%, compared to the $I^-_{3(aq.)}$ contribution in the presence of excess $NaI_{(aq.)}$ and under the high-concentration conditions associated with the blue curves shown in Figure 4.1b. This also applies to the UV-Vis data subsequently discussed in this Section. Furthermore, considering the 1-2% signal-to-noise (S/N) ratio and up to few-percent relative signal area inaccuracies in all of the XPS measurements presented in this thesis work, and assuming $I^-_{3(aq.)}$ and $I_{2(aq.)}$ I-atom ionisation cross-sections within two orders-of-magnitude of each other, it is also estimated that the residual $I_{2(aq.)}$ contribution in the concentrated solution XPS signals is below <0.1%, and is correspondingly negligible in the XPS measurements.

4.1.2 Residual $I^-_{(aq.)}$ and I^-_2-to- $I^-_{3(aq.)}$ Conversion Efficiency

The blue and green curves in Figure 4.1b highlight that the residual $I^-_{(aq.)}$ anions in the mixed solutions may make significant contributions to the overall XPS signals. As a result, additional UV-Vis absorption spectroscopy measurements were performed using 10 μm absorption cells over a broad reagent concentration range. The goals of such measurements were to estimate the degree of conversion of $I_{2(aq.)}$ to $I^-_{3(aq.)}$ as well as the concentrations of the residual $I^-_{(aq.)}$ contributions as a function of initial reagent concentrations. For that purpose, $I^-_{3(aq.)}$ solutions were prepared with different I_2 concentrations (25- 250 mM) as well as I_2-to-NaI concentration mixing ratios. The mixing ratios are defined as $[I^-_{(aq.)}]$:$[I_{2(aq.)}]$ = *x*:1, where *x* = 1.4–10.0. An example of such a measurement with x=2 and assignments of the associated optical absorption bands is shown in Figure 2.11, Chapter 2.

The $I^-_{3(aq.)}$ C-band absorption signals were found to be spectrally isolated and unsaturated up to $\leq$200 mM concentrations for the reagent concentration range ($[I_{2(aq.)}]_{nominal} \geq$25 mM, $[I^-_{(aq.)}]_{nominal} \geq$37.5 mM) considered here. However, at the higher sample concentrations studied here (*e.g.* $[I_2]_{nominal}$>175 mM and $[I^-]_{nominal}$>350 mM), the D, CTTS 2 and potentially E and CTTS 1 band absorption signals were saturated with the 10 μm path length cell. Hence, the unsaturated $I^-_{3(aq.)}$ C-band absorption signal area was used to characterise the $I_{2(aq.)}$-to-$I^-_{3(aq.)}$ conversion. The C-band peak absorption area was correspondingly determined as a function of $I_{2(aq.)}$ concentration and $I^-_{(aq.)}$-to-$I_{2(aq.)}$ mixing ratio to estimate the $I^-_{(aq.)}$ concentrations in the mixed sample solutions used in the XPS studies. This was achieved by modelling the reagent-concentration-dependent UV-Vis absorption spectra using a multi-peak fit routine and selectively extracting the C-band contributions. The fit routine modelled the C-band features with an exponentially modified Gaussian function, where the B, D, E, CTTS 1, and CTTS 2 band features were modeled with Gaussian profiles. The fit results are exemplarily shown as dashed and dot-dashed curves in Figure 2.11. The fit results from 22 different mixed sample solutions are summarized in Figure 4.2. Figure 4.2a shows the $I^-_{3(aq.)}$ C-band

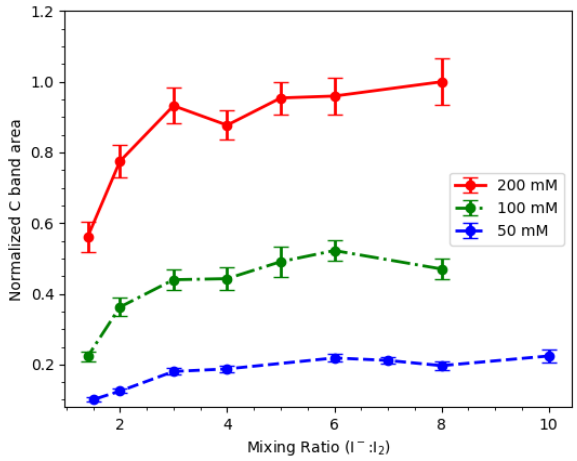

(a) $I^-_{3(aq.)}$ C-band absorption

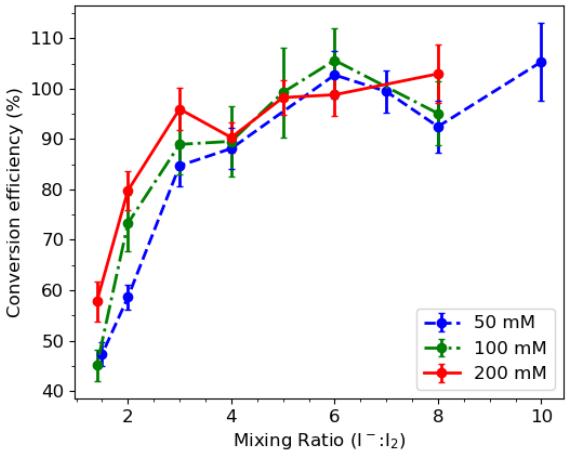

(b) Approximated $I^-_{2(aq.)}$-to-$I^-_{3(aq.)}$ conversion

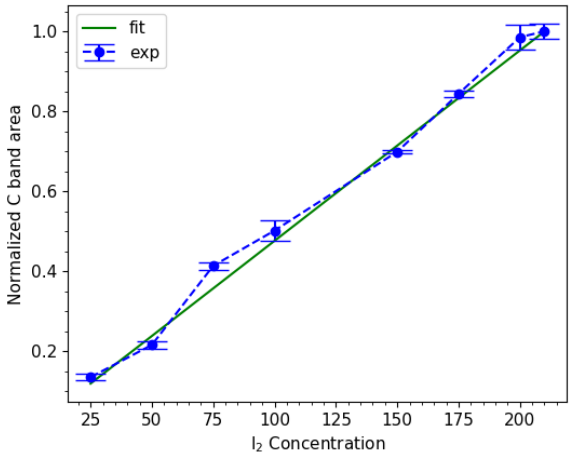

(c) Dependence of $I^-_{3(aq.)}$ absorption signal on $I_{2(aq.)}$ concentration, under excess of $I^-_{(aq.)}$ conditions

Figure 4.2: Panel (a), relative C-band absorption signal of the $I^-_{3(aq.)}$ anion obtained from UV-Vis absorption spectra of solutions with different $I_{2(aq.)}$ concentrations and initial I^--to-I_2 reagent ratio mixtures; 50 mM (blue data), 100 mM (green data), and 200 mM (red data) I_2-concentration data series are plotted. C-band signal areas associated with 200 mM initial I_2 concentrations have been used to normalize the C-band peaks in all of the datasets. Panel (b) shows the estimated conversion efficiencies at different reagent mixing ratios. Panel (c) presents the extracted $I_{3(aq.)}$ C absorption band areas for different initial iodine concentrations at mixing ratios $x > 4.0$ and an associated least-squares linear fit. Error bars represent one standard deviation of the mean of the extracted peak-areas. Further details are provided in the main body of the text. The figures are reproduced with permission from Reference 167, licensed under the Creative Commons Attribution 3.0 Unported License.

areas extracted from solutions with 50 mM (blue data), 100 mM (green data), and 200 mM (blue data) initial I_2 concentrations as a function of $I^-_{(aq.)}$-to-$I_{2(aq.)}$ concentration mixing ratio. For all of the initial I_2 concentrations considered above, the $I^-_{3(aq.)}$ signal generally rises with increased mixing ratio and saturates at ratios of $x \geq 4$.

A full (*i.e.* 100%) conversion of $I_{2(aq.)}$ to $I^-_{3(aq.)}$ is considered to occur when the C-band signal saturates, as shown at mixing ratios of $x \geq 4$ in Figure 4.2a. The associated data are re-plotted in Figure 4.2b to highlight the $I_{2(aq.)}$-to-$I^-_{3(aq.)}$ conversion efficiency as a function of the reagent mixing ratio. Up to the $x \sim 4$ mixing ratio, the initial iodine concentration as well as the iodide-to-iodine concentration mixing ratio used to prepare the solutions determines the degree of conversion from $I_{2(aq.)}$ and $I^-_{(aq.)}$ to $I^-_{3(aq.)}$. Within the error bounds, the

C-band absorbance was found to be invariant at ratios of $x \geq 4$. Therefore, C-band areas extracted from the $x = 4 - 10$ mixing ratio data were averaged and plotted against the associated initial $I_{2(aq.)}$ concentrations over a 25–210 mM range in Figure 4.2c. A linear fit was applied to the data shown in Figure 4.2c to extract the average C-band area at >210 mM $I_{2(aq.)}$ concentrations by extrapolation. A near linear increase of the C-band absorption signal area is confirmed in Figure 4.2c. The linear fit allowed estimation of the $I_{2(aq.)}$-to-$I^-_{3(aq.)}$ conversion efficiencies for the 250 mM / 350 mM, 210 mM / 420 mM, and 250 mM / 500 mM mixed $I_{2(aq.)}/I^-_{(aq.)}$ solutions used in the XPS experiments. The linear C-band signal increase with I_2 concentration also indicates that $I^-_{3(aq.)}$ anions are predominantly formed under the explored conditions and, therefore, that any higher-order-polyiodide contributions, from multiple $I_{2(aq.)}$ moieties, are negligible[248].

The light blue spectra in Figures 4.3a, 4.3b, and 4.3c show the UV-Vis absorption spectra of the three solution used in the XPS experiments, as recorded using a 10 μm (minimum), path length sample cell. Still, it was not possible to record the undistorted, *i.e.* unsaturated, UV-Vis spectra with such high iodine concentration mixtures (as shown by the oscillatory structure around the D-band absorption peaks in Figures 4.3a, 4.3b, and 4.3c). Therefore, half-concentration mixture UV-Vis spectra are shown by the orange curves in Figure 4.3 to highlight the undistorted C, D, and E & CTTS band ratios associated with the $I^-_{3(aq.)}$ and $I^-_{(aq.)}$ solution components. Adopting this procedure, the overall $I^-_{3(aq.)}$ concentrations of the solutions used in the XPS measurements could be determined. The associated results are shown in Table 4.1.

Table 4.1: Extracted $I^-_{3(aq.)}$ concentrations and $I^-_{2(aq.)}$-to-$I^-_{3(aq.)}$ conversion efficiencies for the 500 mM NaI / 250 mM I_2, 350 mM NaI / 250 mM I_2, and 420 mM NaI / 210 mM I_2 mixed solutions used in XPS studies performed at BESSY II and PETRA III.

$I_{2(aq.)}$ / $I^-_{(aq.)}$ mixtures	$I^-_{3(aq.)}$ con. (mM)	$I^-_{3(aq.)}$ con. (mM)	Conversion efficiency
250 mM / 500 mM	228 $\pm$ 4	272 $\pm$ 4	91 $\pm$ 2%
210 mM / 420 mM	177 $\pm$ 8	243 $\pm$ 8	84 $\pm$ 4%
250 mM / 350 mM	168 $\pm$ 12	182 $\pm$ 12	67 $\pm$ 4%

4.1.3 Electronic Structure Calculations and Spectral Simulations

The experimental results have been interpreted based on the electronic structure calculations and XPS spectral simulations of the I^-_3 anion, performed by Vladislav Kochetov and Sergey I. Bokarev[167]. Two of these molecular geometric structures are explicitly considered in simulating the UV-Vis absorption and XPS spectra here, specifically those were determined via time-resolved X-ray scattering experiments[31,33]. These molecular geometries are referred as the **Lin** and **Bent** geometries below. The former geometry represents a linear structure with asymmetric I–I bond lengths of 2.94 Å and 3.09 Å, close to the geometry extracted for the I^-_3 anion in methanol solutions[31,33]. The latter represents a bent geometry with an angle of 153° and the bond length differences are set to be larger than in the **Lin** case, 2.93 Å and 3.38 Å, which is the **Bent** geometry extracted for the I^-_3 anion in aqueous solutions[31,33]. The highest common $\mathrm{C_s}$ point symmetry group was considered in the calculations. Here, the Polarized Continuum Model (PCM) was used to approximate the water environment and simulate the UV-Vis absorption and XPS spectra. The slower part of the solvent response was calculated only for the singlet initial state. In this case, the final states of the ionized $I^\bullet_3$ molecule were kept frozen. However, the faster part of the solvent response was specifically calculated for each state. The most notable effect in the theoretical calculations including PCM solvation was an overall spectral shift of the calculated photoelectron bands. Such an implicit approach to the treatment of the solvation environment is expected to yield best agreement with the experiment that probe fully hydrated ions, particularly in the bulk region of the solution[167]. Therefore, the calculated spectra are compared to the bulk-sensitive experimental

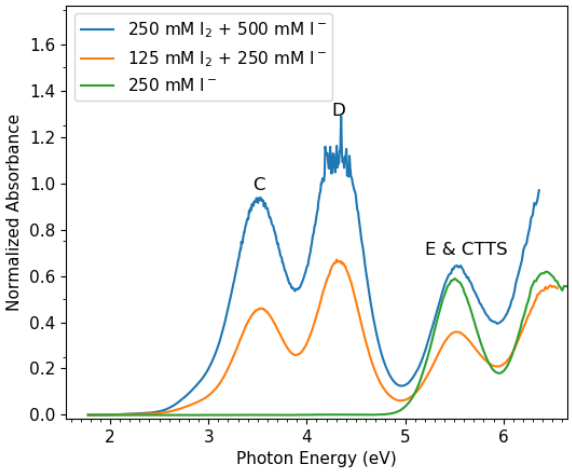

(a) 250 mM NaI, 250/500 mM and 125/250 mM I_2/NaI mixture

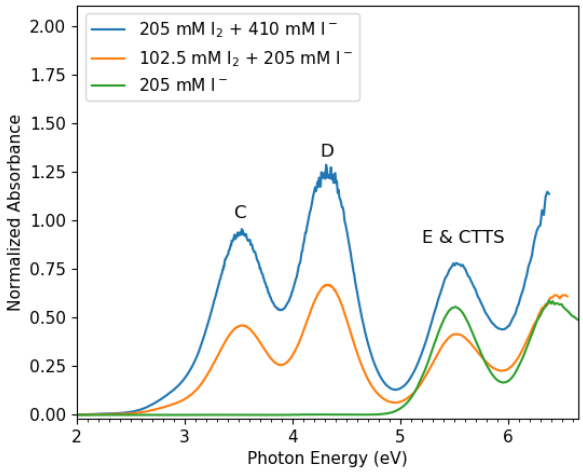

(b) 210 mM NaI, 210/420 mM and 105/210 mM I_2/NaI mixture

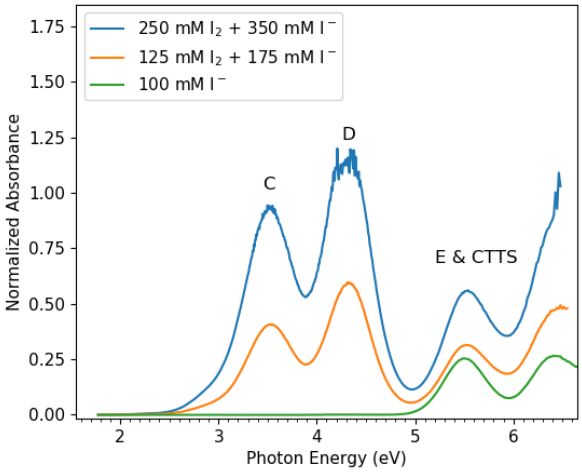

(c) 100 mM NaI, 250/350 mM and 125/175 mM I_2/NaI mixture

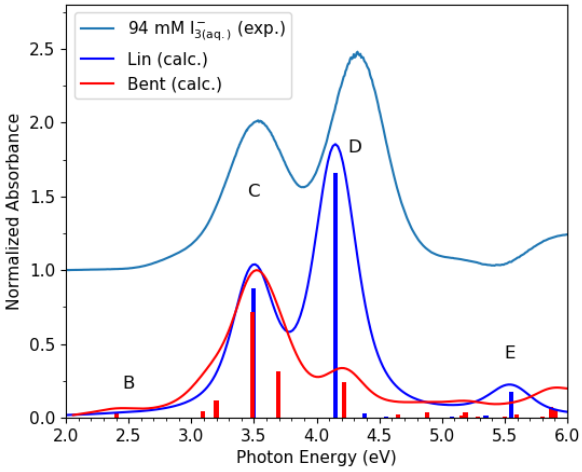

(d) Calculated $I^-_{3(aq.)}$ spectra and isolated $I^-_{3(aq.)}$ experimental spectrum

Figure 4.3: Panel (a)-(c): UV-Vis absorption spectra of the $I^-_{(aq.)}$ and $I^-_{3(aq.)}$ mixed solutions. The D band is saturated in the UV-Vis absorption spectra of 250/500 mM, 210/420 mM, and 250/350 mM I_2/NaI mixture solutions, as shown in panels (a)-(c). Unsaturated (half solute concentration) UV-Vis absorption spectra of 125/250 mM, 105/210 mM and 125/175 mM I_2/NaI mixed solutions are also shown. UV-Vis absorption spectra of reference 250 mM, 210 mM and 100 mM NaI solutions are also respectively shown (green curve). In panel (d), the calculated UV-Vis spectra, considering **Lin** (dark blue) and **Bent** (red) triiodide anion geometries are compared with the experimentally-obtained spectrum from a 125/250 mM I_2/NaI mixture solutions. The above figures are reproduced with permission from Reference 167, licensed under the Creative Commons Attribution 3.0 Unported License

datasets.

Figure 4.3(d) shows the calculated $I^-_{3(aq.)}$ anion UV-Vis spectra calculated for the **Lin** (dark blue curve) and **Bent** (red curve) geometries defined above. The calculations reproduce the spin-orbit split C- and D-band peaks of the $I^-_{3(aq.)}$ anion, with an additional weaker contribution, labeled as the E band, around 5.5–6.0 eV. As mentioned above, the E band spectrally overlaps with the residual $I^-_{(aq.)}$ anion absorption signal. The weaker $I^-_{3(aq.)}$ E band contributions are also identified in the UV-Vis spectra of the solutions implemented in the XPS measurements. Due to the presence of the E band, the combined $I^-_{3(aq.)}$ E and $I^-_{(aq.)}$ CTTS

1 band feature is found to be blue shifted by approximately 40 meV compared to the $^2P_{\frac{3}{2}}$ CTTS 1 band recorded from the pure $I^-_{(aq.)}$ solutions. Correspondingly, the spectral analysis method suggests that a 156 $\pm$ 10 mM residual $I^-_{(aq.)}$ concentration remains in an unsaturated 250 mM/125 mM NaI/I_2 aqueous mixture (see Table 4.1). Therefore, the 125 mM $I^-_{(aq.)}$ background UV-Vis absorption spectrum was intensity scaled by a factor of 156 mM/125 mM and subtracted from the mixed solution absorption spectrum to isolate the $I^-_{3(aq.)}$ contributions and a high-energy peak centre at $\sim$5.9 eV in the experimental UV-Vis difference spectrum, light blue curve in Figure 4.3d. Furthermore, considering the C- and D-band intensity ratio between the calculated and experimental UV-Vis absorption spectra of $I^-_{3(aq.)}$ anion, the experimental spectra is found to be in much better agreement with the calculated **Lin** geometry spectrum. Similar conclusions are also drawn in the later Section 4.8 from XPS data: that is, the triiodide anion predominatly takes on a near-linear, but bond-length asymmetric, geometry in aqueous solution.

4.2 Liquid-Jet XPS Experimental Details

The XPS experiments on aqueous triiodide were primarily performed at the U49-2 PGM-1 undulator beamline at BESSY II[168] using the SOL^{3}PES end station[235]. Additional high-energy-resolution XPS experiments were performed at the P04 undulator beamline at PETRA III[169] using the EASI end station[238]. In the XPS measurements, laminar liquid microjets of the aqueous solutions were introduced to the experimental vacuum chambers by forcing the liquids through 30 μm orifice-diameter fused silica micro-capillaries[83] using HPLC pumps. The solution flow rate was set to 0.65-0.80 ml s^{-1}. The jet temperature was adjusted to minimize the gas-phase contributions in the XPS measurements, specifically to 5° C (SOL^{3}PES instrument) or 10° C (EASI instrument). $\sim$30-50 cm prior to sample injection region, a gold wire was immersed in the flowing and electrically-conductive sample solution in order to electrically ground the solutions to the XPS experimental setups. The associated experimental setups (SOL^{3}PES and EASI) are described in Chapter 3 and in reference 167.

The surface or bulk regions of the liquid samples were predominantly probed by simply varying the KE of the PEs by changing the implemented photon energy in the experiment[10]. Previous theoretical[249] and experimental[11] studies on $NaI_{(aq.)}$ samples revealed that the solutions evolve from interfacial to bulk conditions over a $\sim$1 nm length scale. In the mixed triiodide/iodide sample solution, the bulk conditions are assumed to pertain over similar length scales. Thus, 150 eV or 200 eV photon energies were used in the XPS experiments to probe the aqueous-gas interface and record valence and I $4d^{-1}$ core level spectra. Such photon energies generate PEs with KEs of 90–190 eV, engendering surface sensitive conditions, *i.e.* electron effective attenuation lengths (EALs) of $\sim$1 nm[10]. Alternatively, 600 eV photon energies generated PEs with KEs of 540–590 eV, allowing predominant investigation of the bulk region of the aqueous solution, via EALs of $\sim$3 nm[10]. The photon energy was chosen in a similar way to probe the core I $3d^{-1}$ levels that will give a similar KE distribution as that recorded from the valence and I $4d^{-1}$ core level spectra. The aqueous triiodide I $3d^{-1}$ core level XPS spectra were recorded with predominant surface and bulk sensitivities by implementing 725 eV and 1175 eV photon energies, respectively, correspondingly to $\sim$100 eV and $\sim$550 eV electron KEs, respectively.

4.3 XPS Data Collection and Analysis Procedure

The as-measured XPS spectra are shown in Figure 4.4. Figure 4.4 highlights the contributions from both the liquid- and gas-phase of the water solvent, $I^-_{(aq.)}$ solute, $I^-_{3(aq.)}$ solute, $Na^+_{(aq.)}$ counter ions, as well as a broad secondary and inelastically-scattered, electron background signal. All aqueous solution XPS spectra

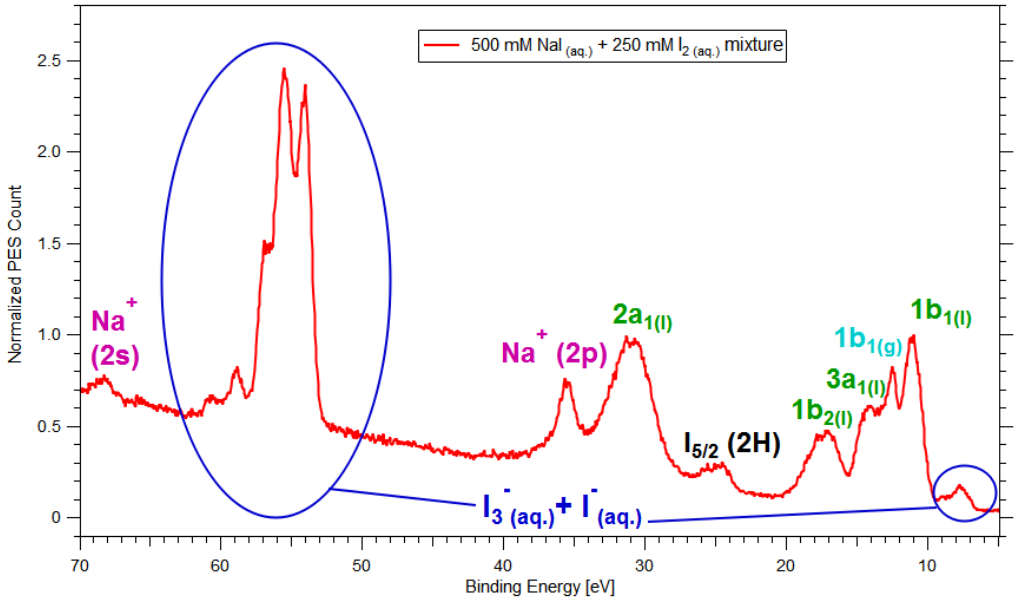

Figure 4.4: As-measured valence and I 4d core level XPS spectra of a mixed 500 mM $Na^{+}_{(aq.)}$, 272 mM $I^{-}_{(aq.)}$, and 228 mM $I^{-}_{3(aq.)}$ solution, recorded using a photon energy of ∼600 eV at BESSY II. The spectra highlight a broad secondary electron background with an increasing spectral contribution from low to high BE[84]. Different spectral features of the primary, direct photoelectron peaks from the solvent (liquid-phase, green, and gas-phase, light blue), $Na^{+}_{(aq.)}$ counter-ion (pink), and $I^{-}_{3(aq.)}$ sample ion (dark blue) are also highlighted. Additionally, residual beamline second harmonic signals are labeled as '$I_{\frac{5}{2}}$ (2H)'. The figures are reproduced with permission from Reference 167, licensed under the Creative Commons Attribution 3.0 Unported License.

measured from liquid microjet sample sources display such inelastically scattered broad secondary electron background contributions, with such features being ubiquitous in condensed-phase XPS experiments[84].

Background Subtraction: The XPS signals from a 210 mM $I^{-}_{2(aq.)}$/ 420 mM $I^{-}_{(aq.)}$ mixed solution (red color) are shown in Figure 4.5. The XPS spectra and UV-Vis absorption spectra displayed above initially that this solution has contributions from gas and liquid phase water, 177 mM $I^{-}_{(aq.)}$, 243 mM $I^{-}_{3(aq.)}$, and 420 mM Na^{+}. A 210 mM $NaI_{(aq.)}$ background photoelectron spectrum (black color) was recorded under the same experimental conditions as the mixed solution measurements (similar jet flow rate, jet temperatures, and resulting base pressure in the chamber). In order to remove the residual $I^{-}_{(aq.)}$ contributions, water signals, and $Na^{+}_{(aq.)}$ contributions from the mixed solution spectra and isolate the $I^{-}_{3(aq.)}$signal, an intensity-scaled 210 mM $NaI_{(aq.)}$ background photoelectron spectra was subtracted from the mixed solution spectra; the UV-Vis absorption measurements, described in Section 4.1 allowed the determination of the concentrations of $I^{-}_{3(aq.)}$ and residual $I^{-}_{(aq.)}$. In the case of the 210 mM/420 mM $I_{2(aq.)}/I^{-}_{(aq.)}$ mixture, UV-Vis absorption band analysis indicates that ∼177 mM $I^{-}_{3(aq.)}$ and ∼243 mM residual $I^{-}_{(aq.)}$ concentrations occur in the equilibrated solution. Specifically, the reference specta were scaled by factors of 243 ± 8 mM/210 mM and subtracted from the sample spectra, allowing comparisons to be made over the valence and core-level spectral measurement ranges.

In Figure 4.5, the sample solution (red curves), concentration-corrected background solution (black curves), and difference XPS spectra (green curves) produced in the aforementioned analysis are presented for exemplary high photon energy data sets. Therein, the valence and I 4d spectra are shown (top panel, as recorded at a 600 eV photon energy at PETRA III) along with corresponding solvent O 1s and solute I 3d spectra (bottom panel, recorded at a 1175 eV photon energy). A three-point rolling average smoothing algorithm was

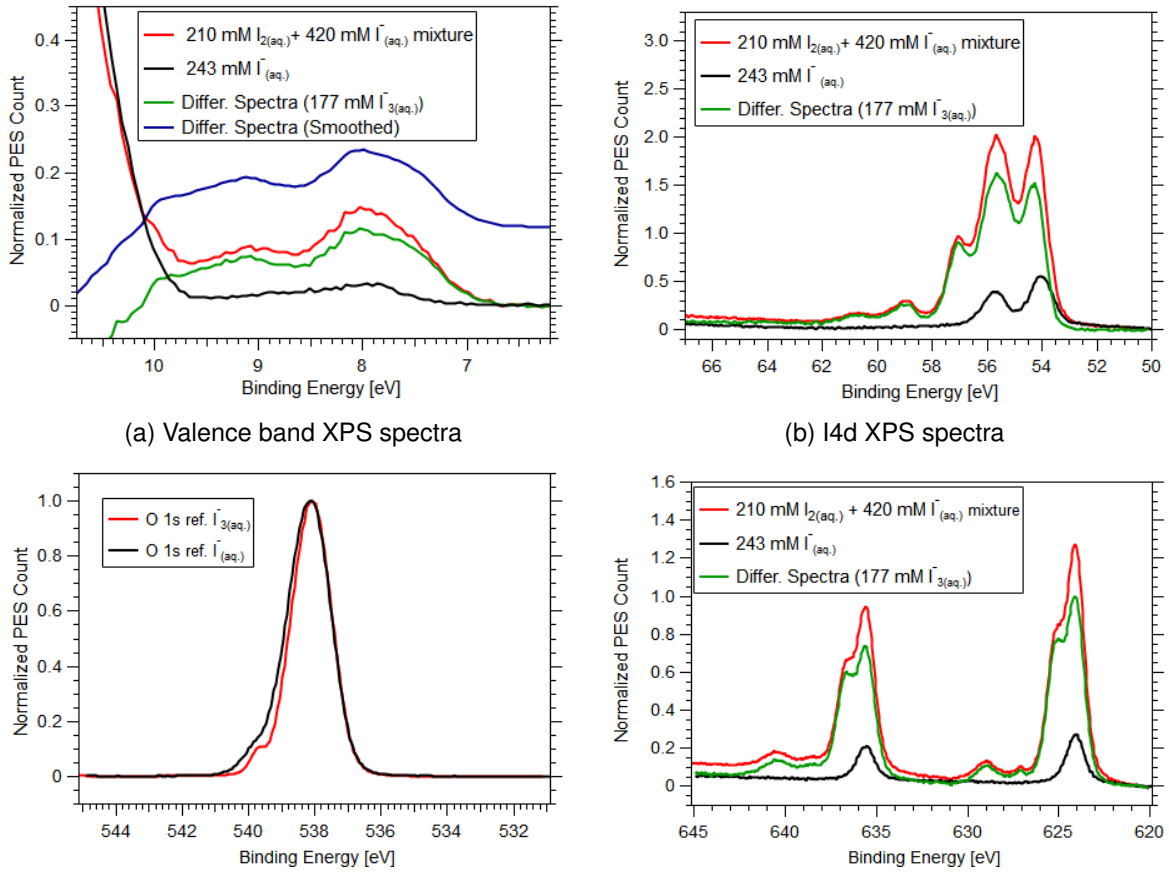

(a) Valence band XPS spectra

(b) I4d XPS spectra

(c) O1s XPS spectra

(d) I 3d XPS spectra

Figure 4.5: Bulk-sensitive valence and I 4d core level XPS spectra of the mixed $Na^{+}_{(aq.)}$, $I^{-}_{(aq.)}$, and $I^{-}_{3(aq.)}$ solutions (red), 243 mM NaI solution (black), and associated difference curves (green) that isolate the valence, I 4d, and I 3d contributions from the $I^{-}_{3(aq.)}$ solute. The 243 mM NaI solution reference spectra was obtained by scaling the as-measured 210 mM NaI XPS specta to take into account the residual $I^{-}_{(aq.)}$ contributions in the mixed solutions. The valence and I $4d^{-1}$ spectra are shown in the top panel of the figure and were recorded at a photon energy of 600 eV. The O 1s and I $3d^{-1}$ spectra are shown in the bottom panel of the figure and were recorded at a photon energy of 1175 eV. The liquid water $1b_1$ peak was used to calibrate the BEs for the valence and I 4d measurements, whereas the liquid water O 1s peak was used to BE calibrate the I 3d measurements. The spectra were recorded at PETRA III using a magic angle collection geometry with respect to the synchrotron light polarisation. The figures are reproduced with permission from Reference 167, licensed under the Creative Commons Attribution 3.0 Unported License.

applied to the bulk-sensitive valence band data recorded at PETRA III to improve the signal-to-noise ratio (SNR). The datasets recorded at BESSY II were also analyzed using a similar procedure, but were in this case smoothed using a 6-point rolling average method prior to plotting and fitting.

The valence and core level XPS spectra analysis procedure is exemplified in Figure 4.5. The mixed solution spectra and reference/ background spectra were fit using a set of Gaussian functions to extract the liquid water $1b_1$ peak positions. Subsequently, the spectra were BE shifted so that the $1b_1$ peak centres were set to their (nearly-neat water) reference BE values of 11.33 ± 0.04 eV[66,243] and both $1b_1$ peak intensities were normalized to one. It was assumed that the BEs of the liquid water $1b_1$ valence band signal was unperturbed by the solutes. The signal intensity of the background NaI XPS spectra was then scaled according to the residual $I^{-}_{(aq.)}$ concentration of the mixed solution determined from the UV-Vis spectral analysis, and then subtracted from the mixed solution spectra (see Figure 4.5a). For example, 210 mM reference NaI spectra, recorded under similar conditions to the sample spectra, were intensity scaled by a factor of 243/210 and

subtracted from the 210 mM/420 mM I_2 and I^- mixed solution spectra. The associated reference NaI spectra scaling by a factor of $1.2\pm^{0.1}_{0.1}$ accounted for the determined 243 $\pm$ 8 mM residual $I^-_{(aq.)}$ concentration in this solution. The resulting spectra are shown in Figure 4.5a. The I 4d core level spectra were recorded under the same conditions as the valence XPS spectra. Correspondingly, the spectra were BE shifted and their respective intensities were normalized using the values extracted from the valence spectra analysis. Background $NaI_{(aq.)}$ I 4d spectra were scaled using the same scaling factor ($1.2\pm^{0.1}_{0.1}$) to essentially remove the $I^-_{(aq.)}$ features, according to the extracted residual $I^-_{(aq.)}$ concentration in the mixed solutions. The normalised and scaled $NaI^-_{(aq.)}$ background spectrum was then subtracted from the mixed solution data to extract the $I^-_{3(aq.)}$ contributions in the I 4d spectral region. The associated spectra are shown in Figure 4.5b.

For the I 3d XPS analysis, similar to the valence analysis, the solvent O 1s data of the liquid- and gas-phase were fitted using cumulative Voigt-profiles, instead of Gaussian profiles, and were shifted to reference BE values of 538.10 ± 0.05 eV with respect to the local vacuum level[66,136]. It was assumed that the BEs of the liquid water O 1s/$1a_1$ core-levels were unaffected by the solutes. The background signal scaling was initially performed using O 1s spectra associated with the solvent molecules in the sample and reference/ background solutions, as shown in Figure 4.5c. Finally, concentration corrected/intensity scaled background spectra were subtracted from the corresponding mixed solution spectra. The associated spectra are shown in Figure 4.5d.

Using this background signal subtraction procedure, the residual $I^-_{(aq.)}$ XPS signatures are considered to be removed from the mixed solution spectra (*i.e.* Figure 4.4) and only $I^-_{3(aq.)}$ contributions remain. XPS peak intensity (signal area) errors were fitted to be $\sim$3% or less in all of the cases where the I^- and I^-_3 signals spectrally overlapped. These errors are taken into account in all of the subsequent data analysis. The robustness of the data analysis procedure is quantified using the $I^-_{(aq.)}$ concentration errors determined in the UV-Vis spectral analysis and the reproducibility of the background subtracted $I^-_{3(aq.)}$ data.

Fitting Procedure Figures 4.6b, 4.7b, and 4.8b show the background-subtracted experimental valence, I 4d, and I 3d XPS spectra of aqueous triiodide solutions and associated cumulative fittings. Linear baseline corrections were also applied to the background subtracted data, specifically over the 5-11 eV, 50-65 eV, and 618-636 eV and 632-645 eV BE ranges for the valence (Figure 4.6), I 4d (Figure 4.7), and I 3d $I^\bullet_{3(aq.)}$ $\Omega = \frac{5}{2}$ and I 3d $I^\bullet_{3(aq.)}$ $\Omega = \frac{3}{2}$ (Figure 4.8) ionisation spectral regions, respectively. Valence and core-level, $I^-_{3(aq.)}$ difference spectra recorded at BESSY II were further smoothed using a 6-point moving average method, prior to fitting.

The valence band spectra shown in Figure 4.6 were modelled using a pair of Gaussian peaks. The higher BE region is over-subtracted due to a reduced signal-to-background ratio in the spectral overlap region associated with the intense liquid water valence bands. Such over-subtraction results in further uncertainties in determining the Peak 2 spectral position in the valence band. Hence, the reported BE and FWHM (Table 4.2 and A.1) related to Peak 2 should be seen as the lower limits. Similarly, the smoothed I 4d and I 3d experimental spectra recorded in BESSY II were modelled using cumulative, five-and eight-component Voigt-profile peak fits, respectively. The Voigt-profile fitting takes the inhomogenous and any lifetime peak broadening effects into account. Conversely to the BESSY II results, the I 4d and I 3d data shown in Figures 4.6, 4.7, and 4.8, recorded at PETRA III were modelled without smoothing.

4.4 Results and Discussion

In the following section, the various spectral features shown in Figures 4.6, 4.7, and 4.8 and illustrated in Figure 4.9, are assigned to specific ionization pathways. The valence, 4d, and 3d ionization pathways are respectively highlighted by the red, light purple, and blue bracketed numbers in Figure 4.9. Similar peak numbers, assignments, and associated as-measured energetics are summarized in Table 4.2 and in Appendix Section A.1.

Vladislav Kochetov and Sergey I. Bokarev have been performed all of the theoretical calculations with the `OpenMolcas` package.[250]. The PE spectra were simulated at the sudden approximation level, which is defined as the squared norms of Dyson Orbital[251,252]. In order to compared with the experimental results, the simulated valence, I $4d^{-1}$, and I $3d^{-1}$ PE spectra for the **Lin** and **Bent** structures have been shifted in BE by about -0.8 eV, +2.8 eV, and +13.5 eV, respectively. Finally, the stick spectra corresponding to the geometric structures were convolved with Gaussians with 0.85 eV, 1.05 eV, and 1.25 eV FWHM for the valence, I $4d^{-1}$, and I $3d^{-1}$ PE spectra, respectively, to reproduce the experimental peak widths. More details about the theoretical calculations and spectral simulations are described in References 167,253.

4.4.1 Valence XPS Spectra

The aqueous triiodide anion is expected to show a broad structural distribution that covers fully symmetric and asymmetric geometries with different bond lengths and bent geometries[28,31,33]. Considering this fact, the XPS spectra were simulated by Vladislav Kochetov and Sergey I. Bokarev for two different geometries, which were proposed based on experimental X-ray scattering data: **Lin** and **Bent**. The experimental (left panel, top trace) and calculated (left panel, bottom trace) bulk-solution valence band spectra of $I^-_{3(aq.)}$ are shown in Figure 4.6. Bulk-sensitive valence band spectra BEs and FWHMs are shown in the top section of Table 4.2. The BEs and peak widths were extracted from cumulative Gaussian fits to the $I^-_{(aq.)}$-background-subtracted $I^-_{3(aq.)}$ sample solution data sets. Similar results are reported for the surface-sensitive experiments in Appendix Section A.1.

Two distinct PE bands are highlighted in Figure 4.6 (peak 1 and 2), with a separation of about 1.5 eV. Both of them shows significant spectral asymmetry. As shown in the UV-Vis absorption studies, section 4.1, a $\sim$0.8 eV spin-orbit coupling is expected to influence the valence band electronic structure of $I^-_{3(aq.)}$. The calculated valence spectra indicates an average $\sim$0.6 eV final-state spin-orbit splitting. Such a splitting remains unresolved in the simulated spectra when the simulated spectra were convolved with a $\sim$0.8 eV FWHM Gaussian to qualitatively match the experimental data, which is subject to inhomogeneous broadening in the aqueous phase. Moreover, the calculation predicts a 0.2 eV VIE shift between the **Lin** and **Bent** geometries of the aqueous triiodide anion.

Comparison between experimental and simulated valence XPS spectra, unfortunately give little insight into the geometric structure of the $I^-_{3(aq.)}$ anion. The final spin-orbit states and molecular geometry dependence of the valence BEs appear to be hidden in the experimental PE spectra by the underlying solute geometric structural distribution and/or inhomogeneous broadening due to the fluxional, aqueous environment.

The asymmetric spectral profile of Peaks 1 and 2 in Figure 4.6 are assigned based on the theoretical spectral simulation and are ascribed to a superposition of PE spectra associated with a continuous structural distribution spanning the **Lin** and **Bent** geometric structures, ionization to form at least two different radical electronic states with a BE difference of $\sim$1.5 eV and an unresolved $\sim$0.8 eV final-state spin-orbit splitting. The lower BE PE band (Peak 1, 7.83$\pm$0.05 eV) in Figure 4.6 is attributed to a number of 1h ionization signals,

Table 4.2: Bulk-sensitive valence (top section), core I 4d (middle section), and core I 3d (bottom section) electron BEs and peak FWHMs of aqueous triiodide obtained from the XPS experiments. The BEs and widths of Peaks 1 and 2 were extracted from cumulative Gaussian profile fits to the background-subtracted XPS data, with these BEs being marked by a ‡ to highlight that they represent final spin-orbit state averaged values. The spin-orbit-state resolved BEs and total FWHMs of the core-level features (Peaks 3-15) were determined via cumulative Voigt profile fits to the background subtracted data, the functional form of which accounted for non-negligible lifetime broadening effects. The table reports average values of the fitted BEs and FWHMs for all of the measurements performed at the BESSY II and PETRA II facilities. Ionic I atom, central I atom, terminal I atom, $I^{\bullet}_{3(aq.)}$ radical spin-orbit state, single-hole process, and two-hole-one-electron SU process are denoted as *i*, *c*, *t*, $\Omega_{\mathrm{radical}}$, 1h, and 2h1e, respectively. All spectral assignments were made based on the theoretical caclulations and XPS spectral simulations.

	Peak	Assignment			Ionization Energetics	
		Atom(s)	Electronic Transition	Final State ($\Omega_{\mathrm{radical}}$)	BE (eV)	FWHM (eV)
Val.	1	All	$(54a'/23a'',\ n)^{-1}/(56a',\ n)^{-1}$	1h (3/2& 1/2)	7.81 ± 0.05 ‡	1.24 ± 0.04
	2	All	$(53a'/22a'',\ \pi)^{-1}$	1h (3/2 & 1/2)	9.28 ± 0.05 ‡	1.25 ± 0.11
Core I 4d	3	*i*	$4d^{-1}$	1h (5/2)	54.21 ± 0.05	0.97 ± 0.04
	4	*c, t*	$4d^{-1}$	1h (5/2)	55.60 ± 0.04	1.54 ± 0.04
	”	*i*	$4d^{-1}$	1h (3/2)	”	”
	5	*c, t*	$4d^{-1}$	1h (3/2)	57.11 ± 0.04	0.87 ± 0.07
	”	*c*	$4d^{-1}, (54a'/23a''/56a',\ n)^{-1}, (57a',\ \sigma^*)^1$	2h1e (5/2)	”	”
	6	*c*	$4d^{-1}, (54a'/23a''/56a',\ n)^{-1}, (57a',\ \sigma^*)^1$	2h1e (3/2)	59.03 ± 0.05	1.17 ± 0.06
	”	*i, t*	$4d^{-1}, (54a'/23a''/56a',\ n)^{-1}, (57a',\ \sigma^*)^1$	2h1e (5/2)	”	”
	7	*i, t*	$4d^{-1}, (54a'/23a''/56a',\ n)^{-1}, (57a',\ \sigma^*)^1$	2h1e (3/2)	60.75 ± 0.06	1.14 ± 0.13
Core I 3d	8	*i, t*	$3d^{-1}$	1h (5/2)	624.12 ± 0.10	1.18 ± 0.07
	9	*c*	$3d^{-1}$	1h (5/2)	625.22 ± 0.10	1.31 ± 0.12
	10 †	*c*	$3d^{-1}, (54a'/23a''/56a',\ n)^{-1}, (57a',\ \sigma^*)^1$	2h1e (5/2)	627.32 ± 0.10	0.85 ± 0.07
	11	*i,t*	$3d^{-1}, (54a'/23a''/56a',\ n)^{-1}, (57a',\ \sigma^*)^1$	2h1e (5/2)	629.02 ± 0.10	1.59 ± 0.10
	12	*i, t*	$3d^{-1}$	1h (3/2)	635.64 ± 0.10	1.26 ± 0.09
	13	*c*	$3d^{-1}$	1h (3/2)	636.75 ± 0.10	1.31 ± 0.09
	14 †	*c*	$3d^{-1}, (54a'/23a''/56a',\ n)^{-1}, (57a',\ \sigma^*)^1$	2h1e (3/2)	638.78 ± 0.10	0.79 ± 0.07
	15	*i,t*	$3d^{-1}, (54a'/23a''/56a',\ n)^{-1}, (57a',\ \sigma^*)^1$	2h1e (3/2)	640.57 ± 0.11	1.84 ± 0.05

‡ These valence BE values are the as-measured, final spin-orbit state averaged peak positions and differ from the spin-orbit-state resolved values estimated and reported in Figure 4.9 by +0.27 eV. See the main body of the text for details.

† The origins of these features remains ambiguous and the signals could alternatively be assigned to superimposed signatures of the calculated Lin and Bent spectra. See the main body of the text for details.

specifically, $(54a'/23a'',\ n)^{-1}$, $(55a'/24a'',\ \pi^*)^{-1}$, and $(56a',\ n)^{-1}$. The higher BE valence PE band (Peak 2, 9.3 ± 0.05 eV) is assigned to a $(53a'/22a'',\ \pi)^{-1}$ 1h ionization process. In the experimentally recorded PE spectra, the high-BE $(53a'/22a'',\ \pi)^{-1}$ solute MO is observed to merge with the tail of the HOMO ionization,

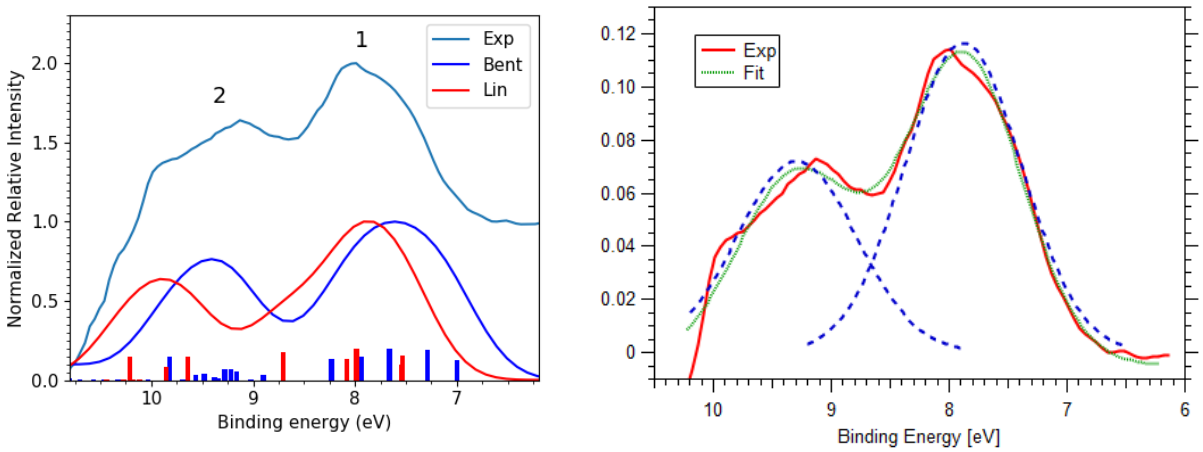

(a) Valence band

(b) Gaussian fit

Figure 4.6: (Panel (a), top trace) Bulk-sensitive experimental valence band spectrum recorded using a 600 eV photon energy at the P04 beamline at PETRA III, with an energy resolution of 80 meV. The $I^-_{3(aq.)}$ solute concentration was ∼180 mM. The intensity-scaled and background-subtracted $I^-_{3(aq.)}$ valence spectrum was smoothed using a 3-point rolling average routine. (Left panel, bottom traces) Calculated $I^-_{3(aq.)}$ PE spectra of asymmetric linear (red curve, Lin) and asymmetric bent (dark blue curve, Bent) geometric structures described in Section 4.1.3 and, with further details provided in reference 167. In order to match the experimental spectra, both of the simulated spectra were globally shifted by -0.8 eV and finally convoluted with Gaussians (FWHM 0.8 eV). (Panel (b)) Gaussian fits to the experimental spectrum, as used to model the bulk-sensitive valence PES spectra. The figures are reproduced with permission from Reference 167, licensed under the Creative Commons Attribution 3.0 Unported License.

$1b^{-1}_{1(l)}$, feature of the aqueous solvent (see section 4.1). All higher BE valence ionization signals, such as the $(52a', \sigma)^{-1}$ channel of the solute $I^-_{3(aq.)}$ anion, are consequently hidden by the predominant aqueous solvent ionization signals. Similar surface-sensitive valence XPS spectra were also recorded. It was found, that within the experimental uncertainties, the energetics of the PE peaks 1 and 2 are found to be equivalent in the surface- and bulk-sensitive measurements; the results highlight that the valence electronic energetics of the $I^-_{3(aq.)}$ molecule are unaffected, on a ∼50 meV energy scale, as we increase our sensitivity to the aqueous bulk.

4.4.2 Core-Level XPS Spectra

It has been shown that valence band PE spectra are rather insensitive to the variation of the $I^-_{3(aq.)}$ bond lengths and angle. However, it should be possible to investigate such symmetry reductions using core-level PES and comparison of experimental and theoretical XPS spectra[160]. As a result, the inner shell electronic energetics of $I^-_{3(aq.)}$ and the associated coupling to the underlying geometric structure of both the solute and solvent molecules are now considered. Initially, the I $4d^{-1}$ core-level XPS spectra are presented, followed by a discussion of the I $3d^{-1}$ core-level XPS spectra.

I $4d^{-1}$ XPS Spectra Bulk-sensitive experimental I $4d^{-1}$ core-level XPS spectra of $I^-_{3((aq.)}$ (top curves, light blue) along with associated spectral simulations (bottom curves, dark blue and red, corresponding to the **Lin** and **Bent** geometries, respectively) are shown in Figure 4.7. Five well-resolved peaks are seen in the I 4d core-level PE spectra in Figure 4.7. The associated spectral positions (BE's) and widths (FWHMs) were obtained by cumulative Voigt profile fitting, shown in Figure 4.7b. These fit results are summarized in the middle section of Table 4.2. Similar results have been obtained from the surface-sensitive experiments, and

are presented in Appendix, Section A.1.

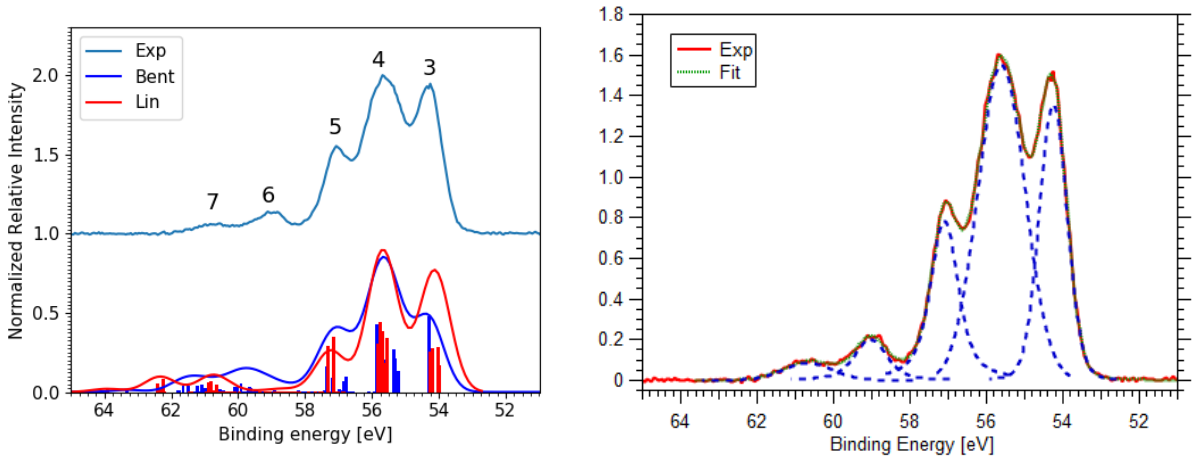

(a) I 4d core-level XPS spectra

(b) Associated Voigt fit

Figure 4.7: (Panel (a), top trace) Bulk-sensitive I 4d core-level XPS spectra of ∼180 mM $I^-_{3(aq.)}$ samples, recorded using a 600 eV photon energy at the P04 beamline at PETRA-III, with an energy resolution of 80 meV. The calculated spectra for the **Lin** (red curve) and **Bent** (dark blue) geometries are shown in the bottom traces. Panel (b) shows the associated five-component cumulative Voigt-profile spectral fits used to model the I 4d core level XPS spectra are shown. The figures are reproduced with permission from Reference 167, licensed under the Creative Commons Attribution 3.0 Unported License.

The surface- and bulk-sensitive results obtained in the XPS studies can be compared to the experimental $I^-_{3(aq.)}$ I $4d^{-1}$ spectra previously published by Josefsson et al.[144], where the presented aqueous I $4d^{-1}$ peak ratios are significantly different due to the different background subtraction procedure employed in comparison to this study, (see the background subtraction section 4.3). In the approach implemented here, no assumption was made about the relative surface activities of the $I^-_{3(aq.)}$ and $I^-_{(aq.)}$ anions, nor their relative valence, I 4d, and I 3d ionization cross-sections. Josefsson *et al.*[144] subtracted the gas-phase I_2 signatures from their aqueous-phase I^-_3 data and took into account the expected stoichiometric ratio between the I^- and I^-_3 species in their solutions in order to scale the aqueous-phase I^- signals to aprroximately one third of those of the I^-_3 signals. They subsequently subtracted the I^- signal as a background contribution. In our experiment, due to the micro-focusing conditions that matched the focal spot size to the liquid-jet sample diameters at the U49-2 PGM-1 and P04 beamlines, our recorded spectra are essentially insensitive to any $I_{2(g)}$. Furthermore, our measured aqueous I^- 4d (and 3d) signals are found to correspond to signifacantly less than one third of the I^-_3 signal levels, as shown in the bulk-sensitive magic angle data in Figure 4.5b (see section 4.3). This was also observed in the surface-sensitive measurements, suggesting the ionization cross-sections of $I^-_{3(aq.)}$ was higher than that of $I^-_{(aq.)}$ at both of the ionization photon energies implemented here. Correspondingly, the background-subtracted $I^-_{3(aq.)}$ $4d^{-1}$ peak ratios reported here are significantly different compared to those presented by Josefsson *et al.* in Reference 144.

Due to spectral overlap in both the bulk- and surface-sensitive I $4d^{-1}$ XPS spectra, it is difficult to assign each of the features to specific terminal (*t*), central (*c*), and ionic (*i*) iodine atom ionization channels, at least based on the experimentally measured dataset alone. Such spectral assignment became possible with the help of the spectral simulations. According to the simulations, the dominant, lowest three BE PE bands should be assigned to the single-active-electron 1h I 4d ionization contributions from the *t*, *c*, and *i* iodine atoms. Peak 3 (54.2±0.05 eV, in the bulk-sensitive results) is assigned to $4d_{5/2}$ ionization of the I^--like *i* atom, where the subscript denotes the final spin-orbit state, $\Omega_{\mathrm{radical}}$, of the produced $I^\bullet_{3(aq.)}$ radical. Peak 4 (55.6±0.04 eV) is determined to have spectral contributions from the overlapping *t* $4d_{5/2}$, *c* $4d_{5/2}$, and *i* $4d_{3/2}$

ionization features. While, Peak 5 (57.2±0.04 eV) is primarily assigned to the overlapping *t* $4d_{3/2}$ and *c* $4d_{3/2}$ ionization channels. The chemical shift between the *i*, *c*, and *t* peaks is around 1.4-1.6 eV.

In the previous Section 4.4.1, the calculated valence spectra suggested a small BE or chemical shift between the **Lin** and **Bent** geometries. However, it was found that the simulated $4d^{-1}$ XPS spectra have notable sensitivities to the molecular geometry via the spectral intensity distribution. The relative peak intensities of the main experimental I $4d^{-1}$ peaks (Peaks 3, 4, and 5) reported in this work are compared to those in the simulated spectra shown in Figure 4.7 and reported elsewhere[144,253]. Based on such a comparison, the measured intensity ratio is found to best match the **Lin** geometry simulated spectrum, potentially with a lesser contribution of the **Bent** geometry. The central 1h features, peak 4, in the **Lin** and **Bent** simulated spectra coincide. Thus, the $4d^{-1}$ simulated spectra were uniformly shifted in BE to best match the experimental PE spectra. Peak 3 and 4 have closer BEs to the central peak in the **Bent** geometry case and exhibit a larger spectral separation in the **Lin** geometry case.

The higher BE PE peaks – peak 6 centred at 59.1±0.1 eV and peak 7 at 60.8±0.1 eV in the bulk-sensitive results – are due to the multi-active-electron process, 2h1e SU ionization features with mixed atomic characters. Such 2h1e, ionization channels have previously been observed from triiodide in aqueous and ethanol solutions[28,144,160,163]. In the absence of electronic correlation effects, the energetics of the 2h1e SU peak positions can be approximated using the C and D absorption band transition energy from the UV-Vis measurements (Section 4.1). Adding the C-band UV-Vis transition energy to the BEs associated with peak 3, 4, and 5 yields ∼57.7 eV, ∼59.1 eV, and ∼60.6 eV, with the latter two peak positions being close to the energetics of SU peaks 6 and 7 in the experimental $4d^{-1}$ XPS spectra. The associated SU peak position of Peak 3, ∼57.7 eV, would spectrally overlap with the high energy side of peak 5. Based on these estimations, peak 6 and 7 are correspondingly assigned to $4d^{-1}$, $(54a'/23a''/56a',\ n)^{-1}$, $(57a',\ \sigma^*)^1$ SU ionisation processes, with production of the Ω=$\frac{5}{2}$ and $\frac{3}{2}$ states of the $I^{\bullet}_{3(aq.)}$ radical. These 2h1e peak positions are found to be ∼3.5 eV higher in BE than the analogous 1h XPS peaks.

The local environment of the I atoms in $I^{-}_{3(aq.)}$ are different, resulting in chemical shifts as well as different charge re-organization effects following ionization. This leads to the situation where the valence excitation energies associated with the SU event are also I-atom-dependent. Such effects are highlighted in the calculated SU features of the I 4d core-level ionization spectra, where the results shown in Figure 4.7 considered additional predominant $(54a'/23a''/56a',\ n) \rightarrow (57a',\ \sigma^*)^1$ valence excitations to produce electronically excited $I^{\bullet}_{3(aq.)}$ states.

The calculations and experimental spectra indicate that the 2h1e SU ionization channels are due to the *t* I-atoms appear at 3.5±0.2 eV higher BEs with respect to the corresponding 1h features. On the other hand, the 2h1e SU ionisation channels of the *i* and *c* atoms are BE-shifted with respect to the 1h peaks by +5.0±0.2 eV and +1.7±0.2 eV, respectively. The average excitation energy is ∼3.5 eV, as expected from the UV-Vis measurement. The energetic separation of peak 6 and 7 of ∼1.7 eV is then primarily associated with the spin-orbit splitting of the ionized I $4d_{5/2}$ and I $4d_{3/2}$ atomic energy levels.

Note that the *i* and *c/t* 1h I atom 4d ionisation channels have similar chemical shifts of 1.4-1.6 eV. This results in significant spectral overlap within the I $4d^{-1}$ core level spectra. The I $4d^{-1}$ calculations also indicate that the BE difference between the main 1h and 2h1e SU PE bands should decrease when moving from the asymmetric **Lin** to the **Bent** molecular geometry (see the red and blue curves in Figure 4.7a). Considering the 1h and 2h peak separations, the calculated spectrum of the **Bent** structure is in better agreement with the experiments. However, an less clear behavior is observed when the main and SU peak intensities and relative positions are compared. This suggest that the aqueous anion adopts an intermediate geometry in

aqueous solution, where both **Lin** and **Bent** geometries are sampled in the fluxional aqueous environment.

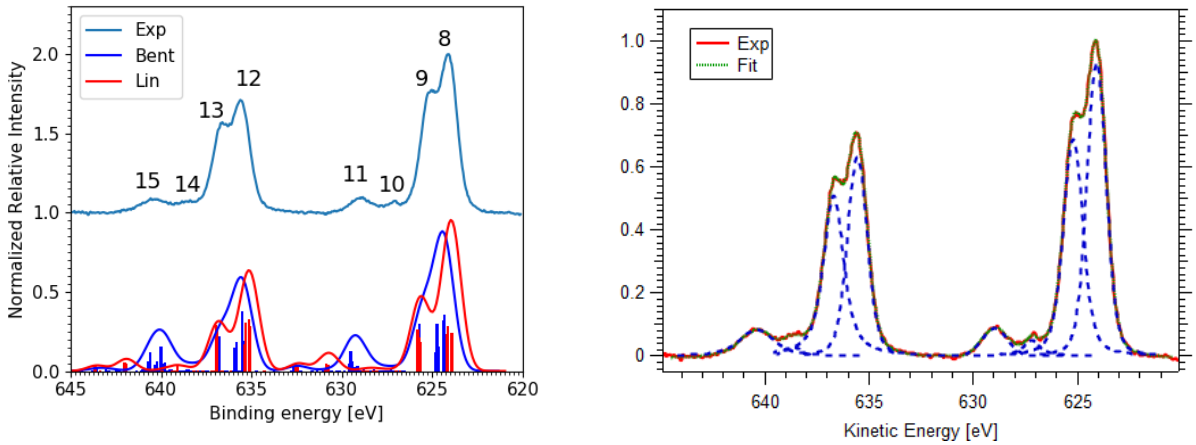

(a) I 3d core-level XPS spectra

(b) Associated Voigt fit

Figure 4.8: (Panel (a), top trace) Bulk-sensitive I 3d core-level XPS spectra of ∼180 mM $I^-_{3(aq.)}$ samples, recorded using a 1175 eV photon energy at the P04 beamline at PETRA-III, with an energy resolution of 200 meV. The calculated spectra for the **Lin** (red curve) and **Bent** (dark blue) geometries are shown in the bottom traces, left panel. (Panel (b)) The associated eight-component cumulative Voigt-profile fits to model the I 3d core level XPS spectra recorded are shown. The figures are reproduced with permission from Reference 167, licensed under the Creative Commons Attribution 3.0 Unported License.

I 3d^{-1} XPS Spectra The left panel of Figure 4.8 shows the background-signal-subtracted experimental and calculated I 3d^{-1} PE spectra of the $I^-_{3(aq.)}$ solute. Similar results were extracted from the data associated with the surface-sensitive experiments. In contrast to the five-features in the I 4d^{-1} core level XPS spectra, eight well-resolved PE peaks are present in the experimental I 3d^{-1} XPS spectra. The bottom section of Table 4.2 shows the BEs and the peak FWHMs extracted from the cumulative Voigt profile fits to the bulk-sensitive I 3d^{-1} XPS spectra along with peak assignments. A comparison between surface- and bulk-sensitive XPS datasets again indicates that the peak BEs and FWHMs does not differ within the uncertainty limits (see Section A.1 in Appendix). The calculated spectra are found to be in reasonable agreement with both the measured bulk- and surface-sensitive I 3d^{-1} spectra.

Eight PE peaks are observed in the experimental I 3d^{-1} spectra due to different I-atom chemical shifts, SU excitations as well as the photodetached spin-orbit splittings. The 3d^{-1} peaks are assigned as follows going from low to high BEs. Peaks 8, 9, 10 and 11 are related to the $\Omega = \frac{5}{2}$ final spin-orbit states and are assigned to the *i* and *t* 1h, *c* 1h, *c* 2h1e SU, and *i* and *t* 2h1e SU ionisation channels, respectively. The higher BE Peaks 12, 13, 14, and 15 in the I 3d^{-1} spectra are the associated $\Omega = \frac{3}{2}$ spin-orbit state analogues.

The I 3d^{-1} XPS spectra exhibit a notable ∼11.5±0.2 eV spin-orbit splitting of the $I^\bullet_{3(aq.)}$ radical final states. Each spin-orbit component displays a secondary splitting of ∼1.1±0.1 eV. According to the spectral simulations, this is related to the chemical shifts between the 1h ionization channels of the different I-atoms, denoted as the *t* and *i* atoms (Peaks 8 and 12) and the *c* atoms (Peaks 9 and 13). The **Lin** geometry calculated spectra highlight a prominent splitting, with a 1.5 eV peak separation. In addition, an unresolvable 0.2 eV chemical shift is predicted between the *i*- and *t*-atom 1h ionisation signatures.

As a result, the spectra highlights the spectral overlap of the *t*- and *i*-atom 1h peaks (Peaks 8 and 12) and two-fold higher intensities are seen than for the higher BE *c*-atom features (Peaks 9 and 13). The **Bent** structure calculations predict fully merged atomic ionization signatures and predict peak separations of about 1.3 eV, 0.9 eV, and 0.4 eV for the *c*–*i*, *c*–*t*, and *i*–*t* I-atoms, respectively. However, when the calculated spectrum is

convoluted with a Gaussian profile to match the spectral broadening in the experimental spectrum, a merged, asymmetric lineshape is observed. Similar integral ionization probabilities are notably calculated for the **Lin** and **Bent** geometry of the molecule. The simulated spectra also indicate a ∼0.4 eV chemical shift between the dominant PE peaks (Peak 8 and 12) associated with the two considered simulated geometries.

The 1h peak separations between the experimental $3d^{-1}$ features – Peaks 8 and 9 and Peaks 12 and 13 – lie between the calculated 1h peak separations for the **Lin** and **Bent** geometries. The experimental peak intensity ratio is ∼3:4 for Peaks 9-to-8 and Peaks 13-to-12 and a reduced peak splitting is observed with respect to the **Lin** geometry calculations. The peak-intensity ratio and ionization yield in the simulated spectra suggests that the average $I^-_{3(aq.)}$ structure lies in between the **Lin** and **Bent** geometries. In combination with the I $4d^{-1}$ XPS spectral analysis, the I $3d^{-1}$ XPS results suggest that the average anion structure is seemingly closest to, but less symmetric than, the **Lin** case.

Similar to the I $4d^{-1}$ spectra, the I $3d^{-1}$ spectra also show a pair of SU features on the higher BE side of the spectrum, with a 1.8±0.3 eV peak separation. The SU peaks occur at BEs of ∼627.3 eV and ∼629.1 eV for the $\Omega = \frac{5}{2}$ (Peaks 10 and 11) and ∼638.7 eV and ∼640.5 eV for the $\Omega = \frac{3}{2}$ (Peaks 14 and 15) ionization channels in the bulk-sensitive I $3d^{-1}$ XPS spectra.

The average energy differences between the 1h and 2h1e features in the experimental spectra are ∼2.1 eV (Peak 9-10 / Peak 13-14), ∼3.1 eV (Peak 8-10 / Peak 12-14), ∼3.8 eV (Peak 9-11 / Peak 13-15), and ∼4.9 eV (Peak 8-11 / Peak 12-15). Similar to the $4d^{-1}$ XPS results, the bulk-sensitive average 1h-to-2h1e feature separation amounts to ∼3.4 eV, which is again in good agreement with the UV-Vis C-band transition energy, ∼3.5 eV. As a result, based on the theoretical simulations, the SU features are assigned to the $(54a'/23a''/56a',\ n) \rightarrow (57a',\ \sigma^*)$ valence SU excitations, accompanied by I $3d^{-1}$ ionization. The variance between the separation of the specific 2h1e-to-1h BE peak pairs are due to the local-environment-dependent chemical shift and valence charge redistribution following ionization.

The calculations also reveal that the 2h1e SU peak BEs and signal intensities depend on the solute geometric structure. Moreover, similar to the I $4d^{-1}$ spectra, the energetic separation of the SU features from the main bands is overestimated by the calculations. Based on the calculations, the lower BE features are ascribed to $3d^{-1}$, $(54a'/56a',\ n)^{-1}$, $(57a',\ \sigma^*)^1$ 2h1e ionisation. The higher BE SU peaks are attributed to $3d^{-1}$, $(52a',\ \sigma)^{-1}$, $(57a',\ \sigma^*)^1$ processes, with an overestimated intensity; related SU features are noteably absent in the $4d^{-1}$ XPS spectra. The calculation indicates that peaks 11 and 15 are related to 2h1e ionization from the *i* I-atoms, located at 4.9±0.2 eV higher BEs than the related 1h ionisation channels in the experimental spectra. This is a similar BE increase as for the *i* atom 2h1e processes observed in the $4d^{-1}$ spectra in the experimental spectra. The 2h1e SU signals for the *t* atom occur at 3.7±0.3 eV higher BE than the 1h counterparts, correlating with the lower-BE ranges of Peaks 11 and 15. This is again consistent with the I $4d^{-1}$ spectral assignments. These theoretical predictions and assignments are supported by the previous spectral assignments of Arbman *et al.*[254], based on their I_3^- in ethanol solution XPS data, where the I $3d^{-1}$ 2h1e SU signals are said to arise from the *t* I-atoms. The calculations also predict significantly lower intensities and BEs for the c I-atoms 2h1e ionization signals compared to the *i*, *t* SU peaks in the **Lin** and **Bent** geometries. The lower BE *c* I-atom SU signals are ascribed to charge redistribution effects following the local photoionisation process and indicate that such ionization channels may be responsible for peaks 10 and 14 in the $3d^{-1}$ spectra. These weak signals occur at 1.8±0.2 eV higher BEs than their corresponding 1h features, which is also in good agreement with the $4d^{-1}$ spectral observations and assignments. The weak *c*-atom SU signal intensities in the **Lin** geometry simulated spectra are expected due to the parity forbidden nature of the linked valence transitions. Although, the reduction of symmetry in going to the **Bent** geometry may be expected to increase the intensity of such ionization transitions, the calculations considering the **Bent** geometry suggest

that these transitions remain suppressed. This implies that peaks 10 and 14 may have an alternative origin. Within the scope of current theoretical treatments, only speculation can be made about the possible origin of peaks 10 and 14. Hence, a firm assignment of these peaks require further theoretical developments and calculations, such as inclusion of explicit solvation as well as a more extensive sampling of the anion nuclear geometry space.

4.5 Electronic Energetics of Aqueous Triiodide and its Photoionized Radical State

Figure 4.9 shows the electronic energetics of aqueous triiodide and its photoionized radical state. Within a simple MO framework, the singlet ground state (GS) electronic structure of the $I^-_{3(aq.)}$ anion, with a bond-length-assymmetric **Bent** solute molecule configuration (C_s point group), is shown in Figure 4.9 A. The valence (unoccupied and occupied, built from the atomic 5p levels), 4d core, and 3d core MOs are shown, where the MOs are labeled according to their symmetries and the energetic ordering is based on calculations. The calculations are described in detail in reference 167. The energetics are referenced to the vacuum level of the solution* and energetically aligned with respect to the aqueous-phase electronic transitions and experimentally determined electron BEs.

The energetics of the occupied MOs were determined via the XPS measurements, where the BE of the lowest unnocupied 57a′(σ^*) MO is estimated by fitting the UV-Vis spectra as well as considering the ionization energy of the HOMO. A spin-orbit splitting of $\sim$0.8 eV is estimated for the HOMO to LUMO transition. The spin-orbit couplings are unresolved in the measured valence XPS spectra (as discussed above section 4.4.1), which is approximately corrected in Figure 4.9 to include the spin-orbit energetics in the excited radical ionization channels. Based on the expected 2:1 degeneracy of the spin-orbit split ground and valence ionized states and ignoring electron-electron correlation effects, the correction amounts to one-third ($\sim$0.33) of the spin orbit splitting, which is subtracted from the spin-orbit averaged valence vertical ionization energies extracted from Figure 4.6 and illustrated in Figure 4.9.

Single-active- and multi-active-electron ionization pathways of $I^-_{3(aq.)}$, and their correpsonding $I^\bullet_{3(aq.)}$ final states are illustrated in Figure 4.9 B, where the processes are denoted as 1h and 2h1e, respectively. In the multi-electronic, multi-reference $I^-_{3(aq.)}$ system, a variety of ionization processes can occur following X-ray photoabsorption. A number of final states can be accessed but just four of these are illustrated in Figure 4.9 B. The minimum ionization energies of the MOs are defined with respect to the 'vacuum level' (shown as a thick dashed black line) and correspond to radical formation in a $\Omega = \frac{3}{2}$ or $\Omega = \frac{5}{2}$ spin-orbit state following the valence or 4d/3d ionisation cases, respectively. The extracted spin-orbit excitation threshold of the photoionized radicals are +0.8 eV ($\Omega = \frac{1}{2}$), +1.5 eV ($\Omega = \frac{3}{2}$), and +11.5 eV ($\Omega = \frac{3}{2}$) for the valence (dashed dark red), 4d (dashed light purple) and 3d (dashed blue) ionization processes, respectively. The valence splitting is determined via UV-Vis measurements (neglecting electron-electron correlations) and the core-level splittings are determined via XPS measurements.

The red dots represent the MO populations, the dark purple arrows illustrate the photoexcitation processes and the grey arrows in Figure 4.9 denote the associated PE energetics. Figure 4.9 B highlights the ionization channels from an I 3d core-level to form a neutral $I^\bullet_{3(aq.)}$ radical in a ground $\Omega = \frac{5}{2}$ or excited $\Omega = \frac{3}{2}$ spin-orbit state. The left-side of panel B depicts single-active-electron ionization processes and the right-side depicts related multi-active-electron ionization processes. The multi-active-electron ionization processes

*The vacuum level is defined as the minimum energy that is required to liberate electrons from the aqueous solute MOs without any structural reorganization/changes to the solute or solvent molecules

involve core-electron ionization, similar to the single-active-electron ionization case, with additional valence excitation channels, $56a'(n) \rightarrow 57a'(\sigma^*)$, *i.e.* highest occupied to lowest unoccupied MO excitation. A single electron is ionized and two hole – 3d core and 5p valence (56a′) – electronically excited $I^{\bullet}_{3(aq.)}$ species are produced either in a $\Omega = \frac{5}{2}$ or $\Omega = \frac{3}{2}$ spin-orbit state. The multi-active-electron (2h1e) processes are driven by electronic correlation and orbital relaxation effects, leading to so-called configuration interaction satellite or SU state features in the photoemission spectrum[255–262]. The MO framework correspondingly fails to describe the aqueous triiodide photoionization processes. The associated electron-electron interactions and bound electronic transitions result in lower KEs of the measured I 4d/3d core electrons. The multi-active-electron, 2h1e features are lowered by ΔKE_{SU} in comparision with the single-active-electron, 1h ionization features, shown in panel B. Although, the 3d ionization channels are shown, similar ionization channels also occur for the 4d (and likely valence) ionization pathways.

4.6 I_3^- Molecular Bond-Length Asymmetry in Aqueous Solution

The calculated, isolated I_3^- I 4d photoionization spectra of Norell *et al.*,[160] show that the terminal, central, and ionic parts of the I_3^- molecule all participate in the 2h1e SU ionization processes. The calculated I 4d photoionization spectra were compared to the experimental solution-phase spectra recorded by Josefsson *et al.*[144] and used to quantify the solvent-induced nuclear geometrical structural asymmetry by comparing the SU and main PE peak intensities. However, the I 4d core-level PE spectra from aqueous LiI/I_2 solutions used by Josefsson *et al.* had Li 1s spectal contributions around a 60.6 eV BE, which coincides with the BE region associated with the I 4d SU ionization features. This prevented Josefsson *et al.* from determining accurate molecular asymmetry in such solutions. In contrast, in the measurements reported here, Na^+ counter ions were implemented, which allowed the SU-to-main peak ratio to be accurately determined.

Based on the procedure reported by Norell *et al.*[160], the average molecular symmetry of $I^-_{3(aq.)}$ can be assessed by comparing the relative peak intensities (peaks 6 and 7) of the 2h1e SU features with respect to those of the 1h ionization peaks (peaks 3, 4, and 5). The molecular asymmetry of the I_3^- anion in different solutions will correspondingly be quantified by dividing the total SU area by the total 1h peak area here. Based on the fit procedure described in Section 4.3, the fitted peak areas of all of the $I^-_{3(aq.)}$ XPS features were extracted. The peak areas of the 2h1e SU features in a given core-level spectra are added to get the total SU contrbutions, where as the peak areas of the 1h features are added to get the 1h contributions.

First, the $I^-_{3(aq.)}$ 4d aqueous solution signal levels are considered from the bulk-sensitive experiments performed in a Magic Angle detection configuration. In this case, a 8.6±1.4% SU-to-main-peak intensity ratio has been extracted. In the perpendicular detection configuration experiments, somewhat higher intensity ratios were extracted. As described in Section 4.1, 500 mM NaI, 250 mM I_2 and 350 mM NaI, 250 mM I_2 aqueous solution mixtures result in different amounts of $I^-_{3(aq.)}$. Nevertheless, within the experimental uncertainty limits, the SU-to-main peak intensity ratios extracted from these two solutions are found to be same, as shown in Table 4.3. Therefore, the SU-to-main peak ratios extracted from the different concentration mixtures were averaged. The averaged perpendicular geometry surface- and bulk-sensitive values are 14.6±3.5% and 13.0±1.3%, respectively for I 4d core-levels in aqueous solution. The I $4d^{-1}$ signal ratios collected under the different, Magic Angle experimental geometry are also shown in table 4.4.

The extracted ratios indicate that the I 4d SU electrons are more efficiently collected in the perpendicular configuration and similar solute geometries persist at the solution-gas interface as well as in the aqueous bulk. However, the relatively large uncertainty range associated with the surface-sensitive ratio extracted from the perpendicular geometry experiments is also noted. It may be that the final-state density and spectral

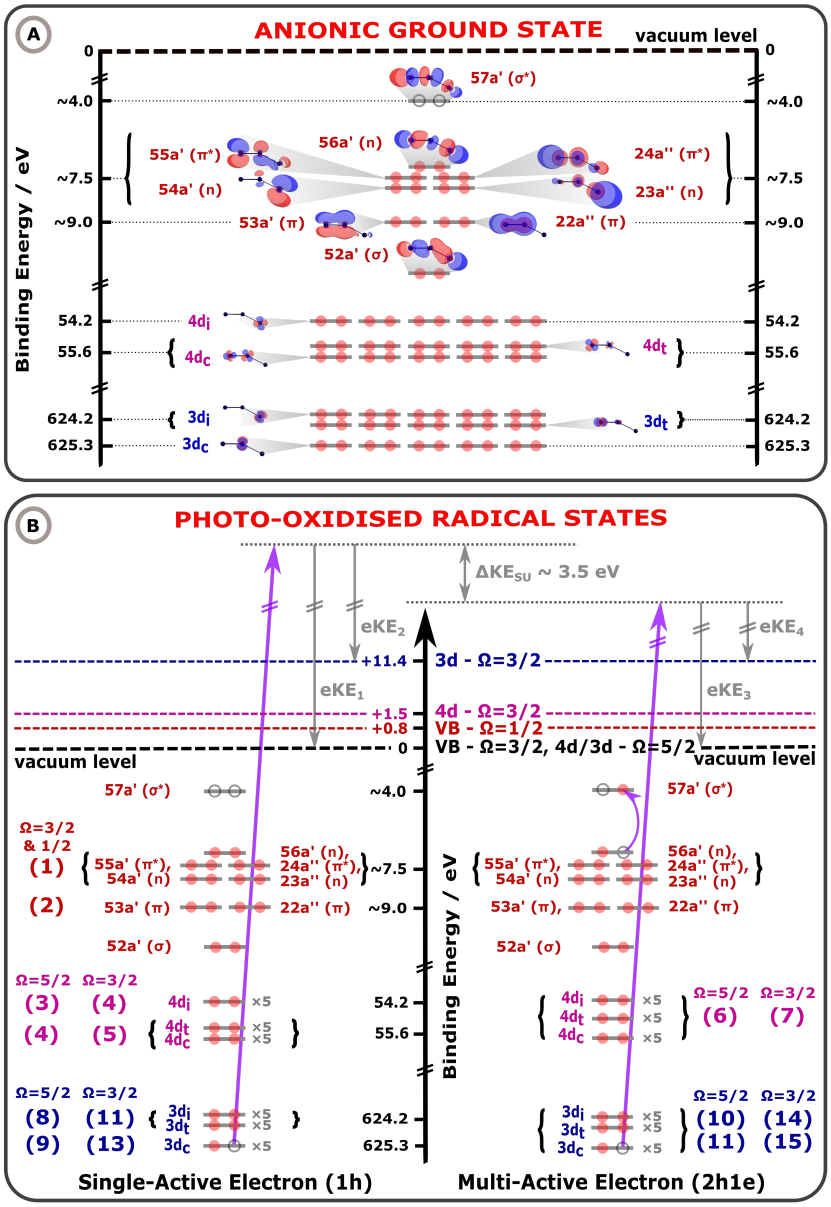

Figure 4.9: Molecular orbital (MO) diagrams of the $I^-_{3(aq.)}$ electronic ground-state (panel A) and exemplary photoionized states $I^\bullet_{3(aq.)}$ (panel B), collectively illustrating single- and multi-active-electron photoionization processes of an aqueous triiodide solute. The MO energetics have been constructed based on the UV-Vis absorption spectra, electron BEs, and photoemission peak assignments reported in this work. In panel A, the electronic ground-state MO energetics and electronic occupations (red circles) of the aqueous anion are depicted, assuming a minimum symmetry C_s point group, bent, asymmetric-bond-length $I^-_{3(aq.)}$ anion geometry. The ionization signature of both the $\Omega = \frac{3}{2}$ and $\Omega = \frac{1}{2}$ spin-orbit states of the $I^\bullet_{3(aq.)}$ radical are unresolved in the measured valence electron BEs, with a ~0.8 eV associated splitting estimated from the UV-Vis absoprtion spectra reported in Figure 2.11. Considering, the respective 2:1 degeneracy of the spin-orbit split final states, an energy of $\frac{0.8}{3}$ eV was subtracted from the measured valence BEs to approximate the lowest energy ionizing transitions to the $\Omega = \frac{3}{2}$ states. Panel B shows associated, exemplary photoionised states. On the left hand side, a 1h single-active-electron, core-ionization ($3d^{-1}$) process is illustrated. On the right hand side, a related final state is shown, as specifically formed via a multi-active-electron $3d^{-1}$, $56a'(n) \rightarrow 57a'(\sigma^*)$ core-ionization process. This results in a 2h1e photoionized species and a lower KE/higher BE PE with respect to the process shown on the left-hand-side of panel B. The spin-orbit excitation thresholds of the photoionised radical system, as determined in this work, are also shown in panel B. The lowest-energy spin-orbit state ionisation limits are illustrated by the thick, black, horizontal dashed line. The valence (+0.8 eV), 4d (+1.5 eV), and 3d (+11.5 eV) spin-orbit excitation thresholds of the radical are respectively represented by the horizontal dark red, light purple, and blue dashed lines towards the top of the panel. The bracketed numbers to the left and right of the MOs in panel B highlight the assignments of the numbered peaks in Figures 4.6, 4.7 and 4.8. The figures are reproduced with permission from Reference 167, licensed under the Creative Commons Attribution 3.0 Unported License.

Table 4.3: Ratio between multi-electron (2h1e, SU) and single-active electron (1h) ionization contributions to the $I^-_{3(aq.)}$ core-level XPS spectra. The corresponding experimental spectra were recorded under a perpendicular electron collection geometry at BESSY II.

Experiment	Aqueous surface	Aqueous bulk
I 4d core (250 mM/500 mM)	15.1±2.0%	12.2±1.2%
I 4d core (250 mM/350 mM)	14.2±4.5%	14.7±1.5%
I 3d core (250 mM/500 mM)	16.2±1.8%	12.3±2.5%
I 3d core (250 mM/350 mM)	20.0±2.4%	12.3±1.9%

Table 4.4: Ratio between multi-electron (2h1e, SU) and single-active electron (1h) ionization contributions to the $I^-_{3(aq.)}$ core-level XPS spectra. The relevent spectra were recorded under a Magic Angle collection geometry at PETRA III. The SU-to-main peak intensity ratios of the previously reported triiodide in ethanol solution spectra[144,254] are also reported. The I 3d and I 4d core level spectra from triiodide in ethanol solution were digitized and subsequently cumulatively fitted with Voigt profiles to extract the associated peak areas.

Experiment	Aqueous surface	Aqueous bulk	Ethanol surface	Ethanol bulk
I 4d core (210 mM/420 mM)	-	8.6±1.4%	5.3±0.8%[144]	
I 3d core (210 mM/420 mM)	17.2±1.3%	12.2±1.1%		8.9±0.6%[254]

overlap in the I $4d^{-1}$ spectra affects the extracted SU-to-main peak intensity ratios. Such spectral overlaps and the variations of partial ionization cross-section due to the different photon energies could obscure any geometrical changes between the different solutions and the probed regions within them.

Similar to previous, isolated I^-_3 anion computational studies[160], further simulations (including PCM effects) show I 4d SU-to-main intensity ratios of 11.2% for fully symmetric linear, 13.1% for the **Lin** geometry, 14.4% for a slightly bent (165° bond angle) variant of the **Lin**, and 20.5% for the **Bent** geometry molecular structures[253]. This result indicates that the increased SU-to-main intensity ratio correlates with the descension of molecular symmetry. The increase of intensity ratio in the calculation is associated with the involvement of other doubly-occupied 5p-like MOs in the 2h1e excitation as well as the increasing role of the *c* I 4d orbitals in the ionization processes. For a fully symmetric structure, the SU transitions from the *c* I-atom are symmetry forbidden. Comparing the theoretical and experimental SU-to-main peak ratios, the bulk-sensitive experimental results are in better agreement with the calculated spectrum associated with the **Lin** geometry configuration. However, the **Bent** geometries may also be sampled, which would be in agreement with the structure reported by Jena *et al.*[28] and the theoretically predicted GS potential energy surface[253].

Furthermore, extended ionization calculations, beyond the sudden approximation, highlights similar 1h and 2h1e relative ionization cross-section at 150 eV and 600 eV photon energies. We have seen that comparison between the 1h main and 2h1e SU core-level ionization peak intensities can provide potential information regarding the $I^-_{3(aq.)}$ solute molecular symmetry. Unfortunately such information was totally inaccessible in the valence XPS measurements and potentially obscured in the I $4d^{-1}$ core-level XPS measurements due to spectral overlap of the photoexcited electronic states. Due to the larger spin-orbit splitting, single- and multi-active-electron XPS features are more readily resolved in the I $3d^{-1}$ core-level spectra in comparison with the I $4d^{-1}$ core-level spectra.

The relative peak intensities between the 1h and 2h1e peak features in the I $3d^{-1}$ spectra will now be considered to investigate the $I^-_{3(aq.)}$ anion geometric structure. The 2h1e SU and 1h main PE features ratio in the bulk-sensitive $I^-_{3(aq.)}$ I 3d XPS spectra was determined to be 12.2±1.1%, by analysing the fit components measured in Magic Angle configuration, shown in Figure 4.8. In the surface-sensitive I $3d^{-1}$ XPS

results, measured under similar conditions, a significantly higher ratio of 17.3±1.3%. Previously recorded XPS spectra of I_3^- in ethanol[144,254] were digitized and SU-to-main peak intensities ratios have been extracted and tabulated in Table 4.4. Note that, unlike in the raw $I^-_{3(aq.)}$ data reported here, there are no residual I^- contributions in the I_3^- in ethanol solution spectra reported in References 144,160 and 254.

Considering similar ionization cross-sections at low and high ionizing photon energies, the observed peak intensity ratio differences in the Magic Angle results further indicate that the triiodide molecule may be more asymmetric at the aqueous solution-gas interface compared to in the bulk. Similar intensity ratios and surface versus bulk differences are also found in the aqueous-phase data recorded in the perpendicular geometry configuration. Similar to the I 4d data, the SU-to-main intensity ratios for the I 3d data were averaged for the perpendicular geometry experimental conditions, the extracted ratios are 18.1±2.1% and 12.3±2.2% for the aqueous surface- and bulk-sensitive experiments, respectively. This further implies that a more asymmetric anion geometry may persist at the sample surface.

The SU-to-main I $3d^{-1}$ peak intensities extracted from the calculations are about 13.4% and 26.6% for the **Lin** and **Bent** structures, respectively. The calculated SU-to-main peak ratio associated with the **Lin** structure is, therefore in better agreement with the experimental XPS spectra, suggesting a near- linear geometry occurs in the aqueous bulk. Similar to the I $4d^{-1}$ case, the overall ionization probabilities are calculated to be near-equivalent at the **Lin** and **Bent** geometries. This further suggests that the underlying geometrical structural distribution of the anion has asymmetric bond-lengths and a near-linear geometry. The surface-sensitive data yields a higher SU-to-main peak intensity ratio that lies between the calculated ratios for the **Lin** and **Bent** geometries and the ratio is higher in comparison to the bulk-sensitive experiments. Based on this observation and assuming equivalent relative 1h and 2h1e ionization cross-sections at both 725 eV and 1175 eV, it is tentatively suggested that the $I^-_{3(aq.)}$ anion is more asymmetric, and perhaps bent, on average, at the aqueous solution interface.

The SU-to-main peak intensity ratio errors summarized in Table 4.3 and 4.4 were calculated by propagating the uncertainties in determining the residual I^- and converted I_3^- concentrations of the different solutions and the errors associated with the fits to the data. Initially, the SU-to-main peak intensity ratios were determined by considering the maximum or minimum uncertainty limits of the extracted solute concentations determined via the UV-Vis measurements. The I_3^- signal variations related to the 420 mM NaI, 210 mM I_2 aqueous solution mixture are shown in Figure 4.10, highlighting the maximum (Max. - 211 mM), mean (Mean - 188 mM), and minimum (Min. - 165 mM) $I^-_{3(aq.)}$ concentrations for the bulk-sensitive core-level I 4d (left panel) and I 3d (right panel) XPS spectra recorded at PETRA III. A similar peak fitting method described in Section 4.3 is also applied to the maximum, mean and minimum concentrations in the $I^-_{3(aq.)}$ difference spectra. Such maximum and minimum concentration $I^-_{3(aq.)}$ spectra are obtained by subtracting the $I^-_{(aq.)}$ background spectra scaled to the minimum and maximum concentrations associated with the uncentainty range of the $I^-_{3(aq.)}$ concentration determined from the UV-Vis analysis. For example, for the bulk-sensitive and Magic Angle configuration data, the maximum and minimum potential $I^-_{3(aq.)}$ concentrations are 185 mM and 169 mM, respectively, for the I 4d data recorded at PETRA III. In that case, the SU-to-main peak intensity ratios are respectively 9.2±1.4% and 8.3±1.3% for the maximum and minimum $I^-_{3(aq.)}$ concentrations, respectively. Again taking into account the maximum and minimum concentrations for $I^-_{(aq.)}$, a similar analysis was performed for the I 3d core-level XPS spectra. The corresponding ratios are 12.1±0.7% and 12.7±1.5%.

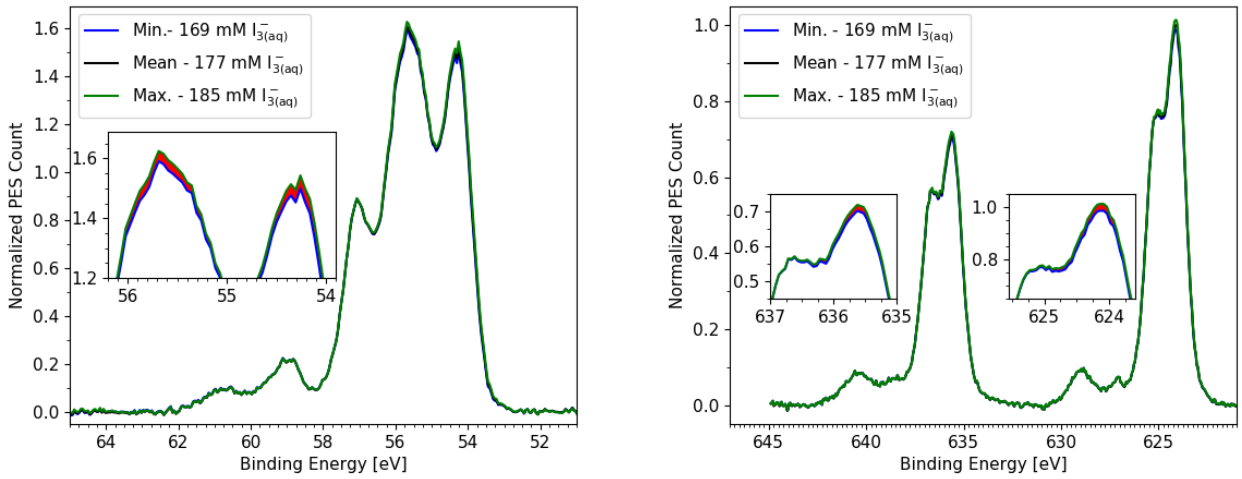

(a) Different intensity levels of I 4d XPS spectra

(b) Different intensity levels of I 3d XPS spectra

Figure 4.10: Different intensity levels- minimimum (min.), mean, and maximum (max.) -of the bulk-sensitive $I^-_{3(aq.)}$ core-level spectral features recorded at PETRA III. The upper and lower bound of the concentrations were determined based on the solute concentration uncertainties determined using UV-Vis spectroscopy. I 4d and I 3d results are presented in the panels (a) and (b), respectively. The red-shaded area denotes the effected regions of the spectral intensity variation where the $I^-_{(aq.)}$ and $I^-_{3(aq.)}$ spectral contributions overlap (red). The associated samples were prepared by mixing 210 mM of iodine with 420 mM of iodide. The figures are reproduced with permission from Reference 167, licensed under the Creative Commons Attribution 3.0 Unported License.

4.7 XPS Spectra of I_3^- in Aqueous and Ethanol Solution

The XPS results recorded from I_3^- in ethanol solutions,[144,254] and I_3^- in aqueous solutions will now be compared. The triiodide anion is expected to adopt less bond-length asymmetric configurations with tighter angular potentials, centred around 180°, in an ethanol solvent compared to in water[28,158].The surface-sensitive I $4d^{-1}$ core-level XPS spectra of I_3^- in ethanol solution recorded by Josefsson *et al.*[144] using a 100 eV photon energy at a Magic Angle configuration was digitized to enable a comparison with the aqueous-phase data reported here. Figure 4.11a shows such comparison.

Similar fitting routines as implemented with the aqueous-phase data were applied to the ethanol I_3^- I 4d XPS data of Josefsson *et al.*[144], Figure 4.11b) in order to explore the relative anion structural distributions. A SU-to-main peak intensity ratio of $\sim$5.3$\pm$0.8% was determined for the ethanol I $4d^{-1}$ spectra. The corresponding aqueous solution results are 14.6$\pm$3.5% and 13.0$\pm$1.3% for the I $4d^{-1}$ surface- and bulk-sensitive experiments, respectively. The significantly lower SU-to-main peak ratio observed from the ethanol solutions under the surface-sensitive conditions indicates that the observed aqueous and ethanol solution differences do not arise from the different experimental conditions implemented in the two studies. Rather, the collective experimental I $4d^{-1}$ results and SU-to-main peak ratios highlight a reduced I_3^- anion molecular symmetry in aqueous solution in comparison to an ethanol solution.

Similarly, bulk-sensitive, Magic Angle aqueous solution I $3d^{-1}$ data is compared to the bulk-sensitive ethanol solution data reported by Arbman *et al.*[254] in Figure 4.12. The ethanol-solution XPS spectra were recorded using monochromatised Al Kα radiation at $\sim$1486 eV. The 1h features of the triiodide PES spectra from both solvents look similar, with $\sim$-0.5 eV and $\sim$-1.0 eV relative chemical shifts observed for the $4d^{-1}$ and $3d^{-1}$ spectra, respectively. Both I $3d^{-1}$ spectra display a similar peak intensity ratio of about 3:4 for Peak 9-to-8 and

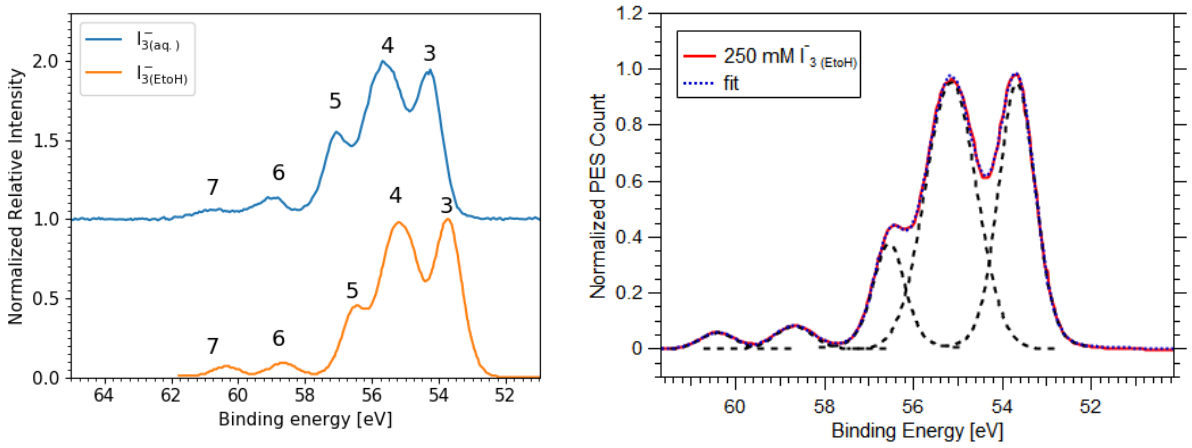

(a) Comparison of I 4d^{-1} core-level XPS spectra (b) Associated fit of ethanol XPS spectra

Figure 4.11: (Panel (a), top trace) Bulk-sensitive I 4d^{-1} core-level XPS spectra recorded at the P04 beamline (blue color, '$I^-_{3(aq.)}$'), and (bottom trace) the bulk-sensitive XPS spectrum recorded from an ethanol solution (orange curves, '$I^-_{3(EtOH)}$'). A spectral shift in peak 3 and different peak ratios (peak 3 and 4) are observed in the ethanol I 4d^{-1} core-level spectra in comparison with those from the aqueous solutions. (Panel (b)) The associated cumulative Voigt profile fit to the ethanol I 4d^{-1} core-level spectra. The top trace in panel (a) of the figure is reproduced with permission from Reference 167, licensed under the Creative Commons Attribution 3.0 Unported License. The panel (a) bottom trace and panel (b) of the figure are reproduced from Reference 144 using the webplot digitizer[196], with permission from the PCCP Owner Society.

Peak 13-to-12. Still, the I 3d^{-1} solute spectra from both solutions display notable spectroscopic differences, particularly, Peak 10 and 14 are present in aqueous solution spectra but are significantly suppressed, or perhaps absent, in the ethanol solution XPS spectra. This is another clear indication of a reduced molecular symmetry in the aqueous solution in comparison to in the ethanol.

Using a similar fitting procedure, exemplified in Figure 4.12b, the degree of asymmetry was quantified in the ethanol solution by calculating the SU-to-main intensity ratio of $\sim$8.9$\pm$0.6%, which is lower in comparison with the aqueous solution (12.2$\pm$1.1%) spectra recorded in similar experimental conditions. Similar to the I 4d^{-1} XPS results, the I 3d^{-1} data further indicates that the I_3^- anion adopts a more asymmetric molecular geometry, on average, in aqueous solution in comparison to in ethanol solution. This result is in full agreement with the theoretical calculations of Jena *et al.*[28], which specifically suggest that this increased assymmetry is related to a greater bond-length disparity, as opposed to a more bent solute geometry in aqueous solution.

The more pronounced spectral intensity of Peaks 10 and 14 in the I 3d^{-1} core-level spectra suggest an increased probability of otherwise improbable or forbidden transitions. The spectral simulations reported here indicate that ionization of the *c* I-atoms are responsible for those peaks, with such transitions becoming allowed in a bond-length assymmetric environment. The geometric bond-length and angular distributions are significantly broader in aqueous solutions in comparison to ethanol solutions[28]. An alternative assignment of the Peaks 10 and 14 may correspondingly be that a minor asymmetric component of a bimodal geometric structural distribution is present and ionized in aqueous solution or that there is a preferential ionization of two different structural components in the aqueous solutions corresponding to more or less symmetric geometries. Advanced molecular structural calculations and spectral simulations would be required to prove any such alternative explanations though. Still, the difference between the experimental aqueous- and ethanol XPS spectral components further highlight the role of the solvent in modifying the electronic as well as geometric structure of I_3^-. Particularly, in lowering the anion molecular symmetry.

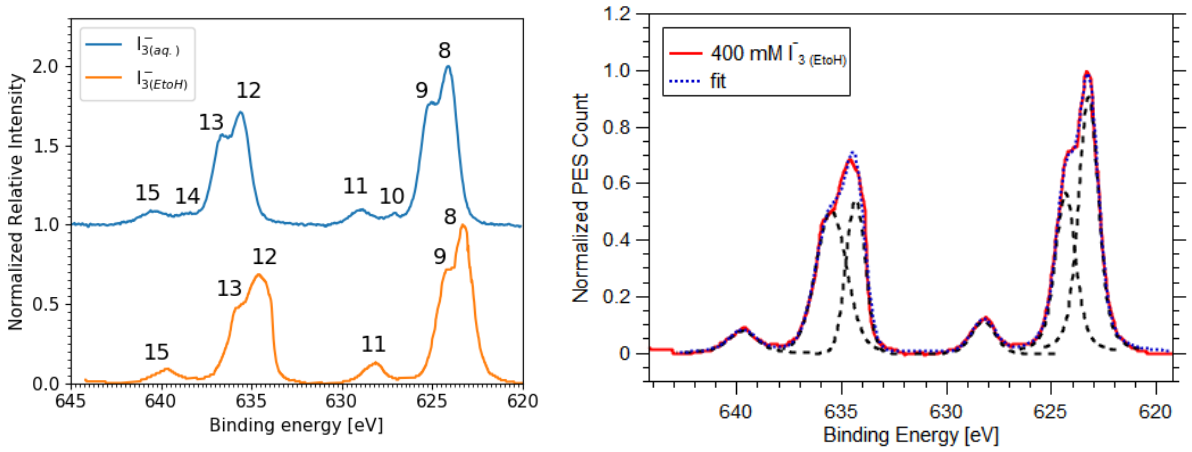

(a) Comparison of I $3d^{-1}$ core-level XPS spectra

(b) Associated fit of ethanol XPS spectra

Figure 4.12: (Panel (a), top trace) Bulk-sensitive, aqueous phase I $3d^{-1}$ core-level XPS spectra recorded at the P04 beamline (blue color, '$I^-_{3(aq.)}$'), and (bottom trace) the bulk-sensitive XPS spectrum from a ethanol solution (orange curves, '$I^-_{3(EtOH)}$'). (Panel (b)) The associated cumulative Voigt profile fit to the ethanol I $3d^{-1}$ core-level spectra. The top trace in panel (a) of the figure is reproduced with permission from Reference 167, licensed under the Creative Commons Attribution 3.0 Unported License. The panel (a) bottom trace and panel (b) of the figure are reproduced using the webplot digitizer[196] from Reference 254, Copyright (1983), with permission from Elsevier.

4.8 Reflections on the Geometric Structure of $I^-_{3(aq.)}$

The findings and inferences from the aqueous-phase XPS measurements and simulated spectra will now be discussed within the context of the previously reported I^-_3 literature. The particular focus is on the triiodide anion geometric structure and whether there is more general support that the $I^-_{3(aq.)}$ anion adopts an average, asymmetric bond length, but near-linear geometry, in aqueous solution.

4.8.1 A Critical Consideration of the $I^-_{3(aq.)}$ Literature

Sakane *et al.* studied I^-_3 in ethanol and water using extended X-ray absorption fine structure (EXAFS) spectroscopy[25]. The study concluded that average I-atom separations become smaller and increasingly broad bond-length distributions occur in going from aprotic, to ethanol, to methanol and aqueous solutions. A number of explanations are given for such broad bond-length distributions in moving from aprotic to an aqueous solvent, such as a greater degree of thermal motion, solvent hydrogen-bond-acceptor capacity, anion bond-length asymmetry, and anion-to-solvent partial charge-transfer. The increased I 4d and I 3d BEs in moving from an ethanol to aqueous solvent support the conclusions derived from the EXAFS results. Still, the room temperature solution-phase EXAFS experiments reported by Sakane *et al.* were not sensitive to longer range scattering processes between the *t* and *i* I atoms. Therefore, direct assessment of the GS equilibrium bond angle of the I^-_3 anion in alcoholic or aqueous solvents was not possible.

Resonant Raman studies on ethanol and aqueous triiodide solutions also highlighted solvent-induced symmetry breaking processes[156,263]. A number of theoretical studies have been carried out in order to explore the origin of the associated anion bond length asymmetries in ethanol and water[28,158,161,264]. However, the bending coordinate as well as equilibrium bond angle in these two solvents were not explored. Kim *et al.*[31] performed DFT simulations considering 32 water molecules using an explicit solvation shell model. The study notably highlighted a bent, optimised $I^-_{3(aq.)}$ geometric structure, with a bond angle of 172° as well as an asym-

metric bond-length. Later *ab initio* molecular dynamics simulations by Jena *et al.*[28] highlighted increasingly broad bond-length asymmetries as well as bond angle distributions when switching the solvent from ethanol, to methanol, and to water. Trajectory averaged bond angles of 170°, with broad angular distributions centered around 180°, were reported in their aqueous-phase simulations. Such results are in agreement with the calculations reported here, which were performed by taking into account implicit interactions between the solute and aqueous solvent, using a polarizable continuum model[253].

Several experimental studies also explored the photodissociation dynamics of I_3^- in a number of different solvents, including ethanol and water[24,32,33,35,265]. Kühne and Vöhringer performed ultrafast optical transient anisotropy experiments in protic solutions and considered their results within a framework of a bent equilibrium geometry of I_3^-. They populated the electronically excited C state and probed the signatures of the photoexcited and polarised I_3^-, I_2^-, and $I^\bullet$ species. Although, the authors had no information about the excited C state potential energy surface along the bond angle coordinate, they considered the measured Boltzmann-like, rotationally excited product-state distribution observed at earlier times to be generated from a bent equilibrium geometry of the I_3^- electronic GS. Follow-up studies were performed to explore the origin of a bent GS geometry[27]. A GS I_3^- anion bond angle of 153° was inferred *in ethanol* by weighting the early-time aniosotropy signals of the assumed diatomic fragment rotational distribution[24]. However, Kühne and Vöhringer also pointed out that their anisotropy measurements could be explained by a linear electronic GS and an electronically excited state with an anisotropic bond angle potential[24]. Interestingly, the predicted bond angle of 153° in ethanol exactly matched the angle reported by Kim *et al.*[31] in their photoexcited I_3^- *aqueous solution* X-ray scattering experiments. This bond angle of 153° was implemented in our **Bent** geometry XPS simulations.

In the X-ray solution scattering results of Kim *et al.*[31], a bond-length asymmetric, bent GS equilibrium configuration of I_3^- in water and a bond-length asymmetric linear geometry of I_3^- in methanol were determined. The XPS spectral simulations reported here were performed in both the **Bent** and **Lin**. As discussed above, the aqueous-phase XPS results reported here are most consistent with simulations that consider the **Lin** geometry. In the x-ray solution scattering experiment of Kim *et al.*[31], the authors recorded the I_3^- anions signals in aqueous, methanol, and acetonitrile solvents, with predominant scattering contributions from the solvent. The I_3^- anions were resonantly excited to the C state, leading to photodissocitation of the I_3^- anion, generation of transient I_2^- and $I^\bullet$ species, as well as vibrationally and likely electronically excited I_3^- anions[35]. The authors specifically considered the background-signal subtracted 100 ps pump-probe delay data and attempted to remove the solvent background signal by subtracting the non-optically-pumped x-ray scattering data from the optically-pumped x-ray data. The difference spectrum was then attributed to the scattering contributions from any excited I_3^- anions, its photodecomposition products, and directly or indirectly heated solvent molecules only. The overall x-ray scattering experimental results of Kim *et al.*[31] were then processed to extract the **Bent** $I_3{}^-$ geometry in aqueous solution, with the bond angle determined to be 153°. However, based on the uncertainties in the determined I-atom positions, a bond angle uncertainty of +27° and -13° can be inferred. Thus, the bond angle reported by Kim *et al.*[31] is also consistent with a linear geometry within the inferred uncertainty range. Moreover, it is here considered that the determined bond angle and associated uncertainty may be a property of the excited state I_3^- anion distribution in aqueous solution, as discussed below.

The non-optically-excited molecules should give a signature of the ground-state at equilibrium. However, such spectral information is deliberately subtracted from the optically pumped, pump-probe signal recorded at around 100 ps in the treatment of Kim *et al.*[31] Therefore, the remaining signals after the subtraction should be the contributions of the photoexcited $I^-_{3(\mathrm{aq.})}$, which are necessarily sensitive to the fate of the electronically

excited parent I_3^- anion, and would be in an electronically, vibrationally, and/or chemically excited state, rather than in the equilibrated electronic GS. Considering the data analysis procedure and reported uncertainty limit in determining the geometric structure, it is suggested that there is in fact little evidence for a bent $I_{3(aq.)}^-$ anion distribution under equilibrium conditions. Therefore, it is also suggested that the reported I_3^- bond angles of 153° in ethanol[24] and aqueous[31] solutions are related to the condition where the triiodide molecule is resonantly photoexcited to its dissociative, electronically-excited C-state. That is, the inference of the non-linear bond angle found in the ethanol data analysis of Kühne and Vöhringer[24] may, as the authors state, alternatively be ascribed to a bent electronically excited state. Furthermore, the bent geometries determined in the aqueous-phase pump-probe x-ray scattering experiments of Kim *et al.* can be related to any excited-state species with lifetimes exceeding 100 ps, such as fragment species trapped within the solvent cage in rovibrationally excited states and/or recombined photoproducts formed in vibrationally excited states with bent geometric structures.

4.8.2 Proposed Geometry: Asymmetric Linear $I_{3(aq.)}^-$ Anion

Based on the UV-Vis and XPS experimental and theoretical results reported here, as well as the previously published literature, it has been inferred that the I_3^- anion predominantly adopts a bond-length asymmetric geometry in its electronic GS in protic solvents, consistent with the existing experimental and theoretical literatures. It is further suggested that an average near-linear I_3^- anion geometry pervades in the bulk of an aqueous solution, in contrast to previous studies that have claimed that a bent structure dominates in aqueous solution. The situation regarding a bent GS equilibrium geometry of the anion cannot yet be settled. However, as notable ambiguities still remain in relation to previous suggestions that the I_3^- anion has a bent GS equilibrium geometry in ethanol and aqueous solutions. Although the results reported here support a bond-length asymmetric, near-linear $I_{3(aq.)}^-$ geometry, our interpretation based on the experimental data and theoretical calculations and spectral simulations cannot simply discard the previously suggested bent geometry with an asymmetric bond-length configuration in water.

Spectral simulations of the explicitly hydrated I_3^- system could be performed to resolve the uncertainties surrounding the I_3^- GS equilibrium geometry, particularly with finer sampling of the nuclear geometric coordinate space. Simulated results could than be tested against existing infrared spectroscopy experiments[164] and perhaps more modern multi-dimensional variants[266–268]. These findings raise a number of questions regarding the molecular structure of the anion, $I_{3(aq.)}^-$. More expansive theoretical calculations would be required to explicitly address partial, interfacial hydration and its effects on the molecular structure in order to explain the origin of more asymmetric electronic GS I_3^- anion geometries at the aqueous-gas-phase interface in comparison to the aqueous bulk. A better understanding of the interfacial I_3^- molecular structure as well as any differences in the anion's interfacial chemistry could be attained based on the spectral simulations of the XPS data reported here. Moreover, the potential energy surface of the $I_{3(aq.)}^-$ optically-bright C and D electronically excited states and their angular anisotropies would be required to further support the inferences reported here regarding the equilibrium GS molecular geometry in comparison with those inferred in pump-probe studies[24,31]. Additional interfacially-sensitive, sum-frequency generation vibrational spectroscopy experiments[269,270] could also be performed to improve our understanding of the $I_{3(aq.)}^-$ anion structure at the aqueous interface.

4.9 Summary of the XPS Studies on the Aqueous Triiodide Anion

Surface- and bulk-sensitive LJ-XPS experiments on $I^-_{3(aq.)}$ were presented. The XPS measurements were combined with *ab-initio*-based electronic structure calculations and spectral simulations, allowing the influence of electronic correlation and geometric structural effects on the aqueous-phase electronic structure in the $I^-_{3(aq.)}$ anion to be identified. The important findings of the XPS studies are:

I UV-Vis absorption spectroscopy has been applied to determine the $I^-_{2(aq.)}$-to- $I^-_{3(aq.)}$ conversion efficiency and associated solution concentrations of of the studied triiodide aqueous solutions. Large excess concentrations of $I^-_{(aq.)}$ anions compared to $I_{2(aq.)}$ were required to fully convert hundred-mM concentrations of $I_{2(aq.)}$ into $I^-_{3(aq.)}$.

II The valence XPS results could be used to determine the lowest BEs of the $I^-_{3(aq.)}$ anion with respect to the local vacuum level. The experimental I $4d^{-1}$ and I $3d^{-1}$ XPS results were compared with theoretical simulations to assign the spectral features and indentify the single- and multi-active-electron photoionization channels. Combining electronic structure theory and spectral simulations with the present XPS studies allowed the aqueous-phase ionization energetics to be mapped and to produce associated molecular orbital diagram of aqueous triiodide.

III Comparison of the $I^-_{3(aq.)}$ XPS results with the simulated XPS spectra suggests that the valence ionization features are relatively insensitive to the anion's geometric structure, whereas, core-level I $4d^{-1}$ and I $3d^{-1}$ ionization features are more sensitive to the molecular structure.

IV Following the suggestions of Norrell *et al.*[160], the experimental and theoretical I $4d^{-1}$ and I $3d^{-1}$ SU-to-main peak intensity ratios have been calculated to probe the degree of molecular asymmetry in the $I^-_{3(aq.)}$ solutions. The measured SU-to-main peak intensities in aqueous solution are higher compared to the SU-to-mian peak intensities in ethanol solutions. Similar to the I $4d^{-1}$ results, the I $3d^{-1}$ results indicate relatively higher SU-to-main intensity ratios in aqueous solutions compared to in the ethanol solutions.

V Combined experimental and theoretical results indicate that the $I^-_{3(aq.)}$ anion predominantly adopts a near-linear geometry in the bulk of an aqueous solution. Our results are also consistent with bent geometries being sampled in aqueous solution, but to a lesser degree compared to near-linear geometry. Upon critical analysis and considering the overall effects of optical excitation pulses on $I^-_{3(aq.)}$ anion solutions, this conclusion is also consistent with the previously reported literature on the solvated triiodide molecule.

VI The XPS measurements reported here from the 5p-like valence, 4d core and 3d core-levels also highlight a clear advantage of probing molecules in complex environments via deeper-lying core-levels. The inner shell XPS features are more energetically separated, allowing more differential spectral information to be obtained when probing molecular structure in aqueous solutions.

VII The studied effects are expected to remain isolable in dynamically-evolving, excited aqueous solutions. Thus, future time-resolved XPS experiments on this hydrated system hold the prospect to improve our underestanding of electron-electron correlation phenomena in condensed-phase chemical conversion processes. Indeed, the experimental and theoretical results presented here define many of the relevant spectral features and energy resolution needed to perform and interpret the results of $I^-_{3(aq.)}$ UV-photodissociation experiments performed using the liquid-microjet time-resolved PES techninque.

Chapter 5

Electronic Structure and Molecular Bonding of Aqueous Diazines

Chapter Objectives and Scientific Contributions:

1. Investigation of valence and core-level electronic structure on an absolute energy scale (Section 5.1).
2. Determination of the core-to-valence resonance transitions (Section 5.2), Auger electron emission contributions (Section 5.4), and outer valence ionization energies (Section 5.4) of the aqueous diazine molecules in aqueous solutions.
3. Comparison of the experimental results reported here with the previously reported gas- and aqueous phase studies[175,191,194,271].
4. Identification of solvent-induced changes by probing bonding character and atomic parentage, localization/ de-localization of valence band MOs, intra- and intermolecular charge re-arrangement in the aqueous solutions (Section 5.5).

The dynamic nature, shape, and energetics of the valence occupied, and unocuupied MO's can be considered to determine whether chemical reactions occur, and, if so, the outcome of the processes. The lowest ionization energy of the molecule generally provides information a system's the chemical reactivity, including the charge transfer processes, which are prevalent in aqueous solutions[272]. MO and, more generally, ionization energetics can be determined using XPS techniques, thus revealing valence and element-specific electronic structure information and potentially the driving forces behind chemical processes. This chapter provides a detailed report on the valence and core electronic structure of 500 mM aqueous diazine (pyridazine, pyrimidine and pyrazine) solutions in their ground electronic states. To achieve this, the samples have been studied using the liquid microjet based XPS technique. Initially, non-resonant XPS was implemented to investigate the surface- and bulk-sensitive valence and core-level PE spectra of the aqueous solute molecules. Later, Partial-Electron-Yield (PEY)-XAS and RPES measurements were performed to extract the core-to-valence transitions and further probe the valence electronic structure.

The associated sample preparations and experimental setup have already been discussed in Sections 3.2 and 3.3, Chapter 3. Briefly, 50 mM NaCl was added to the diazine solutions to minimize electrokinetic charging effects[243] and any photoionization-induced charging when the solutions were introduced to the sample chamber using the liquid jet technique. The U49-2 PGM-1 soft x-ray beamline at the synchroton radiation facility source BESSY II[168] was used to probe the electronic structure of the aqueous diazine molecules. The implemented liquid jet nozzle had a 30 μm inner diameter orifice and the sample temperature was stabilized

to $\sim$5° C. The X-ray radiation orthogonally intersected the laminar region of the flowing liquid sample and a hemispherical analyzer[235] was used to collect the photoelectrons.

5.1 Non-Resonant Excitation

5.1.1 Valence PES

Figures 5.1, 5.2, and 5.3 highlight the non-resonant valence photoelectron spectra of the aqueous pyrimidine, pyridazine, and pyrazine solutions, respectively. The left panels of the figures show surface-sensitive PES of the diazine solutions, as probed with a 150 eV photon energy. The right panels shows the bulk-sensitive PES, as recorded using a 680 eV photon energy. At these photon energies, the total energy resolution were $\sim$55 meV and $\sim$210 meV, respectively. For all of the surface-and bulk-sensitive experiments, valence band spectra of a 50 mM NaCl water solution were also recorded as a solvent signal reference spectra. The binding energies of the valence band PE spectra were BE calibrated using (pure) liquid water's $1b_1$ spectral position at 11.33 $\pm$ 0.04 eV[66,243] and then the $1b_1$ peaks of the solution and reference spectra were signal intensity normalized. The reference spectra were subsequently subtracted from the aqueous diazine valence band spectra in order to remove the water solvent background signals. In this case, two assumptions were made. First, the spectral weight of the solute (diazine) ionization features at the liquid water $1b_1$ BE were assumed to be negligible following non-resonant excitation and, second, the 500 mM solute was assumed not to perturb the water electronic structure.

All of the surface, bulk, and reference spectra were recorded at the magic angle at the U49-2 PGM–1 beamline at the BESSY II synchrotron radiation facility. The non-resonant valence solute spectral contributions are denoted by roman numbers in Figures 5.1, 5.2, and 5.3, *i.e.* I, II, III etc. These spectral peaks were identified by comparing the solution spectra to the solvent reference spectra. The red color spectra in all panels are those of the diazine aqueous solutions (500 mM diazine and 50 mM water), where the reference spectra of 50 mM aqueous NaCl solutions (*i.e.* nearly neat water) are plotted in a black color. The difference spectra are shown in green, blue, and purple for the pyridazine, pyrimidine, and pyrazine solutions, respectively. The difference spectra are multiplied by varying factors to better visualize the associated solute signals. The difference spectra shows positive and negative signal contributions, which are highlighted by red and grey color-filled plots. The negative signal contributions arise from the oversubtraction of the solvent signal spectra after normalization to the pure liquid-phase $1b_1$ feature height. The associated spectral positions of the negative spectral features in the difference spectra may indicate solute ionization contributions, which are hidden under the liquid water ionization features, as will be discussed later in Section 5.4. In this section, solute valence ionization features (I, II, III), which do not overlap with the main liquid water PE signals will be discussed. Table 5.1 shows the associated BEs as well as the FWHMs extracted from the non-resonant analysis.

Pyrimidine: The non-resonant valence PE spectra of pyrimidine show three spectral contributions in the surface-and bulk-sensitive PE measurements, see Figure 5.1. The first peak, denoted I, is associated with the HOMO, $(7b_2, n_N)^{-1}$ ionization contribution around $\sim$9.6 $\pm$ 0.04 eV, specifically in the surface-sensitive background-corrected experiments. This non-bonding type MO is associated with the nitrogen lone-pair electrons. Peaks II and III are found in pyrimidine around $\sim$20.5 $\pm$ 0.1 eV and $\sim$24.2 $\pm$ 0.2 eV. These are associated with the $(6a_1)^{-1}$ and $(5b_2)^{-1}$, and $(4b_2)^{-1}$ ionization channels, based on previous gas-phase studies, and are thought to possess σ-bonding character[176]. The extracted BEs of peak II and III are also close to the BEs of the atomic C 2s (19.39 eV) and N 2s (25.41 eV) ionization features[245,275]. Therefore

Table 5.1: Valence and core (N 1s and C 1s) electronic BE's and peak FWHM's, as extracted from the non-resonant XPS measurements performed at BESSY II. Gaussian profile fits were applied to model the valence band features, whereas Voigt-profiles were applied for the core levels. The inhomogeneous broadening contributions, (Gausssian) spectral components of the Voigt-profiles of the core levels are shown in the table. The peaks were assigned based on the previously reported gas-phase studies[175,176,195,273] and the dominant spectral contributions are reported. Average gas-phase BEs of Peak I are shown in the table, which are taken from References 88,176,181,195,274. Further details are shown in Appendix B.1. For Peak II and III, only the dominant atomic characters are mentioned. More details are given in the main body of the text.

Mol.	Peak	Features	Aqueous Surface		Aqueous Bulk		Gas-phase
			BE (eV)	FWHM (eV)	BE (eV)	FWHM (eV)	BE (eV)
Pyridazine	I	$(8b_2, n_N)^{-1}$	9.35 ± 0.05	1.10 ± 0.10	9.30 ± 0.05	1.0 ± 0.03	9.29 ± 0.02[a]
	II	$(C\ 2s)^{-1}$	20.32 ± 0.06	1.20 ± 0.20	20.41 ± 0.06	1.6 ± 0.1	-
	III	$(N\ 2s)^{-1}$	24.86 ± 0.06	1.90 ± 0.20	24.88 ± 0.05	1.90 ± 0.20	-
	IV	$(C\ 1s)^{-1}$	291.20 ± 0.05	1.22 ± 0.05	291.10 ± 0.17	1.27 ± 0.07	291.4 ± 0.2[175] 290.7 ±0.2[175]
	V	$(N\ 1s)^{-1}$	405.54 ± 0.09	0.96 ± 0.10	405.62 ± 0.05	1.05 ± 0.03	404.88 ± 0.2[273]
Pyrimidine	I	$(7b_2, n_N)^{-1}$	9.60 ± 0.04	0.83 ± 0.03	9.57 ± 0.05	0.81 ± 0.10	9.72 ± 0.03[a]
	II	$(C\ 2s)^{-1}$	20.50 ± 0.06	1.10 ± 0.10	20.44 ± 0.10	1.20 ± 0.10	20.8[176]
	III	$(N\ 2s)^{-1}$	24.20 ± 0.04	1.30 ± 0.10	24.25 ± 0.16	1.10 ± 0.16	24.5[176]
	IV	$(C\ 1s)^{-1}$	291.86 ± 0.05 290.57 ± 0.07	1.33 ± 0.05 1.04 ± 0.06	291.68 ± 0.24 290.36 ± 0.16	1.40 ± 0.20 1.10 ± 0.24	292.4 ± 0.2[175] 292.0 ± 0.2[175] 291.1 ±0.20[175]
	V	$(N\ 1s)^{-1}$	404.96 ± 0.12	1.03 ± 0.06	404.88 ± 0.10	1.20 ± 0.07	405.2 ± 0.2[175]
Pyrazine	I	$(6a_g, n_N)^{-1}$	9.46 ± 0.04	0.87 ± 0.10	9.50 ± 0.04	0.95 ± 0.05	9.55 ± 0.07[a]
	II	$(C\ 2s)^{-1}$	20.34 ± 0.06	1.20 ± 0.17	20.54 ± 0.04	0.98 ± 0.08	20.7[176]
	III	$(N\ 2s)^{-1}$	-	-	23.60 ± 0.05	1.00 ± 0.10	24.1[176]
	IV	$(C\ 1s)^{-1}$	291.53 ± 0.10	1.10 ± 0.10	291.46 ± 0.05	1.10 ± 0.07	291.7 ± 0.2[175]
	V	$(N\ 1s)^{-1}$	405.30 ± 0.15	0.92 ± 0.10	405.10 ± 0.13	1.10 ± 0.07	405.6 ± 0.2[175]

[a] Average values, associated references and reported values are given in Appendix B.1

peak II and III are thought to have dominant C 2s and N 2s atomic character. In the isolated phase, due to the formation of molecular bonds via sp^2 hybridization, these features are blue- and red-shifted, respectively. Moreover, due to the H-bond formation in the aqueous-phase, peak II and III are found to be red-shifted compared to in the gas-phase.

Pyridazine: The non-resonant valence PE spectra of pyridazine also show three spectral contributions in the surface- and bulk-sensitive PE experiments, see Figure 5.2, similar to the pyrimidine case. Peak I is assigned to the HOMO, $(8b_2, n_N)^{-1}$, ionization contribution around ∼9.35 ± 0.05 eV. Like in the pyrimidine case, the HOMO is non-bonding type MO, associated with the nitrogen lone-pair electrons. Around ∼20.35 ± 0.10 eV, a small peak, peak II, appears as a high BE shoulder to the water $1b_2$. The other spectral contribution, peak III, is identified around ∼24.90 ± 0.06 eV. The FWHM is rather broad (∼1.90 ± 0.20 eV at FWHM) compared to peak I (∼1.10 ± 0.10 eV FWHM) and II (∼1.20 ± 0.20 eV FWHM). As was the case for pyrimidine, Peak II and III are associated with σ bonding MO's, and have likely dominant C 2s and N 2s atomic character.

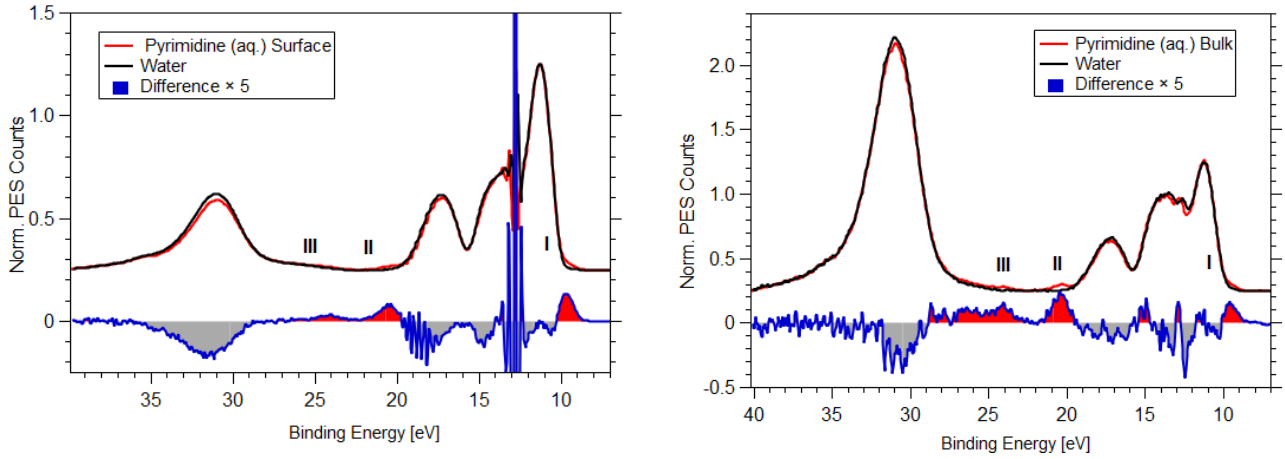

(a) Surface-sensitive valence spectra (b) Bulk-sensitive valence spectra

Figure 5.1: Non-resonant valence spectra of the 500 mM aqueous pyrimidine. The left and right panels show the result of surface- and bulk-sensitive XPS, respectively. The background-corrected XPS spectra of the 500 mM aqueous solute (blue) were obtained by subtracting the water spectra (black) from the aqueous pyrimidine solution spectra (red). More details are given in the main body of the texts.

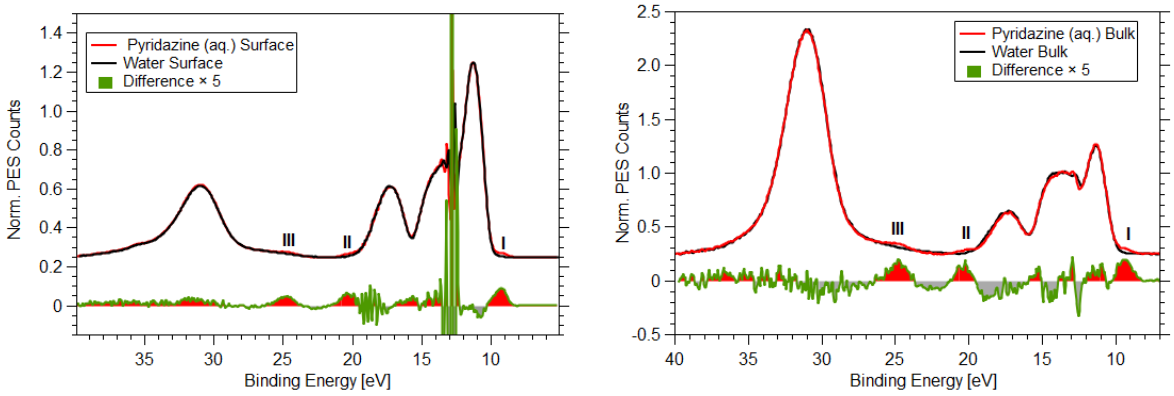

(a) Surface-sensitive valence spectra (b) Bulk-sensitive valence spectra

Figure 5.2: Non-resonant valence spectra of the 500 mM aqueous pyridazine solutions. The left and right panels show the surface- and bulk-sensitive XPS, respectively. The background-corrected XPS spectra of the aqueous solvent (black) were subtracted from the 500 mM aqueous pyridazine solution spectra (red) to isolate the solute contributions (green).

Pyrazine: Aqueous pyrazine solution valence PE spectra are shown in Figure 5.3 and highlight two solute spectral features, peaks I and II. In the bulk-sensitive experiments, there seems to be a weak signature of a less intense third peak, Peak III. Peak I is assumed to be the contribution from the HOMO, $6a_g$, non-bonding molecular orbital, occuring at a VBE of $\sim$9.50 $\pm$ 0.04 eV. Similar to the other diazines, this non-bonding type MO is formed by the nitrogen lone-pair electrons. The dominant contribution to the $\sim$20.4 $\pm$ 0.1 eV spectral feature, peak II, is assigned to $4a_g$/ $2b_{3g}$ ionization[176]. Similar to other diazines, peak II is thought to have dominant C 2s atomic character. A weak, third feature, peak III at 23.6 $\pm$ 0.05 eV appears in the predominantly bulk-sensitive measurements, see Panel B. According to a previous gas-phase study[176], this peak is assigned to the $2b_{2u}$ ionization contribution and, similar to the pyrimidine and pyridazine cases, has dominant N 2s atomic character. Although this peak is not so evident in the surface-sensitive case, this may just be due to the different relative water and pyrazine cross-sections at the 150 eV and 680 eV photon energies implemented to produce Figures 5.3a and 5.3b, respectively.

The experimental and theoretical valence electronic structure studies of isolated gas-phase pyrimidine and

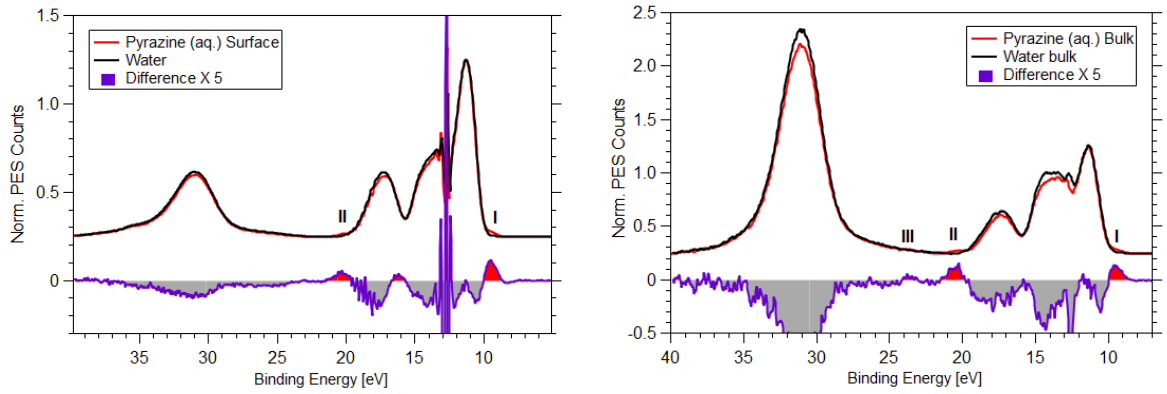

(a) Surface-sensitive valence spectra

(b) Bulk-sensitive valence spectra

Figure 5.3: Non-resonant valence spectra of the 500 mM aqueous pyrazine solution. The left and right panels show the surface-sensitive and bulk-sensitive XPS, respectively. The background–corrected XPS spectra of the aqueous solvent (black) were subtracted from the aqueous pyrazine solution spectra (red) to isolate the solute contributions (purple).

pyrazine molecules conclude that the spectral features at higher BEs (above 18 eV) cannot be described using a single-active-particle picture due to electronic correlation and the associated breakdown of the Koopmans' correlations[176]. Similarly, application of the single particle picture is also invalid in the higher BE range for pyridazine. Hence, such high-energy ionization process can not be assigned to single MO occupation changes, rather multiple MO's are contributing to the ionization process, and only the dominant contributions are mentioned.

The Peak I spectral features, observed in all of the aqueous diazine difference spectra, exhibit slightly assymmetric Gaussian spectral profiles. Such an asymmetric line shape might appear due to the asymmetry of the Frank-Condon profiles of the neutral and correlated cationic states in the aqueous diazines. Another reason for the asymmetry can be underlying contributions from multiple ionization channels and associated MOs. In the 9.0 – 11.8 eV BE range, at least four MO's and ionizing channels contribute to the gas-phase PE spectra[176]. Therefore, apart from having dominant contribution from the lowest-energy HOMO ionization process to the spectral feature denoted as I for all of the aqueous diazine solutions may have small contribution also from the HOMO-1 ionization process.

In the prepared solutions, the solvent concentration is $\sim$110 times higher compared to the solute concentration and thus, assuming equivalent ionization cross-sections, the non-resonant photoelectron spectra ares completely dominated by the water valence band features. With the goal of preferentially ionizing the solute molecules, RPES measurements have been performed to further investigate the valence band features of the aqueous diazines (see Section 5.4), most of which are hidden under the water solvent background signals in the non-resonant experiments.

5.1.2 Core-Level PES

The valence orbitals are formed by the linear combination of the atomic wavefunctions, with different weights of the atoms that form the molecule. Any change in the valence wavefunction due to the hydrogen-bonding environment will also influence the solute and solvent core-level wavefunctions. Core level ionization features, it becomes possible to site- and element-selectively probe the solute molecules and, in the case of the diazines, can provide background-free information about the core-electron BE chemical shifts in different environments, which is usually difficult to extract in the spectrally overlapped valence band region.

The N 1s and C 1s core level photoelectron spectra were recorded for all three aqueous-phase diazines. As discussed above, 150 eV and 680 eV photon energies have been used to record the valence PE spctra. Such photon energies generate electron KEs of ∼140 eV and ∼670 eV, resulting in predominantly surface- and bulk-sensitive XPS measurements. Photon energies were correspondingly chosen to record similar KE electrons following C 1s or N 1s core-level photoionization. As a result, 420 eV and 950 eV photon energies were used to record surface- and bulk-sensitive C 1s photoelectron spectra, respectively. The total energy resolutions of the 420 eV and 950 eV measurments were ∼85 meV and ∼305 meV, respectively. Similarly, in the N 1s core level XPS studies were performed with 540 eV and 1070 eV photon energies, respectively. At these photon energies, the total energy resolutions were ∼105 meV and ∼360 meV, respectively. The surface-sensitive C 1s and N 1s spectra were calibrated using the liquid water $1b_1$ spectral position at 11.33 ± 0.04 eV[66,243]. Alternatively, to calibrate the bulk-sensitive C 1s and N 1s spectra, nearly neat liquid water O 1s spectra and the reference BE position of 538.10 ± 0.05 eV[66,136] was used. Except for the bulk-sensitive pyrimidine and surface-sensitive pyrazine data, all other N 1s and C 1s spectra were recorded using the perpendicular electron detection geometry with respect to the incoming x-ray light. A constant-background subtraction has been applied to all of the core level spectra and then the spectral intensities were normalized to 1.

C 1s PES

Figure 5.4 shows the surface-and bulk-sensitive C 1s core-level photoelectron spectra and associated Voigt-profile fits to the three diazine solutions. Table 5.1 highlights the associated BE's as well as the FWHM's extracted from the Voigt-profile fits. The fitting components highlight the dominant contribution of the inhomogeneous broadening in the aqueous phase. Therefore, only the Gaussian FWHM's of the aqueous diazine fits are reported in the Table 5.1.1.

Pyridazine shows one C 1s XPS peak around ∼291.2 ± 0.1 eV, as obtained through a Voigt-profile fit, with a corresponding Gaussian spectral width of ∼1.2 ± 0.1 eV (FWHM). The pyrimidine C 1s XPS spectra (Figures 5.4a and 5.4b) show two peaks around ∼290.6 ± 0.1 eV and ∼291.9 ± 0.1 eV, with FWHM's of ∼1.3 ± 0.02 eV and ∼1.1 ± 0.1 eV, respectively, at the surface region. Considering the molecular structural symmetry, two and three C 1s XPS peaks can be expected (see Figure 1.1) and were observed in previous gas-phase studies of pyridazine[276] and pyrimidine[175], respectively. In gas-phase pyridazine, two peaks were observed at ∼291.4 eV and ∼290.7 eV. In gas-phase pyrimidine, the C_1 carbon was found to have an increased BE, with C_3 having the lowest. The BE's of the C_1, C_2, and C_3 atomic sites are ∼292.4, ∼292.0 and ∼ 291.1 eV[175].

The XPS results can be attributed to intramolecular charge re-arrangement and bond length changes in going from the gas to aqueous phase[271]. In aqueous pyrimidine, formation of hydrogen bonds and charge transfer processes lead to an increase and decrease in the C_2-N and C_2-C_3 bond lengths, respectively[191,194]. This may result in the BE's of the C_2 and C_3 atomic sites approaching each other. Moreover, inhomogeneous spectral broadening in the aqueous phase leads to overlap of the atom-specific PE spectra, resulting in only two resolvable spectral peaks from the aqueous pyrimidine solutions, as opposed to the expected three. Similar to aqueous pyrimidine, bond length changes and inhomogeneous broadening results in only one XPS peak in the aqueous pyridazine spectra. Thus, the ∼291.2 ± 0.1 eV BE is likely the average of the two spectral contributions in aqueous pyridazine. Thus, similar to aqueous pyridazine, the extracted BE ∼291.9 ± 0.1 eV is thought to be the weighted average BE, with contributions from the C_1 and C_2 atomic sites. In contrast, the spectral feature around ∼290.6 ± 0.1 eV BE is uniquely attributed to the C_3 atomic site.

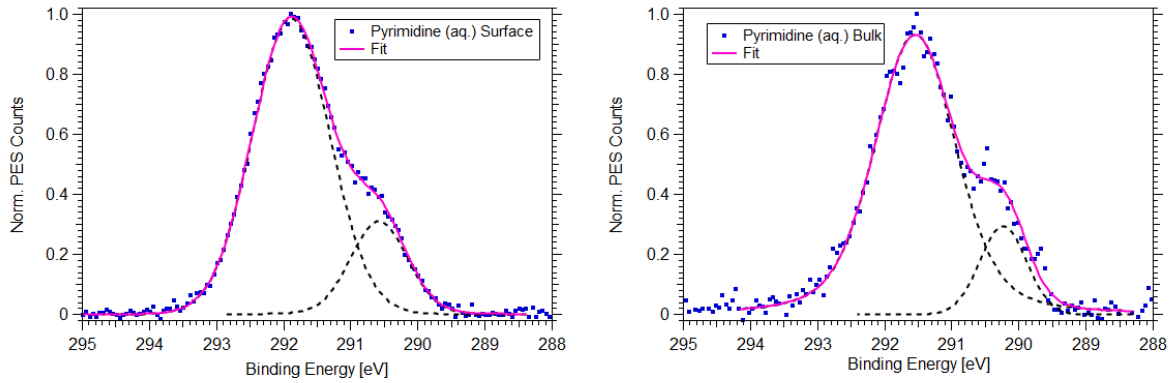

(a) Pyrimidine C 1s surface

(b) Pyrimidine C 1s bulk

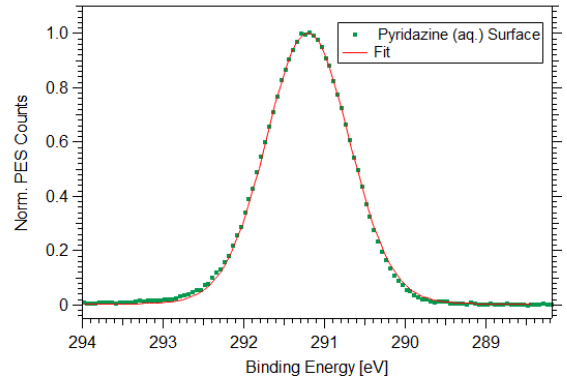

(c) Pyridazine C 1s surface

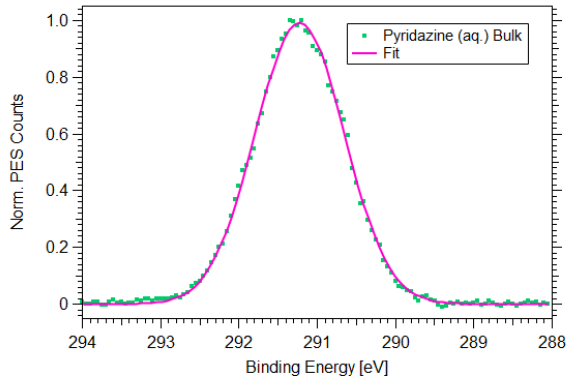

(d) Pyridazine C 1s bulk

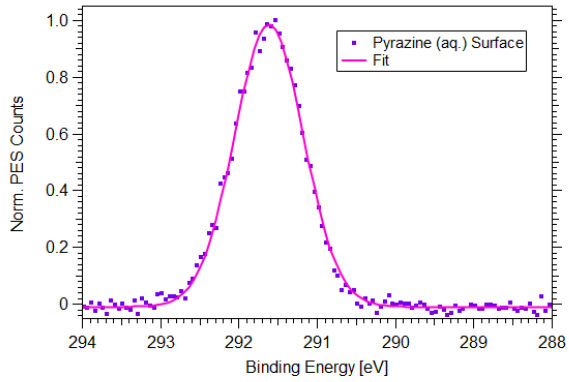

(e) Pyrazine C 1s surface

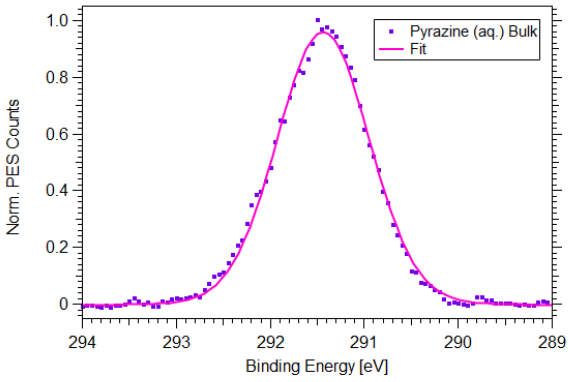

(f) Pyrazine C 1s bulk

Figure 5.4: Non-resonant C 1s XPS spectra of the 500 mM aqueous pyrimidine (top row), pyridazine (middle row), and pyrazine (bottom row) solutions recorded at BESSY II. The left figure panels show the surface-sensitive results recorded using a 420 eV photon energy and the right panels show the bulk-sensitive spectra, recorded using a 950 eV photon energy. The purple-color curves show the associated fits to the data.

The molecular structural symmetry of pyrazine suggest that only one C 1s PE spectral feature should appear, due to the expected four equivalent carbons. In the gas phase, only-one peak is observed around $\sim$291.7 $\pm$ 0.2 eV. A PE peak at $\sim$291.5 $\pm$ 0.1 eV with a FWHM $\sim$1.1 $\pm$ 0.1 eV is found, via Voigt-profile fits, in the aqueous-phase XPS spectra, which is red-shifted compared to the gas-phase BE. Similar intra- and intermolecular charge re-arrangement and bond length distortions are predicted to occur, as for the other isomers, in the aqueous pyrazine solution[194]. The single C 1s PE peak in aqueous pyrazine suggests the measured C 1s core-level XPS spectra are relatively insensitive to any solvent-induced molecular bond length distortions.

N 1s PES

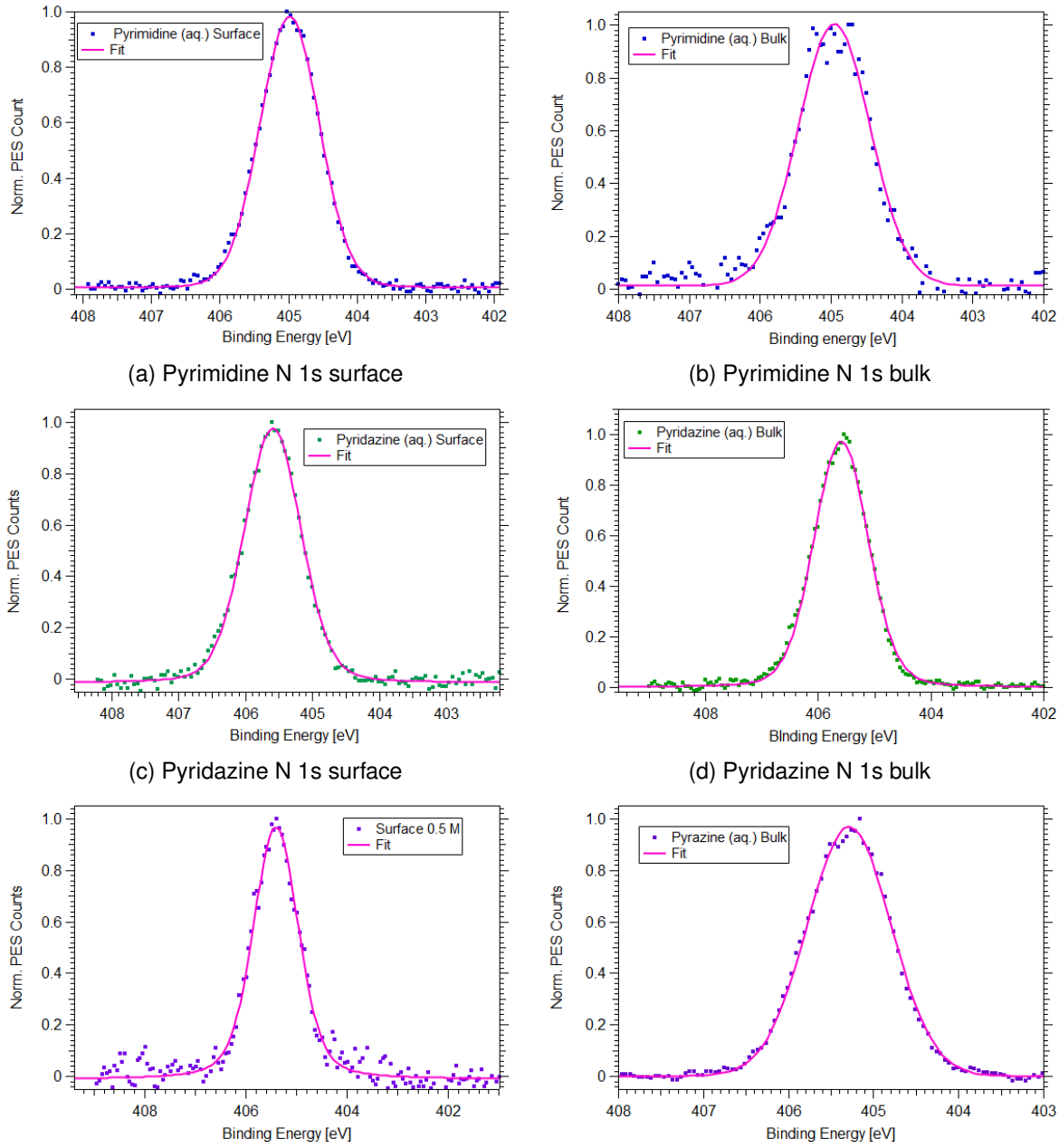

(a) Pyrimidine N 1s surface

(b) Pyrimidine N 1s bulk

(c) Pyridazine N 1s surface

(d) Pyridazine N 1s bulk

(e) Pyrazine N 1s surface

(f) Pyrazine N 1s bulk

Figure 5.5: Non-resonant N 1s XPS spectra of the 500 mM aqueous pyrimidine (top row), pyridazine (middle row), and pyrazine (bottom row) solutions recorded at BESSY II. The left panels show the surface-sensitive results recorded using a 540 eV photon energy and the right panels show the bulk-sensitive spectra recorded using a 1070 eV photon energy. The purple-color curves show the associated fits.

The left and right panels in Figures 5.5 show the surface- and bulk-sensitive N 1s core level photoelectron spectra of the 500 mM aqueous diazine solutions. Based on the symmetry of the isolated molecules, see Figure 1.1, Chapter 2, single N 1s spectral peaks are expected from all of the diazine molecules. As with the C 1s spectra, these peaks are modelled by Voigt profiles. Table 5.1 highlights the associated BE's as well as the FWHM's, extracted from the fits. Similar to the C 1s results, only the Gaussian FWHM components of the aqueous diazine fits are reported in the Table 5.1.1 due to the dominant inhomogeneous broadening in the aqueous phase photoelectron spectra.

The pyridazine solution exhibits an N 1s spectral feature around $\sim$405.5 $\pm$ 0.1 eV in the surface-sensitive

XPS spectra, with a peak FWHM of ∼1.1 ± 0.1 eV. The corresponding gas-phase N 1s BE is ∼404.9 ± 0.2 eV[175]. The pyrimidine aqueous-phase N 1s BE is around ∼ 405.0 ± 0.1 eV, with a peak FWHM of ∼1.0 ± 0.10 eV. The analogous gas-phase N 1s BE occurs at ∼405.2 ± 0.2 eV. The aqueous-phase BE of pyrazine is found around ∼405.3 ± 0.2 eV in the surface-sensitive experiments, with a ∼1.0 ± 0.1 eV FWHM. The corresponding gas-phase N 1s BE occurs at around ∼405.6 ± 0.2 eV.

The valence and core-level PE peak spectral positions and widths, shown in Table 5.1, are found to be invariant within the error limit between the surface- and bulk-sensitive experiments on the aqueous solutions. This suggest that the electronic structure does not differ within the experimental resolution (∼80–300 meV) and when the currently adopted energy referencing scheme is adopted. The valence and core-level PES spectra presented in this chapter does not give a clear indication about the solvent-induced changes in molecular symmetries, which have been reported for pyrimidine and predicted for other isomers[194]. This does not exclude the possibilities of the symmetry breaking processes occurring in the ground and excited state of the aqueous diazines, however. Still, state-of-the-art theoretical calculations and spectral simulations would be required to identify any associated symmetry changes and related XPS signatures in the aqueous solutions.

5.2 C and N pre-K-edges PEY-X-ray Absorption (XA)

Prior to recording the valence band XPS signal of aqueous diazine molecules using resonant excitation, it is necessary to identify the core-to-virtual-valence resonance positions in the aqueous phase. The resonances were recently reported at N pre-K-edge of aqueous pyrimidine[194] and pyridazine[92], but the corresponding spectra at the C pre-K-edge region are, still to our knowledge, yet to be reported. The aqueous-phase resonant photon energies of all of the diazine systems were extracted by recording PEY-XA spectra over the C and N pre-K-edge regions. In this method, the photoelectron spectra were recorded over the BE range 0-45 eV and by varying the photon energy over the pre-K-edge regions of both the C and N atoms in the solute molecules, see the left panels of Figures 5.6, 5.7, and 5.8. The photon-energy-dependent data was subsequently intensity normalised by the photon-energy-dependent beamline flux to reveal the nascent responses of the solutions. The produced figures highlight the resonant enhancement of the valence PE signals as the photon energy is scanned over the 1s-core-to-virtual-valence excitation energies. The right panels of all three figures highlight the PEY-XA spectra of the aqueous solute molecules, which is a proxy of a true transmission-based XA spectroscopy study. The PEY-XA spectra were obtained by integrating the PE signals over the BE axes. The spectra were subsequently smoothed using 3-point moving average method, a constant background subtracted, and the data was intensity normalized at the 1s $\rightarrow$ LUMO transition peaks, as shown in the right panels of Figures 5.6, 5.7, and 5.8.

The previously-reported C and N pre-K-edge gas-phase XA spectra[175] are compared to the respective pre-K-edge PEY-XA spectra recorded in the aqueous-phase in Tables 5.2 and 5.3 and in the right panels of Figures 5.7, 5.6, and 5.8. The gas-phase spectra[175] were digitized using web-plot digitizer[196]. The relevant (smoothed using a 5-point moving averaged) gas-phase C and N XA spectra corresponding to the C 1s $\rightarrow$ LUMO and N 1s $\rightarrow$ LUMO transitions were also normalized. Since, both the gas-and aqueous phase spectra are normalized, the relative intensities of the higher-energy absorption peaks are compared to identify the solvent-induced changes in spectral intensity. Tables 5.2 and 5.3 show the respective resonance energies obtained from the PEY XA spectra at the C and N pre-K-edges of the aqueous-phase systems, respectively. The values reported in the table are the average of values extracted from the data recorded during multiple, different beamtimes and relied on beamline photon energy calibrations using N 1s $\rightarrow$ LUMO transition of N_2 at the beginning of each beamtime. The gas-phase resonances of the diazines near the C and N K-edges

are also included in brackets in Tables 5.2 and 5.3, respectively. The comparison of these numbers with the aqueous-phase analogues indicate the gas-to-liquid-phase spectral shifts, which can provide information on the electronic-structure changes of the aqueous solute compared to the isolated molecule.

Table 5.2: Core-to-virtual-valence transitions and transition photon energies of the 500 mM aqueous diazine molecules, as measured via PEY-XA spectroscopy spectra at the C K-edge at BESSY II. For each section, the first row gives the transition assignments, whereas the second and third rows shows the aqueous- and gas-phase resonances, respectively. More details can be found in the main body of the text.

Peaks	Aq./Gas Pyridazine (C_{2v})	Aq./Gas Pyrimidine (C_{2v})	Aq./Gas Pyrazine (D_{2h})
1	C_3 :1s (b_2) :$\rightarrow \pi^*(a_2)$ 284.9 $\pm$ 0.2 eV 285.5 $\pm$ 0.2 eV[175]	C_3 :1s (a_1) $\rightarrow \pi^*(b_1)$ 285.1 $\pm$ 0.1 eV 284.9 $\pm$ 0.2 eV[175]	1s (b_{1u})$\rightarrow \pi^*(b_{3u})$ 285.4 $\pm$ 0.1 eV 285.4 $\pm$ 0.2 eV[a]
2	C_1 :1s $\rightarrow \pi^*(a_2)$ C_3 :1s (a_1)$\rightarrow \pi^*$ (b_1) 285.8 $\pm$ 0.2 eV 286.2 $\pm$ 0.2 eV[175]	C_2 :1s (b_2)$\rightarrow \pi^*$ (a_2) 285.7 $\pm$ 0.1 eV 285.4 $\pm$ 0.2 eV[175]	1s (b_{1u})$\rightarrow \pi^*$ (a_u) 286.2 $\pm$ 0.1 eV 285.9 $\pm$ 0.1 eV[b]
3	- 286.2 $\pm$ 0.2 eV 286.5 $\pm$ 0.2 eV[175]	C_1 :1s $\rightarrow \pi^*(b_1)$ 286.2 $\pm$ 0.1 eV 285.8 $\pm$ 0.2 eV[175]	-

[a] Ref. 175: 285.3 eV, Ref. 40: 285.4 eV
[b] Ref. 175: 285.8 eV, Ref. 40: 289.0 eV

Table 5.3: Core-to-virtual-valence transitions and transition photon energies of 500 mM aqueous diazine molecules measured using PEY-XA, as recorded at the N K-edge at BESSY II. For each section, the first row gives the transition assignments, whereas the second and third rows shows the aqueous- and gas-phase resonances, respectively. Peak 2 is not present in the pyrazine spectra and, for pyridazine, the transition is very weak in the gas-phase. More details are presented in the main body of the text.

Peaks	Aq./Gas Pyridazine (C_{2v})	Aq./Gas Pyrimidine (C_{2v})	Aq./Gas Pyrazine (D_{2h})
1	1s (b_2)$\rightarrow \pi^*$ (a_2) 399.4 $\pm$ 0.2 eV[aa] 399.0 $\pm$ 0.2 eV[a]	1s (b_2)$\rightarrow \pi^*$ (a_2) 399.2 $\pm$ 0.2 eV[ac] 398.8 $\pm$ 0.2 eV[d]	1s (b_{1u})$\rightarrow \pi^*$ (b_{3u}) 398.9 $\pm$ 0.1 eV 398.8 $\pm$ 0.2 eV[175]
2	1s (b_2)$\rightarrow \pi^*(b_1)$ 400.9 $\pm$ 0.2 eV[ab] 400.0 $\pm$ 0.4 eV[b]	1s (b_2)$\rightarrow \pi^*$ (b_1) 400.2 $\pm$ 0.2 eV[b] 399.9 $\pm$ 0.2 eV[175]	1s (b_{1u})$\rightarrow \pi^*(a_u)$ -
3	1s (a_1)$\rightarrow \pi^*$ (a_2) 403.6 $\pm$ 0.2 eV 402.9 $\pm$ 0.2 eV[c]	1s (b_2)$\rightarrow \pi^*$ (b_1) 403.1 $\pm$ 0.1 eV[c] 402.8 $\pm$ 0.2 eV[e]	1s (b_{1u})$\rightarrow \pi^*$ (b_{2g}) 403.1 $\pm$ 0.1 eV 402.8 $\pm$ 0.2 eV[175]

[aa] Ref. 92: 399.2 eV
[ab] Ref. 92: 400.7 eV
[ac] Ref. 194: 399.0 eV
[a] Ref. 92: 399.0 eV, Ref. 175: 399.0 eV
[b] Ref. 92: 400.3 eV, Ref. 175: 399.6 eV
[c] Ref. 92: 403.1 eV, Ref. 175: 402.7 eV
[d] Ref. 175: 398.8 eV Ref. 88: 398.8 eV
[e] Ref. 175: 402.8 eV Ref. 88: 402.7 eV

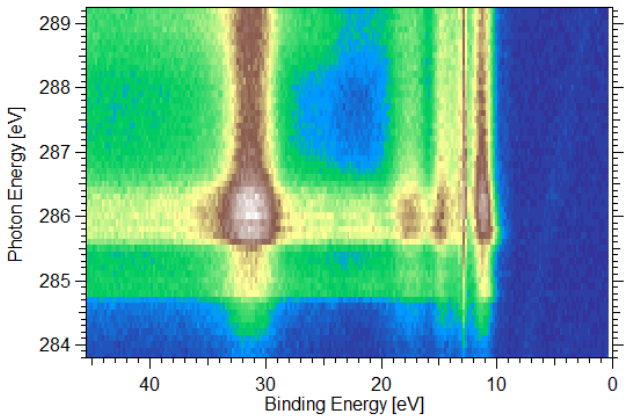

(a) RPES spectra at C pre-K-edge

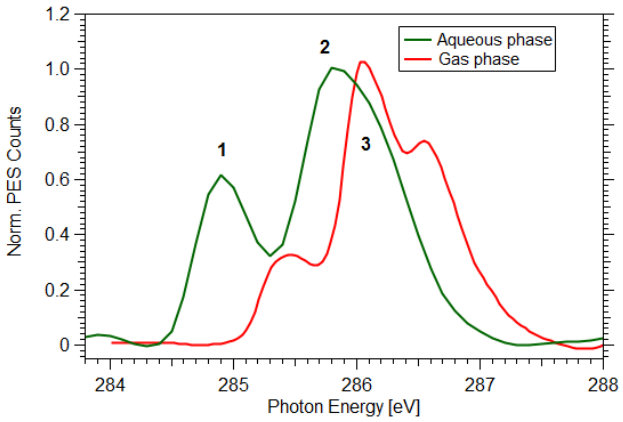

(b) C K-pre-edge PEY

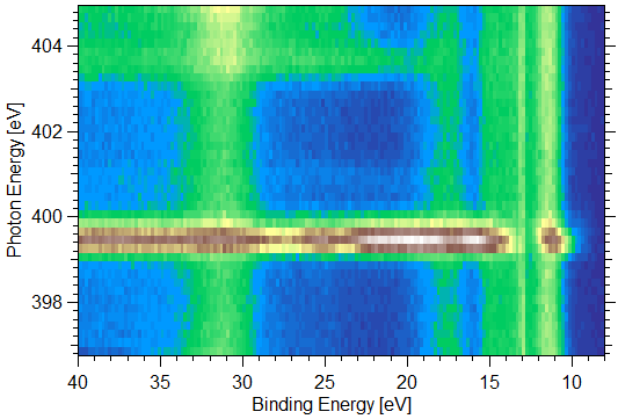

(c) RPES spectra at N pre-K-edge

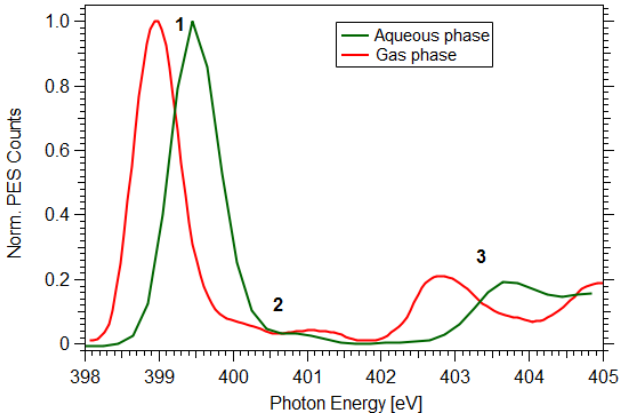

(d) N K-pre-edge PEY

Figure 5.6: Left panels, valence-band spectra of 500 mM aqueous pyridazine recorded while sweeping the photon energies over the C (panel a) and N (panel c) pre-K-edge regions. The data has been intensity normalized by the on-target photon-energy dependence of the beamline flux. When the photon energies match the core-to-valence transition energies, the valence features are enhanced. The right panels highlights the constant-background subtracted and smoothed, integrated PE signal over the full BE range for each photon energy in the aqueous phase (green). The resulting data are termed PEY-XA spectra of pyridazine. Previously reported smoothed gas-phase XAS spectra have been digitized from Reference 175 (red curves) and are shown for comparison with the aqueous-phase data presented here.

Pyridazine PEY-XAS Due to the molecular symmetry of pyridazine, see Figure 1.1, two different C atom (C_1 and C_3) contributions are expected in it's XA spectrum. As shown in Figure 5.6b, two absorption peaks are visible in the PEY spectra, where the second peak is very broad and is thought to contain contributions from multiple electronic transitions. The aqueous-phase peak assignments have been made by comparison with a previous gas phase study[175]. The first peak, Peak 1, around $\sim$284.9 $\pm$ 0.2 eV is assigned to the C_3 atom 1s $\rightarrow$ LUMO transition, with the LUMO having a_2 symmetry, and Peak 2, around $\sim$285.8 $\pm$ 0.2 eV, is thought to be a similar 1s $\rightarrow$ LUMO transition, associated with the C_1 atom. Finally, the third peak, around $\sim$286.2 $\pm$ 0.2 eV is assigned to the LUMO+1 transitions associated with both the C_1 and C_3 atoms. These transitions in aqueous pyridazine are red shifted compared to the previously reported gas-phase[175] core-to-virtual-valence resonances by 0.60 $\pm$ 0.3 eV, 0.4 $\pm$ 0.3 eV, and 0.3 $\pm$ 0.3 eV, respectively.

Similar PEY-XA spectra, recorded over the N pre-K-edge region, are shown in Figure 5.6d. The intense aqueous-phase peak around $\sim$399.4 $\pm$ 0.2 eV corresponds to the N 1s $\rightarrow$ LUMO transition. The peak around $\sim$400.9 $\pm$ 0.2 eV is assigned to a N 1s $\rightarrow$ LUMO+1 transition. The first two transition energies are closely matched to the aqueous-phase results reported by Tsuru *et al.*[92]. According to Reference 92, the

LUMO+1, $3b_1$ orbital, in pyridazine is a delocalized orbital over the N=N moiety and is distributed over all of the C and N atoms. It correspondingly exhibits a low spatial overlap with the N 1s core orbital. The third peak in the PEY-XA spectrum is ascribed to a mixed-valence orbital transition with a dominant contribution from the $3a_2$ MO. The gas-phase transition energy values have been taken from References 92,175 and their average values are shown in the Table 5.3. Unlike, the C 1s pre-K-edge resonances, the N 1s resonances are blue-shifted in aqueous solutions compared to the gas-phase by 0.4 $\pm$ 0.3 eV, 0.9 $\pm$ 0.4 eV, and 0.7 $\pm$ 0.3 eV, respectively[92,175].

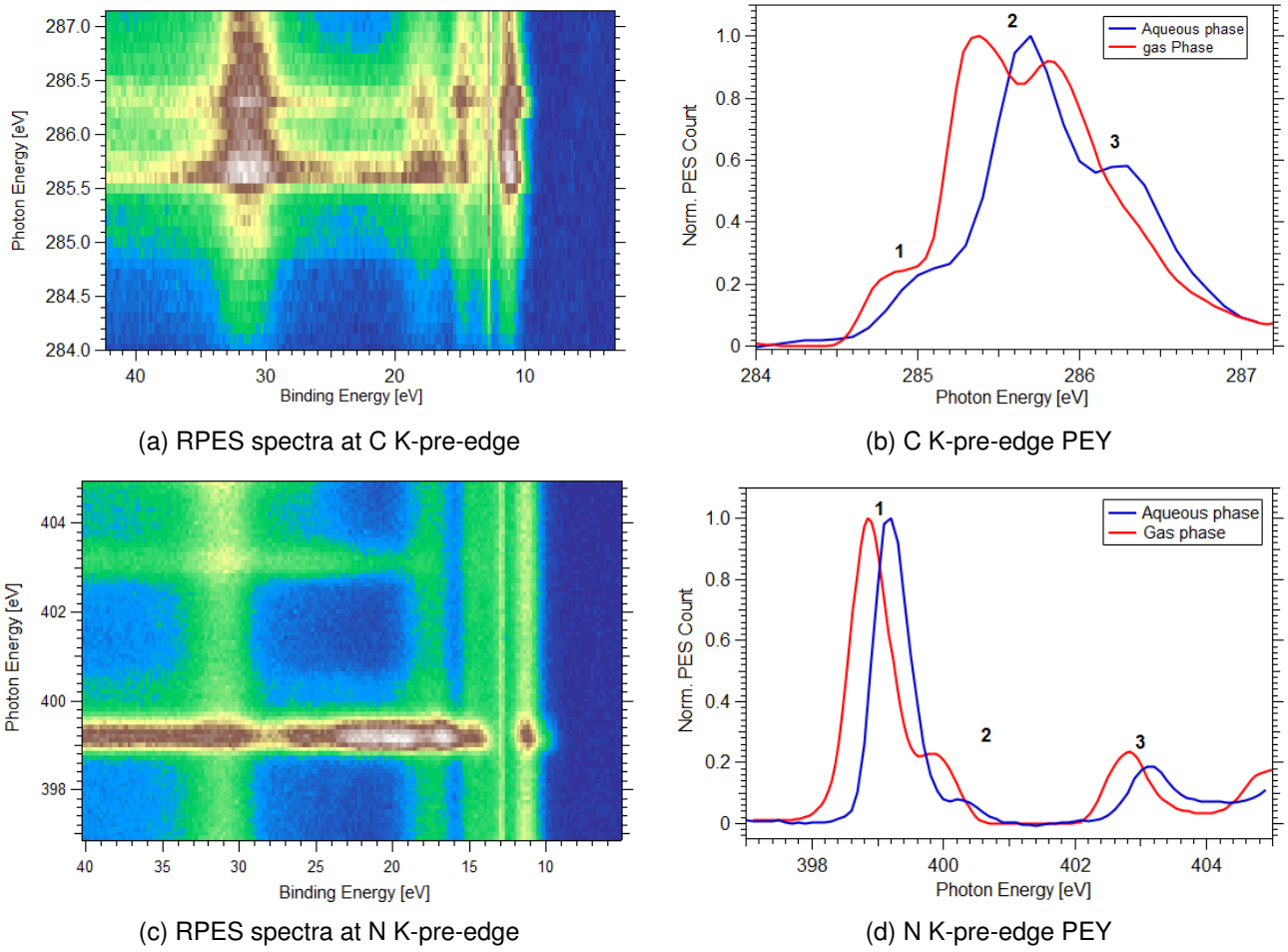

(a) RPES spectra at C K-pre-edge

(b) C K-pre-edge PEY

(c) RPES spectra at N K-pre-edge

(d) N K-pre-edge PEY

Figure 5.7: Left panels, valence-band photoemission spectra of 500 mM aqueous pyrimidine, as measured by sweeping the photon energy over the C (panel a) and N (panel c) pre-K-edges regions. The photon-energy-dependent data have been intensity normalized by the photon-energy-dependent on-target beamline flux. When the photon energies match the core-to-virtual-valence transition energies, the valence photoemission features are enhanced. The right panels show the constant-background subtracted and smoothed, integrated PE signal over the full BE range at each photon energy in the aqueous phase (green). Previously reported smoothed gas-phase XAS spectra have been digitized from Reference 175 (red curves) and are shown for comparison with the aqueous-phase data presented here.

Pyrimidine PEY-XAS The C and N pre-K-edge PEY-XAS spectra of aqueous pyrimidine are shown in Figure 5.7. Figure 5.7b highlights three electronic transitions in the C pre-K-edge region of the aqueous pyrimidine solution. Due to the symmetry of the pyrimidine molecule, three (or more) absorption peaks are expected to be distinguishable and are visible in Figure 5.7b. The first peak corresponds to the C_3 atom, C 1s 1s $\rightarrow$LUMO transitions, where the LUMO again has $a_2(\pi)$ molecular orbital symmetry[174] at a photon energy of $\sim$285.1 $\pm$ 0.1 eV. The second and third peaks around $\sim$285.7 $\pm$ 0.1 eV and $\sim$286.2 $\pm$ 0.1 eV photon energies are associated with the same 1s$\rightarrow$LUMO transition from the C_2 and C_1 atomic sites, respectively.

The resonances are blue shifted in the aqueous phase compare to the gas-phase results[175] by 0.2 ± 0.3 eV, 0.3 ± 0.3 eV and 0.4 ± 0.2 eV.

The related N K-edge resonances are shown in Figure 5.7d. The aqueous-phase N pre-K-edge spectrum also highlights three absorption peaks, like the C 1s spectrum. The first peak occurs at a photon energy of ∼399.2 ± 0.2 eV and is assigned to the N 1s → LUMO transitions. Similar to pyridazine, the second peak at around ∼400.2 ± 0.2 eV photon energy is the transition to the LUMO+1 orbital, where this MO has b_1 molecular symmetry. The first and second core-to-virtual-valence transition energies are notably consistent with those studied in aqueous pyrimidine using RIXS[194]. Finally, the photoabsorption around ∼403.1 ± 0.1 eV is associated with the transition to a state with mixed valence character, where the dominant contribution is attributed to a LUMO+3 excitation, where this MO has $4b_1$ molecular symmetry. Similar to the C pre-K-edge resonances, the N K-edge resonances are differentially blue shifted in the aqueous phase compared to in the gas phase by 0.4 ± 0.3 eV, 0.3 ± 0.2 eV and 0.3 ± 0.2 eV[175].

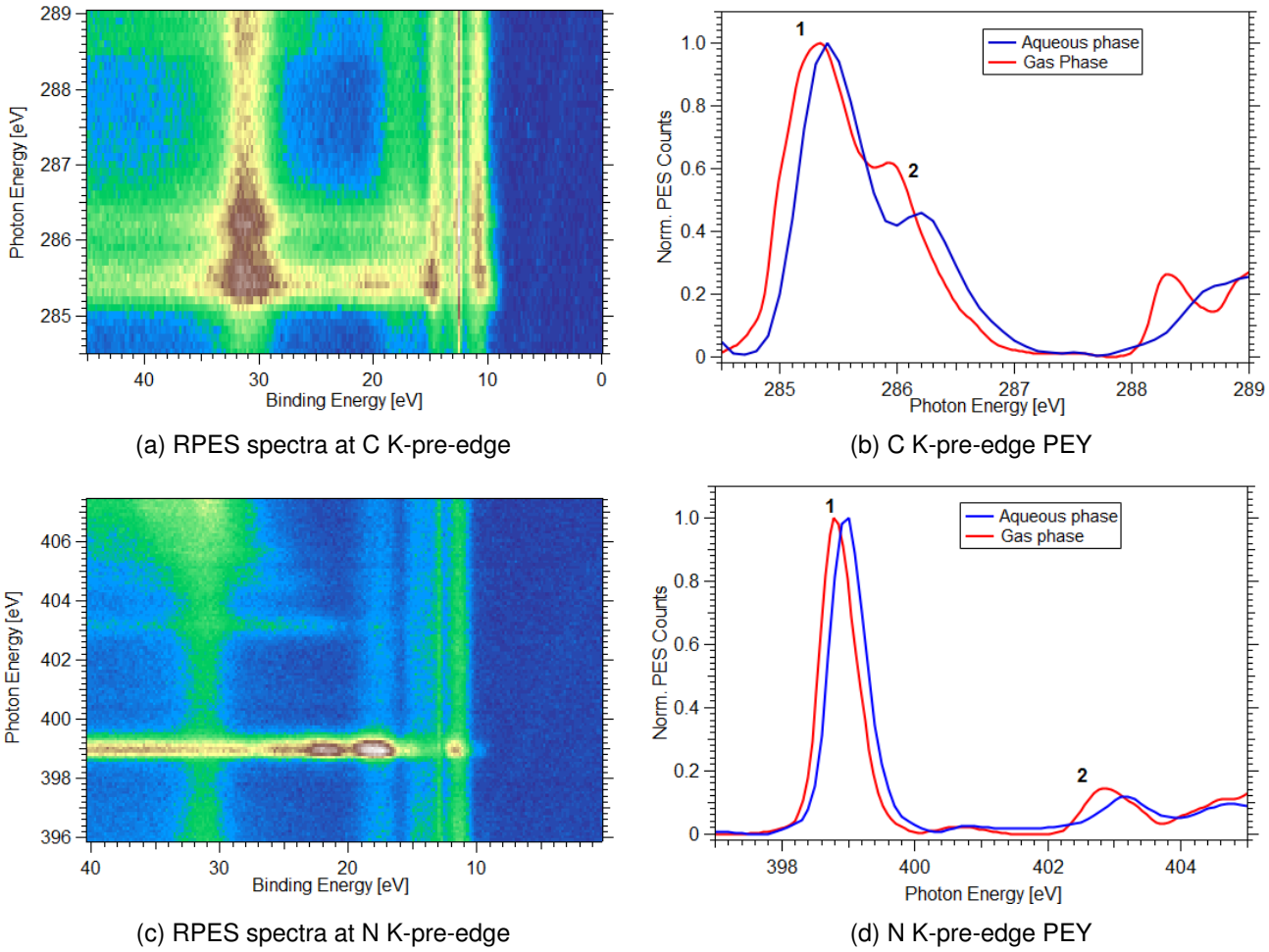

(a) RPES spectra at C K-pre-edge

(b) C K-pre-edge PEY

(c) RPES spectra at N K-pre-edge

(d) N K-pre-edge PEY

Figure 5.8: Left panels, valence-band photoemission spectra of 500 mM aqueous pyrazine solutions, as produced by sweeping the photon energy over the C (panel a) and C (panel c) pre-K-edges regions. The photon-energy-dependent data have been intensity normalized by the photon-energy-dependent on-target beamline flux. When the photon energies match the core-to-virtual-valence transition energies, the valence photoemission features are enhanced. The right panels show the constant background subtracted and smoothed, integrated PE signal over the full BE range at each photon energy in the aqueous phase (blue curves). The photon-energy-dependent data have been intensity normalized by the photon-energy-dependent on-target beamline flux. Previously reported, smoothed gas-phase XAS spectra have been digitized from Reference 175 (red curves) and are shown for comparison with the aqueous-phase data presented here.

Pyrazine PEY-XAS The C pre-K-edge PEY-XAS spectra were recorded from aqueous pyrazine solutions in the 285-289 eV photon energy range, and are shown in Figure 5.8b. Two absorptions peaks are identified at ∼285.4 ± 0.1 eV and ∼286.2 ± 0.1 eV photon energies. The peak around ∼285.4 ± 0.1 eV is assigned to the C 1s → LUMO transition, where the latter has π^* (b_{3u}) molecular symmetry. The second peak is centered at a ∼286.2 ± 0.1 eV photon energy and is ascribed to the C 1s → LUMO+1 excitation, where the LUMO+1 has π^* (a_u) molecular symmetry[40,175]. The gas-phase values are taken from References 40,175 and their average values are shown in Table 5.2. Compared to the previous gas-phase XAS studies[40,175], the observed aqueous-phase resonance, Peak 2, is blue shifted by 0.30 ± 0.1 eV.

The N pre-K-edge PEY-XAS spectrum shown in Figure 5.8d shows two absorption bands. The first one around ∼398.9 ± 0.1 eV is assigned to the N 1s → LUMO transition, where the latter has b_{3u} molecular symmetry. Similar to pyridazine and pyrimidine, the second absorption feature around ∼403.1 ± 0.1 eV is attributed to excitation to a mixed valence character state, where the dominant spectral weight is assigned to LUMO+3, which has b_{2g} molecular symmetry[175]. Again the N pre-K-edge resonances are blue shifted with respect to the gas-phase analogues by 0.1 ± 0.2 eV and 0.3 ± 0.2 eV, respectively[175].

5.3 Resonant Photoelectron Spectroscopy on the Aqueous Diazines

So far, in Section 5.1.1, it was highlighted that the non-resonant XPS measurements provide rather limited information about the valence electronic structure of the aqueous diazines. However, as will be shown in the following sections, resonant excitation provides additional information about the valence electronic structure of the aqueous solutes. In the following sections, the origins of such signal enhancements will be discussed.

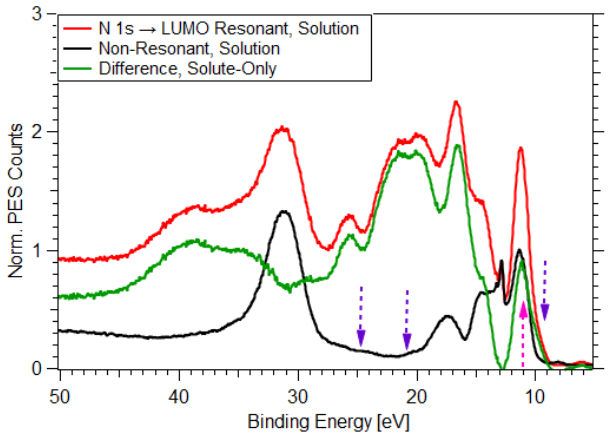

(a) N1s → LUMO resonant and non-resonant excitation, valence photoemission spectra

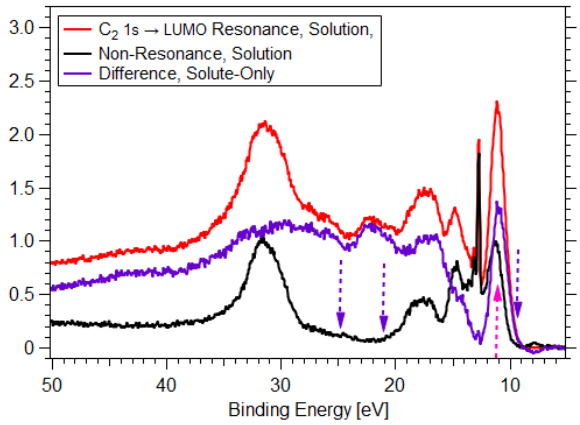

(b) C1s → LUMO resonant and non-resonant excitation, valence photoemission spectra

Figure 5.9: Valence-band photoemission spectra of 500 mM aqueous pyrimidine solutions. The left panel shows the resonant and non-resonant valence band at the N K-pre-edge recorded at ∼399.1 eV and ∼397.0 eV photo energies, respectively. The right panel shows C K-edge resonant and non-resonant valence photoemission spectra were recorded using ∼285.6 and ∼283.0 eV photo energies, respectively. In both cases, non-resonant valence spectra were subtracted from the resonant valence spectra to extract the solute contributions at the N (green) and C (violet) pre-K-edge. The violet arrows indicate the extracted solute feature in non-resonant excitation, whereas the uparrow indicate the spectral enhancement of the solute feature along water $1b_1$ position.

Figures 5.9, 5.10, and 5.11 shows the PE spectra of pyrimidine, pyridazine and pyrazine, respectively. Each of the figures include resonant (red), non-resonant (black) and resonant-non-resonant difference (N 1s, green, C 1s, violet) spectra. These resonant spectra were recorded at the photon energies identified in Figures 5.6, 5.7, and 5.8. The non-resonant spectra were recorded at photon energies below the onset of the pre-edge

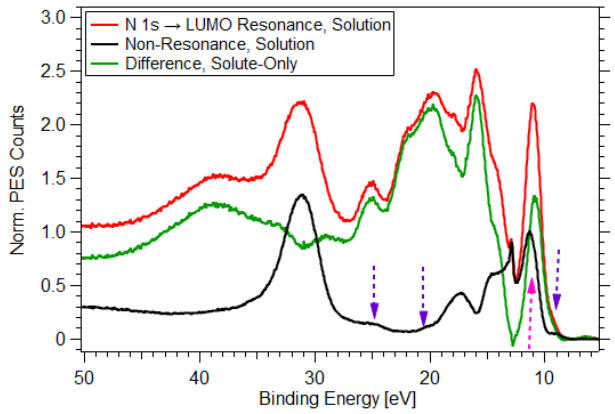

(a) N1s → LUMO Resonant and non-resonant excitation, valence photoemission spectra

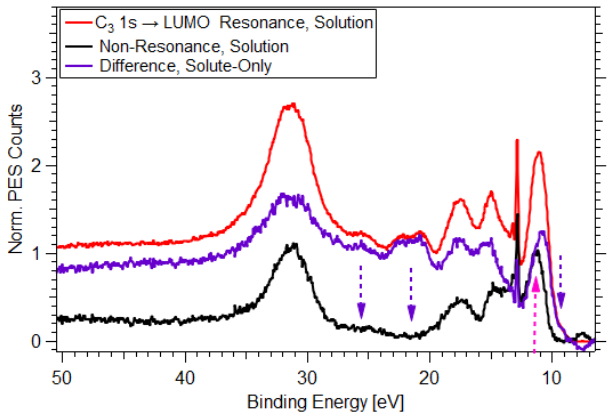

(b) C1s → LUMO resonant and non-resonant excitation, valence photoemission spectra

Figure 5.10: Valence-band photoemission spectra of 500 mM aqueous pyridazine solutions. The left panel shows the resonant (red) and non-resonant valence band signal at the N pre-K-edge, as recorded at ∼399.5 eV and ∼397.0 eV photon energies, respectively. The right panel shows the C K-edge resonant and non-resonant valence photoemission spectra, which were recorded using ∼284.9 eV and ∼283.0 eV photon energies, respectively. In both cases, non-resonant valence spectra were subtracted from the resonant valence spectra to extract the solute contributions at the N (green) and C (violet) pre-K-edge. The violet arrows indicate the extracted solute feature in non-resonant excitation, whereas the uparrow indicate the spectral enhancement of the solute feature along water $1b_1$ position.

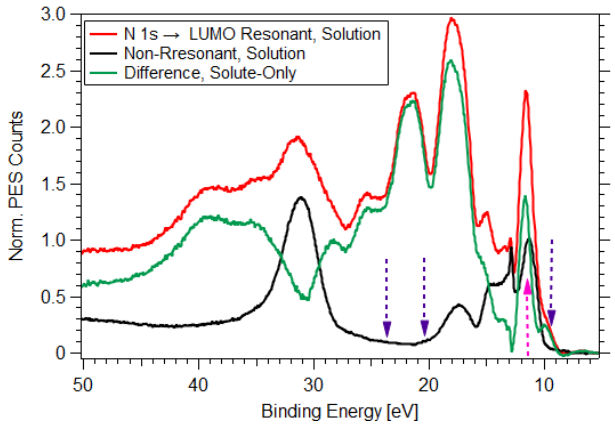

(a) N 1s → LUMO resonant and non-resonant excitation, valence photoemission spectra

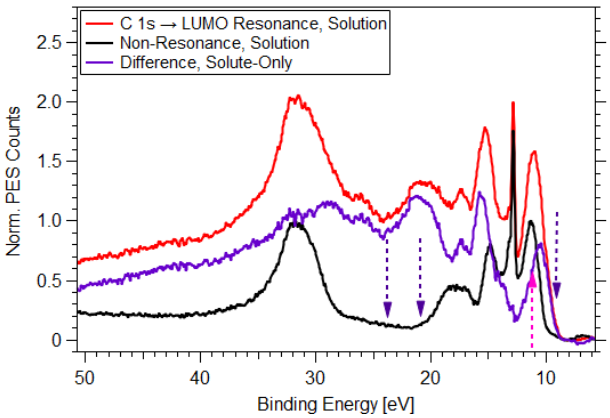

(b) C 1s → LUMO resonant and non-resonant excitation, valence photoemission spectra

Figure 5.11: Valence-band photoemission spectra of 500 mM aqueous pyrazine solutions. The left panel shows the resonant (red) and non-resonant valence band signal at the N pre-K-edge recorded at ∼398.9 eV and ∼397.0 eV photon energies, respectively. The right panel shows the C pre-K-edge resonant and non-resonant valence spectra were recorded using ∼285.4 and ∼283.0 eV photon energies, respectively. In both cases, non-resonant valence spectra were subtracted from the resonant valence spectra to extract the solute contributions at the N (green) and C (violet) pre-K-edge. The violet arrows indicate the extracted solute feature in non-resonant excitation, whereas the uparrow indicate the spectral enhancement of the solute feature along water $1b_1$ position.

absorption features. The violet-colored downward-pointing-arrows indicate the feature BEs extracted in non-resonant XPS experiments (see Table 5.1), where the pink-colored upward-pointing-arrows indicate the water solvent $1b_1$ positions. The left and right panels of the figures show the N and C K-edge valence photoemission spectra. 399.1 eV, 399.5 eV and 398.9 eV photon energies were used to record the resonantly enhanced valence spectra for the pyrimidine, pyridazine, and pyrazine solutions, respectively. These photon energies

were assigned to the N 1s $\rightarrow$ LUMO photoemission spectra and the corresponding electronic spectra are referred to as N 1s $\rightarrow$ LUMO resonantly enhanced valence photoemission spectra. The non-resonant spectra were recorded at a lower photon energies of 397.0 eV. Similarly, the C K-edge resonantly enhanced valence spectra were recorded using $\sim$285.6 eV, $\sim$284.6 eV and $\sim$285.4 eV photon energies for the pyrimidine, pyridazine and pyrazine solutions, respectively. The non-resonant valence spectra recorded in the vicinity of the C K-pre-edge were respectively recorded using 284.1 eV, 283.7 eV and 284.7 eV photon energies for the three diazines, respectively. For the C pre-K-edge measurements, the resonant and non-resonant PE spectra were initially normalized by the photon flux (which is notably highly modulated in this spectra region due to carbon contamination of the beamline x-ray optics). Similar photon flux normalization was also applied to the N pre-K-edge spectra, as shown in Figures 5.9, 5.10, and 5.11

Similar data analysis procedures, such as background subtraction, BE energy calibration as well as signal intensity scaling have been performed for all of the aqueous diazine data sets. The BEs of the non-resonant PE spectra were calibrated using the (nearly-neat) liquid water $1b_1$ spectral position at 11.33 $\pm$ 0.04 eV[66,243]. However, the BE calibration of the resonant valence spectra is not straightforward in the aqueous diazine solution cases. The ionization contributions of the solute energetically overlap with the solvent bands and have significant spectral enhancement and weight following resonant excitation. A complete isolation and calibration of the water, $1b_1$ feature, is correspondingly impossible, at least with the implemented BE referencing scheme[66]. The non-resonant and resonant photon energies are separated by just a few eV and the corresponding spectra were taken under the same experimental conditions. In this case, it is assumed that any BE offset in the non-resonant excitation case is similar to the resonant excitation case. Thus, the same BE calibration factor was applied to both the non-resonant and resonant PE spectra at both the N and C pre-K-edges. The resonant PE spectra were subsequently intensity normalized by the peak height of the solvent $1b_1$ spectral feature in the non-resonant PE spectra recorded using a 283.0 eV photon energy, located 2-3 eV below the resonant absorption onset. The black spectra show the non-resonant excitation spectra and the red curves show the resonant excitation spectra. The red resonantly enhanced spectra have contributions from both the solute and solvent, where the solute features may be selectively resonantly enhanced at different photon energies. In order to isolate the solute features, the non-resonant spectra are subtracted from the resonant spectra to produce the green difference spectra for each of the solute molecules. Here, in the context of resonant excitations, the background-subtracted difference spectra will be referred as the resonantly enhanced valence spectra of the aqueous pyrimidine/ pyridazine/pyrazine solute at the N/C pre-K-edges.

As discussed in Section 2.4.3 in Chapter 2, the resonantly enhanced PE features contain both participator and the spectator processes contributions. The participator-like Auger process imprint the initial-state ionization energies, with the spectral intensities being the convolution between the probabilities of the photoabsorption and photoionization events. Such participator features start to appear in the low BE regions of the photoelectron spectra, whereas the spectator-Auger features occur in relatively high BE regions. For the diazine molecules, the spectator channels start at least at an energy of 4.2-4.5 eV (HOMO-LUMO gap) higher from their lowest ionization energy thresholds. Therefore, below 13 eV, it can be considered that the resonant enhancements are only associated with participator ionization channels. Above 13 eV, the resonantly enhanced valence spectra contain both participator- and spectator-like features[88]. Some spectral enhancement notably occurs at the solvent $1b_1$, $3a_1$, $1b_2$ peaks in Figures 5.9, 5.10 and 5.11, but not at the associated $2a_1$ peaks, as shown in the difference spectra. The outer valence ionization energetics of the gas-phase diazine molecules are congested[176,177,195] and notably overlap with the solvent water molecule ionization features. Here, it will be shown that the resonantly-enhanced ionization of each of the MOs of the aqueous diazine molecules can be correlated with a particular atomic site, which can be selectively excited

at specific C or N pre-K-edge resonances. Although spectral congenstion as well as the broadening in the resonant excitation case causes the spectral features to be merged with each other, the data still provides useful information about the valence electronic structure of the diazine solute molecules in aqueous solutions.

5.4 Resonantly Enhanced Valence Photoemission Band of the Aqueous Diazines

The low BE side of the valence photoemission spectra contain spectral information associated with the four outer valence molecular orbitals of the diazine molecules[176,182,195,277]. The resonantly enhanced valence PE spectra recorded following excitation from the different atomic sites can be considered to highlight the atomic parentage of the valence MO contributions, via the produced participator Auger XPS features. The outer valence ionization contributions are shown over the valence band regions in the a panels and in the lower BE region (<13 eV) in on an expanded scale in the b panels of Figures 5.12, 5.13, and 5.14. The Figures also show the non-resonant solution (black) and bulk-sensitive solute (filled plot) valence spectra. The non-resonant solution valence were recorded close to the N pre-K-edge. The bulk-sensitive solute valence spectra were reproduced from the panel (b) in Figures 5.1b, 5.2b, and 5.3b for pyrimidine, pyridazine, and pyrazine, respectively. All of these were recorded using 150 eV photon energy. The a and b panels highlight the participation of the atomic orbitals associated with particular atomic sites in the construction of the valence molecular orbitals of the diazine molecules. Due to the differences in the fractional atomic orbital parentages of the valence orbitals, the resonantly enhanced participator PE features differ from each other depending on where the core electrons were excited from. Thus, the resonant enhancement of the participator-like Auger spectral intensity varies across the valence bands at different atomic sites, as shown in the outer valence orbital of pyrimidine, pyridazine and pyrazine in panels (a) and (b) in Figures 5.12, 5.13, and 5.14, respectively.

5.4.1 Outer Valence Ionization Channels: BE Region 0-13 eV

Pyrimidine Valence Band Figure 5.12 shows the background-subtracted resoanantly enhanced (valence) XPS spectra recorded at the N and C pre-K-edges of aqueous pyrimidine. The red spectra corresponds to the N pre-K-edge, whereas the green and blue spectra are the resonantly enhanced valence spectra recorded at the C_2- and C_1-atomic site, respectively.

Figures 5.12c and 5.12d show cumulative Gaussian profile fits to the low-binding-energy resonantly enhanced photoemission data associated with the N and C pre-K-edges. These fits have been used to extract the BE's of the valence PE peaks of aqueous pyrimidine. Table 5.4 shows the results obtained from resonant excitation in comparison to those extracted from the non-resonant PE measurements. In order to extract different ionization contributions from spectrally broad resonant valence photoelectron spectra, spectral peak positions and FWHM of the lowest ionizing feature, HOMO, $(7b_2, n_N)^{-1}$, non-bonding MO was during the fitting procedure, while the other parameters were considered to be free parameters. The MO ordering and labelling was made in accordance with a previous gas-phase PES study[176]. The BE around $\sim$10.3 $\pm$ 0.2 eV, with a 1.0 $\pm$ 0.2 eV FWHMs is assigned to the $(2b_1, \pi)^{-1}$ MO ionization channel. According to a previous gas-phase study[88], this MO has dominant C character and this is seemingly retained in the aqueous phase. Another non-bonding $(11a_1, n_N)^{-1}$ MO is associated with the lone pair electrons at the N site of the molecule and is overlapped with the $(1a_2, \pi)^{-1}$ MO contribution. Both of them appear around $\sim$11.2 $\pm$ 0.1 eV. Notably, the spectral intensity of the lone-pair MOs ionization features are lower following N pre-K-edge excitation compared to at the C pre-K-edge. Possible reasons for this will be discussed in Section 5.5.

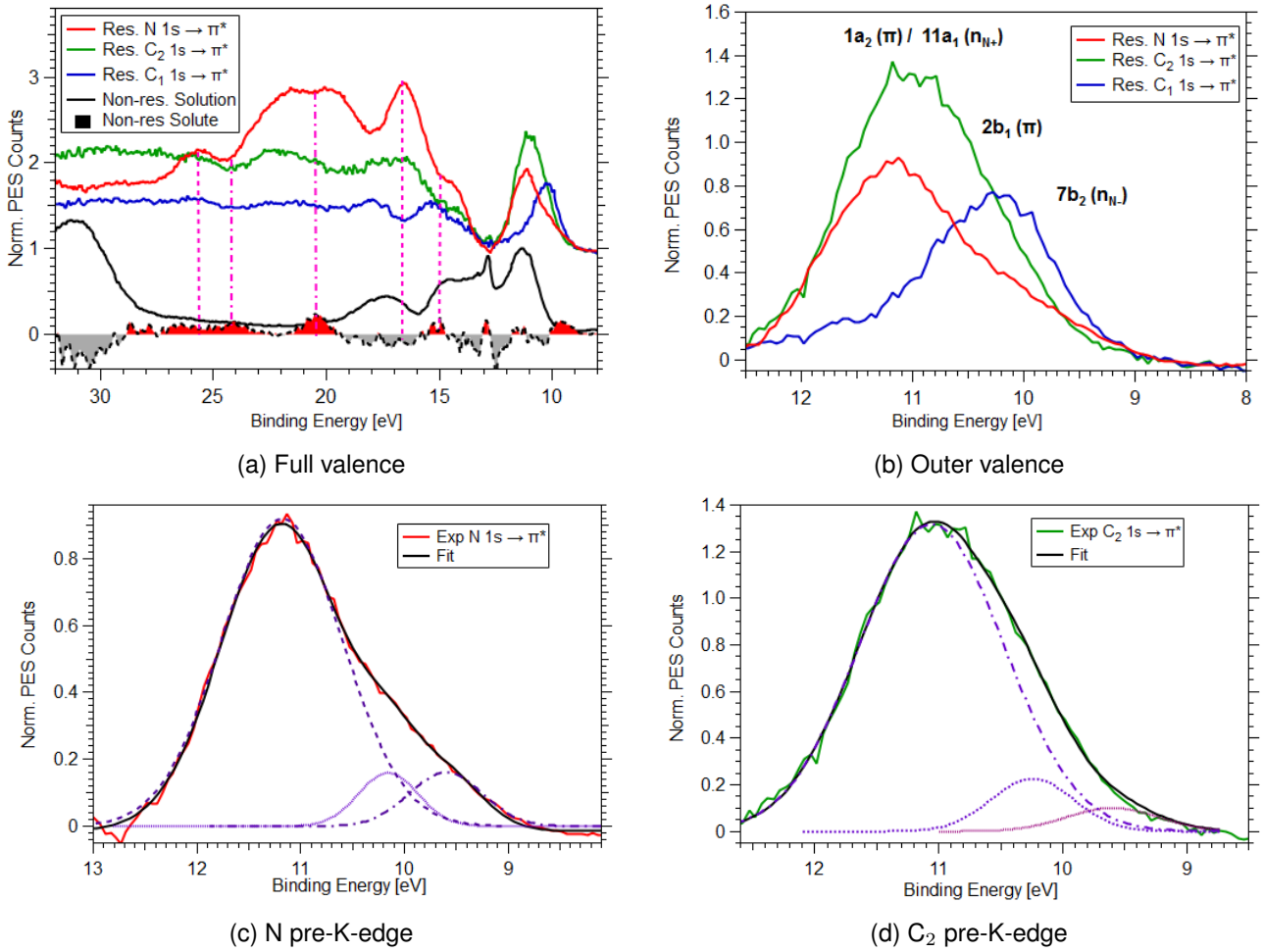

(a) Full valence

(b) Outer valence

(c) N pre-K-edge

(d) C_2 pre-K-edge

Figure 5.12: (Panel a) Background-subtracted resonant valence band XPS spectra of pyrimidine at different XA resonances, N K-edge (red), C K-edge (C_1 atom: blue and C_2 atom: green). All of these resonances corresponds to 1s $\rightarrow$ LUMO excitations. The non-resonant solution (black) and solute valence (filled plot, reproduced from panel (b) in Figure 5.1) spectra are shown. Non-resonant solute spectral intensities, which were recorded using 150 eV photon energy are arbitrarily scaled for visualization. Panel b shows the resonantly enhanced spectra associated with the outer four MOs of aqueous pyrimidine and associated peak assignments. Panel (c) shows a cumulative Gaussian-peak fit to the N-1s $\rightarrow \pi^*$ resonantly enhanced XPS spectrum. Panel (d) shows similar fits at the C_2-1s $\rightarrow \pi^*$ resonantly enhanced XPS spectrum. More details are given in the main body of the texts.

Table 5.4: Pyrimidine outer valence electron BE's and the peak FWHM's obtained from Gaussian fits to the RPES measurement results. The aqueous phase results are compared to the gas phase results. During the fitting procedure, the lowest BE and FWHM fit component was fixed to the lowest-energy ionizing transition values determined from the fits to the non-resonant XPS spectra reported in Section 5.1.1. The ionization channels are assigned based on previous gas-phase studies [177,195]. More details are given in the main body of the texts.

Peak	Features	Resonant		Non-resonant		Gas[a]
		BE (eV)	FWHM (eV)	BE (eV)	FWHM (eV)	BE (eV)
1	$(7b_2, n_N)^{-1}$	9.60 ± 0.04	0.8 ± 0.05	9.60 ± 0.04	0.8 ± 0.05	9.72 ± 0.03
2	$(2b_1, \pi)^{-1}$	10.27 ± 0.20	0.95 ± 0.17	-	-	10.49 ± 0.02
3	$(11a_1, n_N)^{-1}$ $(1a_2, \pi)^{-1}$	11.20 ± 0.14	1.64 ± 0.30	-	-	11.21 ± 0.01, 11.49 ± 0.05

[a] Average values are given, see Appendix Table B.1 for further details.

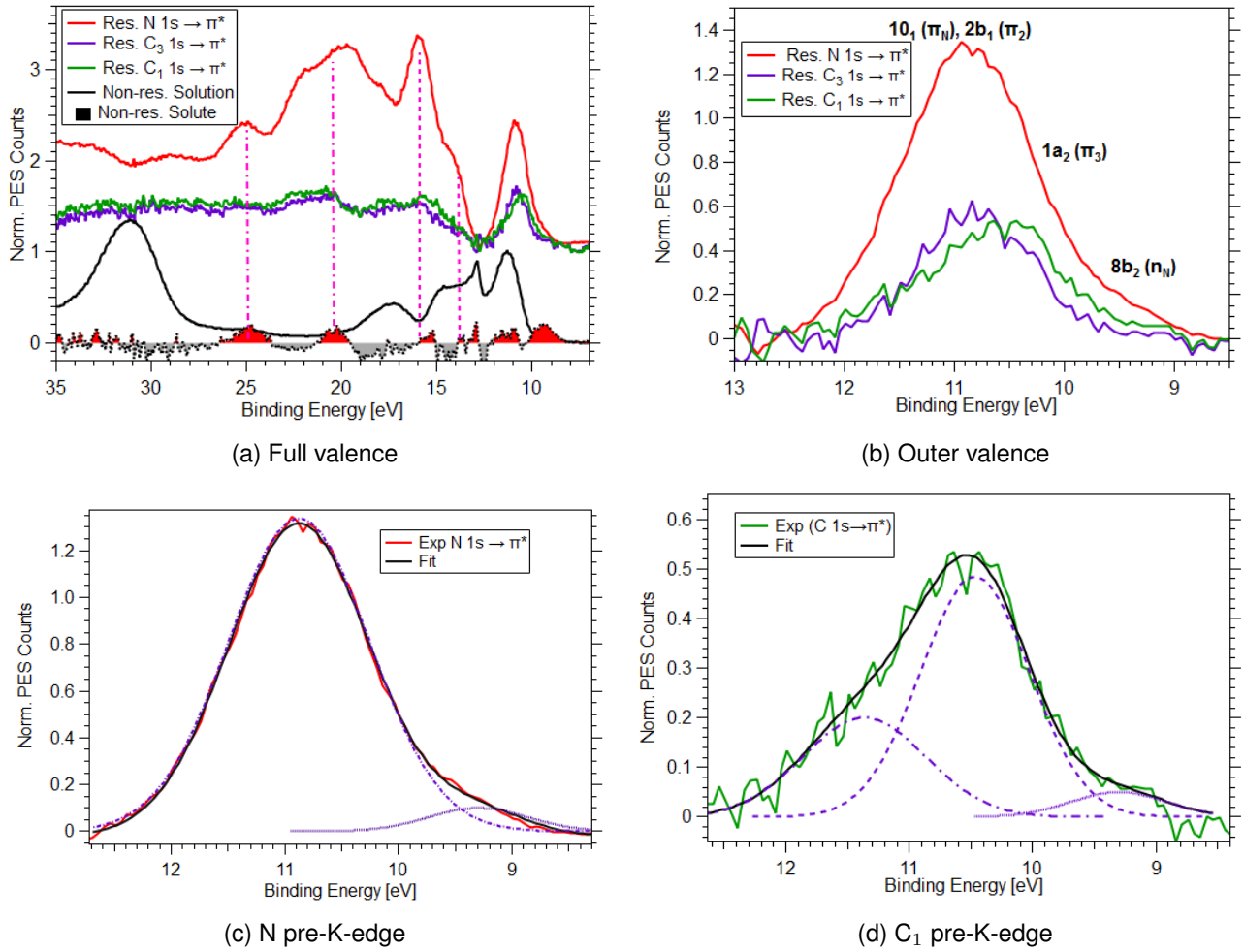

(a) Full valence

(b) Outer valence

(c) N pre-K-edge

(d) C_1 pre-K-edge

Figure 5.13: (Panel a) Background-subtracted resonant valence band XPS spectra of pyridazine at different XA resonances, N K-edge (red), C K-edge (C_1 atom: blue and C_2 atom: green). All of these resonances corresponds to 1s $\rightarrow$ LUMO excitations. The non-resonant solution (black) and solute valence (filled plot, reproduced from panel (b) Figure 5.2) spectra are shown. Non-resonant solute spectral intensities, which were recorded using 150 eV photon energy are arbitrarily scaled for visualization. Panel b shows the outer four MOs of aqueous pyridazine and their assignments. Panel (c) shows a cumulative Gaussian-peak fit to the N-1s $\rightarrow \pi^*$ resonantly enhanced XPS spectrum. Panel (d) shows similar fits at the C_2-1s $\rightarrow \pi^*$ resonantly enhanced XPS spectrum. More details are given in the main body of the texts.

Pyridazine Valence Band Figure 5.13 shows the non-resonant, background-subtracted resonant valence photoelectron spectra of the pyridazine solute, as recorded in the N and C pre-K-edge regions. The spectra are associated with 1s $\rightarrow \pi^*$ resonant transitions in the pyridazine molecule, originating from different atomic sites. A Gaussian fitting analysis was applied with the goal of isolating the outer valence ionization channel signal, produced via participator Auger processes and correspondingly assign valence molecular orbitals contributions. During the fitting procedure, the spectral position and width (FWHM) of the HOMO orbital ionization feature, as determined in the non-resonant XPS experiments described in Section 5.1.1, were fixed based on the non-resonant data analysis, allowing the other MO contributions to be extracted from the spectrally dense and broadened photoelectron spectra. Figures 5.13c and 5.13d show the cumulative Gaussian-profile fits used to extract the participator Auger features associated with the pyridazine solute. Table 5.5 highlights the average BE's and FWHM's extracted from the valence RPES spectra band and enables a comparison between them and the non-resonant aqueous- and previously reported gas-phase results.

The ground-electronic-state orbital assignments have been made in accordance with previous gas phase

Table 5.5: Pyridazine outer valence electron BE's and the peak FWHM's obtained via Gaussian fittings from RPES measurements. The aqueous-phase results are compared to the gas-phase results. During the fitting procedure, the BE and FWHM were fixed to the values of the lowest-energy ionizing transition, as determined in the non-resonant XPS measurements described in Section 5.1.1. The ionization channels were assigned based on the result of gas-phase studies[177,195]. More details are given in the main body of the text.

Peak	Features	Resonant		Non-resonant		Gas[a]
		BE (eV)	FWHM (eV)	BE (eV)	FWHM (eV)	BE(eV)
1	$(8b_2, n_{N-})^{-1}$	9.30 $\pm$ 0.04	1.00 $\pm$ 0.05	9.4 $\pm$ 0.04	1.00 $\pm$ 0.05	9.30 $\pm$ 0.02
2	$(1a_2, \pi_3)^{-1}$	10.80 $\pm$ 0.12	1.34 $\pm$ 0.10	-	-	10.61 $\pm$ 0.00
3	$(2b_1, \pi_2)^{-1}$ $(10a_1, n_{N+})^{-1}$	11.60 $\pm$ 0.25	0.95 $\pm$ 0.30	-	-	11.25 $\pm$ 0.05

[a] Average values are given, see Appendix Table B.2 for further details.

studies[177,195]. The lowest ionization feature, $(8b_2, n_{N-})^{-1}$, peak BE and FWHM was extracted from the non-resonant photoelectron spectra described in Section 5.1.1. The peak BE around 10.8 $\pm$ 0.1 eV is associated with electron removal from a π orbital, which has a slightly higher BE in the aqueous phase. The next two orbitals, $(2b_1, \pi)^{-1}$ and $(10a_1, n_{N+})^{-1}$ also exhibits higher BEs in the aqueous phase. Their contributions to the aqueous-phase were identified at a 11.6 $\pm$ 0.2 eV peak BE. Similar BEs have been extracted from the resonantly enhanced valence PE spectra recorded following photoexcitation from the C_1 or C_3 atomic sites, see Figure 5.13b.

Pyrazine Valence Band Figure 5.14a shows the comparison of the resonance valence bands recorded in the vicinity of the N and C K-edges. The red curve shows the N pre-K-edge data and the green curve shows the C pre-K-edge resonant valence band contributions. The associated four outer-valence ionization channels are shown in more details in Figure 5.14b. The low BE region (8-13 eV) is only associated with participator Auger contributions and provides spectral information about the outer valence ionization channels, which are the four lowest MO contributions in aqueous pyrazine. Figures 5.14c and 5.14d shows the cumulative Gaussian profile fits to the N and C pre-K-edge resonant-excitation valence PE spectra. Table 5.6 shows the extracted BEs and the peak FWHM's associated with the aqueous pyrazine solute.

Similar to the pyridazine and pyrimidine data treatment, the aqueous pyrazine HOMO feature, $(6a_g, n_N)^{-1}$ is fixed at a BE around $\sim$9.5 $\pm$ 0.1 eV during the fitting procedure, based on the BE extracted in the non-resonant experiments. The other ionization peaks were fit as free parameters. The MO's shown in Table 5.6 were extracted from the RPES study on aqueous pyrazine and are assigned in accordance with previous gas-phase studies[176]. Table 5.6 also reports the gas phase valence ionization energetics of pyrazine[176].

As discussed in the non-resonant excitation section, the HOMO, $(6a_g, n_N)^{-1}$, has a slightly lower BE in the aqueous phase. Such a BE difference arises due to the solute hydrogen bonding with the solvent water molecules in the aqueous solutions. The next higher BE's at $\sim$10.2 $\pm$ 0.2 eV and $\sim$10.6 eV $\pm$ 0.3 are extracted from the N and C K-edge resonant valence spectra, respectively, see in Figure 5.14b. As the non-bonding orbitals arise from the N atoms in the pyrazine molecule, it is expected that the corresponding BE's should be most readily extracted by selectively exciting from the N site of the molecule. As a result, the $\sim$10.2 $\pm$ 0.2 eV is assigned to the non-bonding N-lone-pair orbital, $(5b_{1u}, n_N)^{-1}$. The spectral peak around $\sim$10.8 $\pm$ 0.3 eV is assigned to the π-bonding-like molecular orbital of $(1b_{1g}, \pi)^{-1}$ symmetry, which has predominant C-atom electronic structure contributions[40,199]. Considering the previous gas-phase study[176], this finding suggests that the MO ordering between the $(5b_{1u}, n_N)^{-1}$ and $(1b_{1g}, \pi)^{-1}$ changes in the aqueous solution

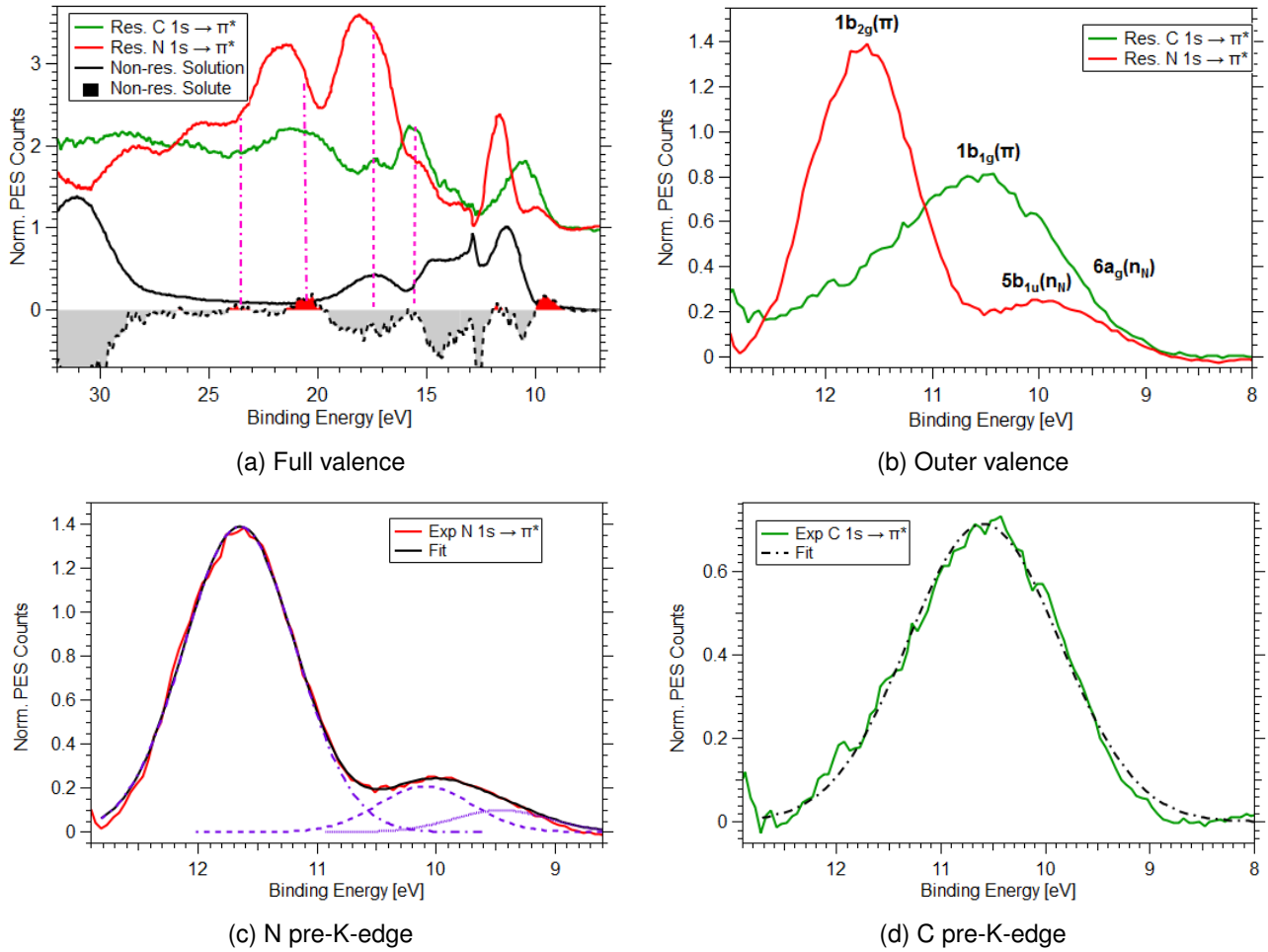

(a) Full valence

(b) Outer valence

(c) N pre-K-edge

(d) C pre-K-edge

Figure 5.14: (Panel a) Background-subtracted resonant valence band XPS spectra of 500 mM pyrazine at different XA resonances, N K-edge (red), C K-edge (green). All of these resonances corresponds to 1s $\rightarrow$ LUMO excitations. The non-resonant solution (black) and solute valence (filled plot, reproduced from panel (b) Figure 5.3) spectra are shown. The non-resonant solute spectral intensities, which were recorded using 150 eV photon energy are arbitrarily scaled for visualization. Panel b shows the outer four MOs of aqueous pyrazine and their assignments. Panel (c) shows a cumulative Gaussian-peak fit to the N-1s $\rightarrow \pi^*$ resonantly enhanced XPS spectrum. Panel (d) shows similar fits at the C_2-1s $\rightarrow \pi^*$ resonantly enhanced XPS spectrum. More details are given in the main body of the texts.

with respect to in the gas-phase. The next higher BE of the $(1b_{2g}, \pi)^{-1}$ MO, around $\sim$11.6 $\pm$ 0.1 eV, is also extracted from the N K-edge resonant valence spectra.

Table 5.6: Pyrazine outer valence electron BE's and the peak FWHM's obtained via Gaussian fits to the RPES measurement data. The aqueous-phase results are compared to the gas-phase results. During the fitting procedure, the BE and FWHM associated with the lowest-energy ionizing transition were fixed to the values determined in the non-resonant XPS experiments reported in Section 5.1.1. The ionization channels are assigned based on the gas-phase studies[176,181,195]. More details are given in the main body of the texts.

Peak	Features	Resonant		Non-resonant		Gas[a]
		BE (eV)	FWHM (eV)	BE (eV)	FWHM (eV)	BE (eV)
1	$(6a_g, n_N)^{-1}$	9.50 $\pm$ 0.04	0.95 $\pm$ 0.05	9.5 $\pm$ 0.04	0.95 $\pm$ 0.05	9.55 $\pm$ 0.07
2	$(5b_{1u}, n_N)^{-1}$	10.22 $\pm$ 0.15	1.20 $\pm$ 0.40	-	-	11.34 $\pm$ 0.02
3	$(1b_{1g}, \pi)^{-1}$	10.60 $\pm$ 0.10	1.65 $\pm$ 0.10	-	-	10.20 $\pm$ 0.01
4	$(1b_{2g}, \pi)^{-1}$	11.64 $\pm$ 0.05	1.20 $\pm$ 0.06	-	-	11.80 $\pm$ 0.01

[aa] Average values are given, see Appendix Table B.3 for further details.

The above discussion highlights that the valence electronic structure of the diazine molecules consist of a high density of ionization channels, many of which have spectrally broad PE features. In addition to the inherent inhomogeneous broadening in the aqueous phase, lifetime broadening comes into play due to the resonant excitation, resulting in increased spectral widths of the photoemission peaks.

5.4.2 Comments on the Inner Valence Ionization Features: BEs Above 13 eV

The non-resonant valence spectrum (difference spectra) of pyrimidine shows two photoelectron bands at 20.5 eV and 24.2 eV. Similarly, pyridazine also shows two photoelectron bands at 20.3 eV and 24.9 eV. Only one photoelectron band around 20.3 eV is identified in pyrazine. These energy positions are marked using dashed-dotted lines in the (a) panels in Figures 5.12, 5.13, and 5.14 and ionization channels are expected to be present in the resonantly enhanced valence band spectra. Only the pyridazine resonantly enhanced valence spectra closely match the non-resonant ionization channels at 20.3 eV and 24.9 eV, while the others seems to be overlapped with the broad spectator Auger channels. Therefore, their features/ spectral peaks are not clearly distinguishable in the resonantly enhanced valence band data.

Another way to identify the resonance Auger feature is to compare the valence spectra at both the C and N pre-K-edges. Similar resonant enhancement/spectral peak positions at both the C and N pre-K-edges can be assigned to the participator Auger channels. Three such spectral positions are marked in the Figure 5.12a using dashed line around 15 eV, 16.5 eV, and 25.5 eV of aqueous pyrimidine. The former two were under the water background in the non-resonant excitation and the latter one was not visible due to too poor a signal-to-noise ratio or having lower ionization cross-sections. Around 15 eV, the C_1 atom has the dominant contribution, whereas around 16.5 eV, the C_2 atom has the dominant contribution. According to previous gas-phase studies[176,195], a number of ionization channel peaks, $(6b_2, \sigma)^{-1}$/ $(9a_1, \sigma)^{-1}$/ $(5b_2, \sigma)^{-1}$, may be present in the 15-17 eV BE region. For pyridazine, two photoelectron peaks, around 14 eV and 16 eV are also resonantly enhanced in both the C and N pre-K-edge resonant valence band spectra and may be the signature of the $(1b_1, \sigma)^{-1}$ and $(6b_2, \sigma)^{-1}$ ionization features[195]. In addition, considering the relatively narrow spectral linewidths of the participator Auger, the photoelectron peaks around 16.5 eV in pyrimidine and 16 eV in pyridazine can be also assigned as the dominant peaks contributions. For pyrazine, both the C and N pre-K-edge resonantly enhanced valence band spectra show enhancement at BEs of around 15.5 eV and 17.5 eV, which may be the signature to the $(4b_{2u}, \sigma)^{-1}$ and $(2b_{3u}, \sigma)^{-1}$/$(5a_g, \sigma)^{-1}$ ionization features[176].

Although, several participator Auger spectral positions can be coarsely identified, a precise characterization of the higher-BE (>13 eV) participator channels require identification of the spectrally-broad spectator Auger features. RPES spectra provide rich information about the photoexcited state but previous aqueous-phase studies have yet to report robust ways to separate the participator and spectator Auger features[20]. Bolognesi *et al.*[88] studied gas-phase pyrimidine and isolated some N K-edge spectator-like Auger processes in resonantly enhanced valence band spectra by comparing the calculated non-resonant N KV_1V_2* Auger spectra. However, the study did not discuss the related participator ionization channels in the higher BE range. Dudde *et al.*[182] performed a RPES study on pyrazine on a Cu substrate, and described the participator process similar to a shake-up process, where the spectator channel behaves like a non-resonant Auger processes. Previous studies show that the non-resonant Auger electron will appear in a lower KE range compared to the resonant (spectator) Auger processes and that some KE shift is required to overlap the spectral profiles of the non-resonant and resonant Auger spectra[88,89]. Therefore, spectator-like Auger spectral features may be identified through comparison with the non-resonant (normal) Auger electron spectra. However,

*K represents the core level hole, V_1 is the relaxing electron's initial state, and V_2 is the emitted electron's initial state.

two notable uncertainties remain. First, the spectral intensity profiles of the spectator-like and non-resonant Auger processes will generally vary with incident photon energy, preventing a direct scaling and subtraction of energy-shifted non-resonant Auger spectra from resonant Auger spectra to isolate the participator contributions. Second, this approach neglects the electronic correlation effects and spectral profile differences that will arise between photoemission peaks associated with the 2h2e non-resonant Auger and 2h1e resonant Auger final states. For these reasons, further comments on the dominant electronic characters of the inner valence (BEs > 13 eV) MO's of the aqueous diazine molecules cannot be reliably made. Rather, the identification and assignments of such resonantly enhanced Auger features require state-of-the-art theoretical calculations of the electronic structure and ionization dynamics of these molecules in the solvent environment to simulate the Auger spectra. Further scientific investigations are correspondingly required to assign and separate the inner-valence participator and spectator resonant-Auger spectral features, which is beyond the scope of this thesis work. .

5.5 Solvent Effects in Aqueous Diazine Solutions:

Valence and Core-level Shifts in the Non-Resonant XPS Study: The BE of the HOMO is slightly lower for the pyrimidine and pyrazine solute, compared to in the gas phase, while pyridazine has a slightly higher BE in aqueous solution compared to in the gas phase. All of the C 1s and N 1s core level BE's are lower in the solutions compared to in the gas phase. Furthermore, the photoemission features are inhomogeneously broadened in the aqueous solutions, due to the distribution and ever-changing local H-bond coordinations, each giving rise to different BE's in the solution phase[140]. Table 5.1 shows the gas-to-aqueous phase BE shifts of the studied ionization channels for all three diazine molecules. The difference in BE between the gas and aqueous phases has a number of causes, such as the electrostatic energy associated with H-bonding in the cationic states not being the same as in the ground states, intermolecular charge screening, induced polarization effects, long-range electrostatic interactions, and/or differences in the molecular relaxation contributions to the final states[140].

The BE's of the aqueous diazines are shifted more in the core-levels ($\sim$0.3-0.5 eV) compared to in the valence bands ($\sim$0.05-0.1 eV). The valence orbitals may be bonded and sp^2-hybridized with the water molecules through hydrogen bonds or other covalent bonds. Depending on the strength of the bonding, charge redistributions can take place between the solute and solvent molecules, with the valence MO character being altered to a greater degree than the core orbitals[140]. The electron density in the valence orbitals are more delocalized, which means that the electronic wavefunctions are distributed through the participating atoms that form the MOs. However, the delocalized valence MO's in the aqueous solutions are less affected compared to the core-levels by electrostatic stabilization[140]. As the electron density in the core levels are highly localized around the atoms, electrostatic stabization effects are more pronounced in the core-levels of the aqueous diazines. Similar behavior is also found in liquid water[66,82,140], as described in Section 2.5.1, Chapter 2. The valence band (HOMO) of water is also found to be less shifted compared to the core-level (O 1s). Specifically, the HOMO, $1b_1$ photoemission peak is shifted by 1.45 eV, where as the O 1s peak is shifted by 1.77 eV[140]. The valence-and core-level BEs shifts in the aqueous diazine solutions are lower than observed for liquid water BEs[140]. Notably, similar to the water system, valence and core-level gas-to-liquid phase BE shifts are also found to be larger in small hydrogen bonded molecules such as ammonia[278]. In contrast, similar to the diazines, the shifts have been found to be smaller for larger polyatomic molecules[279].

Core-Level Energy Shifts Among the Diazine Isomers: The N 1s BE of the diazine molecules decreases from pyridazine to pyrazine and to pyrimidine. The opposite trend is observed for C 1s ionization, *i.e.* pyrim-

idine has the highest and pyridazine has the lowest C 1s BEs, see Section 5.1.2. Neglecting the final state effects after the core (N 1s and C 1s) electron ionization processes will offer further potential insights into the diazine electronic structures. Pyrimidine has the most electronegative N atoms among the diazine molecules, with the N atoms pulling electron density from the neighboring C atoms. Consequently, the C_1 atom in the pyrimidine molecule is more electropositive, see Figure 1.1, Chapter 1. The two N atoms withdraw an equal amount of electron density. Thus, pyrimidine has the highest BE at the C_1 atomic site among the diazines. Relatedly, the diazines are known to be proton acceptor molecules in the aqueous phase[37]. As the highest electronegativity N atom is the better proton acceptor, pyrimidine is predicted to be the best proton accepting agent in the aqueous diazine solutions[37].

Charge Re-arrangement and Change of the Bonding Character As mentioned above in Section 5.1.2, core-level PES measurements can provide background-free, site- and element-specific information about the core-electron BE chemical shifts in different environments. Moreover, a comparison with the previously reported isolated-phase molecule and results from aqueous pyrimidine solution[191,194], the core-level BE chemical shifts suggest changes in the bond lengths of aqueous pyrimidine due to intramolecular charge re-arrangement. Similar conclusions can be drawn from the PEY-XAS results, as shown in Section 5.2.

Panels (b) and (d) of Figures 5.6, 5.7, and 5.8 show the gas-to-liquid phase spectral comparisons at the C and N pre-K-edges of the diazines. Shifts of the gas-to-liquid phase resonance photon energies and changes of spectral intensities are found at both edges. One possible reason for the changes in the spectral intensities, compared to in the gas phase, is variations of the localization or delocalization of the valence band MO's in the aqueous phase. Another possible reason is a change of bonding character in the aqueous phase. As discussed in Chapter 2, the pyrimidine molecule accepts two strong hydrogen bonds via the lone pair electrons of the nitrogen atoms. Hydrogen bond formation in aqueous solution may cause a change of the bonding character[271]. Since the resonant transitions are predominantly governed by dipole selection rules, the change of spectral intensities may reflect the associated changes in bonding character and/or molecular symmetry due to the presence of fluxional hydrogen bonding environments in the aqueous solutions[271,280].

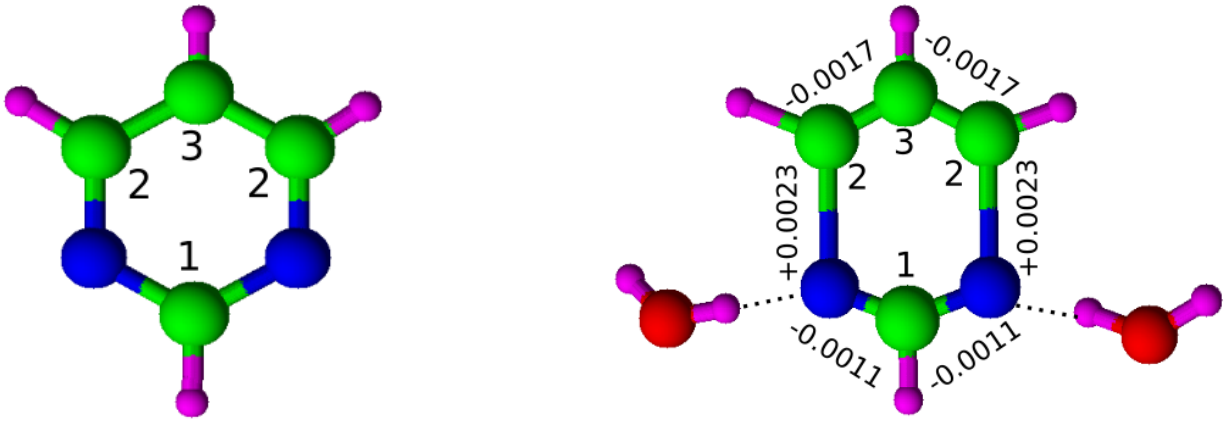

(a) Pyrimidine in isolated phase (b) Pyrimidine in aqueous solution

Figure 5.15: Changes in intramolecular bond lengths in aqueous pyrimidine. The blue, green, and purple color label the N, C, and H atoms, respectively. The bond lengths and concepts for the illustration are taken from the results published in References 191,192.

Gas-to-liquid phase shifts in the core-to-virtual valence transition photon energies could also be related to the changes of the molecular bond lengths due to intra- and intermolecular charge rearrangement processes in the aqueous solution[92,191,271,280]. In aqueous pyrimidine, the gas-to-liquid phase spectral shifts may indi-

cate associated changes of $C_{2/4}$-N and C_1-N bond lengths due to solvation[191,192,194]. Figure 5.15 shows an molecular structure illustration, where the bond length changes are indicated based on the studies performed using vibrational spectroscopy on aqueous pyrimidine[191,192]. Similar effects are also expected in the other diazine isomer molecules. The pyridazine PEY-XAS aqueous phase spectra also highlight noticeable changes in spectral positions and intensities compared to the gas-phase XAS spectra, as shown in Figures 5.6b and 5.6d. The C pre-K-edge spectra are red-shifted, whereas the N pre-K-edge spectra are blue shifted. Similar to pyrimidine and pyridazine, the aqueous pyrazine PEY-XAS spectra show changes of spectral intensities and positions compared to the gas-phase XAS spectra (see Figures 5.7b and 5.8d), again likely reflecting a change of molecular bonding character and redistribution of charge density between the diazine and water molecules in aqueous solution[92]. Similar to the effects exhibited in the UV-Vis absorption study described in Chapter 2, Section 2.5.3, pyridazine shows the highest gas-to-liquid-phase spectral shift of the XA spectra among the diazines.

In all of the studied aqueous solutions, the most intense absorption peak is associated with the N 1s $\rightarrow$ LUMO (π^*) transition, which is much larger than the N 1s $\rightarrow$ LUMO+1 transitions, suggesting that the electronic wavefunction of the LUMO is more core-localized. The N 1s $\rightarrow$ LUMO+1 transitions in pyridazine and pyrimidine are optically allowed, but it is found to be significantly weaker than the N 1s $\rightarrow$ LUMO transition. Such an intensity variation was also found in the previous gas-phase study[175], as well as in a transmission mode XAS study in aqueous solutions[92].

As inferred in the pyrazine resonantly enhanced valence band analysis, the cationic state energetic ordering seemingly changes in the aqueous phase compared to in the isolated phase. Additionally, Figures 5.13b, 5.12b, and 5.14b show a change of spectral intensities between the C and N pre-K-edge outer valence band regions (BEs 9-12 eV range) of the aqueous diazines. As discussed in Section 5.1.1, the spectral intensity associated with the participator Auger photoemisison processes are due to the core-to-valence electric dipole transition matrix overlap integrals associated with the photoabsorption process and the electronic overlap integrals of the highly excited neutral and final cationic states. In the C and N K-edge resonant excitation processes and subsequent participator Auger processes, the final states are the same. The differences lie in the initial and intermediate states. Thus, one possible reason for the differences of the spectral intensity in the N K-edge resonantly enhanced valence PE spectra compared to the analogous C K-edge PE spectra is the difference in the photoabsorption cross-section and photo-excitation probabilities.

A comparison of the valence band spectral intensities following N and C pre-K-edge excitation may also indicate changes of the atomic parentages in forming the valence bands in the aqueous phase. A Mulliken population analysis reported for the gas-phase pyrimidine molecule[88] suggests that in the isolated molecule, three of the four outer valence orbitals– $7b_2$ ($\sim$9.6 eV),$11a_1$($\sim$11.2 eV) and $1a_2$($\sim$11.2 eV)– have dominant N character, while the $2b_1$ ($\sim$10.2 eV) orbital is a C dominated MO. Similar to pyridmine, the non-bonding pyrazine MO's $6a_g$($\sim$9.46 eV) and $5b_{1u}$($\sim$10.2 eV) are formed by the lone pair electrons at the N site and these MO's should have dominant N character. Moreover, considering atomic photoabsorption probabilities, the N 1s $\rightarrow$ LUMO ($\pi*$) transition has a higher cross-section compared to the C 1s $\rightarrow$ LUMO ($\pi*$)[281,282]. Bolognesi *et al.*[88] correspondingly reported higher spectral intensities in the 9-12 eV BE region of the pyrimidine valence band when exciting at the N pre-K-edge, in comparison to the spectral intensity following C pre-K-edge excitation. However, this is not the case in the aqueous pyrimidine and pyrazine systems, as shown in Figures 5.12b and 5.14b. Pyrimidine shows reduced spectral intensities in the 9-12 BE region in the N pre-K-edge resonantly enhanced valence spectra compared to the analogous C pre-K-edge spectra. Reduced spectral contributions are highlighted in Figure 5.14b along the non-bonding orbital spectral positions in the N K-edge resonantly enhanced valence PE spectra of pyrazine. This may indicate a change in

the degrees of localization in the excited state or an increased delocalization of the valence electrons. Such a spectral intensity reduction at the N pre-K-edge resonance may be a signature of the reduced electron density at the N lone pair MO's due to charge transfer processes from the solute to the solvent water molecules[89]. A reduced (increased) population at the N (C) atomic sites may lead to reduced (increased) spectral intensities in their respective resonantly enhanced valence band spectra.

Similar to pyrimidine and pyrazine, the pyridazine non-bonding MO's are formed by the lone-pair electrons at the N site and should have dominant N character in the resonantly enhanced valence PE spectra. In contrast to pyrimidine and pyrazine, the pyridazine RPES study at the N and C site highlights significantly higher spectral weights in the resonantly enhanced valence spectra following N pre-K-edge excitation compared to the C pre-K-edge. Being an isomer of pyrazine and pyrimidine, pyridazine is also expected to display similar behaviors, such as electronic delocalization due to charge transfer processes. Perhaps the difference in the photoabsorption cross-section between the N and C K-edges is large enough that such effects in the pyridazine RPES spectra ae hidden. It can also be that a water-bridge between the two N-atoms allows proton-transfer and/or charge-transfer effects, which affect the electronic structure.

Combining XPS and PEY-XAS (Neglecting Electron-Electron Correlations and Final State Effects): Similar to a former gas-phase XAS study[175], two aqueous-phase x-ray absorption features have been identified for the symmetry-unique C atoms in pyridazine at around $\sim$284.9 $\pm$ 0.2 eV and $\sim$285.8 $\pm$ 0.2 eV. These features have a separation of 0.8 $\pm$ 0.3 eV. Ignoring final state effects, such an energetic separation can be attributed to the energetic gap between the C_1 and C_3 atoms, which is very similar to the gas-phase separation. Considering the average BE (291.2 $\pm$ 0.2 eV) of the two atoms obtained in the XPS measurements and the XAS resonance energy separation of 0.8 $\pm$ 0.3 eV, the BE's of the two atomic sites in the aqueous phase can be concluded to be $\sim$290.8 $\pm$ 0.2 eV and $\sim$291.6 $\pm$ 0.2 eV. Combining the N and C pre-K-edge PEY-XAS resonances with the XPS measurement results and ignoring electron correlation effects, the BE of the LUMO, $2a_2$ orbital is estimated to be $\sim$6.1 $\pm$ 0.2 eV. From the N pre-K-edge PEY-XAS spectrum and ignoring electron-electron correlations, an energy gap of about $\sim$1.5 $\pm$ 0.2 eV between the LUMO and LUMO+1 can be obtained.

Similar to pyridazine, additional information can also be obtained from the PEY-XAS studies on the aqueous pyrimidine and pyrazine solutions. The N pre-K-edge absorptions measurements on aqueous pyrimidine correspondingly suggest energy gaps between the LUMO and LUMO+1 and LUMO+3 of around $\sim$1.1 $\pm$ 0.1 eV and $\sim$4.0 $\pm$ 0.1 eV, respectively. Moreover, combining the N and C pre-K-edge absorption results with the XPS measurement results, the BE of the LUMO, $2a_2$, orbital can be inferred to be $\sim$5.8 $\pm$ 0.2 eV. The C pre-K-edge resonances in pyrimidine allow C_2-to-C_1 atomic spectral separations of 0.5 $\pm$ 0.2 eV to be inferred. Considering the average BEs of the C_1 and C_2 atoms of about $\sim$291.9 $\pm$ 0.1 eV, the other two aqueous-phase BEs can are determined for the C_2 and C_1 atoms, which would be $\sim$291.7 $\pm$ 0.2 eV and $\sim$292.1 $\pm$ 0.2 eV, respectively. The C pre-K-edge absorption measurements on aqueous pyrazine suggest an energy gap of around $\sim$0.8 $\pm$ 0.2 eV between the LUMO and LUMO+1. The N pre-K-edge absorptions measurements suggests an energy gap between the LUMO and LUMO+3 of around 4.2 $\pm$ 0.2 eV, where electron correlation effects have again been neglected. Combining the C and N pre-K-edge absorption results and the XPS measurements, the BE of the LUMO is estimated to be $\sim$6.3 $\pm$ 0.2 eV.

5.6 Summary of XPS and RPES Studies on the Aqueous Diazines

XPS, PEY-XA, and RPES studies have been performed to investigate the electronic structure of the aqueous diazine molecules. The important findings of the XPS and RPES studies are:

I Vertical ionization energies (VIE)'s of the HOMO ionization channels of pyrimidine, $(8b_2)^{-1}$, pyridazine, $(7b_2)^{-1}$, and pyrazine, $(6a_g)^{-1}$, have been determined using non-resonant surface- and bulk-sensitive XPS measurements. The VIE's and FWHM's of the ionization features do not vary with photon energy and, by extension probing depth, within the energy resolution of the experiments. Additional valence band information has been obtained via RPES measurements on the aqueous diazine molecules, which reveal solute signals that are usually hidden under the solvent water background signal. Therefore, combining the XPS and RPES results, the first four valence ionization channel energies have been identified. Such findings are important for the interpretation of the excited-state ionization features in UV-pump and EUV-probe TRPES experiments, as described in Chapter 6. The associated results are summarized in the Table 5.1, 5.4, 5.5, and 5.6.

II Gas-to-liquid phase BE shifts have been identified in the valence and core-level ionization channels. Additionally, PEY-XA spectra of the aqueous diazine molecules highlighted gas-to-liquid phase shifts in the core-to-virtual-valence transition photon energies as well as change in the transition spectral amplitudes. Gas-to-liquid phase ionization or absorption shifts can be related to intra- and intermolecular charge reorganization effects. The change in spectral intensities have been linked to localization/ delocalization of the valence band MO's, or a change to the molecular bonding character in the hybridized valence MO's.

III Two ionization channels in the higher BE region (> 18 eV) have also been obtained in the non-resonant XPS studies on the aqueous diazine. The ionization features have been assigned based on previous gas-phase studies. Additional ionization features are also present in the recorded RPES spectra in the higher BE regions in the form of participator Auger channels. However, these features overlap with the spectator-like Auger channels. Information on the VIE's of the inner valence features are important to identify the changes in the inner valence features in future UV-pump and EUV/soft x-ray (resonant) probe TRPES experiments. However, separation of such channels cannot yet be achieved and are beyond the scope of this thesis.

IV The valence band spectral intensities at the N and C pre-K-edges are compared to try to identify the changes in the atomic parentages and delocalization of the valence ionization channels due to charge re-arrangement processes in the aqueous solution. Moreover, aqueous-phase pyrazine has been inferred to show a change in the ordering of its cationic states, $(1b_{1g}, \pi)^{-1}/(5b_{1u}, n_N)^{-1}$, in comparison to in the gas-phase, based on the resonantly enhanced valence spectra.

V Additional information on the VIE's of the unoccupied valence MOs as well as the splitting of the C 1s core-level BEs have been extracted by combining the XPS and PEY-XA results and neglecting final state effects and electron-electron correlations.

Chapter 6

Photoinduced Electronic Relaxation Dynamics in Aqueous Pyrazine: A Time-Resolved Photoelectron Spectroscopy Study

Chapter Objectives and Scientific Contributions:

1. Investigation of the excited-state electronic structure and associated ultrafast relaxation processes of the solute under PISC-minimized conditions (see Section 6.3 and 6.5).
2. Comparison of results with and without PISC effect and importance of using lower pump-pulse intensity in studying femtosecond relaxation dynamics in the liquid solution using TRPES (see Section 6.7).
3. Data modeling and spectral analysis using the global fitting procedure (see Section 6.6 and 6.8).
4. Comparison of the current results with the previously reported gas-phase time-resolved studies[39,40,50,283] (see Section 6.9).
5. Identification of how the environment (solvent) influences the electronic structure and associated sub-ps relaxation dynamics of the solute in the aqueous-phase (see Section 6.9).
6. Investigation of the involvement of the dark, A_u, state in relaxation dynamics in the aqueous phase, which was predicted theoretically[211,212] and observed experimentally[40] in the gas-phase (see Section 6.9).

To address the points outlined above, 500 mM aqueous pyrazine solutions were studied using the liquid-microjet-based TRPES technique. Laser pulses of 267 nm wavelength and $\sim$25 GW/cm^2 peak intensity were applied to resonantly excite the system from the S_0 to S_2 states under pump-induced-space-charge-minimized conditions. EUV pulses of 32.1 nm wavelength and 45 fs pulse duration were used to monitor the relaxation process by photoionizing the ground and excited states. Details of the sample preparation, energy calibration, and experimental setup are described in Sections 3.2, 3.3.3, and 3.4, respectively.

6.1 Ground-State PE Spectra of Aqueous Pyrazine

In the chapter 5, the cationic state energetics of aqueous pyrazine have been identified by recording non-resonant and resonant x-ray PE spectra of 0.5 M aqueous solutions at the BESSY II synchrotron facility in

Berlin. Table 5.6 in Chapter 5 shows the Vertical Ionization Energies (VIEs) of the first four cationic states of aqueous pyrazine and their symmetries. In this chapter, these cationic state energetics will be used to identify the excited state features in TRPES experiments. The time-resolved study of aqueous pyrazine was carried out with the use of HHG-based EUV radiation. Figure 6.1 highlights the spectra recorded with the EUV pulses alone, with and without the application of a bias voltage of -40V to the liquid microjet. The application of the bias voltage allows the photoemission contributions from the gas phase to be minimized in the recorded spectrum[66]. The photoemission bands associated with the MOs of water and pyrazine are labeled in the figure. The known liquid water $1b_1$ BE of 11.33 $\pm$ 0.04 eV[66,243] has been used to calibrate the kinetic-energy scale. The $1b_1$ spectral intensity of each PE spectrum shown in this chapter has been normalized to one.

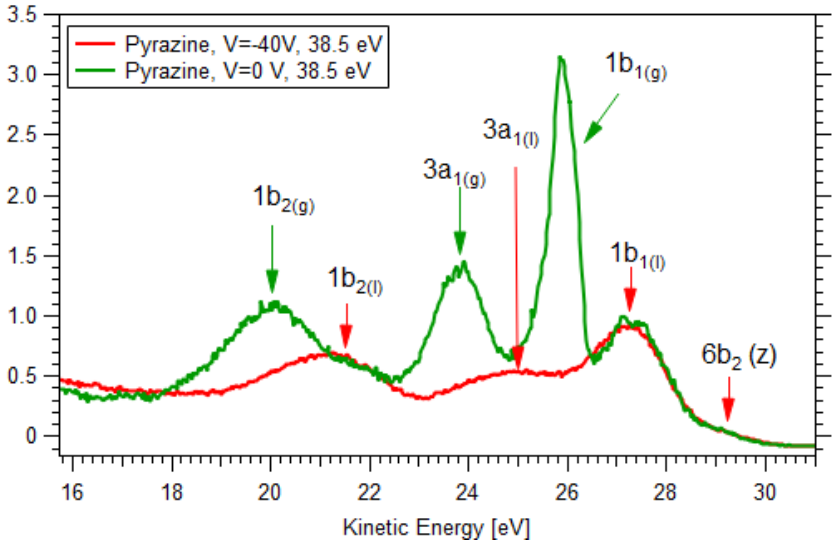

Figure 6.1: EUV-induced photoemission spectra of 500 mM aqueous pyrazine solutions. The red and green curves show results obtained with a bias voltage (V=-40 V) and without a bias voltage applied to the liquid jet, respectively.

Like the case of non-resonant X-ray excitation described in Chapter 5, most of the solute spectral contributions that are shown in Figure 6.1 are hidden under the water background. Only the $(\text{HOMO})^{-1}$ contribution of the aqueous pyrazine, $6b_2$, can be clearly identified in the higher KE range. Due to the larger spot size of the EUV beam ($\sim$60 μm 1/e^2) compared to the liquid microjet size (25 μm), the green spectrum in Figure 6.1 shows a relatively high gas-phase contribution. However, as shown in the red spectrum, the negative bias voltage of -40 V minimizes the gas-phase contributions in the KE window of interest. The pyrazine vapor pressure ($\sim$20 mbar) is comparable with the water vapor pressure. The comparison between the red and green spectra in Figure 6.1 demonstrates that there is almost no gas-phase pyrazine contribution above 26.5 eV KE (or below 12 eV BE) in the steady-state signals.

6.2 Experimental Time-Resolution Charactarization

The experimental setup for liquid microjet-based TRPES is described in Section 3.4 in Chapter 3. The time resolution of the experiments reported here were determined by recording the CC signal of the pump and probe laser beams using 50 mM aqueous NaCl solutions. The advantage of using the 50 mM aqueous NaCl solutions for the CC measurements is that this solution does not absorb 267 nm light (at least at the one-photon level). On the other hand, aqueous pyrazine solutions resonantly light absorb the single-photon level at a 267 nm wavelength, resulting in asymmetric pump-probe signals on top of the CC signal and on the relevant timescale for determining the experimental time resolution. The CC measurements performed with

the $NaCl_{(aq.)}$ solutions were used to determine 65-85 fs time resolutions in the experiments reported here, depending on the details of the laser compressor settings and pump beam line parameters adopted in the different beam times. In Figure 6.2, an example of a CC measurement that was recorded before performing a TRPES experiments is shown.

Figure 6.2 shows the CC signal between 4.67 eV (267 nm) pump and 38.5 eV probe pulses. The applied pump pulse energy was ∼300 nJ in these measurements. The pump beam was guided to the electron spectrometer interaction region via a delay stage, and the time delay between the pump and probe beams was tuned by moving the delay stage platform with 5 fs precision. The CC measurement was performed in the spectrometer WAM mode, which provides a wide electron acceptance angle and, thus, the highest possible electron collection efficiency. A negative retardation voltage (∼-36 eV) was applied to a grid electrode in front of the detector suppress the significantly high PE counts that can saturate the delay-line anode detector and associated detection electronics. The transfer function of the applied retardation potential does not have a step-like response, rather it steeply decreased from the high-to-low KE regions over a KE range of a few eV. Therefore, the retardation voltage affects the shape of the photoelectron spectrum at the low KE region, but does not change the transient response of the photoemission signals.

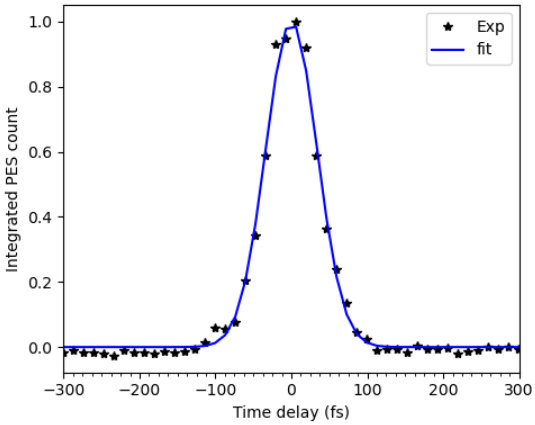

Figure 6.2: Cross-correlation of 267 nm and 32.1 nm pulses, recorded from an 50 mM aqueous NaCl solution.

Figure 6.2 shows the KE-integrated (29.3-32.0 eV) PE counts versus time-delay and highlights the temporal profile of the CC measurement. Due to the applied non-resonant single-pump-photon excitation conditions in the 50 mM aqueous NaCl solution, the temporal profile shown in Figure 6.2 has a symmetric shape. The temporal profile was fitted with a Gaussian function, and a 85 ± 5 fs temporal width (FWHM) has been extracted. This defines the 1+1', *i.e.*, 267 nm + 32 nm, experimental time resolutions. Taking into account an EUV probe pulse width of ∼ 50 fs[134] and the CC width of ∼85 fs, the measurement reveals a pump pulse duration of ∼68 fs, in this specific measurement.

6.3 Minimizing PISC Effects

Space charge effects have already been studied via TRPES of aqueous solutions[135]. Related details are discussed in Section 3.4. The KE shift caused by the photoinduced space charge strongly depends on the peak intensity of the laser pulses, which determines the ionization degree of the liquid medium. Figure 6.3 shows the results of pump-probe studies on 500 mM aqueous pyrazine solutions, performed at three different pump pulse intensities of 25 GW/cm^2, 35 GW/cm^2, and 100 GW/cm^2. This data was notably recorded with a high-pass electron-kinetic-energy filter applied at the electron detector, specificaly via a -24 V voltage application to the pre-detecotor auxiliary voltage grid. The associated time-dependent spectral shifts of the

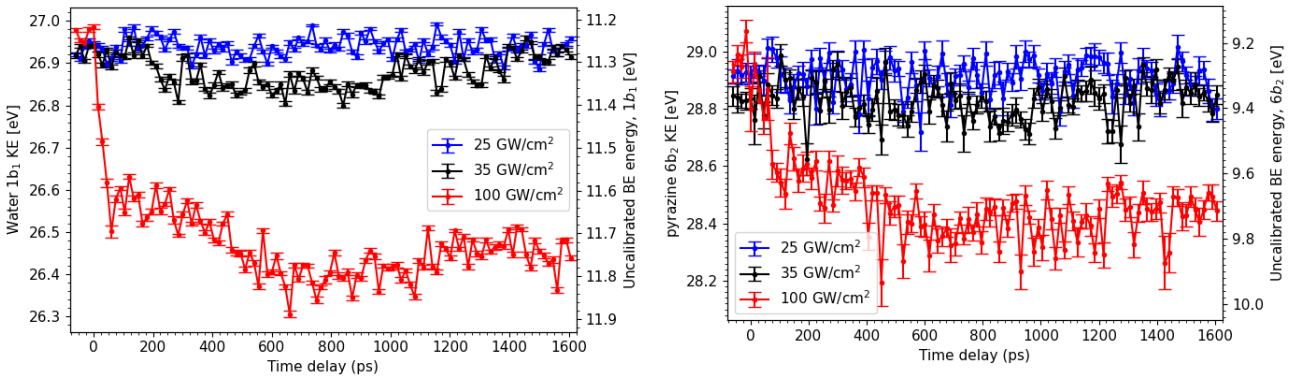

(a) Water $1b_1$ shift

(b) Pyrazine $6b_2$ shift

Figure 6.3: Pump-probe study on 500 mM aqueous pyrazine at three different pump intensity levels. Panels (a) and (b) show the photoelectron KE shift due to the space charge effect on the water $1b_1$ and pyrazine $6b_2$ features, respectively. The data shows the time-delay dependence of the KE shift for three different pump pulse intensities.

lowest-BE solute and solvent photoemission bands have been monitored and presented in Figure 6.3. Figures 6.3a and 6.3b show the KE shift of water $1b_1$ and pyrazine $6b_2$ emission bands as a function of the pump-probe delay times. One can see that the KE shifts increase at higher pump pulse intensities and larger pump-probe time delays (at least out to $\sim$1 ns delays). Application of a high pump pulse intensity of $\sim$100 $\mathrm{GW/cm^2}$ result in a significant KE shift within a 20 ps pump-probe time-delay, which maximizes at a $\sim$ 750 ps time-delay for both the $1b_1$ and $6b_2$ bands, see Figure 6.3. At this intensity level, the maximum KE shifts of the water $1b_1$ and pyrazine $6b_2$ ionization features are 0.6 $\pm$ 0.01 eV and 0.5 $\pm$ 0.04 eV, respectively. These values have been obtained by averaging the KE over the 650-750 ps time-delay range and subtracting the central KE of the peaks from the average KE values recorded at t=-50 ps, where no KE shift is expected. For a moderately high pump pulse intensity of $\sim$35 $\mathrm{GW/cm^2}$, the KE energy shifts of the liquid water $1b_1$ and pyrazine $6b_2$ are much reduced at relatively short pump-probe delays. However, KE shifts remain at a level of 0.1 eV at larger pump-probe delays. At a sufficiently low pump pulse intensity level of about 25 GW/cm^2, it was eventually found that the KE shifts essentially vanishes and cannot be detected in the entire pump-probe window and with in the experimental energy resolution. At this pump pulse intensity, the PISC effect has been minimized and at a 5 KHz experimental repetition rate and using the THEMIS spectrometer there is just enough excited-state signal to enable space-charge-free liquid-phase TRPES experiments.

Another way to cross-check the PISC effects is to measure PE spectra of aqueous pyrazine solutions at a fixed, extended pump-probe delay but at different pulse intensities. Such data are shown in Figure 6.4. A pump-probe delay of 250 ps was chosen in this measurements. The $1b_1$ feature of each pump-probe spectrum is compared to the EUV-only spectrum to highlight the PISC effects. For a high pump intensity of $\sim$100 $\mathrm{GW/cm^2}$, the KE of the water $1b_1$ peak is shifted by about $\sim$ 400 meV. As the pump intensity is decreased to $\sim$25 $\mathrm{GW/cm^2}$, the water $1b_1$ and pyrazine $6b_2$ pump-probe features cannot be differentiated from those measured with the EUV beam alone. This demonstrates that the PISC effects are minimized on an energy scale comparable to the experimental energy resolution.

6.4 Data Collection and Processing Procedure

The TRPES data have been recorded in two ways: fixed delay mode and pump-probe-delay scan mode. The measured KEs of the PEs has been transformed to yield their BEs. The BE scale is calibrated using the

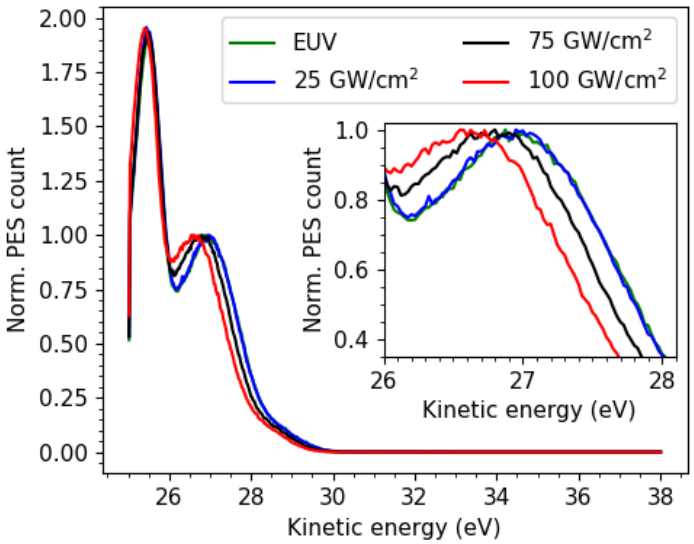

Figure 6.4: Pump pulse intensity-dependent valence PE spectra of 500 mM aqueous pyrazine at a 250 ps pump-probe delay. The inset shows the liquid water $1b_1$ KE region. The PE bands are shifted to lower KE at a higher pump-pulse intensity, whereas no shift is observed with respect to the EUV-only spectrum at a sufficiently low pump-probe intensity of 25 GW/cm^2.

nearly-neat liquid water $1b_1$ BE of 11.33±0.04 eV[66,243]. Correspondingly, it is assumed that the 500 mM pyrazine solute has no effect on the BEs of the water solvent and that the surface dipole potential of nearly-neat liquid water (pure water with 50 mM NaCl added) is equivalent to that of the 500 mM pyrazine aqueous solution. The fixed delay mode data will be discussed in Section 6.5.2. In the scan mode, PE spectra were recorded at different time delays in the range between -400 fs and 250 ps for a short acquisition time of ∼15–20 s. The spectra obtained at different time delays are plotted together, resulting in a 3D map that highlights PE counts versus time delay and BE. Such measurements were repeated to accumulate significant statistics in the spectral range of the excited states. These scans have been added together and an average has been performed to obtain a 3D map with higher signal statistics, as shown in Figure 6.5. At each delay point in the scan mode, the signal is integrated over ∼20 min. The TRPES spectra were recorded at 45 delay points. Among them, 31 delay points were implemented up to 1.0 ps delays, and the rest of them covers up to 250 ps. The results shown in Figure 6.5 are plotted over two different pump-probe delay windows denoted below as shorter and longer time pump-probe TRPES studies. The considered short-time scans cover a delay range from -400 fs to 1200 fs, whereas the long-time scan is from 1.2 ps to 250 ps.

Because of the difference in concentration of the solute compared to the solvent water molecules (500 mM (0.5 M) versus 56 M), TRPES maps (Figure 6.5a) are dominated by the $1b_1$ contributions of liquid- and gas-phase water, which appear at BEs around ∼11.3 eV and ∼12.6 eV, respectively. A small contribution of the pyrazine ground state signal is apparent at BEs around ∼9.5 eV, overlapping with the liquid water $1b_1$ shoulder. In order to visualize the excited state features of aqueous pyrazine, the TRPES maps are shown in a selected BE range of 0-8 eV in Figure 6.5b, for the short (left) and long (right) time scans. The signal-to-noise ratio of the datasets shown in Figure 6.5 is further improved by the application of 200 meV KE binning and a Gaussian filtering operation. The data recorded between -400 fs and -200 fs is averaged to define as a background signal contributions. The PE spectra recorded at each time delay is normalized by the background signal contributions and then the normalized PE spectra are background-subtracted to produce a 2D TRPES map. Such normalization allows the EUV fluctuations in each scan to be largely removed. The normalized and background-subtracted PE spectra will be analyzed below to gain information about the

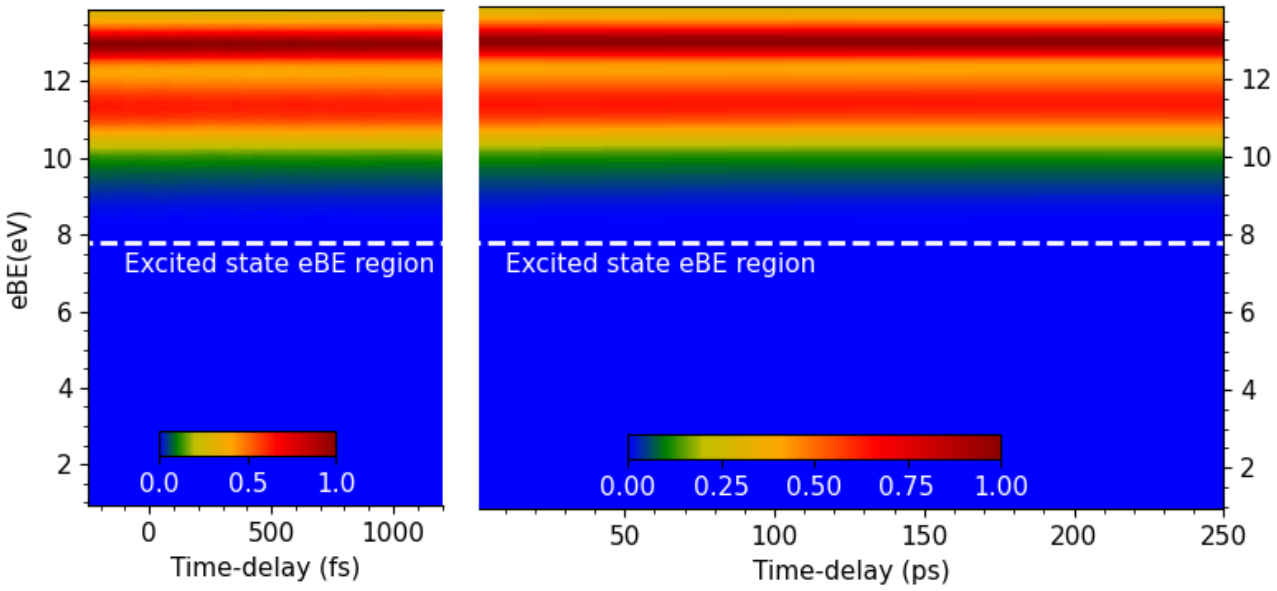

(a) Raw data, full BE range

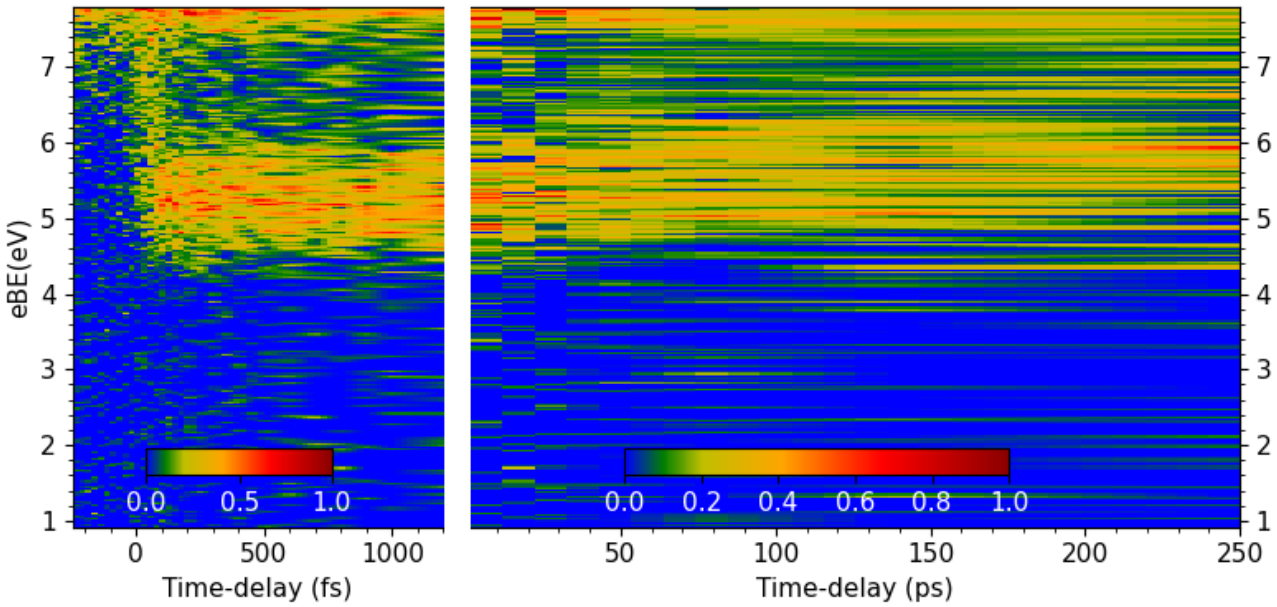

(b) Raw data, excited-state BE range

Figure 6.5: Ultraviolet (UV)-pump and EUV-probed TRPES spectra of 500 mM aqueous pyrazine, as recorded under PISC-minimized conditions (top panel). The short time-scale map (left panels) was recorded up to a delay of 1.2 ps, whereas a long time-scale map (right panels) was recorded up to a delay of 250 ps. The lower panels show the data in the spectral range where the excited state contributions can be seen in greater detail. The experiments were performed using a $\sim$25 GW/cm^2 pump-pulse intensity and with a $\sim$85 fs time resolution. For better data visualization, a linear interpolation was applied along the pump-probe time delay axis to the experimental spectra plotted above.

electronic structure and the underlying dynamics of the aqueous pyrazine excited states. For better data visualization, a linear interpolation was applied along the pump-probe time delay axis of the short time-scale and long time-scale experimental data maps. Therefore, the plotted spectra in Figure 6.5 contain 62 and 28 delay points for the shorter and longer time-scale maps, respectively. Figure 6.6 shows the processed PE signal from the pyrazine excited states, appearing in the $\sim$4.2-7.5 eV BE range. The corresponding

2D TRPES signal map is obtained based on the data processing procedure (binning, normalization, and background-subtraction) introduced above.

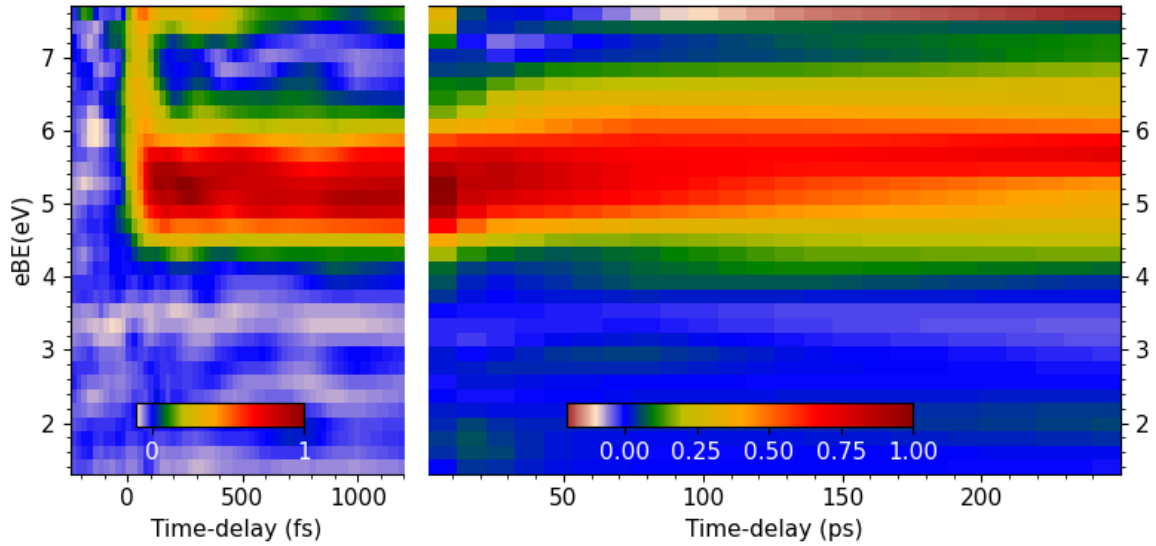

Figure 6.6: UV-pump and EUV-probed TRPES data of 500 mM aqueous pyrazine, recorded under PISC minimized conditions. The figure shows the background-subtracted and processed time-resolved data. The plotted spectra shown above have been interpolated in time for better excited-state signal visualization. See the main body of the text for further details.

Similar data processing, such as binning, filtering, normalization, and background-subtraction, have been applied to the TRPES datasets recorded under conditions where the PISC effect is present, as shown in Figure 6.6. As we have seen in Section 6.3, the PISC changes the KE of the recorded PE's and such shifts are pump-probe delay-dependent. Therefore, the space-charge correction has been applied by calibrating the BE scale of the KE spectra at each time-delay point so that the $1b_1$ peak of liquid water retains a 11.33 eV BE.

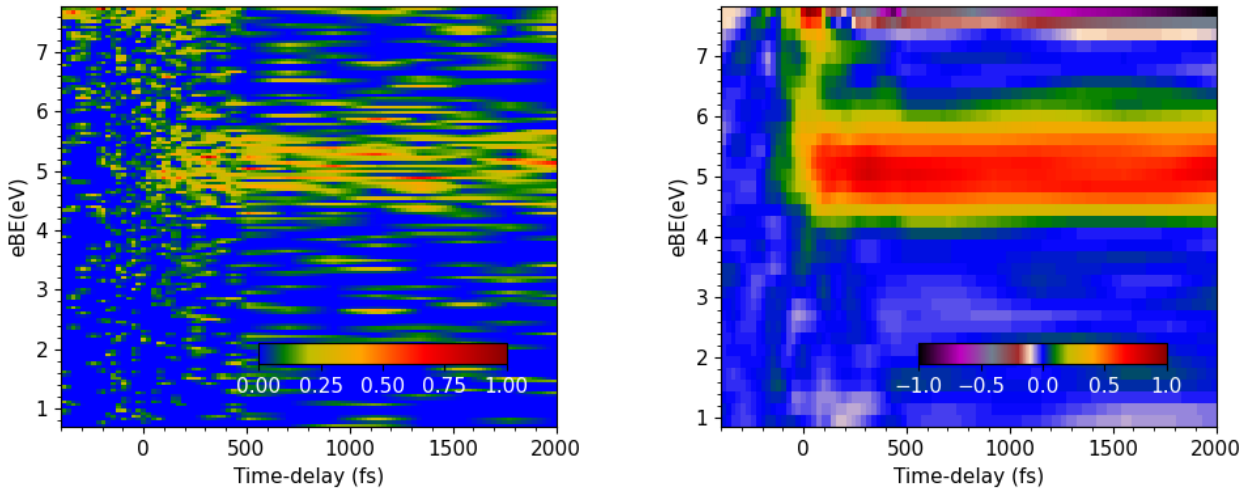

(a) Raw data, excited-state BE range

(b) Processed data, excited-state BE range

Figure 6.7: TRPES spectra of 500 mM aqueous pyrazine that have been recorded where the PISC effect was present. The experiment was performed using an 80 GW/cm^2 pump-pulse intensity and a time-delay increment of 85 fs. The left panel shows the background-corrected data in the spectral range of the low-BE excited state signals. The right panel shows the processed data after performing a five-points moving average, 250 meV binning, and filtering operations.

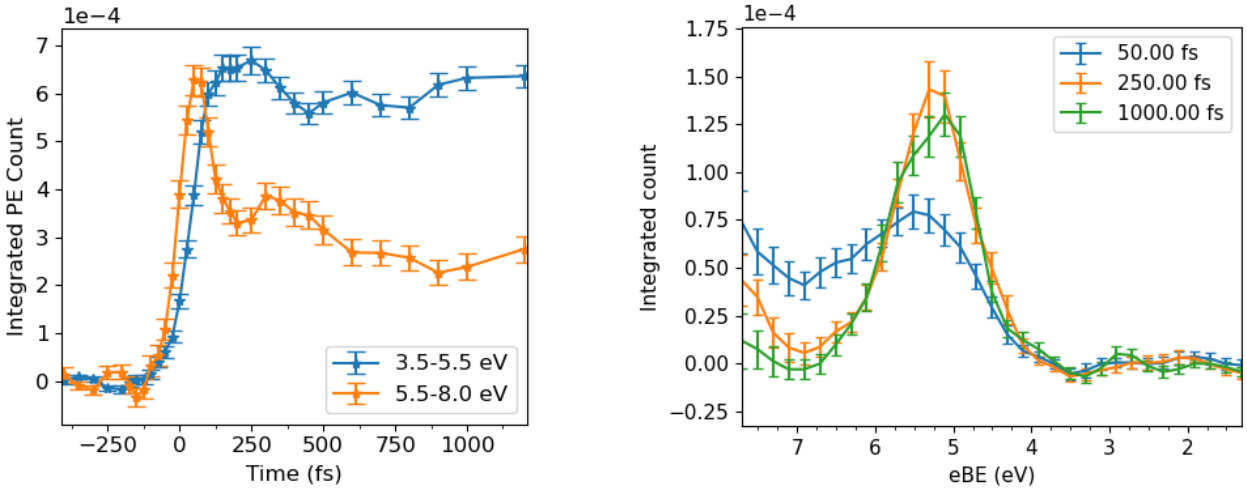

(a) Selected BE ranges

(b) PE spectra at selected delays

Figure 6.8: Short time-scale UV-pump and EUV-probed TRPES data of 500 mM aqueous pyrazine, recorded under PISC minimized conditions. Panel (a) shows the background-subtracted and processed time-resolved data. Panel (b) shows the time-dependent PE signal integrated over the 3.5-7.8 eV BE range.

6.5 TRPES Study with Minimized PISC

The aqueous-phase UV-Vis absorption spectrum and its band assignments (shown in Section 2.5.3 in Chapter 2) and previous gas-phase dynamic studies of pyrazine[40,50] show that excitation at 267 nm transfers population from the ground-state to the S_2 (^1B_2u, $^1\pi\pi^*$) state in aqueous solutions. Although the excited-state symmetries involved in the gas-phase relaxation processes are known[40,50], the associated symmetries in the aqueous phase have yet to be determined. Therefore, the involved electronic states in photoexcited aqueous pyrazine will be denoted as A, B, and C.

6.5.1 TRPES Scan Results (-0.4 fs to 250 ps)

The left panel of Figure 6.6 highlights the pump-probe-delay-dependent PE spectra that cover the excited state region (<8 eV BE) of aqueous pyrazine in the delay range up to 1.2 ps. At very short pump-probe delays, two integrated PE BE ranges (3.5-5.5 eV and 5.5-7.8 eV) are visible in the excited state region in Figure 6.6. In order to follow the population transfer dynamics within the excited state region, the corresponding PE signals are integrated over these two BE ranges to illustrate the associated time-dependent changes, as shown in Figure 6.8a. In the vicinity of the pump-probe time-zero, the signal of the higher BE band (orange) is maximized, and the lower BE band (blue) starts to grow as the pump-probe delay time is increased. Such signal decays and growths indicate population transfer between the two electronic states, in less than 100 fs of the photoexcitation.

Figure 6.8b shows the photoelectron spectra at specifically chosen pump-probe different time delays. At the time-delay of 50 fs, a broad spectral feature spans the BE range of 4.0-7.5 eV. As the pump-probe delay increases beyond ∼200 fs, the spectral weight from the higher BE side is shifted to the lower BE side. The band located at the higher central BE of 7.5 eV, decays fast, whereas the band at the central BE of 5.2 eV grows (see Figure 6.8b). The former spectral component as A and the latter will be linked to state. Regarding the fast time-scale of such decay and growth, it is considered that the population transfer between the excited electronic states takes place via IC. Since the spectral changes are observed within the experimental time

resolution, it is likely that the IC time-scale is even faster. Figure 6.8b also shows the PE spectrum at 250 fs and 1.0 ps time delays. The PE spectra beyond 80 fs time-delays resemble each other. Once the spectral component in the BE range 4.5-6.5 eV appears (see Figure 6.6), the associated excited-state population does not decay within a sub-10 ps time window. That indicates that the population remains in the excited states and no recombination takes place to the ground-state within this time interval. Summarizing this preliminary analysis within the sub-10-ps time-delay window, there are two solute electronic states, A and B that may participate in the electronic relaxation process of photoexcited, aqueous-phase pyrazine. A separate TRPES study on 50 mM NaCl solutions was also performed and shows no excited state contributions in this time window (see in Appendix C.1 for details). Therefore, the contributions to the observed pyrazine solution dynamics from water and the NaCl solute can be excluded.

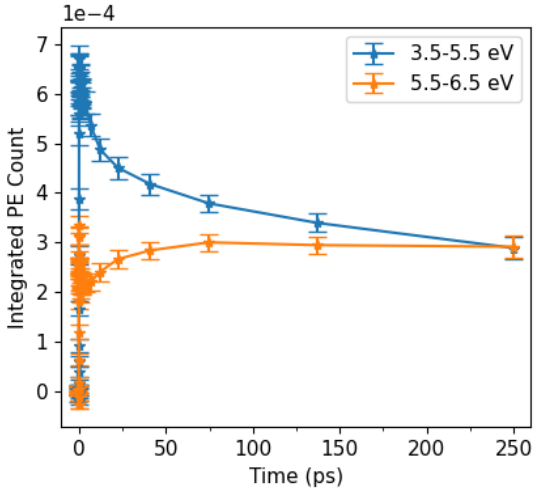

Figure 6.9: Long time-scale UV-pump and EUV-probed TRPES spectra of 500 mM aqueous pyrazine, recorded under minimized PISC conditions. The figure shows the time dependence of the PE signal integrated over the selected BE ranges of 3.5-5.5 eV (blue curve) and 5.5-6.5 eV (orange curve) on the longer time scale, up to +250 ps pump-probe delays.

The TRPES spectra were recorded with an exponential time-delay step sizes in the long-time-delay scans to focus on the long-time relaxation dynamics. The right panel of Figure 6.6 highlights the pump-probe-delay-dependent PE spectra in the BE range (below 8 eV), which covers the excited state region of aqueous pyrazine, and in the time-delay range up to 250 ps. One can see that spectral features appearing in the BE range of 4.2-6.8 eV on a tens-of-ps timescale. The PE signal peak that is initially centered at a BE of 5.2 eV gradually shifts to a higher BE of about 5.6-5.8 eV as the pump-probe delay increases to 100 ps or above. The PE signal peak that appears at 5.8 eV will be assigned and initially denoted as the C state. Figure 6.9 shows the time-dependence of the normalized PE signal integrated over two different BE ranges, region 1: 3.5-5.5 eV and region 2: 5.5-6.5 eV. The signal amplitude of the lower BE band in region 1 decreases, whereas the higher BE band signal increases. This implies that at least two excited states, B and C, are involved in the relaxation process in the 1 ps to 250 ps time window.

6.5.2 Fixed Delay Spectra:

In the fixed delay mode, the PE spectra were recorded at fixed pump-probe time delays for $\sim$27 min. The long acquisition time yields a sufficiently high signal-to-noise ratio in the recorded spectra. Figure 6.10 shows some fixed-delay TRPES spectra of aqueous pyrazine, recorded at a low pump intensity levels of 25 GW/cm^2 (under PISC minimized conditions). Similar to the TRPES spectra in Figure 6.6, only the excited-state region

is considered. At -400 fs negative delay, the PE spectra are similar to the static EUV spectra, and no probe-(EUV-) induced dynamics are observed. Therefore, the -400 fs PE spectrum serves as a reference PE spectrum for normalization and background correction.

Figures 6.10a and 6.10b show several fixed time-delay PE spectra spanning from 0.5 ps to 100 ps. A few fixed-delay PE spectra were recorded beyond the 250 ps time-delay to investigate the relaxation of the long-lived excited state. Figure 6.10c shows spectra taken at pump-probe delays of 250 ps, 500 ps, and 800 ps. A relatively low signal-to-noise ratio signal contribution is seen at a BE of 4.5-6.5 eV at an 800 ps time-delay in the recorded photoelectron spectrum. This likely arises due to the instability of the LJ over an extended measurements time window (27 min), resulting in a larger uncertainty in the extracted spectral intensity, as will be shown below.

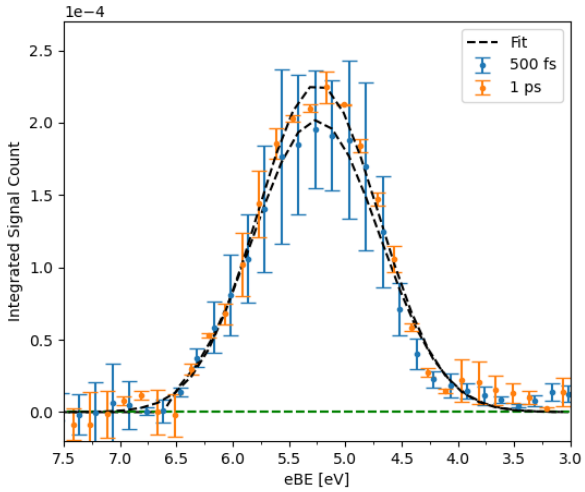

(a) Decay 10 ps dynamics

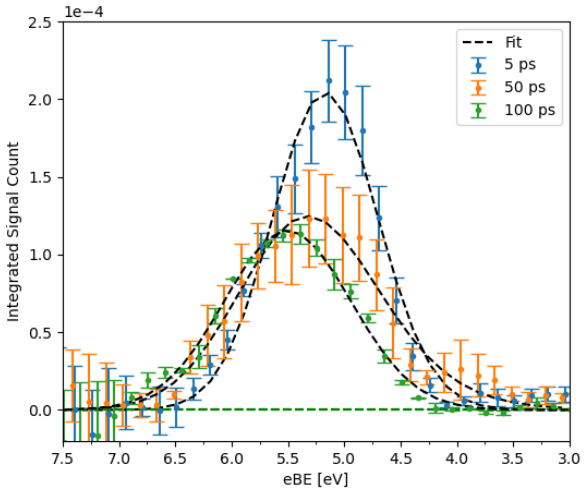

(b) Decay 10 ps dynamics

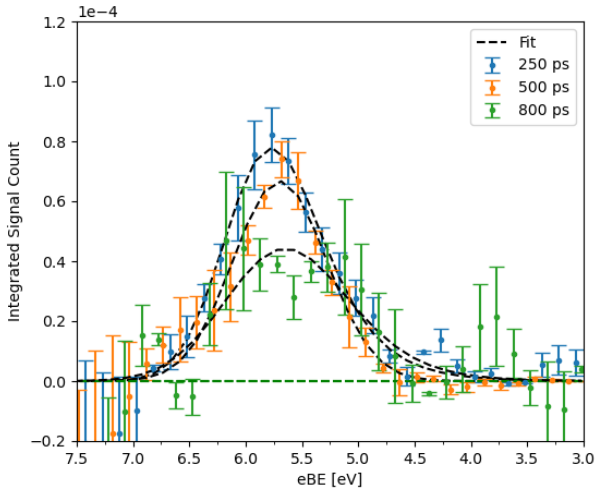

(c) Decay after 200 ps

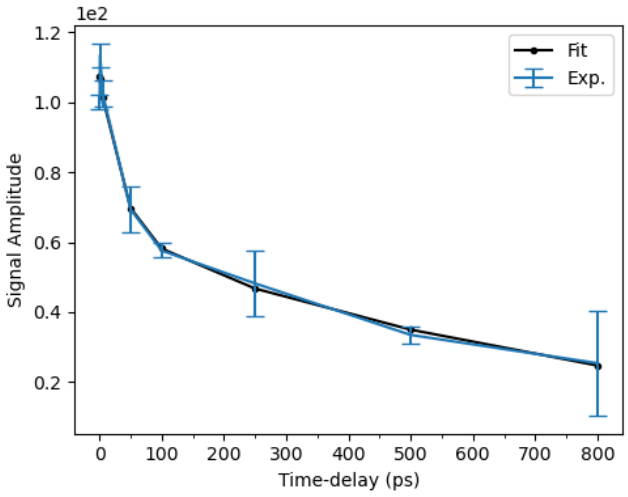

(d) Time-dependent signal amplitude

Figure 6.10: Fixed-delay TRPES spectra of aqueous pyrazine recorded at pump-probe delays of (Panel a) 500 fs, 1 ps, (Panel b) 5 ps, 50 ps, 100 ps, (Panel c) 250 ps, 500 ps, and 800 ps. The data represent an average of two independent measurements. The error bars represent the standard deviations and the dashed black curves shows the associated fits. Panel d shows the extracted spectral amplitudes obtained from exponentially modified Gaussian fittings (as shown in panels a, b, and c) at different pump-probe fixed delays and a bi-exponential fit to extract the possible relaxation time-constants. More details are provided in the main body of the text.

Table 6.1: Electronically excited state BE's and FWHM's, as extracted from the fixed time-delay TRPES study. The PE signal bands are modeled using an exponentially-modified Gaussian functions.

Time-delay (ps)	Binding Energy (eV)	FWHM (eV)
0.5	5.4 $\pm$ 0.1	1.3 $\pm$ 0.1
1	5.4 $\pm$ 0.1	1.2 $\pm$ 0.1
5	5.3 $\pm$ 0.1	1.1 $\pm$ 0.1
50	5.6 $\pm$ 0.2	1.3 $\pm$ 0.1
100	5.6 $\pm$ 0.1	1.2 $\pm$ 0.2
250	6.0 $\pm$ 0.1	0.9 $\pm$ 0.2
500	5.8 $\pm$ 0.1	1.0 $\pm$ 0.1
800	5.9 $\pm$ 0.4	1.2 $\pm$ 0.6

The PE signal bands have been modeled using an exponentially modified Gaussian function, as described in Equation 6.1 [284].

$$\mathrm{EMG} = \mathrm{a}\sqrt{\frac{\pi}{2}}\frac{\sigma}{s}\exp\left(\frac{x-c}{s}+\frac{\sigma^2}{2s^2}\right)\left\{1-erf\left(\frac{x-c}{\sqrt{2}\sigma}+\frac{\sigma}{\sqrt{2}s}\right)\right\} \tag{6.1}$$

Where the fitting parameters a, σ, s, and c denote the peak amplitude, Gaussian width, inverse rate of the exponential decay, and center of the Gaussian, respectively. The FWHM's are 2.35482 times the Gaussian width's. The dashed black color curves in each figure shows the associated fits. Table 6.1 shows the associated BE's and FWHM's of the electronically excited state ionization features. From Figure 6.10 and Table 6.1, three trends have been identified in the ps to sub-ns time window. First, the spectral intensity and position of the PE bands do not change when varying the time-delay from 500 fs to 5 ps, indicating that a single PE signal band is involved, which was populated by the A state within 100 fs. A broad PE band at a BE of 5.4 $\pm$ 0.1 eV with a FWHM of 1.2 $\pm$ 0.1 eV is extracted up to 5 ps time-delay spectrum, as shown in Figure 6.10a and 6.10b. Second, the PE peak positions at 50 ps and 100 ps slightly shift to a BE of 5.6 $\pm$ 0.1 eV with respect to the 5 ps time-delay spectrum, and the spectral amplitude decreases by 31 $\pm$ 10%. Since there is no signal growth at other BEs in the low-BE, excited state spectral region, and considering similar photoionization cross-sections for ionization from different photoexcited states, such spectral amplitude loss can be tentatively attributed to the repopulation of the ground state. Third, The spectral amplitude starts to blue-shift at higher time-delays, as shown by the 100 ps time-delay spectrum in Figure 6.10b. A single broad PE band is visible that peaks at a BE of 5.6 eV at 100 ps. At even higher time-delays, the PE signal band is even further blue-shifted up to 6.0 eV at 250 ps. This may indicate population transfer from the B state to another excited state, where the associated 5.9 $\pm$ 0.1 eV spectral component will be associated with the C state. Within the measurement signal statistics, the spectral position does not change from 250 ps up to 800 ps, but the signal amplitude decreases. This indicates that an excited-state population persists within the C state and perhaps relaxes slowly on a longer than ns time-scale. Compared to the 0.5 ps time-delay data, $\sim$34 $\pm$ 5 % and 25 $\pm$ 10% of the C-state excited state signal spectral density remain at the 500 ps and 800 ps pump-probe time-delays, respectively. The intermediate PE peak component obtained at 50 ps and 100 ps delays can be considered as the weighted average of the B and C signal components. These delays can be considered as the intermediate pump-probe delays during population switching from the B to the C states.

In summary, considering similar photoionization cross-sections of the excited states, the fixed time-delay study and the longer time pump-probe scan results indicate that the excited-state population of the B state divides into two parts. One part seemingly directly repopulates the ground state, whereas the other part is transferred to another excited state, C, that likely subsequently relaxes to the ground state on a ns to μs

timescale. Finally, the time-dependent changes of the B-state spectral amplitude are shown in Figure 6.10d, where the relative signal amplitude of the low-BE electrons (3.5-7.8 eV) recorded at higher time-delays are normalized with respect to PE signal amplitude level at 0.5 ps. A bi-exponential fit is performed to extract the relaxation timescale of the B state. This fit yields two time-constants: 40 $\pm$ 20 ps and 900 $\pm$ 300 ps. The 40 $\pm$ 20 ps component can be attributed to the direct population transfer from the B state to the electronic ground state, whereas the 900 $\pm$ 300 ps time constant is thought to represent the total B state relaxation time via another excited state, labeled C (Note that the C-state relaxation timescale cannot be reliably determined with the few late-time-delay data points and maximum 800 ps pump-probe delay data reported here). The population-transfer time from the B state to the C state and the involved electronic states (A, B, and C) will be discussed in Section 6.6 below.

6.6 Modeling the Ultrafast Relaxation Processes

Considering the preliminary observation of the possible excited state relaxation process, the excited state regions (<7.8 eV) of the TRPES spectra have been modeled using the kinetic models shown as Equations 6.2 and 6.3. For that purpose, two different models, serial and parallel, have been considered for analysis. In both models, the photoexcited S_2 state, denoted as the A state decays to the B state. In the serial model, the B state decays to the C state, whereas in the parallel model, the B state decays biexponentially, with one part repopulating the electronic ground state and another part decaying to produce the C state. Finally, both models assume that the C state decays to the ground state. Using these models, a global-fit spectral analysis has been performed to retrieve the associated time-constants. Generally, the radiative processes are much slower and have lower quantum yields than non-radiative processes in pyrazine[38]. Therefore, within the measurement windows, the TRPES spectra are considered to be only sensitive to the fast, non-radiative processes, which are further considered in the analysis and discussion presented below.

$$\text{Serial}: \ \mathrm{A}\ (\mathrm{S_2}) \xrightarrow{\tau_A} \mathrm{B} \xrightarrow{\tau_B} \mathrm{C} \xrightarrow{\tau_C} \mathrm{S_0} \tag{6.2}$$

$$\text{Parallel}: \ \mathrm{A}\ (\mathrm{S_2}) \xrightarrow{\tau_A} \mathrm{B} \begin{array}{l} \xrightarrow{\tau_{B_1}} \mathrm{S_0} \\ \xrightarrow{\tau_{B_2}} \mathrm{C} \xrightarrow{\tau_C} \mathrm{S_0} \end{array} \tag{6.3}$$

6.6.1 Global Fit Results:

The global-fit method, as described in References 39,130,239, was applied to extract the state-associated spectra and associated time constants for the processed TRPES scan spectra, as shown in Figure 6.6. The details of the global fitting procedure of serial and parallel models are described in Appendix C.2, and the results are collected in Table 6.2. Briefly, both models gives similar results, the τ_{B} time constant in the serial model can be related to the parallel model time constants (τ_{B_1}, τ_{B_2}) using the relationship $1/\tau_{\mathrm{B}}=1/\tau_{\mathrm{B}_1}+1/\tau_{\mathrm{B}_2}$. The associated global-fit results for the parallel model are shown in Figures 6.11a. Figure 6.11b shows the residuals, which are obtained by subtracting the fitted spectra from the processed experimental spectra. The residual signal levels are within the noise limit of the experimental spectra. Therefore, any low frequency oscillations in the residual maps, particularly with an oscillation period below 500 fs, will be ignored in the subsequent discussion.

The extracted state-associated spectra highlight the excited-state signal contributions in Figure 6.12a. The extracted time-constants for the serial and parallel relaxation model are shown in Table 6.2. The associated

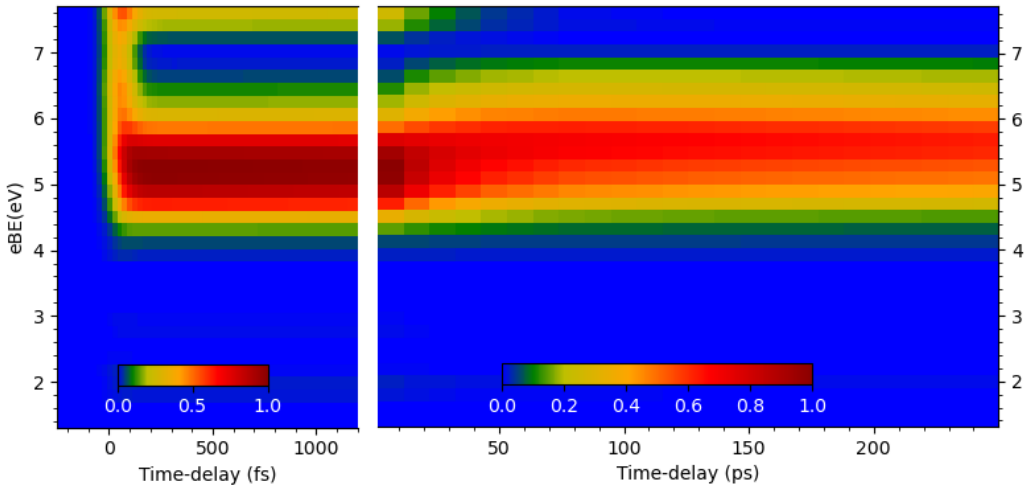

(a) Global-fitting of TRPES spectra

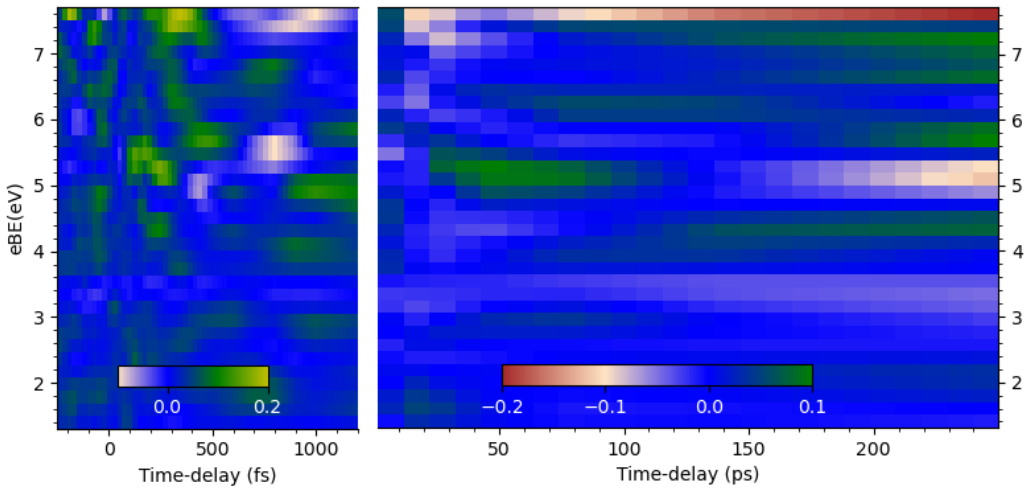

(b) Fitting residuals

Figure 6.11: Global fits to the shorter timescale TRPES spectra of aqueous pyrazine. Panel (a) shows the fitted spectra using a three-excited-state parallel relaxation model, as described in Equation 6.3. Panel (b) shows the residuals associated with the experimental data and global fits.

Table 6.2: Extracted exponential decay time-scales in serial and parallel relaxation models under PISC minimized conditions. The time-constants were extracted from the data sets from two different data sets; the average time constants are presented in the table. One of the dataset is shown in Figure 6.6.

Time-constants	Serial	Parallel
τ_{A}	40 $\pm$ 20 fs	40 $\pm$ 20 fs
τ_{B}	25 $\pm$ 5 ps	35 $\pm$ 10 ps, 120 $\pm$ 30 ps
τ_{C}	> 2 ns	> 2 ns

fit components of the A, B, and C excited states are shown using blue, green, and red colored curves, respectively. The retrieved A state spectrum shows spectrally broad contributions. Figure 6.12b and 6.12c show the time-dependent BE-integrated signal count within two different BE regions, region 1: 5.5-7.8 eV and region 2: 3.5-5.5 eV. The spectral amplitude is transferred from region 1 to region 2, indicating population transfer from the A state to the B state via IC. An associated time constant of 40 $\pm$ 20 fs is extracted from the global fitting analysis.

The global fitting procedure nicely reproduces the signatures of the excited states and their spectral peak

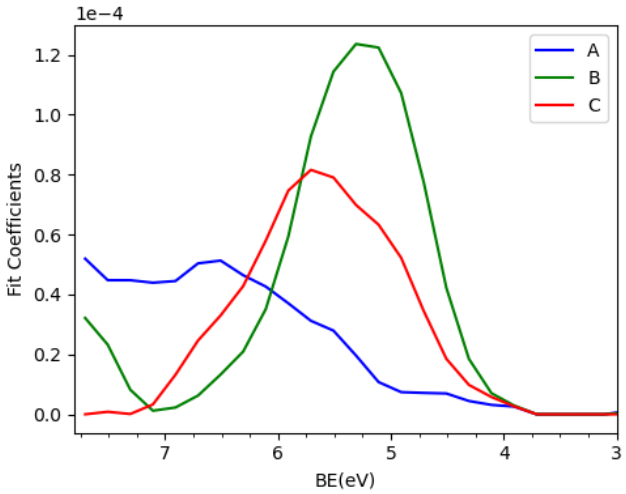

(a) State associated spectra

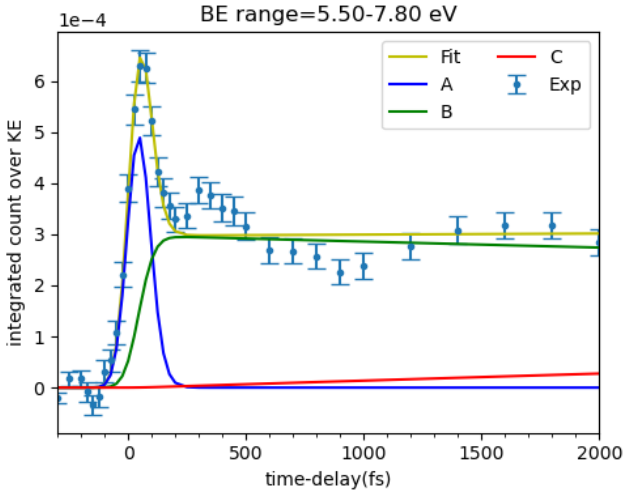

(b) BE: 5.5- 7.8 eV

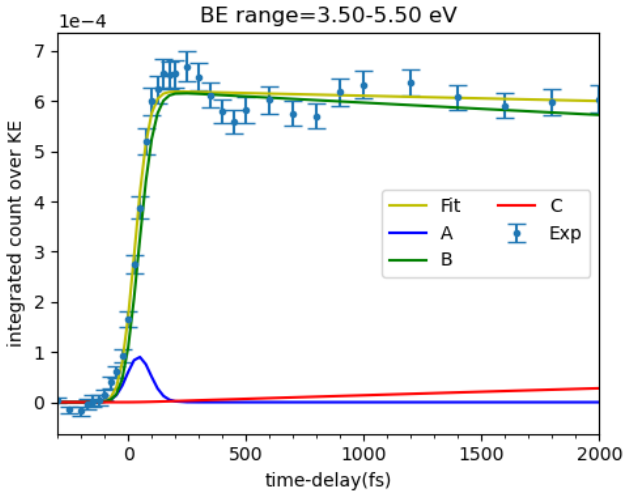

(c) BE: 3.5-5.8 eV

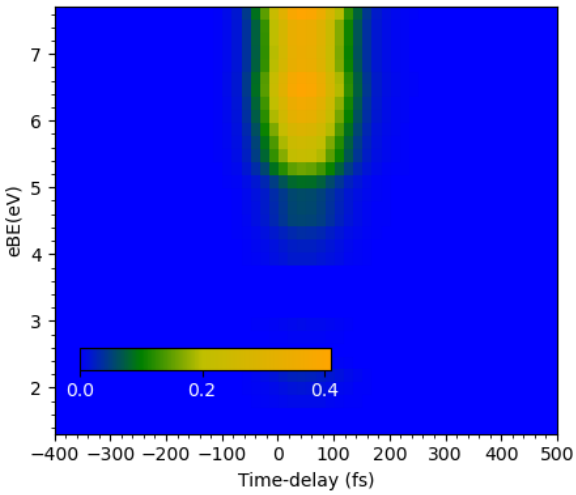

(d) Retrieved A state TRPES spectra

Figure 6.12: Global fit results of the shorter timescale TRPES spectra of aqueous pyrazine. Panel (a) shows the spectral fit coefficients, representing the state-associated spectra. Panel (b) and (c) show the time-dependent PE signals associated with different BE regions and the corresponding total fits and fit components. Panels (b) shows the retrieved A state spectro-temporal dependence, as extracted from the from global fits.

positions. Figures 6.12d, 6.13a and 6.13b show the retrieved A, B and C spectra as a function of time in a 2D maps. The retrieved A state spectra exhibits a pair of peaks within a BE range of 5.0-7.5 eV, and the origin of these peaks will be discussed in Section 6.6.2. Notably, the retrieved A state spectrum and time-dependent integrated photoelectron spectrum (BEs: 5.5-8.0 eV), shown in Figure 6.8a, highlights a delay in the photoelectron count growth after time zero. Comparisons between the aqueous pyrazine and aqueous NaCl solution signal gorwths are shown in the Appendix, Section C.1, Figure C.1. As shown in Figure 6.2, the time-zero is defined as the maximum of the non-ressonant coherent artifact when the pump and probe pulse overlap is maximised. The temporal offset of the aqueous NaCl CC signal peak and the aqueous pyrazine signal peaks may indicate the Frank-Condon region (vibronic wavefunction overlap between the S_0- and S_2-state) for the pump-pulse and the electronically excited state is not the most favorable Frank-Condon position (overlap between the S_2 and correlated cation states) for ionization. That is, it takes some finite time for the excited wavefunction to travel from the photoabsorption Frank-Condon point to the point where ionization is most favorable. Such a scenario is absent in gas-phase TRPES studies[39,50,283], and may indicate either a

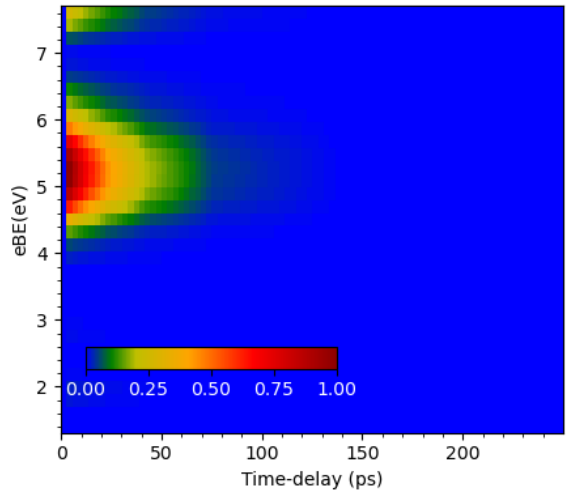

(a) Retrieved B state TRPES spectra

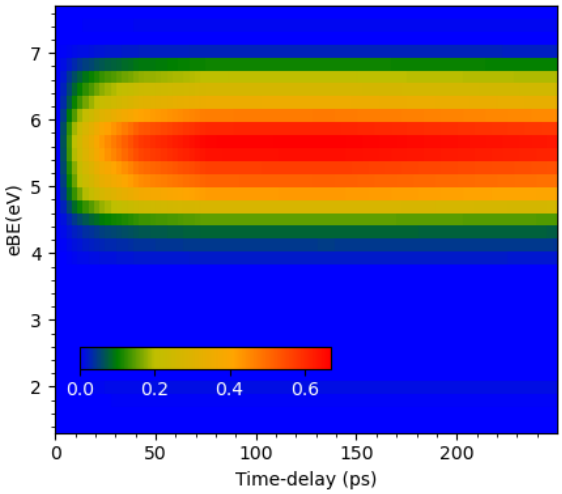

(b) Retrieved C state TRPES spectra

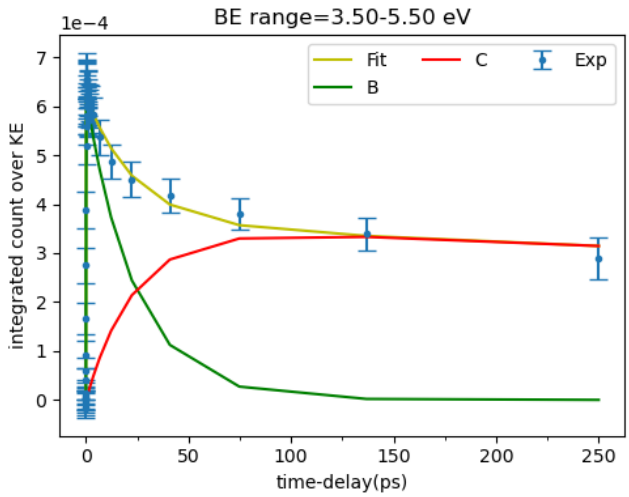

(c) BE region: 3.5-5.5 eV

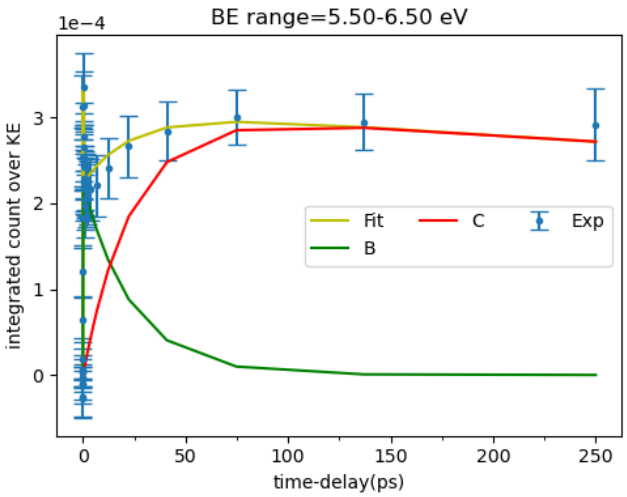

(d) BE region: 5.5-6.5 eV

Figure 6.13: Retrieved state associated spectra and their time decay obtained through global fitting analyses. Panel (a) and (b) shows retrieved B and C TRPES spectra extracted from global fitting method, respectively. Panel (c) and (d) time-dependent integrated PE counts and associated fittings over 3.5-5.5 eV and 5.5-6.5 eV BE regions, respectively. More details are given in the texts.

shift of the Frank-Condon points in the electronically excited or cationic states with respect to the equilibrium ground state geometry of pyrazine in going from the gas to the aqueous phase.

The retrieved B and C state spectra have PE signal peaks at BEs of 5.3 $\pm$ 0.2 eV and 5.8 $\pm$ 0.2 eV, respectively (see also Figure 6.12a). The results are consistent with the fixed time-delay study (see Table 6.1). Figures 6.13c and 6.13d show the time-dependent, BE-integrated PE counts and associated fit results over two different BE ranges, 3.5-5.5 eV and 5.5-6.5 eV. The global fits using the parallel model yields three lifetimes: 35 $\pm$ 10 ps, 120 $\pm$ 30 ps, and 3 $\pm$ 1 ns. The first one is attributed to the time scale for the B state to repopulate the ground state. The 120 $\pm$ 30 ps time constant is assigned to the relaxation time scale in going from the B to C states. Since the TRPES spectra were recorded up to 250 ps, the last time constant obtained from the analysis only gives an indication of a greater than ns decay time of the C state and the extracted value has no specific meaning. This result is also consistent with the fixed time-delay data, which hints that around 25 $\pm$ 10% of the remaining population decays on ns timescale. In order to accurately determine these time constants, the TRPES spectra would need to be recorded beyond a ns time-delays.

6.6.2 State Assignments:

A and B States: In the vicinity of the time zero of the pump-probe measurement, a broad spectral component is visible between 4.5-7.8 eV BEs. This broad spectral band has a small contribution of the pump-probe-laser coherent artifact that results in a narrow symmetric Gaussian profile around the time zero. Beyond that, the $S_0 \rightarrow S_2$ resonant excitation using a 267 nm pump laser wavelength produces excited-state signal contributions that have a temporal offset with respect to the coherent artifact, as shown in Appendix C. According to the gas-phase studies[39,50,283], the initially excited S_2 ($1B_{2u}$) state Koopmans correlates[49,75] with the D_1 and D_3 cationic states. Similar behavior is also seen in aqueous pyrazine. Since the the D_1 and D_2 cationic states seem to change their ordering in the aqueous phase (Section 5.4.1), the S_2 state is thought to correlate with the D_2 and D_3 cationic states in the aqueous phase. The experimentally obtained and fitted TRPES data shows a PE signal contribution spanning from 6.8-7.8 eV that decays quickly within 40 $\pm$ 20 fs. Considering the VIE of the D_3 cationic states (11.6 $\pm$ 0.1 eV Section 5.4.1), this signal contribution can be assigned to a $D_3 \leftarrow S_2$ ionization channel. Moreover, the retrieved A-state spectrum shows additional PE signal contributions in the lower BE range that spans up to 5.2 eV. Due to the lower VIE of the spectrally broad peak associated with the D_2 state (10.6 $\pm$ 0.1 eV, Section 5.4.1), the $D_2 \leftarrow S_2$ ionization contribution is expected to be in the BE range from 5.2-6.4 eV and thus, the retrieved dominant signal contribution in this BE region is assigned to $D_2 \leftarrow S_2$ ionization. The second BE region is expected to have multiple cationic state contributions: D_0, D_1, and D_2. Therefore, the $D_2 \leftarrow S_2$ ionization contributions will likely overlap with the other cationic state contributions, as shown in Figure 6.12a. However, in less than 100 fs pump-probe time-delay window, the BE region spanning from 5.8-7.8 eV gives a clear signature of the S_2 state, although it has a small spectral overlap with the coherent artifact signals, which are expected to be weak at the pump intensity conditions implemented in these measurements. Such a scenario was expected, based on previous gas-phase TRPES studies, where the clear signature of the S_2 state was identified via ionization to the D_3 cation state[39].

With in the cross-correlation time window, the B-state signal appears. Considering the previously-reported gas-phase studies[39,40], the B state feature (BE at 5.2 eV) is a signature of the S_1 ($^1B_{3u}$, $n\pi^*$) excited state of pyrazine. The first retrieved 40 $\pm$ 20 fs time constant is correspondingly assigned as the upper limit of the $S_2 \rightarrow S_1$ IC time scale. A better time resolution is needed to directly monitor the state switching process in aqueous pyrazine. The $S_2 \rightarrow S_1$ transition happens through IC in the gas-phase[39,40] via the ν_{6a} electronic-state, coupling vibrational mode, with a fundamental vibrational angular frequency of 583 cm^{-1}. With coherent population of multiple discrete ν_{6a} vibrational levels in the gas phase, this results in a $\sim$60-fs oscillatory period in the TRPES data[39]. According to an excited-state Raman spectroscopy study[285], this oscillation frequency increases to 602 cm^{-1} in 100 mM aqueous pyrazine. Using the LJ TRPES technique and the currently achievable time-resolution, it was not possible to observe such periodic electronic-state coupling behavior in the aqueous-phase, nor was it possible to determine whether such vibronic wavepacket motion persists in aqueous solution. The lack of oscillatory structure observed so far in the aqueous pyrazine solution TRPES measurements may be attributed to inhomogeneous broadening of the vibronic manifold in the aqueous solution, related vibronic decoherence effects in the aqueous-phase, or the limited time resolution of the current experiments.

C State: The S_1 state relaxes to another lower lying electronic state on a 120 $\pm$ 30 ps timescale. Several electronic states are, or are thought to be, located below the singlet S_1 states in previous gas-phase pyrazine, including the singlet dark ^1A_u and a number of triplet states[174]. The singlet-to-triplet population transfer is expected to be comparatively slow compared to the singlet-to-singlet transitions, with the former expected

to occur on a hundreds-ps time scale, based on gas-phase studies[39,286,287]. Therefore, the 4.5-6.5 eV PE signal components can be the signature of a triplet, T ($^3B_{3u}$, nπ^*), state that is populated via the $S_2 \rightarrow S_1 \rightarrow$ T cascaded process. The population growth time-scale of the triplet, T, state is about 120 $\pm$ 20 ps. An energy gap of 0.5 eV was predicted between the S_1 and T state origins in the gas phase[288,289]. In the gas-phase TRPES spectra[39], the triplet state PE signal appears at a lower BE than expected, as a favorable Frank-Condon overlap between the vibrationally hot T levels and D_0 gives the highest ionization probability. A similar situation may also arises in the recorded aqueous phase TRPES spectra. Although the liquid-phase signal arises from a weighted average of BE components (as mentioned in Section 6.5.2), the aqueous-phase PE signal peak at a BE of around 5.6 $\pm$ 0.1 eV and 100 ps time-delay can still be attributed to the $D_0 \leftarrow T^{***}$ ionization pathway. According to the fixed-delay data, as shown is Figures 6.10b and 6.10c, the triplet state is long-lived and is thought to relax over an extended time scale to the ground state, S_0, via ISC.

The observation of a long-lived triplet state is also consistent with the aqueous-phase laser photolysis experiments reported in reference 290. Bent *et. al.*[290] reported the T (^3B_u, nπ^*) triplet state lifetime of about 4.5 μs, which is referred as an 'infinite dilution' decay constant. The authors also show that the generally measured aqueous pyrazine triplet state lifetimes are reduced due to self-quenching (ground-state pyrazine quenches T-state pyrazine on a timescale that depends on the pyrazine concentration) and quenching by inorganic ions, such as Cl^-, as implemented in the current experiments. Therefore, it is expected that a relatively shorter triplet state decay time constant would be extracted in aqueous-phase TRPES experiments with 500 mM pyrazine and 50 mM NaCl solutions in comparison to the timescale reported in reference 290. An ISC-mediated relaxation from the triplet manifold to the vibrationally hot ground state is also expected based on previous gas-phase studies[39].

Depending on the hydrogen bonding configuration around the pyrazine electronically excited states, additional excited-state relaxation channels may open on longer timescales in the aqueous pyrazine solutions. Reimers *et el.*[185] theoretically predicted a potential PCET channel between pyrazine and water molecules in aqueous pyrazine. Such a photochemical channel is stated to be facilitated by a partial charge transfer process from a solvent proton donor to the pyrazine electron donor and requires an activation energy of about 0.6-0.8 eV above the S_1 minimum. An energy gap of 0.4 eV is predicted between the minimum of the S_1 and PCET states in aqueous pyrazine[185]. If the S_1 and PCET states both couple to ionic states with similar energetics, the PES signature of the latter state would be located at a BE of 5.9 $\pm$ 0.1 eV, would be expected to be populated in hundreds of ps, and would likely be long-lived[185]. Correspondingly, another potential contribution to the C state signal could be from a PCET state of aqueous pyrazine.

Notably, the S_1-to-PCET state transition state is calculated to occur significantly below the minimum of the S_2 electronic state and could correspondingly be accessed following 267-nm excitation of aqueous pyrazine. However, as of yet, there does not seem to be any experimental evidence for PCET processes occurring in aqueous pyrazine samples – at least within the singlet manifold – suggesting that the PCET transition state is not accessed following 267-nm excitation and IC from S_2 to S_1. The S_1-state fluorescence spectrum of pyrazine in water indicates that the photoexcited molecules do not undergo photochemical transformations within the >100 ps S_1-state fluorescence lifetime[185,190], which suggests that any PCET processes occur on a longer timescale, at least following photoexcitaiton of the S_1 state from the ground state. Interestingly, the products of potentially related proton transfer reactions were observed by Bent et al. in the their ns-time-resolution transient absorption experiments, particularly when an isopropanol quencher and H-atom doner was added to the aqueous pyrazine solutions[290]. Signatures of the protonated and doubly protonated monohydropyrazyl radical (PzH) and dihydrocation radical (PzH_2^+) products appeared on 30 ns and 1 µs timescales

[*] **denotes a hot vibrationally excited-state

in aqueous solution, respectively, following 265 nm excitation. These products were shown to be produced via the relaxed T state, but it was also considered that they may be formed via the S_1 singlet analogue on a faster timescale than was accessible in those measurements. Still, considering the results reported here, the ns-time-resolution experiments[290], and previous ultrafast-time-resolution gas-phase TRPES work[39], the assignment of the 'C-state' signal to the T_1 ($^3B_{3u}$, $n\pi*$) state seems to be well supported. It is correspondingly suggested that any proton transfer processes in pure pyrazine aqueous solutions can only occur with low quantum yields on sub-ns timescales and that such phenomena predominantly occur on >ns timescales following ISC to the triplet manifold. Here it is suggested that further investigation of proton transfer processes and protonated photoproduct formation would require dedicated state-of-the-art theoretical calculations and spectral simulations that explicitly considered the water solvent molecules.

6.7 TRPES Study on 500 mM Pyrazine Under Space-Charge Conditions

As shown in Section 6.3, PISC results in time-delay-dependent PE KE shifts. Such energetic shifts become larger at longer pump-probe time delays (> 10 ps), influencing the electronic relaxation dynamics. However, the energetic shift is not so large in shorter (< 1 ps) time delays. When the pump-probe intensity is lowered to avoid PISC effects with a 5 kHz light source and the THEMIS 600-EP spectrometer system, the acquisition time is very long and requires over seven working days to achieve reasonable data statistics. However, most of the UV pump and EUV probe TRPES studies focusing on shorter time dynamics have been performed with high pump pulse intensities that easily lead to PISC effects[41,42,126,128,130]. It is often assumed that PISC effects are negligible at shorter pump-probe delays, so the energetics and associated relaxation dynamics are nearly unperturbed. When PISC-induced energetic shifts are observed in condense-phase TRPES experiments, they are generaly corrected using mean-field models[135,246]. These models assume that only the energetics of the outgoing electrons are effected by the PISC and that the underlying dynamic processes are unaffected.

TRPES experiments that implement high pump pulse intensities allow higher signal-to-noise ratio PE signals to be recorded in a short acquisition time. However, an experimental verification has yet to be reported on the underlying assumption that these pump pulse intensities do not effect the dynamic processes that occur in condensed-phase samples. Therefore, similar UV-pump and EUV-probe TRPES experiments as reported in Section 6.3 have been recorded in the shorter time delay range at high pump-pulse intensities that produce a non-negligible PISC on hundred-ps timescales. The pump laser pulse intensities were 80 GW/cm^2, *i.e.*, approximately three times higher than in the PISC-minimized conditions. The experiments were performed with variable pump-probe delay steps between -400 fs to 2000 fs (2 ps).

Modelling Electronic Relaxation and a Comparison of Results With and Without the Space-Charge Effect Global fit analyses have been performed on the TRPES dataset shown in Figure 6.14 to extract the excited state signal contributions and associated dynamics when the PISC effect is present. Similar to minimized PISC conditions, a two-excited-state (A and B) relaxation model was considered up to 2 ps. The extractable time constant, τ_{A}, represents the decay from A to the B state. The associated model is shown in Equation 6.4

$$\mathrm{S}_0 \longrightarrow \mathrm{A} \xrightarrow{\tau_{\mathrm{A}}} \mathrm{B} \tag{6.4}$$

The reconstructed TRPES spectra are shown in Figure 6.14a. The state-associated spectra are shown in Figure 6.14b. The time-dependent fitting components at two different BE ranges, 5.8-7.3 eV and 3.5-7.3 eV

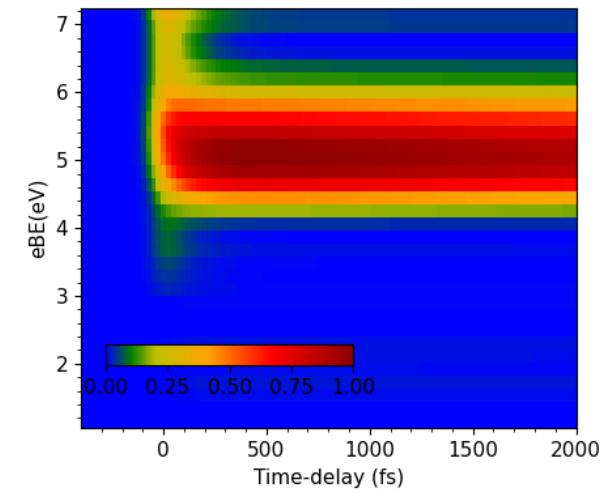

(a) Global-fit

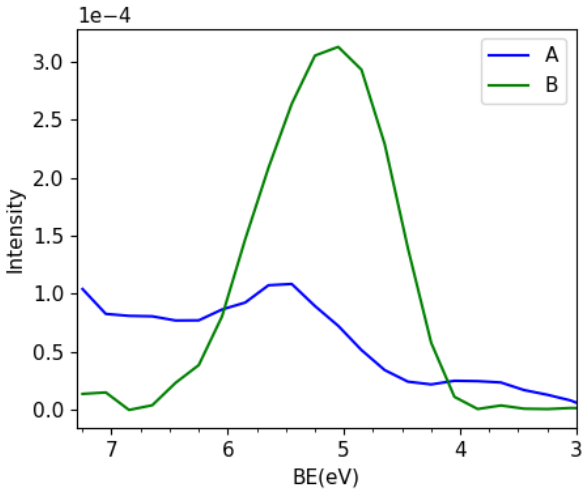

(b) State-associated spectra

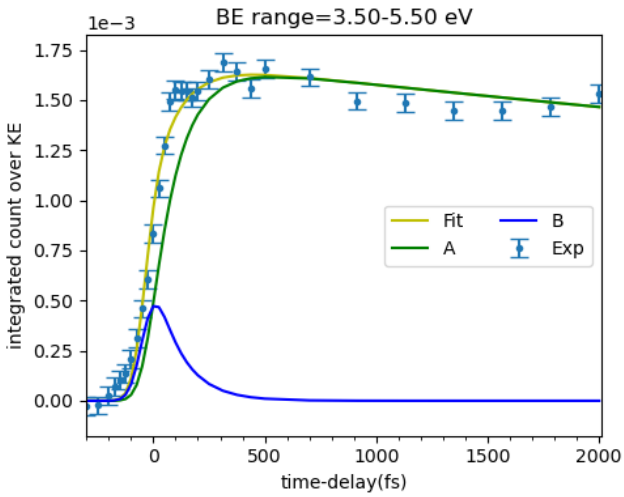

(c) Time-dependence, BE: 3.5-5.5 eV

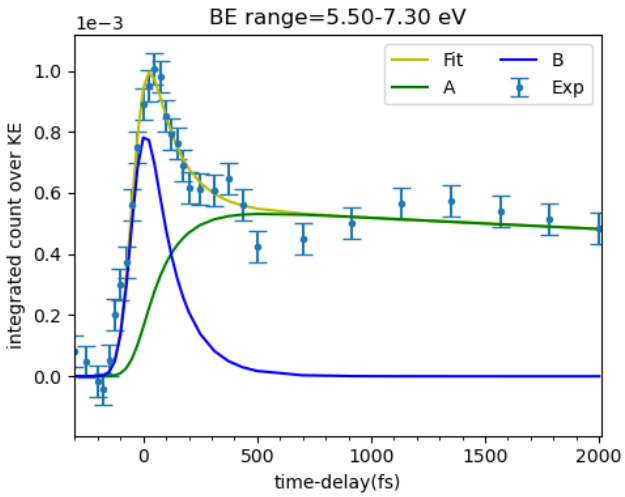

(d) Time-dependence, BE: 5.5-7.3 eV

Figure 6.14: Two-excited-state model and global fit to the TRPES spectra of aqueous pyrazine recorded under PISC conditions. Panel (a) shows the time-resolved spectra reproduction using the global fit method; the associated experimental data is shown in Fig. 6.7. Panel (b) shows the extracted state-associated spectra. Panel (c) and (d) show the associated fits of the time-dependent PE signal in two different BE regions.

Table 6.3: Exponential decay time-constants of the PISC-minimized conditions compared to the conditions where the PISC effect is present. In the latter case, a charging correction was performed.

Time-constants	Without space-charge	With space-charge
τ_A	40 $\pm$ 20 fs	105 $\pm$ 20 fs

are shown in Figure 6.14c and 6.14d, respectively. The former BE range highlights the fastest decay region. The extracted time-constants are 105 $\pm$ 20 fs and 15 $\pm$ 5 ps. The experiment was performed with a 85 $\pm$ 10 fs time resolution. The later time constant of 15 ps is ignored since it is outside of the measurement time window. A clear signature of the A state is identified in the higher BE region, as shown in Figure 6.14b. Compared with the PISC minimized datasets, a change of the relaxation lifetime of the A state is found. This may be an indication that a mean-field, energetic space-change correction may not adequate to retrieve the associated relaxation time when compared to the PISC minimized condition. Alternatively, there may be an early-time signature of a multi-pump-photon process underlying the S_2-S_1 state IC dynamics that were resolved at lower pump pulse intensities. To the author's knowledge, the results reported here represent the first time that it has

been possible to record LJ-TRPES data under conditions where space-charge effects cannot be detected. Otherwise, early-time PISC effects were ignored or energetically mean-field corrected. The variation from the PISC-minimized and PISC condition data reported here correspondingly warrants further research and greater consideration by the time-resolved LJ-PES research community.

6.8 Relaxation Model in Aqueous Solution

The exponential decay profiles of the state-populations are equivalent in both serial and parallel model. As mentioned before, the B-state decay time-constant (τ_{B}) obtained in the serial model is equivalent to the time-constants ($\tau_{\mathrm{B}_1}, \tau_{\mathrm{B}_2}$) obtained in the parallel model and both models reproduce the experimental spectra nicely. More details of the equivalence of the serial and parallel relaxation models are discussed in Appendix C. More details about the equivalence of the serial and parallel relaxation models are provided in Appendix C. The parallel relaxation model is considered to best describe the relaxation processes in aqueous pyrazine, due to the similarity of the aqueous-phase data to the previously reported gas-phase results[39], which were best described using a related parallel excited-state relaxation model. Moreover, considering similar ionization cross-sections of the involved S_1 and T states, the parallel relaxation model may explain the loss of excited-state population at around ~40-50 ps pump-probe delays in the BE range of 3.5 to 5.5 eV. Within this model and based on this assumption, a triplet-state quantum yield of 0.65 $\pm$ 0.20 can be calculated. This has been observed reproducibly in the TRPES scans and fixed-delay spectra, as shown in Figures 6.9 and 6.10, respectively. The loss of excited-state populations are also consistent with the ns-photolysis experimental results reported by Bent *et al.*. The excited-state populations decay can occur to a number of channels, *i.e.*, ground-state recombination[39], dark-A_u-state[40] population, hydrated-electron generation[290], proton-transfer processes[185,290], etc. Photochemistry in aqueous pyrazine (at infinite dilution) has been reported to occur on ns-to-μs timescales[290]. The current experiments have not found any signature of the dark-A_u-state or hydrated-electron generations within the probed experimental temporal window; more details will be discussed in Section 6.9. Therefore, similar to the gas-phase studies reported by Horio et.al., ground-state recombination seems to be most probable. Direct observation of a ground-state recovery would confirm such findings and, therefore, further time-resolved studies are required to explore the excited-state population loss.

267 nm Excitation in Aqueous Pyrazine, $S_0 \rightarrow S_2$

$$\mathrm{A}\ (\mathrm{S}_2, {}^1\mathrm{B}_{2u}) \xrightarrow{\tau_{\mathrm{A}}} \mathrm{B}\ (\mathrm{S}_1, {}^1\mathrm{B}_{3u}) \begin{array}{l} \xrightarrow{\tau_{\mathrm{B}_1}} \mathrm{S}_0 \\ \xrightarrow{\tau_{\mathrm{B}_2}} \mathrm{C}, (\mathrm{T}, {}^3\mathrm{B}_{3u}) \xrightarrow{\tau_{\mathrm{C}}} \mathrm{S}_0 \end{array} \tag{6.5}$$

Associated relaxation timescales,

$$\begin{aligned} \tau_{\mathrm{A}} &= 40 \pm 20\ \mathrm{fs} \\ \tau_{\mathrm{B}_1} &= 35 \pm 10\ \mathrm{ps} \\ \tau_{\mathrm{B}_2} &= 120 \pm 30\ \mathrm{ps} \\ \tau_{\mathrm{C}} &\geq 3\ \mathrm{ns} \end{aligned}$$

Equation 6.5 in the box above shows the optimized relaxation model for aqueous pyrazine solutions following $S_0 \rightarrow S_2$ excitation using 267 nm laser pulses. The associated timescales obtained from global fits to the TRPES spectra are also shown below the model. The parenthesis in the kinetic scheme shows the associated electronic states symmetries. As mentioned above, only the excited-state spectral region has

been considered using the global fitting method. Additional experiments with a much higher signal-to-noise ratio would be needed to identify the changes of the solute ground state signals, which are usually hidden under the shoulder of the dominant water $1b_1$ signal contributions. To record such data under PISC-free conditions, significantly higher repetition rate laser systems would be required.

Based on the fixed delay and TRPES scan analyses, and considering similar photoionization cross-sections of the electronically excited-states, the following relaxation model is proposed, as shown in the box above. In summary, the population from the S_2, $^1B_{2u}$, state relaxes to the S_1, $^1B_{3u}$, state on a 40 $\pm$ 20 fs timescale. The S_1, $^1B_{3u}$, state relaxes in parallel to the vibrationally hot, S_0, ground state, ^1A_g, and the T_1, $^3B_{3u}$, triplet state. The S_1 ($^1B_{3u}$) state to ground state relaxation occurs in 35 $\pm$ 10 ps. The S_1 ($^1B_{3u}$) state to T_1 ($^3B_{3u}$) population transfer takes place on a 120 $\pm$ 30 ps timescale. Finally, the populations are expected to return to the vibrationally hot ground state well beyond a single ns timescale.

6.9 Solvent-Induced Changes in Aqueous pyrazine

The excited-state TRPES features are spectrally broad, having a FWHM of about 0.75 - 0.95 eV. The dominant peak width contributions in the studied aqueous solutions arises due to inhomogeneous broadening and likely represents the statistical distribution of different molecular configurations *e.g.* broken or unbroken H-bond, orientations-of the neighboring water molecules[82]. Spectral broadening may also arise due to the short lifetime of the electronically excited states and the high density of valence states of pyrazine. VIE's due to $D_3 \leftarrow S_2$, $D_0 \leftarrow S_1$, and $D_0 \leftarrow T$ are notably decreased by 0.2 - 0.4 eV in the aqueous solution compared to previous gas-phase TRPES studies (see Chapter 2 and Reference 39).

Changes in Relaxation Time The extracted time-constants for $S_2 \rightarrow S_1$ and $S_1 \rightarrow S_0$ are slightly larger in the aqueous phase, indicating relatively slower relaxation processes in the solutions. The extracted $S_2(A) \rightarrow S_1$ (B) and $S_1(B) \rightarrow S_0$ IC happens in 40 $\pm$ 20 fs and 35 $\pm$ 10 ps, respectively; the relaxation dynamics via IC are nearly two times slower in aqueous solutions compared to in the gas phase[39,40]. Two possible causes may result in the slower $S_2 \rightarrow S_1$ IC times. First, the limited time resolutions of 65-85 fs in the present aqueous phase TRPES studies sets an upper limit on the fastest relaxation timescales that can be extracted. If the underlying dynamics are much shorter than the time resolution of the experiments, then the true excited-state population exponential decay may not be clearly observed. It is also noted that the pump-pulse excitation is close to the $S_0 \rightarrow S_2$ 0-0 transition energy in the aqueous phase[186]. Therefore, the system receives much less excess vibrational energy in the aqueous phase, relaxes relatively slowly to the singlet, S_1 state; related wavelength-dependent S_1-state relaxation times were also reported in gas-phase pyrazine[39]. A relatively slower relaxation timescale for a $S_1 \rightarrow S_0$ IC process may indicate a slightly increased barrier height from the S_1 potential minimum to the S_1/S_0 conical intersection points or faster vibrational relaxation of the S_1 state in aqueous solution, which slows down the S_1-to-S_0 population transfer time.

Additionally, solvation effects in the electronically excited state may also play a role during the relaxation processes. The electronic polarizability in the excited state may differ from that in the ground state and may launch a readjustment of the water molecules in the aqueous medium. Dynamic solvation may occur on hundreds of fs and ps timescales in aqueous solution[126,291–293]. Such solvation dynamics can affect the excited-state relaxation time in aqueous pyrazine compared to the gas-phase molecules. The $S_2 \rightarrow S_1$ IC time scale is unlikely to be influenced due to the short lifetime (sub- 50fs), but the $S_1 \rightarrow S_0$ and $S_1 \rightarrow T_1$ timescales will likely be affected. However, the current TRPES study can not isolate the solvation process and the solvation timescales from the excited-state population dynamics in the aqueous pyrazine solutions.

Absence of any Dark A_u State TRPES Signal: As discussed in Chapter 2, according to gas-phase theoretical calculations[206], the position of the ^1A_u state is above the S_1 state at the S_0 equilibrium geometry and photoionization is allowed from both the ^1A_u and S_1 states to D_0 in terms of a Koopmans' correlations[49]. Therefore, any $D_0 \leftarrow A_u$ state PE signal contributions should appear in the lower BE region in the aqueous-phase TRPES experiments. In the recorded liquid-jet TRPES spectra, only a single PE signal contribution at a BE of 5.2 eV was extracted, which is populated in less than 50 fs and does not change within a sub-10 ps time window. This is consistent with the previous gas-phase TRPES study[39], where no A_u signal contributions were detected. However, a recent gas-phase TRXAS study reports the involvement of ^1A_u state, which is stated to be populated by a $S_2 \rightarrow S_1 \rightarrow A_u$ cascaded process.

The present study employed a relatively high probe photon energy that was sufficient to ionize all populated neutral states. Therefore, it was expected to observe the PE signal contributions from any dark ^1A_u state population in the excited state region. Optically dark excited states have been noted to be populated with much smaller quantum yields in aqueous-phase pyrimidine derivatives in comparison to their gas-phase counterparts[284]. This effect was ascribed to the destabilization of the dark states, induced by hydrogen bonding[284]. Such a spectral shifting of the ^1A_u state would lead to the conical intersection between the (S_2, $^1B_{1u}$) and ^1A_u states having an increased barrier height, particularly with respect to the S_2-to-S_1 state crossing and the S_1 state minimum. Such a scenario would result in a much lower quantum yield for ^1A_u state formation in aqueous solution compared to in the gas-phase. This may explain why the associated signal contributions were not visible in the present TRPES studies, although it would not explain the lack of ^1A_u signal in the previous gas-phase TRPES experiments[39]. Another reason or a lack of a distinct ^1A_u signal could be that the ^1A_u ionization signal spectrally overlaps with the S_1 state ionization signal. In that case, high energy resolution experiments and the detection of photoelectron angular distribution would be required to isolate any signal contribution from the A_u state.

QY of the Triplet State(s): Considering the C state as the triplet state and assuming similar photoionization cross-sections of the S_1 and T state, the associated quantum yield was found to be around 0.65 ± 0.20. Here, the average value is reported after taking into account the results of three different LJ-TRPES experimental beamtimes. This has been determined by taking into account the spectral amplitude of the 500 fs and 250 ps fixed time-delay datasets, as shown in Figure 6.10a and 6.10b. At these fixed time-delay positions, the T and S_1 states are fully populated. The S_1 state will not be relaxed and statically at its equilibrium geometry after 500 fs. The aqueous-phase quantum yield value obtained here is consistent with the triplet-state quantum yield of 0.87 ± 0.10, reported by Bent *et.al.* in aqueous pyrazine[290]. A slight discrepancy in the mean value may occur due to the assumption of similar state-specific photoionization cross-sections in the 500 fs (S_1-state) and 250 ps (T-state) photoelectron spectra. In later gas-phase work, the associated quantum yield was found to be 0.13 following $S_0 \rightarrow S_2$ excitation[38,39]. An increased aqueous-phase quantum yield for triplet-state formation may result from solvent-induced shifting of the excited-state potential energy surfaces and can be attributed to a relatively decreased barrier height for $S_1 \rightarrow$ T state population transfer or a singlet-triplet potential energy surface crossing region that is more frequently sampled by the excited-state wavepacket. Moreover, molecular distortion in the aqueous phase can increase spin-orbit-coupling between the S_1 and T states and facilitate $S_1 \rightarrow$ T state ISC; for example, as shown by Penfold *et al.*[294], out-of-plane molecular distortion can substantially increases spin-orbit-coupling. In such cases, the extracted relaxation time could be expected to be even lower compared to in gas-phase studies[39]. However, although a decreased barrier height with an increased spin-orbit-coupling or greater sampling of a singlet-triplet curve crossing would facilitate higher ISC quantum yields, associated solvation dynamics in the liquid phase may

also increase the relaxation timescale. Relatedly, Bent *et al.*[290] also reported a high triplet state quantum yield of 1.0 in aqueous pyrimidine, which is much higher than the corresponding gas-phase quantum yield of 0.08[38]. Arpa *et al.*[295] attributed the high triplet state quantum yield in aqueous pyrimidine to the relative inaccessibility of S_1/S_0 internal conversion funnels during electronic relaxation in aqueous pyrimidine. It may be that the quantum yield for triplet formation is higher in aqueous pyrazine phase than in gas-phase pyrazine for similar reasons.

Possibility of Hydrated Electron Generation: In the present TRPES experiment, a clear signature of solvated electron was not observed in the BE range of 3.2-4.2 eV. Hydrated electron signals have been observed in several aromatic aqueous solutions, *e.g.* phenol[119], indole[120], following 266 nm excitation. Their excited-state electronic wavefunction propagates via a dissociative state, allowing hydrated electron generation. Depending on the potential energy surfaces and probing depths of the probed solution-phase species, a specific pump-probe time-delay is required to monitor hydrated electron signatures. Previously, the pump-probe time-delay was varied from hundreds of fs to ns to identify hydrated electron signals[16,119,123,290]. In the present experiment, the TRPES scan and fixed time-delay spectra were recorded up to 800 ps, which may not enough to observe the hydrated electron features if they are formed via excited triplet states in pyrazine. In the future, recording TRPES spectra, or alternative time-resolved spectroscopy, data beyond several a ns time-delay window may exclude the possibility of solvated electron generation in aqueous pyrazine following 267 nm excitation.

6.10 Summary of the TRPES Study on Aqueous Pyrazine

Liquid-microjet based TRPES experiments have been performed to investigate the ultrafast relaxation processes on 500 mM aqueous pyrazine solutions. For that purpose, TRPES scans and fixed time-delay spectra have been recorded under PISC-minimized conditions with 65-85 fs time-resolutions. Global fit analyses have been performed to extract the state-associated-spectra and the associated time constants. An associated parallel relaxation model has been proposed. The electronic state symmetries and relaxation processes are interpreted based on the previously reported gas-phase TRPES[39] and TRXAS[40] studies. The proposed relaxation modeling is based on the observation of excited-state signal components in the higher BE region of the recorded TRPES spectra. Similar photoionization cross-sections of the S_1 and T_1 states have been assumed to estimate the quantum yield for triplet state formation, although it is not clear whether this cross-section assumption is valid. At present, several scientific questions remain unanswered. Are solvated electrons formed within the 10 fs to 800 ps probed time window and how are the pyrazine excited-states modified in the aqueous phase? What are the solvation timescales in the different excited states? Do proton transfer or PCET processes occur following 267 nm excitation in aqueous pyrazine and, if so, what are the associated timescales and quantum yields? State-of-the-art theoretical calculations are necessary that explicitly consider the local hydration environment of aqueous pyrazine to help answer these questions. Such calculations are necessary to extract the photoionization cross-sections of the electronically excited states and describe the multi-dimensional, excited-state potential energy surfaces of aqueous pyrazine and extract more details about the relaxation dynamics.

The important findings of the TRPES study on aqueous pyrazine are

I From the experimental results, the excited-state VIE's were found to be 7.0 $\pm$ 0.1 eV, 5.4 $\pm$ 0.1 eV, and 5.9 $\pm$ 0.1 eV for the Frank-Condon region at the S_2 state and the relaxed, equilibrium geometries of the S_1 and T states, respectively.

II Spectral broadening and peak shifting, as well as changes of the relaxation time scales are found in the aqueous environment. The relaxation pathways in aqueous pyrazine are found to be similar to those observed in gas-phase pyrazine. However, the relaxation time scales are relatively slower and the extracted time constants are 40 $\pm$ 20 fs, 35 $\pm$ 10 ps, and 120 $\pm$ 30 ps for the $S_2 \rightarrow S_1$, $S_1 \rightarrow S_0$, and $S_1 \rightarrow$ T transitions, respectively. The bi-exponential decay in the longer time scale decays are also consistent with the fixed delay studies on aqueous pyrazine.

III An increased ISC mediated triplet state quantum yield, 0.65 $\pm$ 0.20 has been estimated in the aqueous phase, which is consistent with that extracted in previous work[290]. The excited-state triplet populations are long-lived and are expected to survive on many ns to μs timescales, based on previous work[290]. The changes in relaxation timescales and increased triplet-state quantum yields are attributed to the changes in barrier heights and the dynamics solvation processes that occur in the aqueous phase.

IV The current study highlights the importance of choosing a proper pump pulse intensity to minimize the PISC effect, particularly when using a relatively low repetition rate laser system, in order to study the nascent relaxation dynamics of condensed-phase systems. Otherwise, spectral signatures and relaxation timescales of the excited states are found to be modified in a moderately high pump intensity regime where PISC effects are present.

V The present femtosecond TRPES experiments highlights additional information, *i.e.*, excited-state energetics, singlet-to-singlet and singlet-to-triplet state decays after photoexcitation of aqueous pyrazine, which were not observed by Bent *et al.*[290] in the laser photolysis experiments using 15 ns laser pulses.

Chapter 7

Conclusions, Limitations, and Future Work

LJ-based PES experimental results on aqueous triiodide and diazine solutions have been presented in this thesis work. The associated BE's of the solute ground- and excited-state ionization features have been reported, which were calibrated using the liquid water, $1b_1$, ionization feature.

The solvent-induced effects on the molecular structure of $I^-_{3(aq.)}$ have been probed by ionizing the I 3d and I 4d core levels and analyzing the single-and multi-electron ionization channels. The experimental results have been interpreted using electronic structure calculations and associated spectral simulations, which were performed by Vladislav Kochetov and Sergey I. Bokarev. The results reveal molecular electronic energetics, a predominantly near-linear molecular structure in the bulk of an aqueous solution, and a solvent-dependent change of molecular bond length asymmetry. In addition, a larger bond length asymmetry is found at the liquid-vacuum interface region compared to in the bulk region. Considering the steady-state diazine work, non-resonant XPS measurements provide little information on the lowest valence ionization channels of the aqueous diazines. This has been circumvented by performing RPES studies. The results have been compared to the previously reported gas-phase results to identify the solvent-dependent changes of the molecular electronic structure. The results suggest an alteration of the C-N and C-C bond lengths in the aqueous diazines, and highlight changes of bonding character and atomic parentages due to intra- and intermolecular charge re-arrangement in the aqueous environment, compared to in the gas phase,. Finally, LJ-TRPES experiments have been presented to highlight excited-state relaxation dynamics in aqueous pyrazine. The excited-state BE's have been reported and associated ultrafast relaxation timescales have been extracted based on a global fit analysis. In the aqueous phase, the electronic relaxation pathways are found to be similar to in the gas-phase[39,40]. However, in the solution phase, the relaxation timescales are relatively slower and the triplet state quantum yield is found to be much higher compared to in the previously reported gas-phase studies[39]. Such changes are attributed to dynamic solvation processes and shifting of the electronic states due to solute-solvent interactions in the aqueous phase. Furthermore, the results highlights the importance of minimizing PISC effects while performing UV-pumped-EUV-probe TRPES studies on aqueous solutions.

7.1 Limitations, Areas of Improvement, and Potential Experiments

The experimental approach to investigate the ground and excited state features presented in this thesis have several limitations, which can be improved upon in the future. Several experiments are also proposed to gain additional information on the studied molecules.

Energy Calibration The nearly neat liquid water $1b_1$ and O 1s ionizing features– 11.33 $\pm$ 0.04 eV[66] and 538.1 $\pm$ 0.10 eV[136], respectively– have been used to calibrate the valence band and core-level BE's of the systems studied in this thesis. Thus, the results presented in this research work highly depend on the accuracy of these values, which are based on this assumption that the solute molecule does not perturb the electronic structure of the solvent molecule. This assumption is not general and cannot be applied to all systems at all concentrations. In order to find the effect of the solute molecules on the solvent electronic structure, an alternative approach is required[66,84]. Thürmer *et al.*[66] reported a study that has been performed using a biased liquid jet. In that approach, they found that the vertical ionization energy of the liquid water $1b_1$ molecular orbital remains similar to the neat water result (actually recorded with < 50 mM NaCl or NaI to maintain solution electrical conductivity) in a 2 M aqueous NaI solution. However, when switching to the surface-active tetrabutylammonium iodide (TBAI) 12.5 mM (half monolayer) and 25 mM (full monolayer) concentrations, the VIE of liquid $1b_1$ was found to be 10.8 $\pm$ 0.05 eV and 10.7 $\pm$ 0.05 eV, respectively, which is significantly lower than the corresponding VIE of neat water. An approach was taken to incorporate a biased liquid jet in the present TRPES measurements. However, due to time-constraints, a complete TRPES measurements using a biased jet was not possible. In the future, the biased liquid-jet and the methodology presented in reference[66] can be used in PES experiments to study the aqueous molecules reported in this thesis. This will verify or improve the energy calibration of the ground and excited state ionization channels studied in this thesis work.

Possible Dimer, Trimer, or Higher-Order Complex Formation: The possibilities of dimer, trimer, or higher-order complex formations of aqueous diazine samples have been characterized by monitoring the bulk-sensitive UV-VIS measurements. Bulk-sensitive UV-VIS measurements show no changes in the relative intensities of the absorption bands between 0.1 mM and 500 mM concentrations. If complexes start to appear well below the concentration detection limit (<0.1 mM), then the possibility of dimer, trimer, higher-order complex formation can not be ignored. Future studies are required to exclude the complex formation between the solute and solvent (water) molecules, particularly in the electronically excited states. In this respect, a wide range of concentration (10^{-4} mM to 10^{-1} mM) dependent UV-Vis absorption studies are required to monitor the changes in the absorption band. Additionally, Transient Absorption Spectroscopy (TAS) experiments could be performed using low and high solute concentrations to monitor any changes in the relaxation processes.

Improved Data Collection Efficiency and Stabilized EUV Sources for TRPES Studies The signal-to-noise ratio is low in the presented TRPES experimental results, which have been performed at a 5 kHz repetition rate using low pump laser pulse intensities. Several approaches can be pursued to improve the data collection efficiency. Generally, delay-line detectors have 10 ns dead times and are limited to operation at a few electron counts per laser shot and the 3D detector is also essential for the operation of the ARTOF spectrometer. Unfortunately, there is no economic way to improve on this dead time. However, the repetition rate of the laser system can be increased, and the whole TRPES setup could be operated at much higher repetition and electron count rates, e.g. 500 kHz instead of 5 kHz. Alternatively, the electron collection efficiency could be increased by using a magnetic-bottle spectrometer, which should give a $\sim$40-fold improvement in electron collection efficiency, although this would limit the maximum usefully detectable photoelectron kinetic energy and be at the expense of kinetic energy and angular resolution. The KE window of the recorded PE features using the low-angular dispersion mode depends on the central KE of the PEs. With the currently implemented angle-resolved TOF spectrometer, negative bias voltage application to the liquid jet would help to shift the PEs to higher central KEs and thereby allow the KE window to be increased. Additionally, this

would broaden out the gas-phase contributions so that they make negligible contributions to the individual liquid-phase peaks in the recorded PE spectra[66]. At the same time, the associated changes in the inner valence band features in TRPES experiment could, in principle, be monitored. At present, time-dependent changes in the inner valence ionization channels were not possible to obtain due to the inherent fluctuations of the EUV photon source. However, these fluctuations arise from the 1% energy and average power stability of the driving laser and the HHG process and are difficult to significantly diminish, although modern Yb:YAG laser technologies have the potential to offer an up to 10-fold improvement in shot-to-shot energy and average power stability over the currently implemented Ti:Sa laser technologies. As the significant EUV laser fluctuations transfer noise to the solute and solvent ground-state features, changes in the ground-state signals were difficult to track and any time-dependent spectral changes at higher BEs than the liquid solvent $1b_1$ BE could not be resolved with the current setup. Stable EUV sources, and improved electron collection efficiencies, are all necessary to extract ground-state bleach and recovery, as well as inner-valence solute dynamics, signals using the LJ-PES technique.

Calibration of Resonant Optical Excitation Energies at the Liquid-Vaccum Interface In the pyrazine TRPES experiments, the probe photon energy used to monitor the valence electron relaxation processes in the TRPES experiment was 38.2 eV, which is surface-sensitive for the aqueous solution, with a $\sim$1 nm probing depth[10,11]. However, the excitation wavelength, 267 nm for the pyrazine $S_2 \leftarrow S_0$ transition was chosen based on the bulk-sensitive UV-Vis measurement, adopting the assumption that the electronic excitation energy does not change between the liquid-vacuum-interface and bulk region. In the future, an aqueous pyrazine sample can be investigated using tunable pump wavelengths and EUV-probe LJ-PES or surface-second harmonic generation[296] techniques to see if there is any change in the resonant excitation wavelength at the surface region of the solution compared to in the bulk of the solution. As mentioned above, concentration-dependent UV-Vis measurements, as a bulk-sensitive technique, cannot exclude the possibility of dimer formation at the surface region of the solution, although previous interfacially-sensitive LJ-PES work suggests that such processes do not occur in aqueous pyrazine solutions, which display behaviors that are consistent with a homogeneous distribution in the aqueous phase[126]. Concentration-dependent surface SFG measurements could be performed to investigate the possibilities of any dimer, trimer, or higher-order complex formation at the liquid-vacuum interface region of aqueous pyrazine solutions. Any change in the excitation energy profile in the liquid-vacuum interface region of the solution would indicate a change or shift of the excited-state electronic states in the surface region of the solution, and may correlate with an alteration of the relaxation pathways[13–18]. Additionally, TAS could be performed using UV-based ultrashort laser pulses to monitor the bulk-sensitive electronic relaxation, which could be compared to the dynamics observed in the EUV TRPES measurements.

Photodissociation Dynamics of Aqueous Triiodide Triiodide anions in ethanol/methanol solution show photodissociation dynamics on a 300 fs timescale[24–35]. UV-pump-EUV-probe experiments could be performed to monitor such a photochemical processes in an aqueous solution. A potential experiment could be performed where the molecule may be excited at $\sim$350 nm (C-band) or $\sim$290 nm (D-band), and a 100 eV probe could be used to monitor the photodissociation and photoproduct dynamics via the changes to the resulting direct, single-active-electron and multi-electronic SU photoemission features. The 4d core-level TRPES experiment could provide background-free information not only about the time-dependent behavior of the molecular bond-length asymmetry but also the expected photodissociation dynamics of the aqueous triiodide molecule. Additionally, surface-sensitive TRPES experiments could be compared with yet-to-be-performed bulk-sensitive TAS experiments to identify any associated changes in photochemistry in the two

different regions of the aqueous solution.

Core-level TRPES Studies of Aqueous Pyrazine The TRPES experiments on aqueous pyrazine highlight the excited-state electronic structure and associated relaxation dynamics. Valence electronic states are highly sensitive to any changes in the valence electronic structure. However, the valence region is generally highly spectrally congested, as observed in the recorded TRPES spectra. Moreover, in the aqueous phase, additional inhomogeneous linewidth broadening occurs and the isolation of the individual valence ionization features in a dense manifold of signals can rarely be achieved. One way to identify different electronic state contributions is to record PADs[107], where states with different Dyson orbital symmetries are expected to display different angular distributions[39]. The excited-state electronic relaxation dynamics can also be probed using core-level TRPES measurements[297,298]. X-ray TAS experiments on gas-phase pyrazine have already highlighted the spectral signal separation of the S_1 and ^1A_u states[40]. Such core-level TAS experiments could also be performed on aqueous pyrazine samples to probe the possible role of the ^1A_u state in the condensed-phase relaxation dynamics.

This thesis work is an initial step towards understanding the behavior of a simple polyatomic molecules and associated changes in the liquid environment, especially in aqueous solution, which is the key medium of the biological/ biochemical processes in our daily life. The experimental data presented here provides essential information for further theoretical electronic structure calculations and associated spectral simulations that aim to model ground- and photoexcited-state polyatomic molecular behaviors in aqueous solutions. The presented UV-pump-EUV-probe experimental procedures notably apply to any condensed-phase time-resolved study and should be carefully considered when trying to perform condensed-phase TRPES experiments. The associated data analysis and key results can be the basis for identifying and interpreting the time-dependent changes in the ground- and excited-state features to study even more complex polyatomic molecules, *i.e.*, DNA building blocks in the liquid phase. Considering the limitations of the applied experimental methods and instrumentation, this thesis work will not only motivate performance of liquid-microjet based valence and core-level photoelectron spectroscopy experiments at higher photon-flux, for example at intense soft x-ray FEL sources, but also lead to the development of high-photon-flux and high-repetition-rate table-top soft x-ray sources to study electron-electron correlation phenomena in condensed-phase chemical conversion processes, and photophysics and photochemistry in aqueous solutions with fs/sub-fs time-resolutions.

Appendix A

XPS Analysis of Aqueous Triiodide

The presented content in this appendix has been adapted or directly taken from the publication: MS Ahsan, V Kochetov, D Hein, SI Bokarev, and I Wilkinson. *"Probing the molecular structure of aqueous triiodide via x-ray photoelectron spectroscopy and correlated electron phenomena",* Physical Chemistry Chemical Physics, 24(25):15540–15555, 2022. DOI: https://doi.org/10.1039/D1CP05840A. Published by the PCCP Owner Societies. This work is licensed under the Creative Commons Attribution 3.0 Unported License.

A.1 Surface-versus Bulk- Sensitive BE's and FWHM's

Table A.1: Valence (top section), core I 4d (middle section), and core I 3d (bottom section) electron BEs and peak FWHMs of aqueous triiodide extracted from the surface- and bulk-solution-sensitive XPS studies. The results reported in the table were obtained from cumulative Gaussian and Voigt profile fittings to the background subtracted valence (peaks 1-2) and core-level (peaks 3-15) spectra, respectively. A '*' represents the final spin-orbit state averaged values. The values reported here are the averages of all of the measurements performed at the BESSY II and PETRA III facilities and the different employed detection geometries have no effect on the BEs and FWHMs extracted from the PE peaks.

	Peak	Surface Energetics		Bulk Energetics	
		BE (eV)	FWHM (eV)	BE (eV)	FWHM (eV)
Val.	1	7.9 ± 0.1 *	1.3 ± 0.1	7.8 ± 0.1 *	1.2 ± 0.1
	2	9.2 ± 0.04 *	0.8 ± 0.04	9.3 ± 0.1 *	1.3 ± 0.1
Core I 4d	3	54.2 ± 0.04	0.8 ± 0.04	54.2 ± 0.05	1.0 ± 0.04
	4	55.5 ± 0.04	1.7 ± 0.1	55.6 ± 0.04	1.5 ± 0.04
	5	57.1 ± 0.05	0.8 ± 0.1	57.2 ± 0.04	0.9 ± 0.1
	6	59.0 ± 0.05	1.0 ± 0.2	59.1 ± 0.05	1.2 ± 0.1
	7	60.7 ± 0.1	1.3 ± 0.5	60.8 ± 0.1	1.1 ± 0.1
Core I 3d	8	624.2 ± 0.1	1.2 ± 0.1	624.1 ± 0.1	1.2 ± 0.1
	9	625.3 ± 0.1	1.3 ± 0.1	625.2 ± 0.1	1.3 ± 0.1
	10	627.3 ± 0.1	1.2 ± 0.1	627.3 ± 0.1	0.9 ± 0.1
	11	629.1 ± 0.1	1.3 ± 0.2	629.0 ± 0.1	1.6 ± 0.1
	12	635.7 ± 0.1	1.1 ± 0.01	635.6 ± 0.1	1.3 ± 0.1
	13	636.7 ± 0.1	1.3 ± 0.1	636.8 ± 0.1	1.3 ± 0.1
	14	638.7 ± 0.1	1.0 ± 0.2	638.8 ± 0.1	0.8 ± 0.1
	15	640.5 ± 0.1	1.7 ± 0.1	640.6 ± 0.1	1.8 ± 0.1

A.2 I^- and I_2 Mixing Ratio Dependence Study in $I^-_{3(aq.)}$ Preparation

NaI and I_2 solutes were mixed in aqueous solution at various ratios, specifically 2:1 and 7:5 ratios, to prepare different concentrations of $I^-_{3(aq.)}$. 500 mM NaI and 250 mM I_2 or 350 mM NaI and 250 mM I_2 were mixed in aqueous solution to prepare ∼228 mM or ∼168 mM $I^-_{3(aq.)}$ solutions. Associated XPS signal contributions were recorded in a perpendicular geometry conditions at BESSY II. Related $I_{3(aq.)}$ and $I_{3(aq.)}$ concentrations were determined using UV-Vis spectroscopy, as described in Section 4.1, a similar data analysis treatment as that described in Section 4.3 was applied. Within the uncertainty limit s of the measurements, the measured BEs between the two different solutions did not change, and SU-to-main peak intensity ratios, shown in Table 4.3 are found to be unaffected when different mixing ratios of I_2 and $I^-_{(aq.)}$ were used in preparing the $I^-_{3(aq.)}$ solutions.

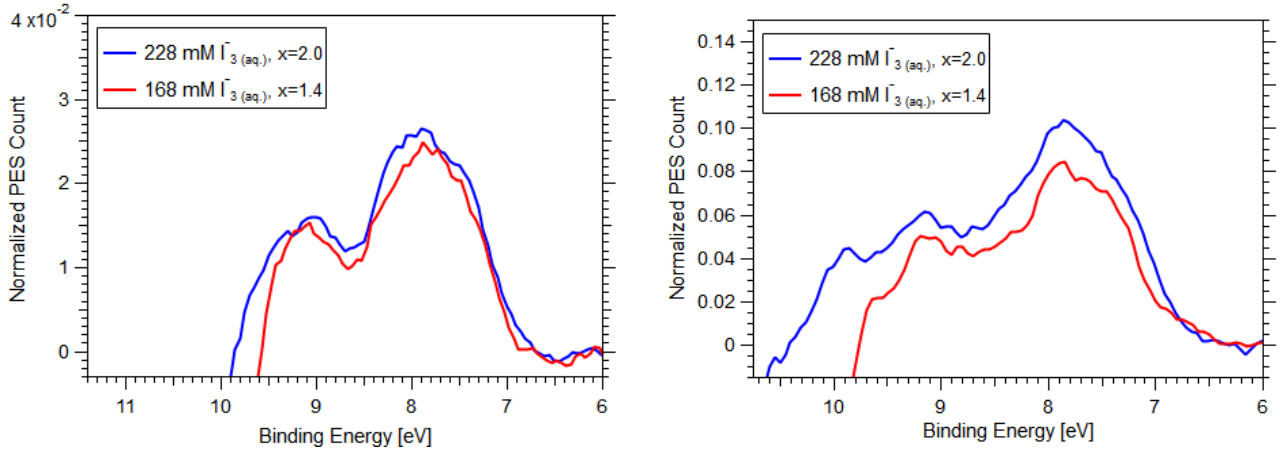

Figure A.1: Smoothed XPS spectra of $I^-_{3(aq.)}$ recorded at BESSY II. The left panel shows surface-sensitive spectra and the right panel shows the bulk-sensitive spectra. The solutions were prepared by mixing NaI and I_2 solutes at different mixing ratios of x=2.0 and 1.4, to produce ∼228 mM and ∼168 mM, respectively. See the main body of the text for further details. The figures are reproduced with permission from Reference 167, licensed under the Creative Commons Attribution 3.0 Unported License.

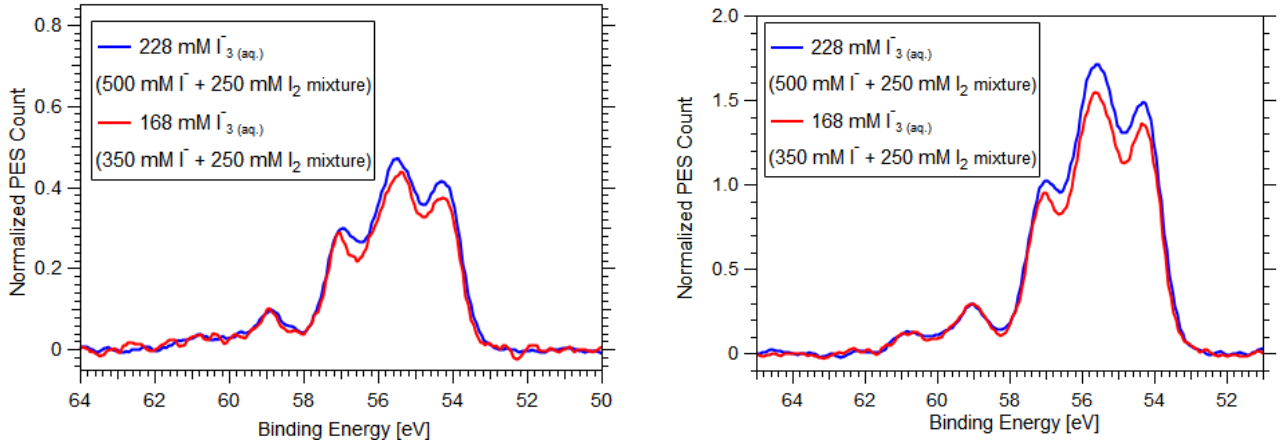

Figure A.2: Surface-(left) and bulk-(right) sensitive smoothed I 4d core-level XPS spectra of $I^-_{3(aq.)}$ recorded at BESSY II. The $I^-_{3(aq.)}$ solutions concentrations were determined to be 228 mM and 168 mM, where NaI and I_2 solutes were mixed at different mixing ratios of x=1.4 and 2.0, respectively. The figures are reproduced with permission from Reference 167, licensed under the Creative Commons Attribution 3.0 Unported License.

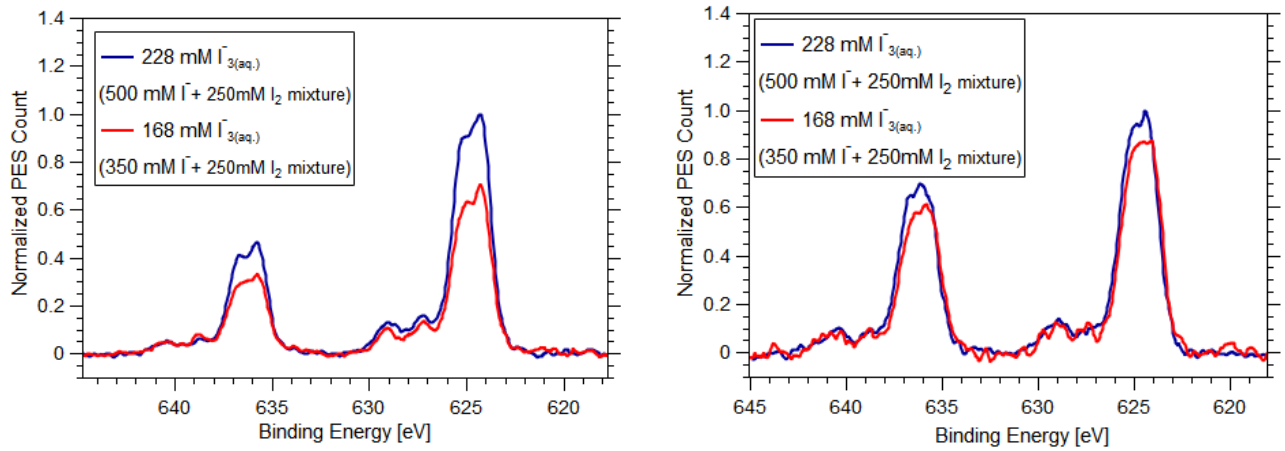

Figure A.3: Surface-(left) and bulk-(right) sensitive smoothed I 3d core-level XPS spectra of $I^-_{3(\mathrm{aq.})}$ recorded at BESSY II. The $I^-_{3(aq.)}$ solutions concentrations were determined to be 228 mM and 168 mM, where NaI and I_2 solutes were mixed at different mixing ratios of x=1.4 and 2.0, respectively. The figures are reproduced with permission from Reference 167, licensed under the Creative Commons Attribution 3.0 Unported License.

Appendix B

Steady-State Measurements and Analysis

B.1 X-ray Spectroscopy of the Diazine Molecules in the Gas-Phase

Table B.1: Pyrimidine gas-phase BE's reported in the literature. The MO assignments are ordered based on the most recent literature from Reference 176.

Ionization channels	Holland *et al.*[176]	Kishimoto *et al.*[195]	Gleiter *et al.*[181]	Bolognesi *et al.*[88]†	O'Keeffe *et al.*[274]†	Average
$(7b_2, n_N)^{-1}$	9.8	9.7	9.73	9.63	9.73	9.72 ± 0.03
$(2b_1, \pi)^{-1}$	10.5	10.5	10.41	10.49	10.53	10.49 ± 0.02
$(11a_1, n_N)^{-1}$	11.2	11.22	11.23	11.22	11.2	11.21 ± 0.01
$(1a_2, \pi)^{-1}$	11.5	11.5	11.39	11.66	11.4	11.49 ± 0.05
$(6b_2, \sigma)^{-1}$	14.4				14.4	
$(9a_1, \sigma)^{-1}$	15.8				15.95	
$(5b_2, \sigma)^{-1}$	17.0	16.88			16.95	
$(7a_1, \sigma)^{-1}$, $(4b_2, \sigma)^{-1}$	20.8					
$(6a_1, \sigma)^{-1}$	24.5					
$(3b_2, \sigma)^{-1}$	26.6					

† The ionization energetics reported by Bolognesi *et al.*[88] and O'Keeffe *et al.*[274] assigned to the ionization channel ordering reported by Holland *et al.*[176]

Table B.2: Pyridazine gas-phase BE's reported in the literature. The MO assignments are ordered based on the most recent literature from Reference 195.

Ionization channels	Kishimoto *et al.*[195]	Gleiter *et al.*[181]	Average
$(8b_2, n_N)^{-1}$	9.27	9.31	9.29 ± 0.02
$(1a_2, \pi)^{-1}$	10.61	10.61	10.61 ± 0.00
$(2b_1, \pi)^{-1}$	11.2	11.3	11.25 ± 0.05
$(10a_2, n_N)^{-1}$	11.3	11.3	11.30 ± 0.00
$(1b_1, \pi)^{-1}$	13.97	-	-
$(6b_2, \sigma)^{-1}$	15.9	-	-

Table B.3: Pyrazine gas-phase BE's reported in the literature. The MO assignments are ordered based on the most recent literature from Reference 176.

Ionization channels	Holland *et al.*[176]	Kishimoto *et al.*[195]	Gleiter *et al.*[181]	Average
$(6a_g, n_N)^{-1}$	9.40	9.61	9.63	9.55 ± 0.07
$(1b_{1g}, \pi)^{-1}$	10.20	10.20	10.18	10.19 ± 0.01
$(5b_{1u}, n_N)^{-1}$	11.30	11.38	11.35	11.34 ± 0.02
$(1b_{2g}, \pi)^{-1}$	11.80	11.80	11.77	11.79 ± 0.01
$(4b_{2u}, \sigma)^{-1}$	15.0	15.0		
$(2b_{3u}, \sigma)^{-1}$, $(5a_g, \sigma)^{-1}$	17		16.97	
$(4a_g, \sigma)^{-1}$, $(2b_{3g}, \sigma)^{-1}$	20.7			
$(2b_{2u}, \sigma)^{-1}$	24.1			

† The MO's ordering reported by Gleiter *et al.*[181] is different

B.2 Concentration-Dependent Studies on the Aqueous Diazines

A relatively high concentration of 500 mM was chosen for the XPS and TRPES studies on the aqueous diazine species. The goal of such measurements was notably to study the monomer in the aqueous phase, *i.e.* a single diazine molecule surrounded by and interacting with water molecules. A 125 mM concentration is close to the lower sensitivity limit of the experimental technique with the 5 kHz light source and angle-resolved time-of-flight spectrometer, and any uniformly distributed concentration below 100 mM will result in a poor signal-to-noise ratio of the recorded signals. Self-association processes in aqueous solutions are expected to lead to additional bonding interactions between the diazine molecules. If such self-association processes occur between ground-state solute molecules, an associated concentration-dependent change of the UV-Vis absorption[299–303] and/or PE spectra would be expected[299]. Initially, two different aqueous diazine concentrations (0.25 mM and 500 mM) were chosen for solution-phase UV-Vis absorption spectroscopy measurements. Then concentration-dependent (over 100 mM) valence and core-level XPS studies were performed on aqueous pyrimidine. Although such XPS studies have been performed on aqueous pyrimidine solutions, similar results are expected to be applicable to the other isomers.

UV-Vis Measurements Figure B.1 shows normalized spectral profiles of the concentration-dependent UV-Vis measurements of pyridazine (panel a), pyrimidine (panel b), and pyrazine (panel c). The concentration-dependent results are compared to extract the changes associated with solute-solute-molecule interactions. 10 ± 0.5 mm and 10 ± 2 μm absorption cell path lengths were used to measure the 0.25 ± 0.1 mM and 500 ± 30 mM concentration solution absorption spectra, respectively. The insets in Figure B.1 show the results of the concentration-dependent measurements, which were normalized by the concentration and cell length to obtain the molar absorption co-efficients. For such UV-Vis absorption measurements, initially 500 ± 30 mM of 10 mL sample solutions were prepared and diluted in 10-12 steps to obtain 0.25 mM solutions. In that case, the initial error of the sample concentration was propagated into the final 0.25 mM solutions. Therefore, the involved uncertainties in path lengths and prepared sample concentrations restrict the direct comparison of the molar absorption co-efficients and the extraction of any meaningful information on the possibilities of the dimer or higher-order complex formation in the aqueous phase. Therefore, the intensity normalized and averaged spectra are compared. The normalized absorbance results show that the ground-state spectral features, *i.e.*, absorption peaks, peak intensity ratios, and peak widths of the diazine solutes do not change in the concentration range from 0.25 mM to 500 mM. A concentration-dependent change of molar absorption co-efficients were found in the pyrimidine and pyrazine solutions, which were previously reported

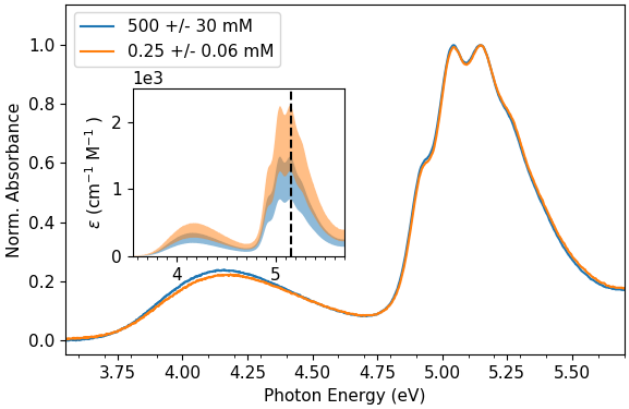

(a) Pyridazine (aq.) solutions

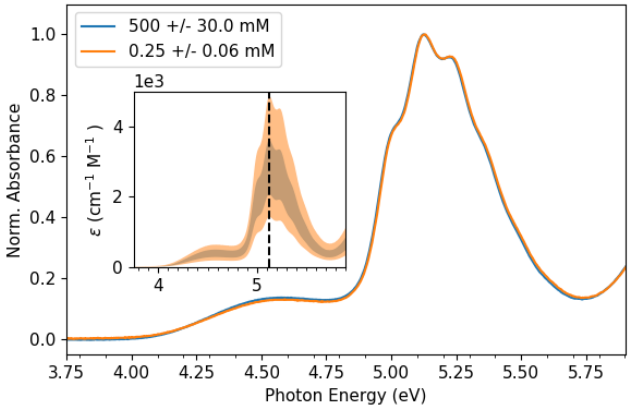

(b) Pyrimidine (aq.) solutions

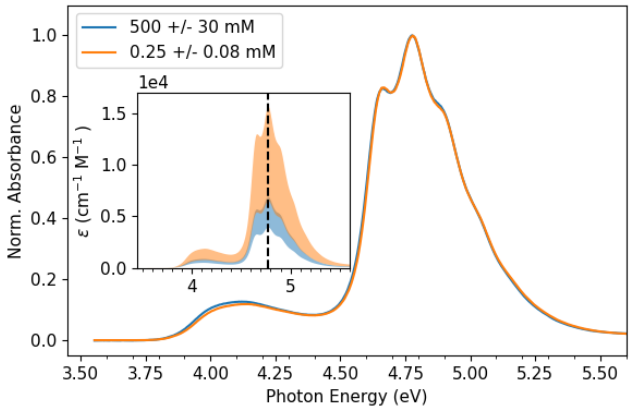

(c) Pyrazine (aq.) solutions

Figure B.1: Concentration-dependent UV-VIS absorption measurements of the diazine aqueous solutions. For each diazine solutes, 0.25 mM and 500 mM UV-VIS absorption measurements are presented. The inset shows the normalized spectral profiles of all the diazine. More details are given in the main body of the texts.

for pyrimidine and pyrazine, and ascribed as self-association behaviors[189].

Previous UV-Vis absorption measurement reports on numerous aqueous solutions highlight that self-association not only generally results in changing concentration-dependent molar absorption co-efficients but that it also reshapes and shifts the spectral absorption profiles[299–303]. However, the present UV-Vis studies show that the spectral profiles are unaffected as a function of solute concentration. Therefore, self-association behavior in the aqueous diazine can not be confirmed based on only a concentration-dependent change of molar absorption co-efficients within the studied concentration range (0.25 - 500 mM). A careful sample preparation method and further studies are required to confirm any self-association behavior in the aqueous diazine solutions. Notably, the present analysis does not exclude the possibilities of dimer formation if it starts to happen below a 0.25 mM concentration, which is well below the detection limit of the experimental UV-Vis absorption setup. Furthermore, the analysis reported here will generally be insensitive to excited-state association of the diazine molecules, with such exciplex formation expected to occur on picosecond to nanosecond timescales. Concentration-dependent transient absorption work would be required, for example, to probe whether excited state complexes form at 500 mM aqueous diazine concentrations following UV excitation.

XPS Measurements The valence electronic structure of the aqueous diazines have been studied using a 150 eV photon energy, whereas the C 1s and N 1s core-level energetics have been studied using 420 eV

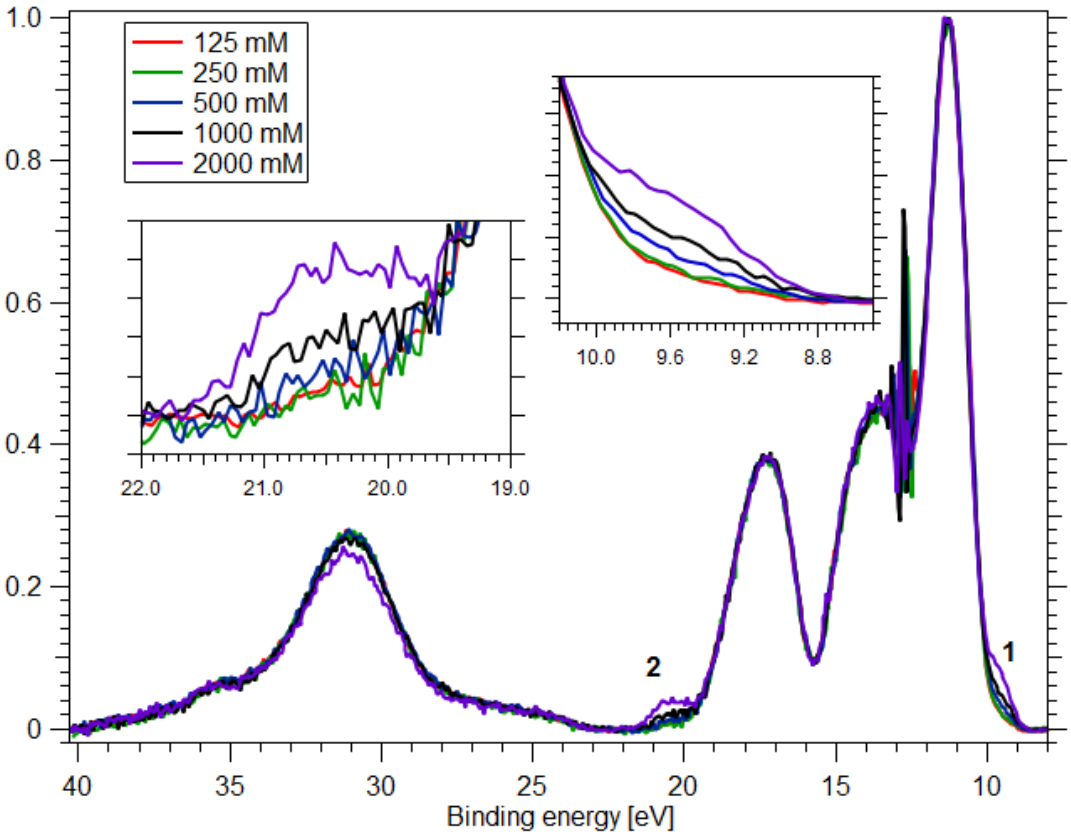

(a) Valence PE spectra

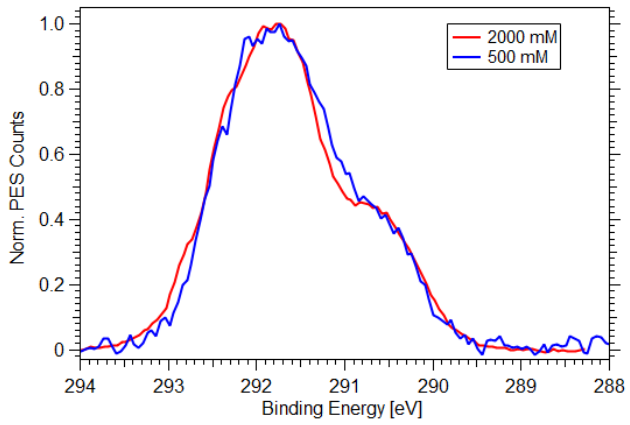

(b) C 1s core-level

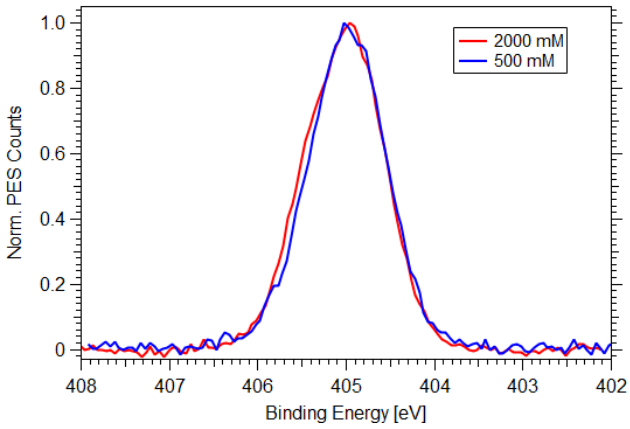

(c) N 1s core-level

Figure B.2: Concentration-dependence (125–2000 mM) of the valence (panel (a)), C 1s (panel (b)) and N 1s (panel (b)) core-level PE spectra of aqueous pyrimidine recorded at BESSY II using 150 eV, 420 eV and 540 eV photon energies, respectively. The labels 1 and 2 highlight two different valence solute ionization channels. Both of N 1s and 2000 mM C 1s spectra were recorded at the Magic angle geometry, whereas, 500 mM C 1s spectrum were recorded at the perpendicular geometry with respect to the incoming X-ray beam.

and 540 eV photon energies, respectively. In all of the valence PE experiments, the spectrometer electron-collection axis was oriented perpendicular to the polarization of the x-ray light. Table B.4 shows the extracted BEs and the peak FWHMs. Two valence solute BEs have been identified and the extracted values do not vary with the solute concentration. Similar behavior has been identified from the C 1s and N 1s core-level XPS spectra, which highlights that the extracted BE's do not change in the studied 500 mM and 2000 mM solute concentration range. This study indicates that at least within a 125 mM to 2000 mM concentration range,

Table B.4: Concentation dependence of the electron binding energies recorded in surface-sensitive aqueous pyrimidine XPS experiments. The valence and core (N and C 1s) electron BE's and FWHM's are extracted and reported, based on the non-resonant XPS measurements performed at BESSY II.

Features	Concentrations	Aqueous Surface	
		BE (eV)	FWHM (eV)
Valence, I	125 mM	9.59 $\pm$ 0.05	0.78 $\pm$ 0.04
	250 mM	9.58 $\pm$ 0.05	0.80 $\pm$ 0.08
	500 mM	9.63 $\pm$ 0.04	0.84 $\pm$ 0.04
	1000 mM	9.61 $\pm$ 0.04	0.84 $\pm$ 0.03
	2000 mM	9.62 $\pm$ 0.05	0.83 $\pm$ 0.03
Valence, II	125 mM	20.53 $\pm$ 0.05	1.09 $\pm$ 0.12
	250 mM	20.55 $\pm$ 0.07	1.06 $\pm$ 0.15
	500 mM	20.50 $\pm$ 0.06	1.11 $\pm$ 0.10
	1000 mM	20.56 $\pm$ 0.04	1.26 $\pm$ 0.09
	2000 mM	20.54 $\pm$ 0.04	1.33 $\pm$ 0.05
$(C1s)^{-1}$, I	500 M	291.86 $\pm$ 0.05	1.33 $\pm$ 0.02
	2000 M	291.85 $\pm$ 0.05	1.27 $\pm$ 0.03
$(C1s)^{-1}$, II	500 mM	290.57 $\pm$ 0.06	1.04 $\pm$ 0.06
	2000 M	290.47 $\pm$ 0.05	0.87 $\pm$ 0.05
$(N1s)^{-1}$	500 mM	405.04 $\pm$ 0.10	1.03 $\pm$ 0.03
	2000 mM	405.05 $\pm$ 0.05	1.01 $\pm$ 0.03

the electronic structure of aqueous pyrimidine does not change; a BE-shift would be expected if significant self-association occurred in the aqueous phase[299].

Appendix C

Time-Resolved Measurements and Analysis

C.1 TRPES on 50 mM NaCl in Water

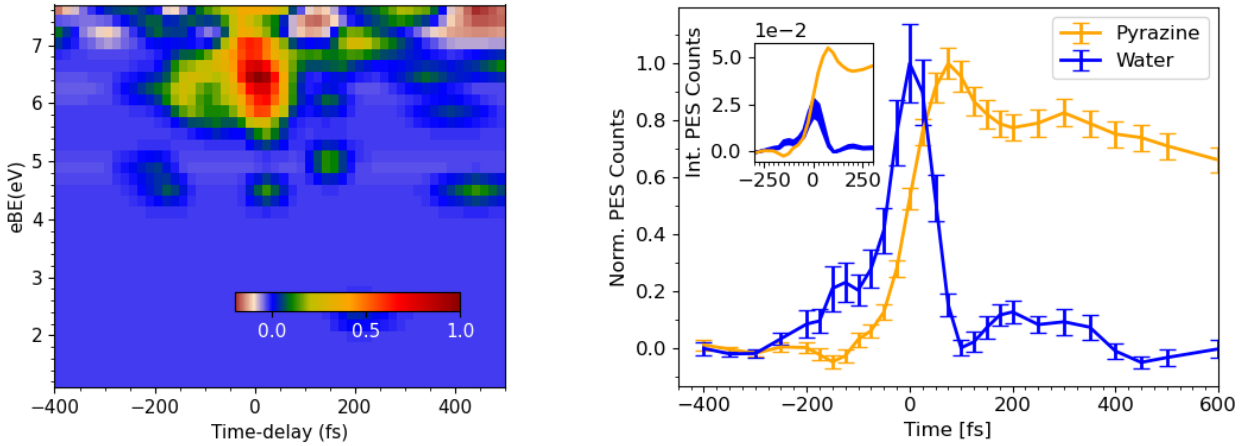

(a) Time-resolved study on 50 mM NaCl in water

(b) Time-dependent integrated PES count

Figure C.1: LJ-based TRPES study performed on a 50 mM aqueous NaCl solution. After energy binning and filtering operations, panel (a) shows the experimental TRPES data. The right panel shows the integrated PES count versus time delay, highlighting a narrow Gaussian-like profile of 85 fs width (blue). Panel (b) also highlights the BE-integrated TRPES data of 500 mM aqueous pyrazine (orange) plotted on top of the water solvent data. Both curves were normalized to 1. The inset shows the BE-integrated PE counts of the data recorded from both solutions under similar acquisition conditions, normalized by the ratio of the two acquisition times. More details are provided in the main body of the text.

The aqueous pyrazine solution was mixed with 50 mM NaCl to avoid electrokinetic charging effects. Therefore, a separate time-resolved experiment has been performed on the 50 mM NaCl aqueous solutions to confirm that there are no underlying electron dynamics associated with NaCl or water. The pyrazine solution experiments were performed using 75 fs, 60 nJ, 267 nm pump pulses at the sample target with a peak intensity of $\sim$25 GW/cm^2 and 38.5 eV EUV probe photon pulses with $\sim$45 fs durations and $\sim$15 pJ energies, corresponding to peak intensities of 22 MW/cm^2. Figure C.1a shows the 2D map of the time-resolved photoelectron spectra of 50 mM NaCl in water. The intensity normalized, BE-integrated (5.0-7.8 eV) data is shown as a function of pump-probe time delay in Figure C.1b. Despite the presence of a noisy background, this data highlights the essentially symmetric shape of the signal around the time-zero with a FWHM of 85 fs. This signal is due to the cross-correlation contribution or instrument response function of the pump and probe laser pulses and it defines the temporal response of the experiment. This confirms that no underlying dynamics

occurs following UV or EUV excitation of the 50 mM NaCl aqueous solutions; otherwise, an exponential decay signature would be observed within the instrument response time around the time-zero. Such a finding is consistent with the results reported by Miura *et al.*[284]. However, a small asymmetric decay is observed in the negative pump-probe time delay, which may arise due to relatively low signal-to-noise ratio of the recorded PE CC signal. A BE-integrated TRPES spectrum of 500 mM aqueous pyrazine (orange) is also plotted in Figure C.1b and on top of the CC signal recorded from water. This data shows that there is a time-delay in the signal growth from the sample solutions, which is the time the photoexcited-state wavepacket takes to move from the Frank-Condon point to the point where the photoionization probability is maximised. A comparison of the time-integrated photoelectron counts with in the BE range 5.0 eV to 7.8 eV is shown in the inset of Figure C.1b. The TRPES spectra of 50 mM NaCl in water (blue curve) and 500 mM aqueous pyrazine (orange curve) were effectively recorded for 2.5 minutes and 12-18 minutes, respectively; the latter range is linked to the instability of the LJ over the seven-working-day measurement period of the pyrazine data and a corresponding 15-minute average pyrazine acquisition time is considered in the following. In contrast, the water TRPES spectra were recorded within a short time window in a working day. Considering the uncertainties of the experimental conditions over different working days and the associated experimental instabilities, the water spectrum shown in the inset is multiplied by factor of 6 $\pm$ 1.5 to directly compare with the aqueous pyrazine temporal profile. Within the uncertainly limit of the integrated water signal profile, the result shows that the pyrazine PE signal counts dominate in the recorded TRPES spectra from the aqueous pyrazine solution. However, in order to directly compare the time-integrated TRPES spectra of both solutions, the TRPES spectra need to be recorded under exactly the same experimental conditions, ideally with an experimental setup that offers higher electron collection efficiency.

C.2 Global-Fit Analysis Procedure

The following set of differential equations describes the population dynamics of the ground and excited states using a parallel kinetic model (see Equation 6.3). This model was utilized in order to model the experimental data presented in Chapter 6.

$$\begin{aligned}
\frac{\mathrm{d[G]}}{\mathrm{dt}} &= -\mathrm{I(t)[G]} \\
\frac{\mathrm{d[A]}}{\mathrm{dt}} &= \mathrm{I(t)[G]} - \mathrm{k_1[A]} \\
\frac{\mathrm{d[B]}}{\mathrm{dt}} &= \mathrm{k_A[A]} - (\mathrm{k_{B_1}} + \mathrm{k_{B_2}})\mathrm{[B]} \\
\frac{\mathrm{d[C]}}{\mathrm{dt}} &= \mathrm{k_{B_2}[B]} - \mathrm{k_C[C]}
\end{aligned} \tag{C.1}$$

The time-dependent photoexcitation rate of state A from the ground state, G, is defined as:

$$\mathrm{I(t)} = \mathrm{A_{pc}} \exp\big(-\frac{\mathrm{t}^2}{2\Delta \mathrm{t}_{\mathrm{pp}}^2}\big)$$

where $\Delta \mathrm{t_{pc}}$ is the pump pulse duration. The $\mathrm{A_{pc}}$ term includes the contributions of the pump-pulse intensity envelope and the solute absorption cross-sections. In order to model the experimental data, as shown in Figure 6.6, the above differential equations were solved using the initial conditions, G(0)=1, A(0)=0, B(0)=0, C(0)=0.

An iterative least-square fitting method (Python package lmfit, minimize) was applied to perform the global fits, the results of which are shown in Figure 6.11. The 2D map of a TRPES scan spectra can be expressed

as:

$$\mathrm{F(E,t)} = \mathrm{Cf_A(E)} \cdot \Big[\mathrm{A(t)} \otimes \mathrm{g(t)}\Big] + \mathrm{Cf_B(E)} \cdot \Big[\mathrm{B(t)} \otimes \mathrm{g(t)}\Big] + \mathrm{Cf_C(E)} \cdot \Big[\mathrm{C(t)} \otimes \mathrm{g(t)}\Big] \tag{C.2}$$

The coefficients $\mathrm{Cf_{A,B,C}(E)}$ described the photoelectron BE distributions for the electronically excited states and define their state-associated spectra. The solutions of the differential equations are A(t), B(t), and C(t). g(t) is defined as the cross-correlation or instrument-response function. The time-dependent state populations, X(t), are determined by taking the convolution between the solutions of the differential equations and cross-correlation function. X(t) is defined as:

$$\mathrm{X(t)} = \sum_{\mathrm{D_q=A,B,C}} \mathrm{D_q(t)} \otimes \mathrm{g(t)}$$

Fit Routine: At the starting point of the fitting procedure, the initial values of the time constants and the energy coefficients ($\mathrm{Cf_{A,B,C}(E)}$) are generated. The set of differential equations (see Equations. C.1) are solved by using the initial values of the time-constants, which are then convolved with the instrumental response function (CC) to get the time-dependent state populations, X(t). The energy coefficients are multiplied with the time-dependent state population to generate the initial guess of the TRPES datasets ($\mathrm{F_{fit}}$) for the fitting algorithm (Equation C.2). The fitting algorithm compares $\mathrm{F_{fit}}$ and $\mathrm{F_{exp}}$, and minimizes their difference in each iteration step. The difference is parameterized as a reduced-chi-square χ^2_{red} value, $\chi^2_{\mathrm{red}} = |(\mathrm{F_{exp}} - \mathrm{F_{fit}})|^2/(\mathrm{N} - \mathrm{N_{var}})$. For each initial value set, the χ^2_{red} value is minimized, unless the local minima within a given set of initial values was found. In order to find the global minimum in the multi-dimensional search space, the same fitting routine was implemented with different sets of initial values of the time constants and energy coefficients. Finally, the χ^2_{red} values obtained from each iteration are compared. Among them, the fit parameters (time-constants (τ_{i}) and the energy coefficients ($\mathrm{A(E), B(E), C(E)}$)) corresponding to the lowest χ^2_{red} value were taken as the best results of the fits. Typically, 30-35 sets of initial values were chosen to reach the convergence for such a global fit analysis. At the point of convergence, the χ^2_{red} remains unchanged within the tolerance level of 10^{-11}.

Functional Form of the Solutions of the Differential Equations: To demonstrate the expected (BE-integrated) population dynamics of S_2-excited aqueous pyrazine, the differential equation set presented above (Equations C.1) was solved by neglecting the ground-state populations to produce Figure C.2b. This was achieved by setting the initial population values as A(0)=1,B(0)=0,C(0)=0. The approximate solutions of the above coupled differential equations for a parallel three-state model, see Equation C.1, are shown below:

$$\begin{aligned}
\mathrm{A(t)} &= \mathrm{e}^{-\mathrm{k_A t}} \\
\mathrm{B(t)} &= -\frac{\mathrm{k_1\,(k_A - k_C)\,e^{-k_A t}}}{\mathrm{k_A^2 - k_A\,(k_{B_1} + k_{B_2} + k_C) + k_{B_1}k_C + k_{B_2}k_C}} - \\
&\quad \frac{\mathrm{k_A\,(k_{B_1} + k_{B_2} - k_C)\,e^{-t\left(k_{B_1} + k_{B_2}\right)}}}{\mathrm{-k_A\,(k_{B_1} + k_{B_2} - k_C) + k_{B_1}^2 + k_{B_1}\cdot(2k_{B_2} - k_C) + k_{B_2}^2 - k_{B_2}k_C}} \\
\mathrm{C(t)} &= \frac{\mathrm{k_A k_{B_2} e^{-t\left(k_{B_1} + k_{B_2}\right)}}}{\mathrm{-k_A\,(k_{B_1} + k_{B_2} - k_C) + k_{B_1}^2 + k_{B_1}\cdot(2k_{B_2} - k_C) + k_{B_2}^2 - k_{B_2}k_C}} + \\
&\quad \frac{\mathrm{k_A k_{B_2} e^{-k_C t}}}{\mathrm{k_1\,(k_{B_1} + k_{B_2} - k_C) - k_{B_1}k_C - k_{B_2}k_C + k_C^2}} + \frac{\mathrm{k_A k_{B_2} e^{-k_A t}}}{\mathrm{k_A^2 - k_A\,(k_{B_1} + k_{B_2} + k_C) + k_{B_1}k_C + k_{B_2}k_C}}
\end{aligned} \tag{C.3}$$

Where $\mathrm{k} = 1/\tau$.

Similarly, the related serial model (see Equation 6.2) is described by:

$$\begin{aligned}
\frac{\mathrm{d[G]}}{\mathrm{dt}} &= -\mathrm{I(t)[G]} \\
\frac{\mathrm{d[A]}}{\mathrm{dt}} &= \mathrm{I(t)[G]} - \mathrm{k_A[A]} \\
\frac{\mathrm{d[B]}}{\mathrm{dt}} &= \mathrm{k_A[A]} - \mathrm{k_B[B]} \\
\frac{\mathrm{d[C]}}{\mathrm{dt}} &= \mathrm{k_B[B]} - \mathrm{k_C[C]}
\end{aligned} \tag{C.4}$$

Similar to the parallel model, the set differential equations describing the serial model (see Equation 6.2) were solved by neglecting the ground-state population and setting the initial state population values as A(0)=1,B(0)=0,C(0)=0. The approximate solutions of the above coupled differential equations for a serial three-state model are shown below. . The associated (BE-integrated) temporal profiles are shown in the left panel of Figure C.2a.

$$\begin{aligned}
\mathrm{A(t)} &= \mathrm{e^{-k_A t}} \\
\mathrm{B(t)} &= -\frac{\mathrm{k_A\,(k_A - k_C)\,e^{-k_A t}}}{\mathrm{k_A^2 - k_A\,(k_B + k_B) + k_B k_C}} + \frac{\mathrm{k_A\,(k_B - k_C)\,e^{-k_B t}}}{\mathrm{k_A\,(k_B - k_C) - k_2^2 + k_2 k_3}} \\
\mathrm{C(t)} &= \frac{\mathrm{k_A k_B e^{-k_C t}}}{\mathrm{k_A\,(k_B - k_C) - k_2 k_3 + k_3^2}} - \frac{\mathrm{k_A k_B e^{-k_B t}}}{\mathrm{k_A\,(k_B - k_C) - k_2^B + k_B k_3}} + \frac{\mathrm{k_A k_B e^{-k_A t}}}{\mathrm{k_A^2 - k_A\,(k_B + k_C) + k_B k_C}}
\end{aligned} \tag{C.5}$$

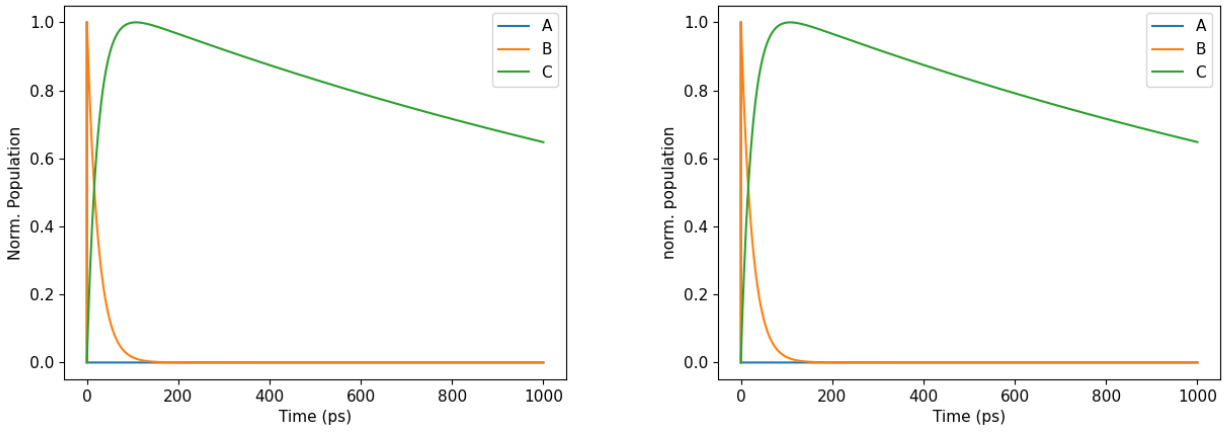

(a) Serial (b) Parallel

Figure C.2: The solutions of the differential equations for the serial (eq. C.5) and parallel (eq. C.3) models, after neglecting the ground-state contributions, are shown left and right panels, respectively. The figures highlight the excited-state decays. The considered time-constants are 40 fs, 25 ps and 2 ns for the serial decay model, whereas the parallel model considers 40 fs, 35 ps, 120 ps, and 2 ns time-constants. In both cases, the assumed pump and probe pulse duration were 45 fs and 50 fs, respectively. The considered exemplary time-constants are within the error bounds of the time-constants obtained from the experimental data, as shown in Table 6.2.

Comparison Between the Serial and Parallel Kinetic Models: A comparison of the second part of Equations C.3 and C.5 show that the $\mathrm{k_B}$ in the serial model is the summation of the $\mathrm{k_{B_1}}$ and $\mathrm{k_{B_2}}$ rate coefficients

obtained in the parallel model, where k is related to the relaxation time-constants by $\mathrm{k_x} = 1/\tau_\mathrm{x}$, x=A, B, C, etc.´ Therefore, Equations C.5 and C.3 result in similar excited-state decay behavior. Such equivalence is shown in Figure C.2, which shows the exact solutions of the serial and parallel kinetic models. In this respect, additional information on the possible relaxation timescales can be obtained in the parallel model, under the assumption of similar photoionization cross-sections of the involved excited-states, as described in Chapter 6.

Bibliography

[1] HH Fielding and GA Worth. Using time-resolved photoelectron spectroscopy to unravel the electronic relaxation dynamics of photoexcited molecules. *Chemical Society Reviews*, 47(2):309–321, 2018.

[2] E Brini, CJ Fennell, M Fernandez-Serra, B Hribar-Lee, M Luksic, and KA Dill. How water's properties are encoded in its molecular structure and energies. *Chemical Reviews*, 117(19):12385–12414, 2017.

[3] SG Harrellson, MS DeLay, X Chen, AH Cavusoglu, J Dworkin, HA Stone, and O Sahin. Hydration solids. *Nature*, 619:500–505, 2023.

[4] M Chaplin. Do we underestimate the importance of water in cell biology? *Nature Reviews Molecular Cell Biology*, 7(11):861–866, 2006.

[5] CL Perrin. Symmetries of hydrogen bonds in solution. *Science*, 266(5191):1665–1668, 1994.

[6] D Ben-Amotz and R Underwood. Unraveling water's entropic mysteries: A unified view of nonpolar, polar, and ionic hydration. *Accounts of Chemical Research*, 41(8):957–967, 2008.

[7] Y Zeng, A Li, and T Yan. Hydrogen bond dynamics in the solvation shell on proton transfer in aqueous solution. *The Journal of Physical Chemistry B*, 124(9):1817–1823, 2020.

[8] RM Lynden-Bell, JC Rasaiah, and JP Noworyta. Using simulation to study solvation in water. *Pure and Applied Chemistry*, 73(11):1721–1731, 2001.

[9] P Jungwirth and DJ Tobias. Specific ion effects at the air/water interface. *Chemical Reviews*, 106(4):1259–1281, 2006.

[10] S Thürmer, R Seidel, M Faubel, W Eberhardt, JC Hemminger, SE Bradforth, and B Winter. Photoelectron angular distributions from liquid water: effects of electron scattering. *Physical Review Letters*, 111(17):173005, 2013.

[11] N Ottosson, M Faubel, SE Bradforth, P Jungwirth, and B Winter. Photoelectron spectroscopy of liquid water and aqueous solution: Electron effective attenuation lengths and emission-angle anisotropy. *Journal of Electron Spectroscopy and Related Phenomena*, 177(2-3):60–70, 2010.

[12] I Persson, J Werner, O Björneholm, YS Blanco, Ö Topel, and ÉG Bajnóczi. Solution chemistry in the surface region of aqueous solutions. *Pure and Applied Chemistry*, 92(10):1553–1561, 2020.

[13] MF Ruiz-Lopez, JS Francisco, MTC Martins-Costa, and JM Anglada. Molecular reactions at aqueous interfaces. *Nature Reviews Chemistry*, 4(9):459–475, 2020.

[14] CJC Jordan, EA Lowe, and JRR Verlet. Photooxidation of the phenolate anion is accelerated at the water/air interface. *Journal of the American Chemical Society*, 144(31):14012–14015, 2022.

[15] TAA Oliver, Y Zhang, A Roy, MNR Ashfold, and SE Bradforth. Exploring autoionization and photoinduced proton-coupled electron transfer pathways of phenol in aqueous solution. *The Journal of Physical Chemistry Letters*, 6(20):4159–4164, 2015.

[16] R Kusaka, S Nihonyanagi, and T Tahara. The photochemical reaction of phenol becomes ultrafast at

the air–water interface. *Nature Chemistry*, 13(4):306–311, 2021.

[17] Y Zhang, TAA Oliver, MNR Ashfold, and SE Bradforth. Contrasting the excited state reaction pathways of phenol and para-methylthiophenol in the gas and liquid phases. *Faraday Discussions*, 157:141–163, 2012.

[18] D Lesnicki, V Wank, JD Cyran, EHG Backus, and M Sulpizi. Lower degree of dissociation of pyruvic acid at water surfaces than in bulk. *Physical Chemistry Chemical Physics*, 24(22):13510–13513, 2022.

[19] T Ishiyama, T Tahara, and A Morita. Why the photochemical reaction of phenol becomes ultrafast at the air–water interface: The effect of surface hydration. *Journal of the American Chemical Society*, 144(14):6321–6325, 2022.

[20] R Seidel, S Thürmer, and B Winter. Photoelectron spectroscopy meets aqueous solution: studies from a vacuum liquid microjet. *The Journal of Physical Chemistry Letters*, 2(6):633–641, 2011.

[21] R Seidel, B Winter, and SE Bradforth. Valence electronic structure of aqueous solutions: Insights from photoelectron spectroscopy. *Annual Review of Physical Chemistry*, 67:283–305, 2016.

[22] M Faubel, B Steiner, and JP Toennies. Photoelectron spectroscopy of liquid water, some alcohols, and pure nonane in free micro jets. *The Journal of Chemical Physics*, 106(22):9013–9031, 1997.

[23] Y Suzuki, K Nishizawa, N Kurahashi, and T Suzuki. Effective attenuation length of an electron in liquid water between 10 and 600 ev. *Physical Review E*, 90(1):010302, 2014.

[24] T Kühne and P Vöhringer. Transient anisotropy and fragment rotational excitation in the femtosecond photodissociation of triiodide in solution. *The Journal of Physical Chemistry A*, 102(23):4177–4185, 1998.

[25] H Sakane, T Mitsui, H Tanida, and I Watanabe. XAFS analysis of triiodide ion in solutions. *Journal of Synchrotron Radiation*, 8(2):674–676, 2001.

[26] CJ Margulis, DF Coker, and RM Lynden-Bell. A monte carlo study of symmetry breaking of I_3^- in aqueous solution using a multistate diabatic hamiltonian. *The Journal of Chemical Physics*, 114(1):367–376, 2001.

[27] T Koslowski and P Vöhringer. Is solvated I_3^- angular? *Chemical Physics Letters*, 342(1-2):141–147, 2001.

[28] NK Jena, I Josefsson, SK Eriksson, A Hagfeldt, H Siegbahn, O Björneholm, H Rensmo, and M Odelius. Solvent-dependent structure of the I_3^- ion derived from photoelectron spectroscopy and ab initio molecular dynamics simulations. *Chemistry–A European Journal*, 21(10):4049–4055, 2015.

[29] U Banin, A Waldman, and S Ruhman. Ultrafast photodissociation of I_3^- in solution: direct observation of coherent product vibrations. *The Journal of Chemical Physics*, 96(3):2416–2419, 1992.

[30] U Banin and S Ruhman. Ultrafast photodissociation of I_3^-. coherent photochemistry in solution. *The Journal of Chemical Physics*, 98(6):4391–4403, 1993.

[31] KH Kim, JH Lee, J Kim, S Nozawa, T Sato, A Tomita, K Ichiyanagi, H Ki, J Kim, S Adachi, et al. Solvent-dependent molecular structure of ionic species directly measured by ultrafast x-ray solution scattering. *Physical Review Letters*, 110(16):165505, 2013.

[32] KH Kim, H Ki, KY Oang, S Nozawa, T Sato, J Kim, TK Kim, J Kim, S Adachi, and H Ihee. Global reaction pathways in the photodissociation of I_3^- ions in solution at 267 and 400 nm studied by picosecond x-ray liquidography. *ChemPhysChem*, 14(16):3687–3697, 2013.

[33] K Hwan Kim, J Kim, J Hyuk Lee, and H Ihee. Topical review: molecular reaction and solvation visualized by time-resolved X-ray solution scattering: structure, dynamics, and their solvent dependence.

Structural Dynamics, 1(1):011301, 2014.

[34] S Schott, L Ress, J Hrušák, P Nuernberger, and T Brixner. Identification of photofragmentation patterns in trihalide anions by global analysis of vibrational wavepacket dynamics in broadband transient absorption data. *Physical Chemistry Chemical Physics*, 18(48):33287–33302, 2016.

[35] K Ledbetter, E Biasin, JPF Nunes, M Centurion, KJ Gaffney, M Kozina, M-F Lin, X Shen, J Yang, XJ Wang, et al. Photodissociation of aqueous I_3^- observed with liquid-phase ultrafast mega-electron-volt electron diffraction. *Structural Dynamics*, 7(6):064901, 2020.

[36] MT Zanni, BJ Greenblatt, AV Davis, and DM Neumark. Photodissociation of gas phase I_3^- using femtosecond photoelectron spectroscopy. *The Journal of Chemical Physics*, 111(7):2991–3003, 1999.

[37] JE Del Bene. Molecular orbital theory of the hydrogen bond.: XVI. A comparative study of pyridine and the diazines as proton acceptors in ground and excited n$\rightarrow \pi$* states. *Chemical Physics*, 15(3):463–472, 1976.

[38] I Yamazaki, T Murao, T Yamanaka, and K Yoshihara. Intramolecular electronic relaxation and photoisomerization processes in the isolated azabenzene molecules pyridine, pyrazine and pyrimidine. *Faraday Discussions of the Chemical Society*, 75:395–405, 1983.

[39] T Horio, R Spesyvtsev, K Nagashima, RA Ingle, Y Suzuki, and T Suzuki. Full observation of ultrafast cascaded radiationless transitions from S_2 ($\pi\pi^*$) state of pyrazine using vacuum ultraviolet photoelectron imaging. *The Journal of Chemical Physics*, 145(4):044306, 2016.

[40] V Scutelnic, S Tsuru, MI Pápai, Z Yang, M Epshtein, T Xue, E Haugen, Y Kobayashi, A Krylov, KB Møller, et al. X-ray transient absorption reveals the ^1A_u (nπ*) state of pyrazine in electronic relaxation. *Nature Communications*, 12(5003), 2021.

[41] A Moguilevski, M Wilke, G Grell, SI Bokarev, SG Aziz, N Engel, AA Raheem, O Kühn, IY Kiyan, and EF Aziz. Ultrafast spin crossover in $[Fe(II)(bpy)_3]^{2+}$: revealing two competing mechanisms by extreme ultraviolet photoemission spectroscopy. *ChemPhysChem*, 18(5):465–469, 2017.

[42] N Engel, SI Bokarev, A Moguilevski, AA Raheem, R Al-Obaidi, T Möhle, G Grell, KR Siefermann, B Abel, SG Aziz, et al. Light-induced relaxation dynamics of the ferricyanide ion revisited by ultrafast XUV photoelectron spectroscopy. *Physical Chemistry Chemical Physics*, 19(22):14248–14255, 2017.

[43] J Ojeda, CA Arrell, L Longetti, M Chergui, and J Helbing. Charge-transfer and impulsive electronic-to-vibrational energy conversion in ferricyanide: Ultrafast photoelectron and transient infrared studies. *Physical Chemistry Chemical Physics*, 19(26):17052–17062, 2017.

[44] T Yonezawa, H Kato, H Saito, and K Fukui. MO interpretation of some physico-chemical properties of alkyl compound. *Bulletin of the Chemical Society of Japan*, 35(11):1814–1818, 1962.

[45] AI Krylov. From orbitals to observables and back. *The Journal of Chemical Physics*, 153(8):080901, 2020.

[46] P Fulde. *Electron correlations in molecules and solids*, volume 100. Springer Science & Business Media, 1995.

[47] RL Martin. Many-electron effects in photoelectron spectroscopy. Deviations from Koopman's one-electron model, satellite structure, configuration interaction, mechanisms. Technical report, California Univ., Berkeley (USA). Lawrence Berkeley Lab., 1976.

[48] GA Gallup. The lewis electron-pair model, spectroscopy, and the role of the orbital picture in describing the electronic structure of molecules. *Journal of Chemical Education*, 65(8):671, 1988.

[49] M Hackmeyer and JL Whitten. Configuration interaction studies of ground and excited states of poly-

atomic molecules II. The electronic states and spectrum of pyrazine. *The Journal of Chemical Physics*, 54(9):3739–3750, 1971.

[50] T Horio, T Fuji, Y Suzuki, and T Suzuki. Probing ultrafast internal conversion through conical intersection via time-energy map of photoelectron angular anisotropy. *Journal of the American Chemical Society*, 131(30):10392–10393, 2009.

[51] DJ Tannor. *Introduction to quantum mechanics: a time-dependent perspective*. University Science Books, 2007.

[52] A Jablonski. Efficiency of anti-Stokes fluorescence in dyes. *Nature*, 131(3319):839–840, 1933.

[53] A Stolow. Time-resolved photoelectron spectroscopy: non-adiabatic dynamics in polyatomic molecules. *International Reviews in Physical Chemistry*, 22(2):377–405, 2003.

[54] CM Marian. Spin–orbit coupling and intersystem crossing in molecules. *Wiley Interdisciplinary Reviews: Computational Molecular Science*, 2(2):187–203, 2012.

[55] W Domcke and G Stock. Theory of ultrafast nonadiabatic excited-state processes and their spectroscopic detection in real time. *Advances in Chemical Physics*, 100:1–169, 1997.

[56] J Kommandeur, WA Majewski, WL Meerts, and DW Pratt. Pyrazine: An "exact" solution to the problem of radiationless transitions. *Annual Review of Physical Chemistry*, 38(1):433–462, 1987.

[57] J Jortner and MA Ratner. *Molecular electronics*. Blackwell Science Oxford, 1997.

[58] RW Schoenlein, LA Peteanu, RA Mathies, and CV Shank. The first step in vision: femtosecond isomerization of rhodopsin. *Science*, 254(5030):412–415, 1991.

[59] N Huse, TK Kim, L Jamula, JK McCusker, FMF De Groot, and RW Schoenlein. Photo-induced spin-state conversion in solvated transition metal complexes probed via time-resolved soft X-ray spectroscopy. *Journal of the American Chemical Society*, 132(19):6809–6816, 2010.

[60] S Hüfner. *Photoelectron spectroscopy: principles and applications*. Springer Science & Business Media, 2013.

[61] K Siegbahn. Electron spectroscopy for atoms, molecules, and condensed matter. *Reviews of Modern Physics*, 54(3):709, 1982.

[62] DW Turner. Molecular photoelectron spectroscopy. *Philosophical Transactions for the Royal Society of London. Series A, Mathematical and Physical Sciences*, 268(1184):7–31, 1970.

[63] DW Turner and MA Jobory. Determination of ionization potentials by photoelectron energy measurement. *The Journal of Chemical Physics*, 37(12):3007–3008, 1962.

[64] H Hertz. Ueber einen einfluss des ultravioletten lichtes auf die electrische entladung. *Annalen der Physik*, 267(8):983–1000, 1887.

[65] A Einstein. On a heuristic viewpoint concerning the production and transformation of light. *Annalen der Physik*, 17:132–148, 1905.

[66] S Thürmer, S Malerz, F Trinter, U Hergenhahn, C Lee, DM Neumark, G Meijer, B Winter, and I Wilkinson. Accurate vertical ionization energy and work function determinations of liquid water and aqueous solutions. *Chemical Science*, 12(31):10558–10582, 2021.

[67] G Olivieri, A Goel, A Kleibert, D Cvetko, and MA Brown. Quantitative ionization energies and work functions of aqueous solutions. *Physical Chemistry Chemical Physics*, 18(42):29506–29515, 2016.

[68] LP Ramírez, A Boucly, F Saudrais, F Bournel, J Gallet, E Maisonhaute, AR Milosavljević, C Nicolas, and F Rochet. The fermi level as an energy reference in liquid jet X-ray photoelectron spectroscopy

studies of aqueous solutions. *Physical Chemistry Chemical Physics*, 23(30):16224–16233, 2021.

[69] M Pugini, B Credidio, I Walter, S Malerz, F Trinter, D Stemer, U Hergenhahn, G Meijer, I Wilkinson, and B Winter. How to measure work functions from aqueous solutions. *Chemical Science*, 14(35):9574–9588, 2023.

[70] T Suzuki. Ultrafast photoelectron spectroscopy of aqueous solutions. *The Journal of Chemical Physics*, 151(9):090901, 2019.

[71] WE Spicer. The use of photoemission to determine the electronic structure of solids. *Le Journal de Physique Colloques*, 34(C6):C6–19, 1973.

[72] B Baron, P Chartier, P Delahay, and R Lugo. Photoelectron emission by solutions. *The Journal of Chemical Physics*, 51(6):2562–2572, 1969.

[73] P Delahay. Photoelectron emission spectroscopy of aqueous solutions. *Accounts of Chemical Research*, 15(2):40–45, 1982.

[74] JV Ortiz. Dyson-orbital concepts for description of electrons in molecules. *The Journal of Chemical Physics*, 153(7):070902, 2020.

[75] T Koopmans. Über die zuordnung von wellenfunktionen und eigenwerten zu den einzelnen elektronen eines atoms. *physica*, 1(1-6):104–113, 1934.

[76] H Siegbahn. Electron spectroscopy for chemical analysis of liquids and solutions. *The Journal of Physical Chemistry*, 89(6):897–909, 1985.

[77] I Watanabe, JB Flanagan, and P Delahay. Vacuum ultraviolet photoelectron emission spectroscopy of water and aqueous solutions. *The Journal of Chemical Physics*, 73(5):2057–2062, 1980.

[78] H Siegbahn and K Siegbahn. ESCA applied to liquids. *Journal of Electron Spectroscopy and Related Phenomena*, 2(3):319–325, 1973.

[79] M Faubel, S Schlemmer, and JP Toennies. A molecular beam study of the evaporation of water from a liquid jet. *Zeitschrift für Physik D Atoms, Molecules and Clusters*, 10(2):269–277, 1988.

[80] KR Wilson, BS Rude, J Smith, C Cappa, DT Co, RD Schaller, M Larsson, T Catalano, and RJ Saykally. Investigation of volatile liquid surfaces by synchrotron X-ray spectroscopy of liquid microjets. *Review of Scientific Instruments*, 75(3):725–736, 2004.

[81] J Kohno, F Mafuné, and T Kondow. Mechanisms of ion ejection from liquid beam under irradiation of laser by simultaneous detection of ions produced inside a liquid beam and ejected into a vacuum. *The Journal of Physical Chemistry A*, 104(2):243–248, 2000.

[82] B Winter, R Weber, W Widdra, M Dittmar, M Faubel, and IV Hertel. Full valence band photoemission from liquid water using EUV synchrotron radiation. *The Journal of Physical Chemistry A*, 108(14):2625–2632, 2004.

[83] B Winter and M Faubel. Photoemission from liquid aqueous solutions. *Chemical Reviews*, 106(4):1176–1211, 2006.

[84] S Malerz, F Trinter, U Hergenhahn, A Ghrist, H Ali, C Nicolas, C Saak, C Richter, S Hartweg, L Nahon, et al. Low-energy constraints on photoelectron spectra measured from liquid water and aqueous solutions. *Physical Chemistry Chemical Physics*, 23(14):8246–8260, 2021.

[85] S Thürmer, M Ončák, N Ottosson, R Seidel, U Hergenhahn, SE Bradforth, P Slavíček, and B Winter. On the nature and origin of dicationic, charge-separated species formed in liquid water on X-ray irradiation. *Nature Chemistry*, 5(7):590–596, 2013.

[86] N Ottosson, G Öhrwall, and O Björneholm. Ultrafast charge delocalization dynamics in aqueous elec-

trolytes: new insights from Auger electron spectroscopy. *Chemical Physics Letters*, 543:1–11, 2012.

[87] MA Brown, M Faubel, and B Winter. X-ray photo-and resonant Auger-electron spectroscopy studies of liquid water and aqueous solutions. *Annual Reports Section" C"(Physical Chemistry)*, 105:174–212, 2009.

[88] P Bolognesi, P O'Keeffe, Y Ovcharenko, L Avaldi, and V Carravetta. Resonant Auger spectroscopy at the carbon and nitrogen K-edges of pyrimidine. *The Journal of Chemical Physics*, 136(15):154308, 2012.

[89] D Menzel. Ultrafast charge transfer at surfaces accessed by core electron spectroscopies. *Chemical Society Reviews*, 37(10):2212–2223, 2008.

[90] D Hollas, MN Pohl, R Seidel, EF Aziz, P Slavíček, and B Winter. Aqueous solution chemistry of ammonium cation in the Auger time window. *Scientific Reports*, 7(1):1–10, 2017.

[91] W Bambynek, B Crasemann, RW Fink, H-U Freund, H Mark, CD Swift, RE Price, and PV Rao. X-ray fluorescence yields, Auger, and Coster-Kronig transition probabilities. *Reviews of Modern Physics*, 44(4):716, 1972.

[92] S Tsuru, B Sharma, M Nagasaka, and C Hättig. Solvent effects in the ultraviolet and X-ray absorption spectra of pyridazine in aqueous solution. *The Journal of Physical Chemistry A*, 125(33):7198–7206, 2021.

[93] KD Mudryk, R Seidel, B Winter, and I Wilkinson. The electronic structure of the aqueous permanganate ion: aqueous-phase energetics and molecular bonding studied using liquid jet photoelectron spectroscopy. *Physical Chemistry Chemical Physics*, 22(36):20311–20330, 2020.

[94] EF Aziz, N Ottosson, M Faubel, IV Hertel, and B Winter. Interaction between liquid water and hydroxide revealed by core-hole de-excitation. *Nature*, 455(7209):89–91, 2008.

[95] I Unger, R Seidel, S Thürmer, MN Pohl, EF Aziz, LS Cederbaum, E Muchová, P Slavíček, B Winter, and NV Kryzhevoi. Observation of electron-transfer-mediated decay in aqueous solution. *Nature Chemistry*, 9(7):708–714, 2017.

[96] KL Reid. Photoelectron angular distributions. *Annual Review of Physical Chemistry*, 54(1):397–424, 2003.

[97] A Moguilevski. *Ultrafast Electron Dynamics in Transition Metal Complexes Studied in Solution by Means of Time-Resolved XUV Photoemission Spectroscopy*. PhD thesis, Freie University Berlin, 2018.

[98] T Suzuki. Time-resolved photoelectron spectroscopy of non-adiabatic electronic dynamics in gas and liquid phases. *International Reviews in Physical Chemistry*, 31(2):265–318, 2012.

[99] T Suzuki. Femtosecond time-resolved photoelectron imaging. *Annual Review of Physical Chemistry*, 57:555–592, 2006.

[100] S Gozem, R Seidel, U Hergenhahn, E Lugovoy, B Abel, B Winter, AI Krylov, and SE Bradforth. Probing the electronic structure of bulk water at the molecular length scale with angle-resolved photoelectron spectroscopy. *The Journal of Physical Chemistry Letters*, 11(13):5162–5170, 2020.

[101] AH Zewail. Femtochemistry: atomic-scale dynamics of the chemical bond using ultrafast lasers (nobel lecture). *Angewandte Chemie International Edition*, 39(15):2586–2631, 2000.

[102] F Krausz and M Ivanov. Attosecond physics. *Reviews of Modern Physics*, 81(1):163, 2009.

[103] A Krylov, TL Windus, T Barnes, E Marin-Rimoldi, JA Nash, B Pritchard, DGA Smith, D Altarawy, P Saxe, C Clementi, et al. Perspective: computational chemistry software and its advancement as illustrated through three grand challenge cases for molecular science. *The Journal of Chemical Physics*,

149(18):180901, 2018.

[104] M Ben-Nun and TJ Martínez. Ab initio quantum molecular dynamics. *Advances in Chemical Physics*, 121:439–512, 2002.

[105] A Stolow. Femtosecond time-resolved photoelectron spectroscopy of polyatomic molecules. *Annual Review of Physical Chemistry*, 54(1):89–119, 2003.

[106] A Stolow, AE Bragg, and DM Neumark. Femtosecond time-resolved photoelectron spectroscopy. *Chemical Reviews*, 104(4):1719–1758, 2004.

[107] G Wu, P Hockett, and A Stolow. Time-resolved photoelectron spectroscopy: from wavepackets to observables. *Physical Chemistry Chemical Physics*, 13(41):18447–18467, 2011.

[108] S. N. Dixit and V McKoy. Theory of resonantly enhanced multiphoton processes in molecules. *The Journal of Chemical Physics*, 82(8):3546–3553, 1985.

[109] KR Siefermann, Y Liu, E Lugovoy, O Link, M Faubel, U Buck, B Winter, and B Abel. Binding energies, lifetimes and implications of bulk and interface solvated electrons in water. *Nature Chemistry*, 2(4):274–279, 2010.

[110] Y Tang, H Shen, K Sekiguchi, N Kurahashi, T Mizuno, Y Suzuki, and T Suzuki. Direct measurement of vertical binding energy of a hydrated electron. *Physical Chemistry Chemical Physics*, 12(15):3653–3655, 2010.

[111] A Lübcke, F Buchner, N Heine, IV Hertel, and T Schultz. Time-resolved photoelectron spectroscopy of solvated electrons in aqueous NaI solution. *Physical Chemistry Chemical Physics*, 12(43):14629–14634, 2010.

[112] XF Gao, DJ Hood, X Zhao, and GM Nathanson. Creation and reaction of solvated electrons at and near the surface of water. *Journal of the American Chemical Society*, 145(20):10987–10990, 2023.

[113] Y Yamamoto and T Suzuki. Ultrafast dynamics of water radiolysis: Hydrated electron formation, solvation, recombination, and scavenging. *The Journal of Physical Chemistry Letters*, 11(14):5510–5516, 2020.

[114] F Buchner, HH Ritze, M Beutler, T Schultz, IV Hertel, and A Lübcke. Role of alkali cations for the excited state dynamics of liquid water near the surface. *The Journal of Chemical Physics*, 137(2):024503, 2012.

[115] S Karashima, Y Yamamoto, and T Suzuki. Ultrafast internal conversion and solvation of electrons in water, methanol, and ethanol. *The Journal of Physical Chemistry Letters*, 10(16):4499–4504, 2019.

[116] D Luckhaus, Y Yamamoto, T Suzuki, and R Signorell. Genuine binding energy of the hydrated electron. *Science Advances*, 3(4):e1603224, 2017.

[117] Y Yamamoto, S Karashima, S Adachi, and T Suzuki. Wavelength dependence of UV photoemission from solvated electrons in bulk water, methanol, and ethanol. *The Journal of Physical Chemistry A*, 120(8):1153–1159, 2016.

[118] MH Elkins, HL Williams, AT Shreve, and DM Neumark. Relaxation mechanism of the hydrated electron. *Science*, 342(6165):1496–1499, 2013.

[119] JW Riley, B Wang, JL Woodhouse, M Assmann, GA Worth, and HH Fielding. Unravelling the role of an aqueous environment on the electronic structure and ionization of phenol using photoelectron spectroscopy. *The Journal of Physical Chemistry Letters*, 9(4):678–682, 2018.

[120] G Kumar, A Roy, RS McMullen, S Kutagulla, and SE Bradforth. The influence of aqueous solvent on the electronic structure and non-adiabatic dynamics of indole explored by liquid-jet photoelectron spectroscopy. *Faraday Discussions*, 212:359–381, 2018.

[121] H Okuyama, Y Suzuki, S Karashima, and T Suzuki. Charge-transfer-to-solvent reactions from i- to water, methanol, and ethanol studied by time-resolved photoelectron spectroscopy of liquids. *The Journal of Chemical Physics*, 145(7):074502, 2016.

[122] S Karashima, Y Yamamoto, and T Suzuki. Resolving nonadiabatic dynamics of hydrated electrons using ultrafast photoemission anisotropy. *Physical Review Letters*, 116(13):137601, 2016.

[123] J Nishitani, Y Yamamoto, CW West, S Karashima, and T Suzuki. Binding energy of solvated electrons and retrieval of true UV photoelectron spectra of liquids. *Science Advances*, 5(8):eaaw6896, 2019.

[124] BA Erickson, ZN Heim, E Pieri, E Liu, TJ Martinez, and DM Neumark. Relaxation dynamics of hydrated thymine, thymidine, and thymidine monophosphate probed by liquid jet time-resolved photoelectron spectroscopy. *The Journal of Physical Chemistry A*, 123(50):10676–10684, 2019.

[125] E Titov, J Hummert, E Ikonnikov, R Mitrić, and O Kornilov. Electronic relaxation of aqueous aminoazobenzenes studied by time-resolved photoelectron spectroscopy and surface hopping tddft dynamics calculations. *Faraday Discussions*, 228:226–241, 2021.

[126] CW West, J Nishitani, C Higashimura, and T Suzuki. Extreme ultraviolet time-resolved photoelectron spectroscopy of aqueous aniline solution: enhanced surface concentration and pump-induced space charge effect. *Molecular Physics*, 119(1-2):e1748240, 2021.

[127] ZN Heim and DM Neumark. Nonadiabatic dynamics studied by liquid-jet time-resolved photoelectron spectroscopy. *Accounts of Chemical Research*, 55(24):3652–3662, 2022.

[128] J Hummert, G Reitsma, N Mayer, E Ikonnikov, M Eckstein, and O Kornilov. Femtosecond extreme ultraviolet photoelectron spectroscopy of organic molecules in aqueous solution. *The Journal of Physical Chemistry Letters*, 9(22):6649–6655, 2018.

[129] Y Yamamoto, Y Suzuki, G Tomasello, T Horio, S Karashima, R Mitríc, and T Suzuki. Time-and angle-resolved photoemission spectroscopy of hydrated electrons near a liquid water surface. *Physical Review Letters*, 112(18):187603, 2014.

[130] AA Raheem, M Wilke, M Borgwardt, N Engel, SI Bokarev, G Grell, SG Aziz, O Kühn, IY Kiyan, C Merschjann, et al. Ultrafast kinetics of linkage isomerism in $Na_2[Fe(CN)_5NO]$ aqueous solution revealed by time-resolved photoelectron spectroscopy. *Structural Dynamics*, 4(4):044031, 2017.

[131] I Jordan, M Huppert, MA Brown, JA van Bokhoven, and HJ Wörner. Photoelectron spectrometer for attosecond spectroscopy of liquids and gases. *Review of Scientific Instruments*, 86(12):123905, 2015.

[132] I Jordan, M Huppert, D Rattenbacher, M Peper, D Jelovina, C Perry, A von Conta, A Schild, and HJ Wörner. Attosecond spectroscopy of liquid water. *Science*, 369(6506):974–979, 2020.

[133] EL Falcao-Filho, V Gkortsas, A Gordon, and FX Kärtner. Analytic scaling analysis of high harmonic generation conversion efficiency. *Optics Express*, 17(13):11217–11229, 2009.

[134] J Metje, M Borgwardt, A Moguilevski, A Kothe, N Engel, M Wilke, R Al-Obaidi, D Tolksdorf, A Firsov, M Brzhezinskaya, et al. Monochromatization of femtosecond XUV light pulses with the use of reflection zone plates. *Optics Express*, 22(9):10747–10760, 2014.

[135] R Al-Obaidi, M Wilke, M Borgwardt, J Metje, A Moguilevski, N Engel, D Tolksdorf, A Raheem, T Kampen, S Mähl, et al. Ultrafast photoelectron spectroscopy of solutions: space-charge effect. *New Journal of Physics*, 17(9):093016, 2015.

[136] B Winter, EF Aziz, U Hergenhahn, M Faubel, and IV Hertel. Hydrogen bonds in liquid water studied by photoelectron spectroscopy. *The Journal of Chemical Physics*, 126(12):124504, 2007.

[137] Y Maréchal. *The hydrogen bond and the water molecule: the physics and chemistry of water, aqueous*

and bio-media. Elsevier, 2006.

[138] IW Kuo and CJ Mundy. An ab initio molecular dynamics study of the aqueous liquid-vapor interface. *Science*, 303(5658):658–660, 2004.

[139] J Niskanen, M Fondell, CJ Sahle, S Eckert, RM Jay, K Gilmore, A Pietzsch, M Dantz, X Lu, DE McNally, et al. Compatibility of quantitative X-ray spectroscopy with continuous distribution models of water at ambient conditions. *Proceedings of the National Academy of Sciences*, 116(10):4058–4063, 2019.

[140] T Fransson, Y Harada, N Kosugi, NA Besley, B Winter, JJ Rehr, LGM Pettersson, and A Nilsson. X-ray and electron spectroscopy of water. *Chemical Reviews*, 116(13):7551–7569, 2016.

[141] K Nishizawa, N Kurahashi, K Sekiguchi, T Mizuno, Y Ogi, T Horio, M Oura, N Kosugi, and T Suzuki. High-resolution soft X-ray photoelectron spectroscopy of liquid water. *Physical Chemistry Chemical Physics*, 13(2):413–417, 2011.

[142] MN Pohl, E Muchová, R Seidel, H Ali, Š Sršeň, I Wilkinson, B Winter, and P Slavíček. Do water's electrons care about electrolytes? *Chemical Science*, 10(3):848–865, 2019.

[143] J Nishitani, CW West, and T Suzuki. Angle-resolved photoemission spectroscopy of liquid water at 29.5 eV. *Structural Dynamics*, 4(4):044014, 2017.

[144] I Josefsson, SK Eriksson, N Ottosson, G Öhrwall, H Siegbahn, A Hagfeldt, H Rensmo, O Björneholm, and M Odelius. Collective hydrogen-bond dynamics dictates the electronic structure of aqueous I_3^-. *Physical Chemistry Chemical Physics*, 15(46):20189–20196, 2013.

[145] B O'regan and M Grätzel. A low-cost, high-efficiency solar cell based on dye-sensitized colloidal Tio_2 films. *Nature*, 353(6346):737–740, 1991.

[146] M Grätzel. Photoelectrochemical cells. *Nature*, 414(6861):338–345, 2001.

[147] M Grätzel. Conversion of sunlight to electric power by nanocrystalline dye-sensitized solar cells. *Journal of Photochemistry and Photobiology A: Chemistry*, 164(1-3):3–14, 2004.

[148] G Boschloo and A Hagfeldt. Characteristics of the iodide/triiodide redox mediator in dye-sensitized solar cells. *Accounts of Chemical Research*, 42(11):1819–1826, 2009.

[149] C Law, O Moudam, S Villarroya-Lidon, and B O'Regan. Managing wetting behavior and collection efficiency in photoelectrochemical devices based on water electrolytes; improvement in efficiency of water/iodide dye sensitised cells to 4%. *Journal of Materials Chemistry*, 22(44):23387–23394, 2012.

[150] F Bella, S Galliano, M Falco, G Viscardi, C Barolo, M Grätzel, and C Gerbaldi. Unveiling iodine-based electrolytes chemistry in aqueous dye-sensitized solar cells. *Chemical Science*, 7(8):4880–4890, 2016.

[151] H Choi, RT Bise, AA Hoops, and DM Neumark. Photodissociation dynamics of the triiodide anion (I_3^-). *The Journal of Chemical Physics*, 113(6):2255–2262, 2000.

[152] AA Hoops, JR Gascooke, AE Faulhaber, KE Kautzman, and DM Neumark. Two$-$ and three$-$body photodissociation of gas phase I_3^-. *The Journal of Chemical Physics*, 120(17):7901–7909, 2004.

[153] L Zhu, K Takahashi, M Saeki, T Tsukuda, and T Nagata. Photodissociation of gas-phase I_3^-: product branching in the visible and UV regions. *Chemical Physics Letters*, 350(3):233–239, 2001.

[154] R Nakanishi, N Saitou, T Ohno, S Kowashi, S Yabushita, and T Nagata. Photodissociation of gas$-$phase I_3^-: Comprehensive understanding of nonadiabatic dissociation dynamics. *The Journal of Chemical Physics*, 126(20):204311, 2007.

[155] U Banin and S Ruhman. Ultrafast photodissociation of I_3. Coherent photochemistry in solution. *The Journal of Chemical Physics*, 98(6):4391–4403, 1993.

[156] AE Johnson and AB Myers. Solvent effects in the raman spectra of the triiodide ion: observation of dynamic symmetry breaking and solvent degrees of freedom. *The Journal of Physical Chemistry*, 100(19):7778–7788, 1996.

[157] SK Eriksson, I Josefsson, N Ottosson, G Öhrwall, O Björneholm, H Siegbahn, A Hagfeldt, M Odelius, and H Rensmo. Solvent dependence of the electronic structure of I^- and I_3^-. *Journal of Physical Chemistry B*, 118:3164–3174, 2014.

[158] FS Zhang and RM Lynden-Bell. Solvent-induced symmetry breaking. *Physical Review Letters*, 90(18):185505, 2003.

[159] CJ Margulis, DF Coker, and RM Lynden-Bell. Symmetry breaking of the triiodide ion in acetonitrile solution. *Chemical Physics Letters*, 341(5-6):557–560, 2001.

[160] J Norell, G Grell, O Kühn, M Odelius, and SI Bokarev. Photoelectron shake-ups as a probe of molecular symmetry: 4d XPS analysis of I_3^- in solution. *Physical Chemistry Chemical Physics*, 20(30):19916–19921, 2018.

[161] H Sato, F Hirata, and AB Myers. Theoretical study of the solvent effect on triiodide ion in solutions. *The Journal of Physical Chemistry A*, 102(11):2065–2071, 1998.

[162] ASP Gomes, L Visscher, H Bolvin, T Saue, S Knecht, T Fleig, and E Eliav. The electronic structure of the triiodide ion from relativistic correlated calculations: a comparison of different methodologies. *The Journal of Chemical Physics*, 133(6):064305, 2010.

[163] Philipp MS. Photoelektronenspektroskopie wässriger triiodid-lösungen. *Diplomarbeit im Fachbereich Chemie der Freien Universität Berlin*, 2005.

[164] W Gabes and DJ Stufkens. Electronic absorption spectra of symmetrical and asymmetrical trihalide ions. *Spectrochimica Acta Part A: Molecular Spectroscopy*, 30(9):1835–1841, 1974.

[165] MJ Blandamer and MF Fox. Theory and applications of charge-transfer-to-solvent spectra. *Chemical Reviews*, 70(1):59–93, 1970.

[166] SE Bradforth and P Jungwirth. Excited states of iodide anions in water: a comparison of the electronic structure in clusters and in bulk solution. *The Journal of Physical Chemistry A*, 106(7):1286–1298, 2002.

[167] MS Ahsan, V Kochetov, D Hein, SI Bokarev, and I Wilkinson. Probing the molecular structure of aqueous triiodide via x-ray photoelectron spectroscopy and correlated electron phenomena. *Physical Chemistry Chemical Physics*, 24(25):15540–15555, 2022.

[168] T Kachel. The plane grating monochromator beamline U49-2 PGM-1 at BESSY II. *Journal of Large-Scale Research Facilities JLSRF*, 2:72, 2016.

[169] J Viefhaus, F Scholz, S Deinert, L Glaser, M Ilchen, J Seltmann, P Walter, and F Siewert. The variable polarization XUV beamline P04 at PETRA III: optics, mechanics and their performance. *Nuclear Instruments and Methods in Physics Research Section A: Accelerators, Spectrometers, Detectors and Associated Equipment*, 710:151–154, 2013.

[170] H Hartley and NP Campbell. LXIX.—the solubility of iodine in water. *Journal of the Chemical Society, Transactions*, 93:741–745, 1908.

[171] BK Shrikanth and MS Hegde. Formation and structure of iodine: water (H_2O-I_2) charge-transfer complex. *Journal of Chemical Sciences*, 133(2):1–9, 2021.

[172] KK Innes, IG Ross, and William R Moomaw. Electronic states of azabenzenes and azanaphthalenes: A revised and extended critical review. *Journal of Molecular Spectroscopy*, 132(2):492–544, 1988.

[173] A Bolovinos, P Tsekeris, J Philis, E Pantos, and G Andritsopoulos. Absolute vacuum ultraviolet absorption spectra of some gaseous azabenzenes. *Journal of Molecular Spectroscopy*, 103(2):240–256, 1984.

[174] M Stener, P Decleva, DMP Holland, and DA Shaw. A study of the valence shell electronic states of pyrimidine and pyrazine by photoabsorption spectroscopy and time-dependent density functional theory calculations. *Journal of Physics B: Atomic, Molecular and Optical Physics*, 44(7):075203, 2011.

[175] G Vall-llosera, B Gao, A Kivimäki, M Coreno, J Álvarez Ruiz, M de Simone, H Ågren, and E Rachlew. The C 1s and N 1s near edge X-ray absorption fine structure spectra of five azabenzenes in the gas phase. *The Journal of Chemical Physics*, 128(4):044316, 2008.

[176] DMP Holland, AW Potts, L Karlsson, M Stener, and P Decleva. A study of the valence shell photoionisation dynamics of pyrimidine and pyrazine. *Chemical Physics*, 390(1):25–35, 2011.

[177] DMP Holland, DA Shaw, S Coriani, M Stener, and P Decleva. A study of the valence shell electronic states of pyridazine by photoabsorption spectroscopy and time-dependent density functional theory calculations. *Journal of Physics B: Atomic, Molecular and Optical Physics*, 46(17):175103, 2013.

[178] I Linert and M Zubek. A study of the electronic states of pyrimidine by electron energy loss spectroscopy. *Chemical Physics Letters*, 624:1–5, 2015.

[179] R Gleiter, E Heilbronner, and V Hornung. Lone pair interaction in pyridazine, pyrimidine, and pyrazine. *Angewandte Chemie International Edition in English*, 9(11):901–902, 1970.

[180] MJS Dewar and SD Worley. Photoelectron spectra of molecules. II. the ionization potentials of azabenzenes and azanaphthalenes. *The Journal of Chemical Physics*, 51(1):263–267, 1969.

[181] R Gleiter, E Heilbronner, and V Hornung. Photoelectron spectra of azabenzenes and azanaphthalenes: I. pyridine, diazines, s-triazine and s-tetrazine. *Helvetica Chimica Acta*, 55(1):255–274, 1972.

[182] R Dudde, MLM Rocco, EE Koch, S Bernstorff, and W Eberhardt. Core-electron excitations and the electronic decay of core-to-bound-state transitions in condensed azabenzenes. *The Journal of Chemical Physics*, 91(1):20–28, 1989.

[183] B Samir, C Kalalian, E Roth, R Salghi, and A Chakir. Gas-phase UV absorption spectra of pyrazine, pyrimidine and pyridazine. *Chemical Physics Letters*, 751:137469, 2020.

[184] JE Del Bene. Molecular orbital theory of the hydrogen bond. XIII. pyridine and pyrazine as proton acceptors. *Journal of the American Chemical Society*, 97(19):5330–5335, 1975.

[185] JR Reimers and Z Cai. Hydrogen bonding and reactivity of water to azines in their S_1 (n, π*) electronic excited states in the gas phase and in solution. *Physical Chemistry Chemical Physics*, 14(25):8791–8802, 2012.

[186] Z Cai and JR Reimers. The lowest singlet (n, π*) and (π, π*) excited states of the hydrogen-bonded complex between water and pyrazine. *The Journal of Physical Chemistry A*, 111(5):954–962, 2007.

[187] Z Cai and JR Reimers. First singlet (n, π*) excited state of hydrogen-bonded complexes between water and pyrimidine. *The Journal of Physical Chemistry A*, 109(8):1576–1586, 2005.

[188] B Mennucci. Hydrogen bond versus polar effects: an ab initio analysis on n$\rightarrow \pi$* absorption spectra and N nuclear shieldings of diazines in solution. *Journal of the American Chemical Society*, 124(7):1506–1515, 2002.

[189] F Peral and E Gallego. A study by ultraviolet spectroscopy on the self-association of diazines in aqueous solution. *Spectrochimica Acta Part A: Molecular and Biomolecular Spectroscopy*, 59(6):1223–1237, 2003.

[190] H Baba, L Goodman, and PC Valenti. Solvent effects on the fluorescence spectra of diazines. Dipole moments in the (n, π*) excited states. *Journal of the American Chemical Society*, 88(23):5410–5415, 1966.

[191] AM Wright, AA Howard, JC Howard, GS Tschumper, and NI Hammer. Charge transfer and blue shifting of vibrational frequencies in a hydrogen bond acceptor. *The Journal of Physical Chemistry A*, 117(26):5435–5446, 2013.

[192] AA Howard, GS Tschumper, and NI Hammer. Effects of hydrogen bonding on vibrational normal modes of pyrimidine. *The Journal of Physical Chemistry A*, 114(25):6803–6810, 2010.

[193] D Singh, J Popp, and RK Singh. Fourier transform raman and dft study of blue shift C–H stretching vibration of diazines on hydrogen bond formation. *Zeitschrift für Physikalische Chemie*, 225(6-7):785–798, 2011.

[194] S Eckert, V Vaz da Cruz, M Ochmann, I von Ahnen, A Föhlisch, and N Huse. Breaking the symmetry of pyrimidine: solvent effects and core-excited state dynamics. *The Journal of Physical Chemistry Letters*, 12(35):8637–8643, 2021.

[195] N Kishimoto and K Ohno. Collision energy resolved penning ionization electron spectroscopy of azines: Anisotropic interaction of azines with He*(2^3s) atoms and assignments of ionic states. *The Journal of Physical Chemistry A*, 104(30):6940–6950, 2000.

[196] A Rohatgi. Webplotdigitizer: Version 4.6, 2022.

[197] B Winter, S Thürmer, and I Wilkinson. Absolute electronic energetics and quantitative work functions of liquids from photoelectron spectroscopy. *Accounts of Chemical Research*, 56(2):77–85, 2023.

[198] Y Suzuki, T Fuji, T Horio, and T Suzuki. Time-resolved photoelectron imaging of ultrafast $S_2 \rightarrow S_1$ internal conversion through conical intersection in pyrazine. *The Journal of Chemical Physics*, 132(17):174302, 2010.

[199] G Tomasello, A Humeniuk, and R Mitric. Exploring ultrafast dynamics of pyrazine by time-resolved photoelectron imaging. *The Journal of Physical Chemistry A*, 118(37):8437–8445, 2014.

[200] W Domcke, DR Yarkony, and H Köppel. *Conical intersections: theory, computation and experiment*, volume 17. World Scientific, 2011.

[201] C Woywod, W Domcke, AL Sobolewski, and H Werner. Characterization of the $S_2 - S_1$ conical intersection in pyrazine using ab initio multiconfiguration self-consistent-field and multireference configuration-interaction methods. *The Journal of Chemical Physics*, 100(2):1400–1413, 1994.

[202] Thorsten Gerdts and Uwe Manthe. A microscopic description of dissipation in systems with strong vibronic coupling: the S_1 and S_2 absorption spectra of pyrazine. *Chemical Physics Letters*, 295(3):167–174, 1998.

[203] A Raab, Graham A Worth, H-D Meyer, and LS Cederbaum. Molecular dynamics of pyrazine after excitation to the S_2 electronic state using a realistic 24-mode model hamiltonian. *The Journal of Chemical Physics*, 110(2):936–946, 1999.

[204] M Thoss, WH Miller, and G Stock. Semiclassical description of nonadiabatic quantum dynamics: application to the S_1–S_2 conical intersection in pyrazine. *The Journal of Chemical Physics*, 112(23):10282–10292, 2000.

[205] U Werner, R Mitrić, T Suzuki, and V Bonačić-Koutecký. Nonadiabatic dynamics within the time dependent density functional theory: Ultrafast photodynamics in pyrazine. *Chemical Physics*, 349(1-3):319–324, 2008.

[206] M Sala, S Guérin, and F Gatti. Quantum dynamics of the photostability of pyrazine. *Physical Chemistry Chemical Physics*, 17(44):29518–29530, 2015.

[207] M Sala, B Lasorne, F Gatti, and S Guérin. The role of the low-lying dark nπ* states in the photophysics of pyrazine: a quantum dynamics study. *Physical Chemistry Chemical Physics*, 16(30):15957–15967, 2014.

[208] M Kanno, Y Ito, N Shimakura, S Koseki, H Kono, and Y Fujimura. Ab initio quantum dynamical analysis of ultrafast nonradiative transitions via conical intersections in pyrazine. *Physical Chemistry Chemical Physics*, 17(3):2012–2024, 2015.

[209] TG Dietz, MA Duncan, AC Puiu, and RE Smalley. Pyrazine and pyrimidine triplet decay in a supersonic beam. *The Journal of Physical Chemistry*, 86(20):4026–4029, 1982.

[210] K Sun, W Xie, L Chen, W Domcke, and MF Gelin. Multi-faceted spectroscopic mapping of ultrafast nonadiabatic dynamics near conical intersections: A computational study. *The Journal of Chemical Physics*, 153(17):174111, 2020.

[211] S Tsuru, ML Vidal, M Pápai, AI Krylov, KB Møller, and S Coriani. Time-resolved near-edge x-ray absorption fine structure of pyrazine from electronic structure and nuclear wave packet dynamics simulations. *The Journal of Chemical Physics*, 151(12), 2019.

[212] T Kaczun, AL Dempwolff, X Huang, MF Gelin, W Domcke, and A Dreuw. Tuning UV pump X-ray probe spectroscopy on the nitrogen K edge reveals the radiationless relaxation of pyrazine: ab initio simulations using the quasiclassical doorway–window approximation. *The Journal of Physical Chemistry Letters*, 14(24):5648–5656, 2023.

[213] E Wilson. *An introduction to particle accelerators*. Oxford University Press, 2001.

[214] G Shenoy. Basic characteristics of synchrotron radiation. *Structural Chemistry*, 14(1):3–14, 2003.

[215] M Magnuson. *Electronic Structure Studies Using Resonant X-ray and Photemission Spectroscopy*. PhD thesis, Uppsala University, 1999.

[216] JA Clarke. *The science and technology of undulators and wigglers*, volume 4. OUP Oxford, 2004.

[217] M Fuchs, R Weingartner, A Popp, Z Major, S Becker, J Osterhoff, I Cortrie, B Zeitler, R Hörlein, GD Tsakiris, et al. Laser-driven soft-X-ray undulator source. *Nature Physics*, 5(11):826–829, 2009.

[218] D Strickland and G Mourou. Compression of amplified chirped optical pulses. *Optics Communications*, 55(6):447–449, 1985.

[219] PB Corkum. Plasma perspective on strong field multiphoton ionization. *Physical Review Letters*, 71(13):1994, 1993.

[220] M Lewenstein, Ph Balcou, MY Ivanov, A L'huillier, and PB Corkum. Theory of high-harmonic generation by low-frequency laser fields. *Physical Review A*, 49(3):2117, 1994.

[221] HJ Wörner and PB Corkum. Attosecond spectroscopy. *Handbook of High-resolution Spectroscopy*, 2011.

[222] AL Lytle. *Phase matching and coherence of high-order harmonic generation in hollow waveguides*. PhD thesis, University of Colorado at Boulder, 2008.

[223] MV Frolov, AV Flegel, NL Manakov, and AF Starace. Rescattering effects in the multiphoton regime. *Journal of Physics B: Atomic, Molecular and Optical Physics*, 38(23):L375, 2005.

[224] XF Li, A l'Huillier, M Ferray, LA Lompré, and G Mainfray. Multiple-harmonic generation in rare gases at high laser intensity. *Physical Review A*, 39(11):5751, 1989.

[225] A L'Huillier and P Balcou. High-order harmonic generation in rare gases with a 1-ps 1053-nm laser. *Physical Review Letters*, 70(6):774, 1993.

[226] CM Heyl, J Güdde, A L'Huillier, and U Höfer. High-order harmonic generation with μJ laser pulses at high repetition rates. *Journal of Physics B: Atomic, Molecular and Optical Physics*, 45(7):074020, 2012.

[227] M Lewenstein, P Salieres, and A L'huillier. Phase of the atomic polarization in high-order harmonic generation. *Physical Review A*, 52(6):4747, 1995.

[228] E Constant, D Garzella, P Breger, E Mével, C Dorrer, C Le Blanc, F Salin, and P Agostini. Optimizing high harmonic generation in absorbing gases: Model and experiment. *Physical Review Letters*, 82(8):1668, 1999.

[229] P Salieres, A L'Huillier, and M Lewenstein. Coherence control of high-order harmonics. *Physical Review Letters*, 74(19):3776, 1995.

[230] E Takahashi, Y Nabekawa, T Otsuka, M Obara, and K Midorikawa. Generation of highly coherent submicrojoule soft x rays by high-order harmonics. *Physical Review A*, 66(2):021802, 2002.

[231] J Rothhardt, M Krebs, S Hädrich, S Demmler, J Limpert, and A Tünnermann. Absorption-limited and phase-matched high harmonic generation in the tight focusing regime. *New Journal of Physics*, 16(3):033022, 2014.

[232] J Metje. *Development and Application of a XUV Laser Light Source for Photoelectron Spectroscopy of Solutions*. PhD thesis, Freie University Berlin, 2017.

[233] B Winter. Liquid microjet for photoelectron spectroscopy. *Nuclear Instruments and Methods in Physics Research Section A: Accelerators, Spectrometers, Detectors and Associated Equipment*, 601(1-2):139–150, 2009.

[234] F Buchner. *Time-resolved photoelectron spectroscopy of DNA molecules in solution*. PhD thesis, Freie University Berlin, 2015.

[235] R Seidel, MN Pohl, H Ali, B Winter, and EF Aziz. Advances in liquid phase soft-X-ray photoemission spectroscopy: A new experimental setup at BESSY II. *Review of Scientific Instruments*, 88(7):073107, 2017.

[236] MH Berntsen. *Consequences of a non-trivial band-structure topology in solids: Investigations of topological surface and interface states*. PhD thesis, KTH Royal Institute of Technology, 2013.

[237] SK Eriksson, M Hahlin, JM Kahk, IJ Villar-Garcia, MJ Webb, H Grennberg, R Yakimova, H Rensmo, K Edström, A Hagfeldt, et al. A versatile photoelectron spectrometer for pressures up to 30 mbar. *Review of Scientific Instruments*, 85(7):075119, 2014.

[238] S Malerz, H Haak, F Trinter, AB Stephansen, C Kolbeck, M Pohl, U Hergenhahn, G Meijer, and B Winter. A setup for studies of photoelectron circular dichroism from chiral molecules in aqueous solution. *Review of Scientific Instruments*, 93(1):015101, 2022.

[239] AA Raheem. *Investigations of Photoinduced Ultrafast Dynamics in Metal Coordination Complexes Using Time-Resolved Photoemission and Absorption Spectroscopy*. Freie Universitaet Berlin (Germany), 2019.

[240] Dr. Stefan Böttcher. Kindly provided by specs gmbh. `https://www.specs-group.com/`.

[241] Surface concept. `https://www.surface-concept.com/detectors/line-position-resolving-delayline-detectors/`.

[242] J Nishitani, S Karashima, CW West, and T Suzuki. Surface potential of liquid microjet investigated using extreme ultraviolet photoelectron spectroscopy. *The Journal of Chemical Physics*, 152(14):144503,

2020.

[243] N Kurahashi, S Karashima, Y Tang, T Horio, B Abulimiti, Y Suzuki, Y Ogi, M Oura, and T Suzuki. Photoelectron spectroscopy of aqueous solutions: Streaming potentials of NaX (X= Cl, Br, and I) solutions and electron binding energies of liquid water and X^-. *The Journal of Chemical Physics*, 140(17):174506, 2014.

[244] CE Brion, KH Tan, and GM Bancroft. Synchrotron radiation studies of the Ar $3s^{-1}$ binding-energy spectrum: A comparison of experimental intensities and theory. *Physical review letters*, 56(6):584, 1986.

[245] GH Zschornack. *Handbook of X-ray data*. Springer Science & Business Media, 2007.

[246] LP Oloff, M Oura, K Rossnagel, A Chainani, M Matsunami, T Eguchi, T Kiss, Y Nakatani, T Yamaguchi, J Miyawaki, et al. Time-resolved HAXPES at SACLA: probe and pump pulse-induced space-charge effects. *New Journal of Physics*, 16(12):123045, 2014.

[247] DA Palmer, RW Ramette, and RE Mesmer. Triiodide ion formation equilibrium and activity-coefficients in aqueous-solution. *Journal of Solution Chemistry*, 13(9):673–683, 1984.

[248] VT Calabrese and A Khan. Polyiodine and polyiodide species in an aqueous solution of iodine + ki: theoretical and experimental studies. *The Journal of Physical Chemistry A*, 104(6):1287–1292, 2000.

[249] P Jungwirth and DJ Tobias. Ions at the air/water interface. *The Journal of Physical Chemistry B*, 106(25):6361–6373, 2002.

[250] I Fdez. Galván, M Vacher, A Alavi, C Angeli, F Aquilante, J Autschbach, JJ Bao, SI Bokarev, NA Bogdanov, RK Carlson, LF Chibotaru, J Creutzberg, N Dattani, MG Delcey, SS Dong, A Dreuw, L Freitag, LM Frutos, L Gagliardi, F G, A Giussani, L González, G Grell, M Guo, CE Hoyer, M Johansson, S Keller, S Knecht, G Kovačević, E Källman, G Li Manni, M Lundberg, Y Ma, S Mai, JP Malhado, P Malmqvist, P Marquetand, SA Mewes, J Norell, M Olivucci, M Oppel, QM Phung, K Pierloot, F Plasser, M Reiher, AM Sand, I Schapiro, P Sharma, CJ Stein, LK Sørensen, DG Truhlar, M Ugandi, L Ungur, A Valentini, S Vancoillie, V Veryazov, O Weser, TA Wesołowski, P Widmark, S Wouters, A Zech, JP Zobel, and R Lindh. OpenMolcas: From source code to insight. *Journal of Chemical Theory and Computation*, 15:5925–5964, 2019.

[251] T Åberg. Theory of X-ray satellites. *Physical Review*, 156:35–41, 1967.

[252] G Grell, SI Bokarev, B Winter, R Seidel, EF Aziz, SG Aziz, and O Kühn. Multi-reference approach to the calculation of photoelectron spectra including spin-orbit coupling. *The Journal of Chemical Physics*, 143:074104, 2015.

[253] V Kochetov, MS Ahsan, D Hein, I Wilkinson, and SI Bokarev. Valence and core photoelectron spectra of aqueous I_3^- from multi-reference quantum chemistry. *Molecules*, 28(14):5319, 2023.

[254] M Arbman, S Holmberg, M Lundholm, H Siegbahn, O Gropen, and U Wahlgren. Liquid ESCA measurements and ECP calculations on the 3D spectrum of I_3^-. *Chemical Physics*, 81(1-2):113–119, 1983.

[255] N Watanabe and M Takahashi. Revisiting electron-correlation effects on valence shake-up satellites of neon. *Physical Review A*, 100(3):032710, 2019.

[256] N Kosugi, H Kuroda, and S Iwata. Breakdown of koopmans' theorem and strong shake-up bands in the valence shell region of N_2 photoelectron spectra. *Chemical Physics*, 39(3):337–349, 1979.

[257] N Martensson, S Svensson, and U Gelius. Single and double shake-up processes in the Ne 1s photoelectron spectrum. *Journal of Physics B: Atomic and Molecular Physics*, 20(23):6243, 1987.

[258] MA Brisk and AD Baker. Shake-up satellites in X-ray photoelectron spectroscopy. *Journal of Electron*

Spectroscopy and Related Phenomena, 7(3):197–213, 1975.

[259] DA Shirley, S-T Lee, S Süzer, RL Martin, E Matthias, and RA Rosenberg. Electron correlation in atoms from photoelectron spectroscopy. In *Atomic Physics 5*, pages 313–323. Springer, 1977.

[260] M Isinger, RJ Squibb, D Busto, S Zhong, A Harth, D Kroon, S Nandi, CL Arnold, M Miranda, JM Dahlström, E Lindroth, R Feifel, M Gisselbrecht, and A L'Huillier. Photoionization in the time and frequency domain. *Science*, 358(6365):893–896, 2017.

[261] D Nordfors, A Nilsson, S Svensson, U Gelius, H Ågren, et al. X-ray excited photoelectron spectra of free molecules containing oxygen. *Journal of Electron Spectroscopy and Related Phenomena*, 56(2):117–164, 1991.

[262] CC Chusuei, MA Brookshier, and DW Goodman. Correlation of relative X-ray photoelectron spectroscopy shake-up intensity with CuO particle size. *Langmuir*, 15(8):2806–2808, 1999.

[263] W Kiefer and HJ Bernstein. The UV-laser excited resonance raman spectrum of the I_3^- ion. *Chemical Physics Letters*, 16(1):5–9, 1972.

[264] RM Lynden-Bell, R Kosloff, S Ruhman, D Danovich, and J Vala. Does solvation cause symmetry breaking in the I_3^- ion in aqueous solution? *The Journal of Chemical Physics*, 109(22):9928–9937, 1998.

[265] E Gershgoren, U Banin, and S Ruhman. Caging and geminate recombination following photolysis of triiodide in solution. *The Journal of Physical Chemistry A*, 102(1):9–16, 1998.

[266] Martin TZ and Robin MH. Two-dimensional infrared spectroscopy: a promising new method for the time resolution of structures. *Current Opinion in Structural Biology*, 11(5):516–522, 2001.

[267] M Khalil, N Demirdöven, and A Tokmakoff. Coherent 2D IR spectroscopy: molecular structure and dynamics in solution. *The Journal of Physical Chemistry A*, 107(27):5258–5279, 2003.

[268] R Fritzsch, S Hume, L Minnes, MJ Baker, GA Burley, and NT Hunt. Two-dimensional infrared spectroscopy: an emerging analytical tool? *Analyst*, 145(6):2014–2024, 2020.

[269] PB Miranda and YR Shen. Liquid interfaces: A study by sum-frequency vibrational spectroscopy. *The Journal of Physical Chemistry B*, 103(17):3292–3307, 1999.

[270] JP Kraack and P Hamm. Surface-sensitive and surface-specific ultrafast two-dimensional vibrational spectroscopy. *Chemical Reviews*, 117(16):10623–10664, 2017.

[271] M Ekimova, W Quevedo, Ł Szyc, M Iannuzzi, P Wernet, M Odelius, and ETJ Nibbering. Aqueous solvation of ammonia and ammonium: Probing hydrogen bond motifs with FT-IR and soft X-ray spectroscopy. *Journal of the American Chemical Society*, 139(36):12773–12783, 2017.

[272] S Thürmer, R Seidel, W Eberhardt, SE Bradforth, and B Winter. Ultrafast hybridization screening in Fe^{3+} aqueous solution. *Journal of the American Chemical Society*, 133(32):12528–12535, 2011.

[273] P Bolognesi, P O'Keeffe, V Feyer, O Plekan, K Prince, M Coreno, G Mattioli, AA Bonapasta, W Zhang, V Carravetta, Y Ovcharenko, and L Avaldi. Inner shell excitation, ionization and fragmentation of pyrimidine. In *Journal of Physics: Conference Series*, volume 212, page 012002. IOP Publishing, 2010.

[274] P O'Keeffe, P Bolognesi, AR Casavola, D Catone, N Zema, S Turchini, and L Avaldi. An experimental and computational study of the valence photoelectron spectra of halogenated pyrimidines. *Molecular Physics*, 107(19):2025–2037, 2009.

[275] KD Sevier. Atomic electron binding energies. *Atomic Data and Nuclear Data Tables*, 24(4):323–371, 1979.

[276] C Hannay, D Duflot, J-P Flament, and M-J Hubin-Franskin. The core excitation of pyridine and pyridazine: an electron spectroscopy and ab initio study. *The Journal of Chemical Physics*, 110(12):5600–5610, 1999.

[277] P Bolognesi, P O'Keeffe, Y Ovcharenko, M Coreno, L Avaldi, V Feyer, O Plekan, K Prince, W Zhang, and V Carravetta. Pyrimidine and halogenated pyrimidines near edge X-ray absorption fine structure spectra at C and N K-edges: experiment and theory. *The Journal of Chemical Physics*, 133(3):034302, 2010.

[278] T Buttersack, PE Mason, RS McMullen, T Martinek, K Brezina, D Hein, H Ali, C Kolbeck, C Schewe, S Malerz, et al. Valence and core-level X-ray photoelectron spectroscopy of a liquid ammonia microjet. *Journal of the American Chemical Society*, 141(5):1838–1841, 2019.

[279] PR Tentscher, R Seidel, B Winter, JJ Guerard, and JS Arey. Exploring the aqueous vertical ionization of organic molecules by molecular simulation and liquid microjet photoelectron spectroscopy. *The Journal of Physical Chemistry B*, 119(1):238–256, 2015.

[280] M Premont-Schwarz, S Schreck, M Iannuzzi, ETJ Nibbering, M Odelius, and P Wernet. Correlating infrared and X-ray absorption energies for molecular-level insight into hydrogen bond making and breaking in solution. *The Journal of Physical Chemistry B*, 119(25):8115–8124, 2015.

[281] H Ade and AP Hitchcock. NEXAFS microscopy and resonant scattering: composition and orientation probed in real and reciprocal space. *Polymer*, 49(3):643–675, 2008.

[282] BM McLaughlin and CP Ballance. *Photoionization, fluorescence, and inner-shell processes*. AccessScience, McGraw Hill, 2013.

[283] T Horio, Y Suzuki, and T Suzuki. Ultrafast photodynamics of pyrazine in the vacuum ultraviolet region studied by time-resolved photoelectron imaging using 7.8-eV pulses. *The Journal of Chemical Physics*, 145(4):044307, 2016.

[284] Y Miura, Y Yamamoto, S Karashima, N Orimo, A Hara, K Fukuoka, T Ishiyama, and T Suzuki. Formation of long-lived dark states during electronic relaxation of pyrimidine nucleobases studied using extreme ultraviolet time-resolved photoelectron spectroscopy. *Journal of the American Chemical Society*, 145(6):3369–3381, 2023.

[285] MA Montanez, IL Tocón, JC Otero, and JI Marcos. Effect of hydrogen bonding on the vibrational frequencies of pyrazine. *Journal of Molecular Structure*, 482:201–205, 1999.

[286] DB McDonald, GR Fleming, and SA Rice. Intermediate case radiationless decay: the excited state dynamics of pyrazine. *Chemical Physics*, 60(3):335–345, 1981.

[287] I Yamazaki, T Murao, and K Yoshihara. Subnanosecond fluorescence lifetimes of pyrazine-h_4 and -d_4 vapor for photoselected vibrational levels in the S_1 (n, π^*) state. *Chemical Physics Letters*, 87(4):384–388, 1982.

[288] Y Udagawa, M Ito, and I Suzuka. Single vibronic level fluorescence from n, π* state of pyrazine vapor. *Chemical Physics*, 46(1-2):237–249, 1980.

[289] JL Tomer, KW Holtzclaw, DW Pratt, and LH Spangler. Phosphorescence excitation spectroscopy in supersonic jets. The lowest triplet state of pyrazine. *The Journal of Chemical Physics*, 88(3):1528–1538, 1988.

[290] DV Bent, E Hayon, and PN Moorthy. Chemistry of the triplet state of diazines in solution studied by laser spectroscopy. *Journal of the American Chemical Society*, 97(18):5065–5071, 1975.

[291] RA Nome. Ultrafast dynamics of solvation: the story so far. *Journal of the Brazilian Chemical Society*,

21:2189–2204, 2010.

[292] D Sharma, J Léonard, and S Haacke. Ultrafast excited-state dynamics of tryptophan in water observed by transient absorption spectroscopy. *Chemical Physics Letters*, 489(1-3):99–102, 2010.

[293] O Bram, AA Oskouei, A Tortschanoff, F van Mourik, M Madrid, J Echave, A Cannizzo, and M Chergui. Relaxation dynamics of tryptophan in water: a UV fluorescence up-conversion and molecular dynamics study. *The Journal of Physical Chemistry A*, 114(34):9034–9042, 2010.

[294] TJ Penfold, E Gindensperger, C Daniel, and CM Marian. Spin-vibronic mechanism for intersystem crossing. *Chemical Reviews*, 118(15):6975–7025, 2018.

[295] EM Arpa, MM Brister, SJ Hoehn, CE Crespo-Hernández, and I Corral. On the origin of the photostability of DNA and RNA monomers: excited state relaxation mechanism of the pyrimidine chromophore. *The Journal of Physical Chemistry Letters*, 11(13):5156–5161, 2020.

[296] S Yamaguchi and T Tahara. Precise electronic $\chi^{(2)}$ spectra of molecules adsorbed at an interface measured by multiplex sum frequency generation. *The Journal of Physical Chemistry B*, 108(50):19079–19082, 2004.

[297] D Mayer, F Lever, D Picconi, J Metje, S Alisauskas, F Calegari, S Düsterer, C Ehlert, R Feifel, M Niebuhr, et al. Following excited-state chemical shifts in molecular ultrafast X-ray photoelectron spectroscopy. *Nature Communications*, 13(1):198, 2022.

[298] TJA Wolf, RH Myhre, JP Cryan, S Coriani, RJ Squibb, A Battistoni, N Berrah, C Bostedt, P Bucksbaum, G Coslovich, et al. Probing ultrafast $\pi\pi^*$/nπ^* internal conversion in organic chromophores via K-edge resonant absorption. *Nature Communications*, 8(1):29, 2017.

[299] A Ponzi, M Rosa, G Kladnik, I Unger, A Ciavardini, L Di Nardi, E Viola, C Nicolas, N Došlić, A Goldoni, et al. Inequivalent solvation effects on the N 1s levels of self-associated melamine molecules in aqueous solution. *The Journal of Physical Chemistry B*, 127(13):3016–3025, 2023.

[300] N Iza, M Gil, JL Montero, and J Morcillo. Self-association of uracil in aqueous solution. Study of dilute solutions by normal and second derivative UV absorption spectroscopy. *Journal of Molecular Structure*, 175:19–24, 1988.

[301] JC Dearden. Investigation of the self-association of phenols and anilines by ultraviolet spectroscopy. *Canadian Journal of Chemistry*, 41(10):2683–2691, 1963.

[302] A Herbaut and E Baranoff. UV-visible absorption study of the self-association of non-ionic chromonic triphenylenes TP6EOnM (n= 2, 3, 4) in dilute aqueous solutions: impact of chain length on aggregation. *Chimia*, 69(9):520–520, 2015.

[303] A Fernandez-Perez and G Marban. Visible light spectroscopic analysis of methylene blue in water; what comes after dimer? *ACS Omega*, 5(46):29801–29815, 2020.